



Toward aqueous superconcentrated electrolytes for Li-ion battery application

Léa Droguet

► To cite this version:

Léa Droguet. Toward aqueous superconcentrated electrolytes for Li-ion battery application. Materials. Sorbonne Université, 2021. English. NNT : 2021SORUS330 . tel-03553001

HAL Id: tel-03553001

<https://theses.hal.science/tel-03553001>

Submitted on 2 Feb 2022

HAL is a multi-disciplinary open access archive for the deposit and dissemination of scientific research documents, whether they are published or not. The documents may come from teaching and research institutions in France or abroad, or from public or private research centers.

L'archive ouverte pluridisciplinaire **HAL**, est destinée au dépôt et à la diffusion de documents scientifiques de niveau recherche, publiés ou non, émanant des établissements d'enseignement et de recherche français ou étrangers, des laboratoires publics ou privés.

Sorbonne Université

Ecole doctorale 397 - Physique et Chimie des Matériaux

Chimie du Solide et Énergie, Collège de France, UMR 8260

Vers des électrolytes aqueux superconcentrés pour une application dans les batteries Li-ion

Par Léa Droguet

Thèse de doctorat de Physique et Chimie des Matériaux

Dirigée par Jean-Marie Tarascon, Alexis Grimaud et Olivier Fontaine

Présentée et soutenue publiquement le 13 Décembre 2021

Devant un jury composé de :

Prof. Rosa Palacín	Professeure, ICMAB, Barcelona, Spain	Rapporteuse
Dr. Mathieu Morcrette	Ingénieur de Recherche HDR, LRCS, Amiens	Rapporteur
Dr. Frédéric Kanoufi	Directeur de Recherche, ITODYS, Paris	Examinateur
Dr. Corsin Battaglia	Directeur de Recherche, EMPA, Zürich, Suisse	Examinateur
Prof. Jean-Marie Tarascon	Professeur, Chimie du Solide et Énergie, Paris	Directeur
Dr. Alexis Grimaud	Chargé de Recherche, Chimie du Solide et Énergie, Paris	Encadrant
Dr. Olivier Fontaine	Maitre de Conférence, ICGM, Montpellier	Encadrant



Except where otherwise noted, this work is licensed under
<http://creativecommons.org/licenses/by-nc-nd/3.0/>



Sorbonne Université

Ecole doctorale 397 - Physique et Chimie des Matériaux

Chimie du Solide et Energie, Collège de France, UMR 8260

Towards aqueous superconcentrated electrolytes for Li-ion battery

By Léa Droguet

Ph.D. thesis of Physics and Chemistry of Materials

Supervised by Jean-Marie Tarascon, Alexis Grimaud and Olivier Fontaine

Presented and defended publicly on December 13th, 2021

In front of the Jury:

Prof. Rosa Palacín	Professor, ICMAB, Barcelona, Spain	Referee
Dr. Mathieu Morcrette	Research Engineer, LRCS, Amiens	Referee
Dr. Frédéric Kanoufi	Research Director, ITODYS, Paris	Examiner
Dr. Corsin Battaglia	Research Director, EMPA, Zürich, Switzerland	Examiner
Prof. Jean-Marie Tarascon	Professor, Chimie du Solide et Energie, Paris	Ph.D. director
Dr. Alexis Grimaud	Research Scientist, Chimie du Solide et Energie, Paris	Supervisor
Dr. Olivier Fontaine	Associate Professor, ICGM, Montpellier	Supervisor



Except where otherwise noted, this work is licensed under <http://creativecommons.org/licenses/by-nc-nd/3.0/>

Acknowledgements

I would like to express my gratitude to my supervisors in Collège de France, Jean-Marie Tarascon and Alexis Grimaud for giving me the opportunity to work in this extraordinary environment. Their energy and availability to students are truly inspiring and their dedication to science is absolutely impressive. I have learnt a lot from working with and around them. Farther from Collège de France, I would also like to acknowledge my supervisor Olivier Fontaine.

After completed this three years, I am grateful to Fanny, Thomas, Nicolas, Pierre, Damien, Romain, Ivette, Benjamin, Charlotte, Jiaqiang and Laura for the great times spent during this phd journey in and out the lab. Qing, Linje, Biao, Tuncay, Parth and Anshuman and are also thanks for the calm but always warm office atmosphere. I also want to thank all the other talented CSE lab members with whom I shared this journey, all of you ensured a valuable scientific and friendly atmosphere.

I would also like to thank the collaborators without whom part of this thesis would not have been the same: Marie-Francine Lagadec (CSE, Collège de France, Paris) for the E-SEM observations, Thomas Marchandier (CSE, Collège de France) for the time spent on the XRD trials, Maxime Hallot and Christophe Lethien (IEMN, Université de Lille) for the Al_2O_3 -ALD, Matthieu Courty (LRCS, Amiens) for the DSC experiments and Steven Le Vot, Marion Maffre and Mathieu Deschanel (ICGM, Montpellier) for their welcome and help during my stay in Montpellier. I also truly thank Gustavo Hobold, Rui Guo and Betar Gallant (Department of mechanical engineering, MIT, Cambridge) for the technical support (Li/LiF samples, XPS and GC-TCD experiments) and the fruitful discussions.

The French National Research Agency through the Labex STORE-EX project (ANR-10-LABX-76-01) and the Direction Générale de l'Armement through the Agence innovation defense are acknowledge for the financial support.

I acknowledge Prof. Rosa Palacín and Dr. Mathieu Morcrette for agreeing to review this thesis. I also thank Dr. Frédéric Kanoufi and Dr. Corsin Battaglia for accepting to be part of the jury.

Last but not least, I want to express my immensely gratitude to my friends and family for their support during both joyful and difficult moments. Their support goes well beyond these three years.

Table of contents

ACKNOWLEDGEMENTS	5
GENERAL INTRODUCTION AND THESIS OUTLINE.....	13
CHAPTER 1 –INTRODUCTION TO AQUEOUS SUPERCONCENTRATED ELECTROLYTE AND THEIR USE IN LI-ION BATTERY (LIB)	19
1 FROM AQUEOUS SECONDARY BATTERY TO LI-ION BATTERIES (LIB): LOOKING FOR HIGH-ENERGY DEVICES.....	20
2 AQUEOUS SUPERCONCENTRATED ELECTROLYTE: CAN THE MODIFICATION OF THE PHYSICO-CHEMICAL PROPERTIES AND THE INTERFACIAL REACTIVITY UNLOCK THE COMPETITIVENESS OF AQUEOUS LI-ION BATTERIES?	35
3 FURTHER IMPROVING AQUEOUS SUPERCONCENTRATED-BASED LIB, EXPANDING THE ESW LIMIT AT THE NEGATIVE ELECTRODE SIDE.....	48
CONCLUSION OF THE CHAPTER	58
CHAPTER 2 – CYCLING VIABILITY OF AQUEOUS SUPERCONCENTRATED ELECTROLYTES BASED ON 20 MOL/KG LITFSI AND 20 MOL/KG LITFSI : 8 MOL/KG LIBETI	61
INTRODUCTION	62
1 CYCLING PERFORMANCES IN AQUEOUS SUPERCONCENTRATED ELECTROLYTE ON THE NEGATIVE ELECTRODE SIDE: ROLE OF CONCENTRATION, CYCLING RATE AND TEMPERATURE.....	65
2 ORIGIN OF THE PERFORMANCES DECAY: A GAS MONITORING STUDY.....	71
3 SELF-DISCHARGE PROTOCOL TO ASSESS AQUEOUS SUPERCONCENTRATED ELECTROLYTES VIABILITY DURING RESTING PERIOD	78
4 CYCLING VIABILITY ON THE POSITIVE SIDE: A GAS MONITORING STUDY.....	87
CONCLUSION OF THE CHAPTER	91
CHAPTER 3 – INSTABILITY OF NATIVE SEI LEADS TO THE DRYING OUT OF AQUEOUS SUPERCONCENTRATED LI-ION BATTERY	95
INTRODUCTION	96
1 PROBING THE SEI INSTABILITY IN AQUEOUS SUPERCONCENTRATED ELECTROLYTES	97

2 IMPACT OF WATER CONSUMPTION ON ELECTROLYTE CRYSTALLIZATION	106
3 ACTIVATION ENERGY OF DIRECT AND INDIRECT HER IN WISE	111
DISCUSSION AND CONCLUSION OF THE CHAPTER	119
 CHAPTER 4 –MIMICKING INORGANIC-BASED SEI WITH LIF-COATING.	
UNDERSTANDING OF INORGANIC SEI LIMITATIONS IN <i>WATER-IN-SALT</i> ELECTROLYTE.	127
INTRODUCTION	128
1 LIF SOLUBILITY LIMIT IN AQUEOUS SUPERCONCENTRATED ELECTROLYTE	129
2 USING LI/LIF-COATING TO MIMIC INORGANIC-BASED SEI. EXPOSURE TO ATMOSPHERE ENVIRONMENT, AQUEOUS SUPERCONCENTRATED ELECTROLYTE AND COMPARISON WITH THE BEHAVIOR OBSERVED IN ORGANIC ELECTROLYTE	134
3 COMPARISON OF LIF BEHAVIOR WITH Al_2O_3 -COATED LI SAMPLE.....	140
4 FILLING THE STRUCTURAL DEFECTS BY PRESOAKING IN ORGANIC ELECTROLYTE: ASSESSMENT OF THE IMPORTANCE OF AN ORGANIC-INORGANIC BASED SEI	144
CONCLUSION OF THE CHAPTER	150
 GENERAL CONCLUSION AND PERSPECTIVES	155
 REFERENCES.....	161
 APPENDIX	187
 MATERIALS & METHODS.....	209
1 MATERIAL PREPARATION	210
2 ELECTROCHEMICAL CHARACTERIZATIONS.....	214
3 PHYSICO-CHEMICAL CHARACTERIZATIONS.....	221
4 DATA TREATMENT	228
5 PYTHON	236
 LIST OF ABBREVIATIONS	237

RÉSUMÉ EN FRANÇAIS 243

GENERAL INTRODUCTION AND THESIS OUTLINE

General introduction

The replacement of fossil fuels by renewable energies is at the center of the energy transition critically needed to limit climate change. However, limitations of greenhouse gases emission (carbon dioxide (CO_2), methane (CH_4), nitrous oxide (N_2O) and fluorinated gases) may be in conflict with the energy demand. Indeed, as calculated by the International energy agency (IEA), the latter is set to increase by 4.1 % in 2021, mostly due to the increase in demand from emerging markets and developing economies. Hence, despite the contraction of the demand due to the Covid 19 pandemic, in 2020 energy consumption exceeds by 4 % the 2019 level, going back to pre-Covid level. Furthermore, regardless of the scenario taken into account, the energy demand continuously increases (see Figure Introduction. 1 and the description of the scenario in the caption of Figure Introduction. 1).

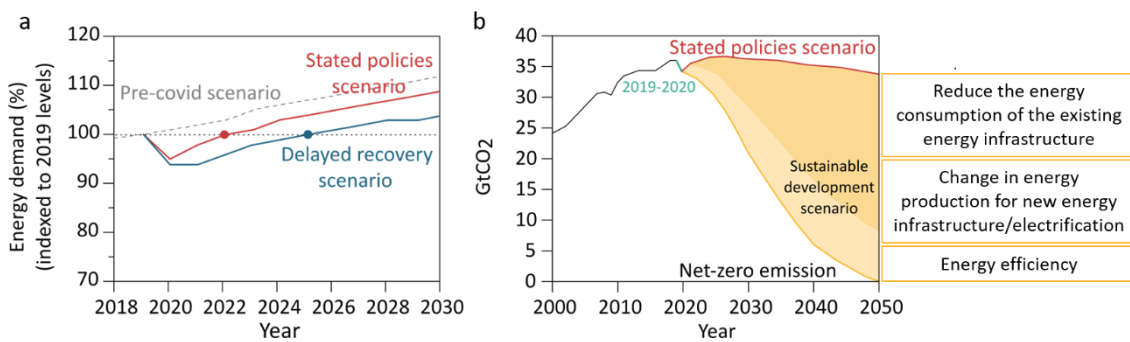


Figure Introduction. 1 (a) Forecast of the global energy demand increase indexed to their level in 2019. Scenario envisioned: (i) pre-Covid scenario, (ii) stated policies which correspond to a situation back to normal, *i.e.* similar to pre-Covid one, in 2022 and (iii) delayed recovery scenario corresponding to a prolonged crisis which would be back to pre-pandemic level in 2025 with strong impact on the energy demand growth). Adapted from Ref¹. (b) Forecast of the worldwide CO_2 emissions (in giga ton per year) until 2030. Adapted from Ref².

As a consequence, impactful policies and major investments in clean energy (up to four trillion USD a year until 2030, as mentioned in the world energy outlook of 2021) need to be set up to reach the sustainable development scenario that considers the fulfillment of the objectives discussed during the Paris agreement (which aim to limit the increase in temperature to 1.5 °C by the end of the century). Even more challenging is the Net zero emission scenario by 2050 (rather than 2070 in the sustainable development scenario). Thus, changes in energy production, reduction in energy consumption, improvement in energy efficiency and innovation in carbon capture can be seen as the main pillars to succeed in meeting these goals, as illustrated in Figure

Introduction. 1b. To succeed in this great challenge, electrification can be seen as one of the main path to develop, among others such as promoting clean energy innovation or changing societal behaviors. Indeed, 75 % of the world electricity demand should be produce from low-carbon energy sources by 2030 (compared to less than 40 % in 2019). Though, electricity produced by renewable energies such as solar or wind power is intermittent, therefore the urgent need for storage devices.

Many applications from electrical, thermal, and mechanical to electrochemical devices can store energy. Among electrochemical ones, batteries market is greatly increasing within the last ten years and is forecasted to grow up even more with the development of Li-ion batteries (LIB) in the transportation market, leading to a global market opportunity to 2050 worth USD 16.2 trillion. Indeed, while Lead-acid battery used to be the most widely used technology, 2020 has seen LIB to dominate the market. This trend is confirmed by forecasts that announce that the LIB market will almost double within the next 10 years, as shown in Figure Introduction. 2a. Such conquest of the market is enabled by technology advances due to cell chemistry innovation, cell engineering and optimization and growth of manufacturing volume than enable to improve performances and reliability while decreasing the cost of the cell (see Figure Introduction. 2b). Though, as LIB battery market is increasing markedly, the anticipation of LIB battery recycling as well as the development of more sustainable battery component is of crucial importance.

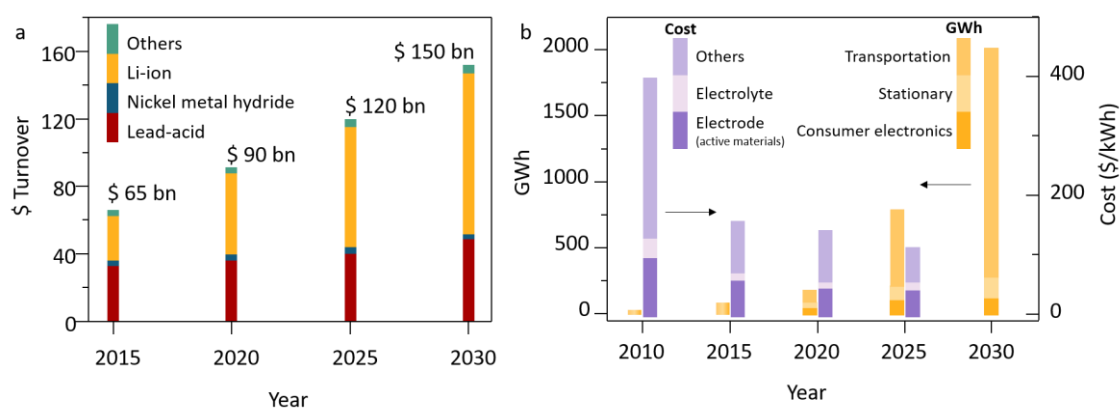


Figure Introduction. 2 (a) Battery market demand in the world (in \$) from 2015 to 2030. (b) Forecast of global annual Li-ion battery (LIB) deployment in all markets in GWh and LIB cell average cost (in purple) as function of time. The cell is based on a 40 Ah pouch cell made of $\text{LiNi}_{0.6}\text{Mn}_{0.2}\text{Co}_{0.2}\text{O}_2$ (NMC₆₂₂) as positive electrode and graphite as negative. Adapted from Ref^{3,4}.

Outline of the thesis

Therefore, the aim of this thesis is to study the practicability of developing LIB using aqueous superconcentrated electrolytes, so-called *Water-in-salt* electrolytes (WiSE). Indeed, this technology would enable the use of environmental-friendly solvent, *i.e.* water, while achieving performances close to commercial LIB.

The thesis is structured in five chapters detailed as follow.

The first chapter briefly summarizes the Lead-acid, Nickel Cadmium, Nickel Metal hydride and commercial LIB battery technologies. Then, the concept of aqueous superconcentrated electrolyte is introduced, giving details on how the solvation structures of such electrolytes impact their physico-chemical properties and interfacial reactivity and consequently the battery performances. Eventually, the modifications regarding electrolyte composition proposed in the literature in the last five years are detailed.

The second chapter describes a systematic study that assesses the practicability of WiSE-based LIB by decoupling parasitic reactions at the negative and positive electrodes and by performing electrochemical characterizations during cycling and self-discharge tests as well as operando gas monitoring. The stability of these electrolyte was determined to suffer from water reduction at the negative electrode both during cycling and resting periods, unlike positive electrode where very limited water oxidation was observed.

Then, in the third chapter, we analyze the stability of the native solid electrochemical interphase (SEI) by electrochemical characterizations, using cyclic voltammetry and impedance spectroscopy. Besides, the irreversible consumption of water which leads to increase in electrolyte concentration was confirmed by differential scanning calorimetry. Based on the electrochemical results, the rate of water consumption during resting period was found to be smaller than the one during cycling, though in the same order of magnitude. The rate of Li^+ delithiation was also found to be different when comparing constant current continuous cycling and self-discharge experiments. To understand these observations, the activation energy of self-discharge process and direct water reduction were determined. Eventually, to summarize and rationalize these electrochemical results, a figure-of-merit was made to compare the performances of WiSE-based LIB with that of commercial LIB and other commercial aqueous secondary

batteries with the largest production volume (Lead-acid, Nickel-Cadmium and Nickel Metal hydride).

Moreover, as LiF is known to be the SEI component in WiSE, and following the first two chapters in which the instability of the native SEI was highlighted, LiF solubility measurements were performed in WiSE electrolyte to determine if LiF dissolution is responsible for the SEI instability. Then, an artificial LiF conformal layer was deposited onto metallic Li (Li/LiF) to assess the protective-power of inorganic coatings against water-based electrolytes. Gas chromatography-mass spectrometry was done to analyze the reactivity of the Li/LiF sample to WiSE exposure as well as the impact of presoaking Li/LiF samples in organic electrolyte to improve the efficiency of these coating toward water reduction. Similar observations were made with conformal Al_2O_3 coatings prepared by atomic layer deposition (ALD).

Altogether, this manuscript highlights that despite the formation of a LiF-inorganic SEI in 20 m LiTFSI, water reduction cannot be avoided at the negative electrode and artificial inorganic coatings are not sufficient to prevent water to access the negative interface. Therefore, the cathodic challenge remains unsolved.

CHAPTER 1 –
INTRODUCTION TO
AQUEOUS
SUPERCONCENTRATED
ELECTROLYTE AND THEIR
USE IN LI-ION BATTERY
(LIB)

1 From aqueous secondary battery to Li-ion batteries (LIB): looking for high-energy devices

1.1 Aqueous secondary batteries

Secondary or rechargeable batteries are nowadays widely used in many applications, from grid storage, electrical transportation to portable devices. As any electrochemical devices, they are made by assembling two electrodes with different redox potentials, separated by an electrolyte which is generally composed of a solvent and a supporting salt. The electrons circulate through the external electrical circuit, thus enabling the reversible energy exchange with the user, as shown in Figure 1. 1.

The history of secondary batteries started more than 150 years ago, in 1859, by the development of rechargeable Lead-acid batteries by Gaston Planté who designed the $\text{Pb} \parallel \text{H}_2\text{SO}_4 \parallel \text{PbO}_2$ cell, as described in Figure 1. 1. The associated electrochemical process is based on a dissolution/precipitation mechanism directly involving the acidic electrolyte. Thanks to their low cost, low self-discharge, maturity and reliability, Lead-acid batteries are still widely used for unit power sources (UPS), starting lighting and ignition in vehicles (SLI) and emergency lighting. However, the specific energy and energy density - calculated as function of the cell voltage (V) and the cell capacity (Ah/kg) (see Equation 1. 1) and expressed either in $\text{Wh/kg}_{\text{cell}}$ or $\text{Wh/L}_{\text{cell}}$ - is limited to 60 $\text{Wh/kg}^{5,6}$.

Equation 1. 1:

$$E_{\text{specific}}^{\text{Wh/kg}} = Q \left(\frac{\text{Ah}}{\text{kg}} \right) \cdot V \text{ (V)}$$

Following this pioneering work, Nickel-Cadmium (Ni-Cd) batteries were introduced in 1909. For this technology, the negative electrode (Cd) endorses a conversion reaction while the positive electrode, NiOOH , is reduced or oxidized upon discharge or charge, respectively, as illustrated in Figure 1. 1b. Besides, their low cost and high rate performances favor the use of Ni-Cd batteries for power tools, and they were introduced in early mobile phone model. However, the “memory effect”, the toxicity of Cd and the limited specific energy ($< 60 \text{ Wh/kg}$) limit the overall performances of this chemistry and called for the development of other technologies. Therefore, from the mid-80s⁷, a second generation of rechargeable batteries was introduced with the design of nickel-metal hydride (Ni-MH) batteries using alkaline electrolyte. Ni-MH batteries use a similar positive electrode than Ni-Cd, NiOOH , but the electrochemistry at the negative

electrode relies on intercalation mechanism rather than conversion one (see Figure 1. 1c). Indeed, upon discharge the hydrogen de-intercalates from the metal hydride (MH) to form a metal alloy (M), and combines with hydroxide anions from the electrolyte to form water. Ni-MH batteries reach high capacity (110 Wh/kg) with a lesser “memory effect” than in Ni-Cd ones. Therefore, they were implemented in commonly-used AA and AAA cells for portable devices, as well as in the first hybrid-electric vehicles (Toyota Prius). Aside from these three chemistries that, until 2015, represented the commercial batteries with the largest production volume and USD turnover^{3,4}, several other aqueous systems were developed in the past decades, including Nickel-iron, Silver-zinc or Silver-cadmium⁷ batteries, which will not be discussed in this section.

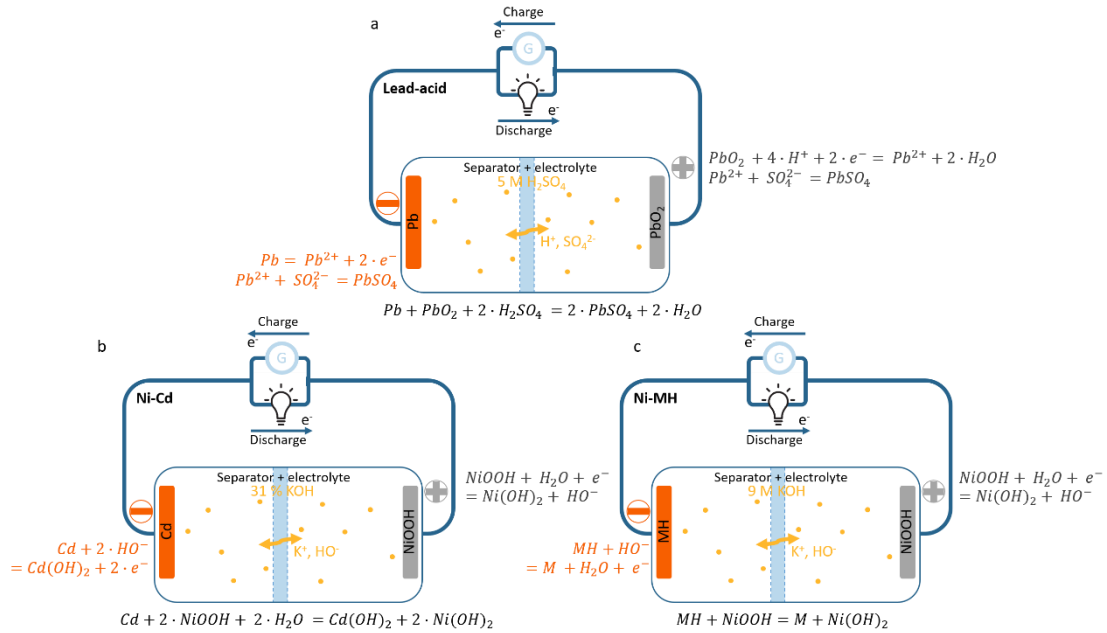
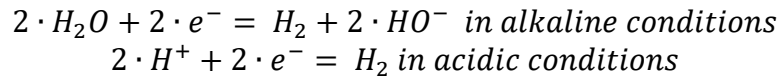


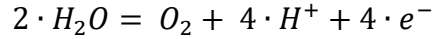
Figure 1. 1 Chemical reactions taking place in (a) Lead-acid, (b) Nickel-Cadmium (Ni-Cd), (c) Nickel-metal hydride (Ni-MH) batteries.

Despite these advances in cell performances, the electrochemical stability window (ESW) of water, and thus of aqueous devices, is limited to 1.23 V, as shown by the yellow zone in Figure 1. 2a. Above this limit, the hydrogen evolution reaction (HER) occurs upon reduction while the oxygen evolution reaction (OER) happens upon oxidation, as described by Equation 1. 2 and Equation 1. 3, respectively.

Equation 1. 2: Hydrogen evolution reaction (HER).



Equation 1. 3: Oxygen evolution reaction (OER).



Cycling aqueous batteries within the thermodynamically stable potential window of water to avoid these parasitic reactions drastically limits the battery voltage and thus the specific energy, as shown in Figure 1. 2b. One obvious way to increase the energy density is to extend the operating voltage beyond the stability window while finding means to handle the gas generated during cycling, as implemented in Lead-acid, Ni-Cd and Ni-MH batteries and discussed in greater details in Chapter 3. To overcome the voltage limitation in aqueous environment, Li-based batteries were introduced using organic electrolyte to replace aqueous proton-based chemistries. Lithium was chosen for its light weight (6.94 g/mol), its low redox potential ($E_{Li^+/Li}^0 = -3.04$ V vs ESH) and its high theoretical capacity (3862 mA.h/g), thus promising high energy batteries, as illustrated in Figure 1. 2b.

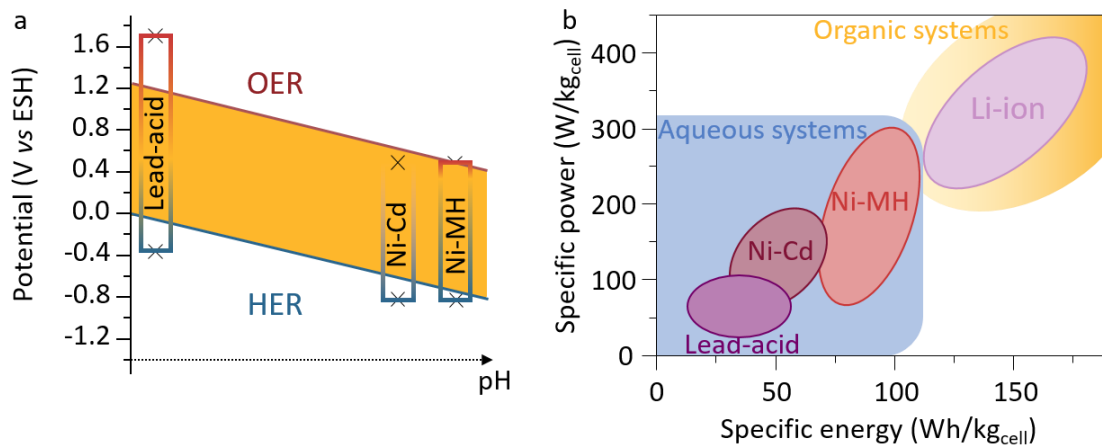
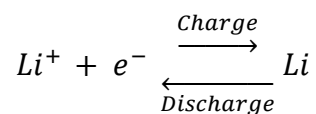


Figure 1. 2 (a) Pourbaix diagram representing the operating voltage of Lead-acid, Ni-Cd and Ni-MH batteries and the electrochemical stability window (ESW) of water (yellow zone) defined by the hydrogen evolution reaction (HER) upon water reduction and the oxygen evolution reaction (OER) upon water oxidation. (b) Ragone plot of secondary aqueous batteries and organic Li-ion batteries (LIB). Adapted from Ref⁵⁻⁹.

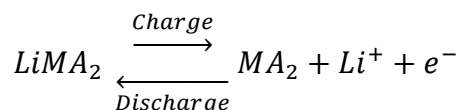
1.2 Li metal and Li-ion battery (LIB)

The development of Li-based batteries started in the 1970s with the use of metallic Li as negative electrode and an intercalation electrode as positive one. This technology was implemented by coupling the use of metallic Li (see Equation 1. 4) with the discovery, notably by Stanley Whittingham, of the reversible insertion of Li^+ cation into chalcogenide-based materials such as TiS_2 or MoS_2 ^{10–13}, as described in Equation 1. 5. These systems were then commercialized by Exxon in 1972 using TiS_2 as positive and Moli Energy in the late 1980¹⁴ using MoS_2 as positive.

Equation 1. 4: Intercalation of Li^+ cation in the positive electrode.



Equation 1. 5: Reaction at the metallic Li electrode.



with M , transition metal and A , oxygen or sulfur

Li metal battery behavior upon discharging and charging is illustrated in Figure 1. 3. The metallic Li negative electrode is separated from the positive electrode by a separator soaked with the aprotic organic liquid electrolyte. Aluminum is used as current collector on the positive side while copper is generally used as current collector on the negative side since metallic Li is known to alloy with Al, inducing a volume change causing pulverization of Al. As shown in Figure 1. 3b, during charge, metallic Li is plated at the negative, which can lead to dendrite growth that can short-circuit the cell and inflame the organic electrolyte, causing severe safety issues¹⁵. One way to improve safety was to replace the liquid flammable electrolyte by a less flammable polymer one which also prevents dendritic growth. However, to ensure good conductivity (σ) of Li^+ cations, polymer electrolytes need to be heated up to $\approx 60^\circ\text{C}$, thus limiting the user-friendliness for portable applications.

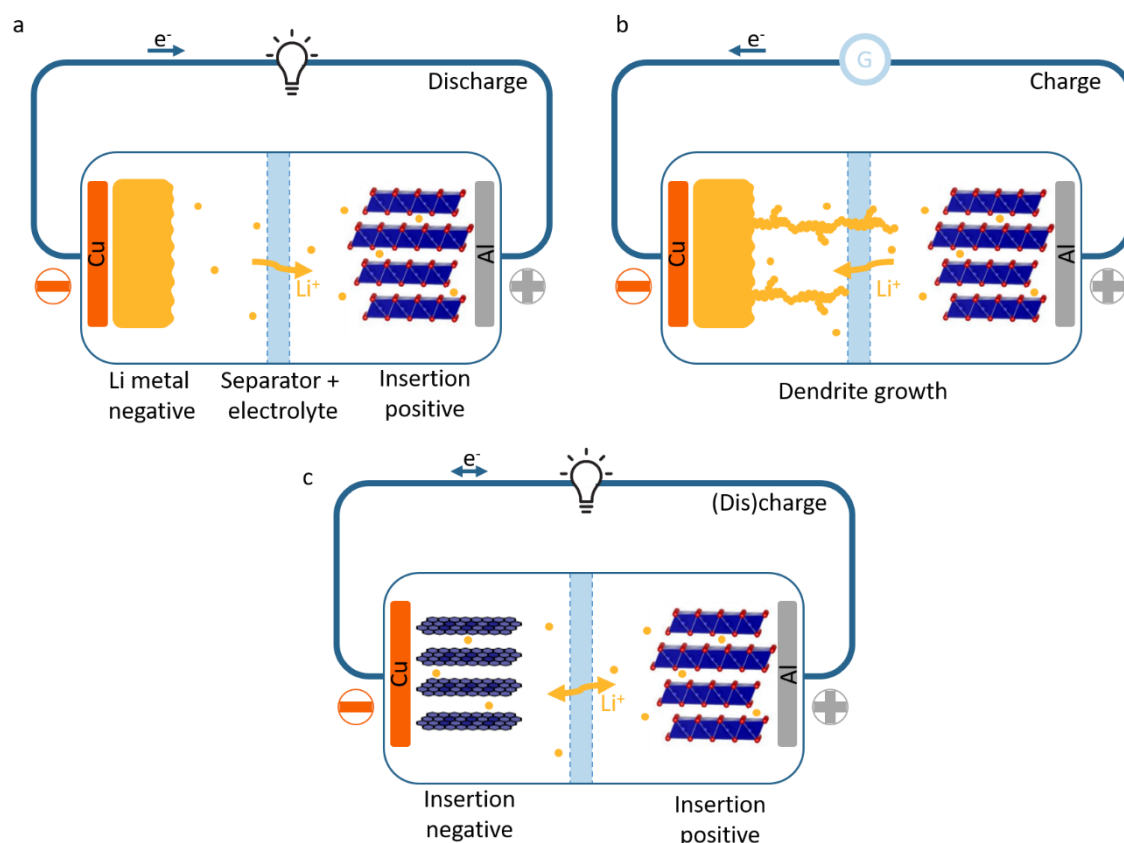


Figure 1. 3 Scheme of (a-b) a Li metal battery, (c) a Li-ion cell. In this schematic view, only Li^+ cations are drawn. Solvent molecules and counter anions are not shown. Ionic and electronic flows are symbolized with arrows. (a) Upon discharge. (b) Upon charge. (c) The metallic Li negative electrode is replaced by an insertion electrode to make a Li-ion cell.

In 1980, John Goodenough and coworkers replaced sulfur-based positive electrode by oxygen-based one (thus taking advantage of the greater electronegativity of oxygen) and paved the way for the integration of lithium-containing transition metal oxide $Li_{1-x}CoO_2$ (LCO) positive electrodes with high potential ($E_{Li\text{ insertion}} > 3\text{ V vs } Li^+/Li$). Following this pioneering work, numerous studies were carried out, including for reducing the Co content that has rapidly become a concern for large scale commercialization due to ethical, cost, and toxicity as well as due to limitations in the reversible capacity achieved by LCO – reversible discharge capacity of 140 mAh/g is attainable in practice, compared to 275 mAh/g theoretically available. Therefore, many researches then focused on partially substituting Co in $LiMO_2$ ($M = Co, Ni, Mn, Al \dots$) layered materials. While Co was found necessary to stabilize the electrode structure^{16,17}, it was partially substituted with Ni to achieve greater capacity ($> 150\text{ mA.h/g}$). Besides, the partial substitution of Ni by Al or Mn was found to thermally stabilize the electrode, thus giving birth to the NCA and NCM (or NMC)-families in which several ratio of Ni:Co:Al or Ni:Co:Mn were

developed^{18,19}. Cobalt-free positive electrodes also emerged relying on cheap and abundant materials as well as their thermally stable properties, despite their lower capacity and potential. Mn is generally used in spinel structure²⁰, LiMn_2O_4 (LMO) and Fe with polyanionic compounds ($(\text{XO}_4)^{3-}$ ($\text{X}=\text{S}, \text{P}, \text{Si}, \text{As}, \text{Mo}, \text{W}$)), with the well-known olivine LiFePO_4 (LFP) for example.

Besides achieving greater potential and reversible capacity, the development of lithiated positive electrode unlocked the use of non-lithiated intercalation electrode to replace metallic Li as negative material, giving birth to the so-called Li-ion rocking-chair battery²¹, as illustrated in Figure 1. 3c. To realize the concept of high potential rocking-chair battery, intercalation material operating at low potential were required. Carbonaceous materials (soft or hard carbons) were first envisioned as alkali-ions intercalation materials. However, Li^+ intercalation in these materials (below 1 V vs Li^+/Li)^{22,23} was initially found to cause electrode exfoliation, owing to the use of propylene carbonate (PC)-solvent which co-intercalates during charge, thus initially impeding the commercialization of LIB.

Indeed, commercial electrolyte solvents for aprotic batteries are generally based on carbonate esters, as they enable high Li-salt dissolution and dissociation. One cyclic and one linear carbonate are generally mixed to combine their properties. Linear esters such as dimethyl carbonate (DMC), ethyl methyl carbonate (EMC) or diethyl carbonate (DEC) have low viscosity (0.59 mPa.s for DMC, 0.65 mPa.s for EMC and 0.75 mPa.s for DEC), thus enabling good transport properties. In contrast, cyclic ester such as ethylene carbonate (EC) or propylene carbonate (PC) show high dielectric constant (89.78 for EC and 64.92 for PC), and thus preferentially solvate Li^+ cations. The key to realize commercial LIB was the replacement of PC co-solvent by EC, preventing solvent co-intercalation into graphite while forming a stable passivation layer, and thus improving the reversibility of Li (de)intercalation into graphite^{24,25}.

Eventually, in 1983, Yoshino was able to successfully cycle LCO with a petroleum coke negative electrode²⁶. Following this demonstration, LCO/petroleum coke cells were commercialized by Sony in 1991. Then graphite electrodes were developed without solvent co-intercalation²⁴ and remains widely used thanks to its high capacity (392 mAh/g at low potential ($E < 0.3$ V vs Li^+/Li)) and good battery performances with high coulombic efficiency²⁷.

Moreover, safety, low cost, environmental friendliness, wide liquid stability temperature range and a broad electrochemical stability window are essential

properties for electrolytes²⁸. Therefore, electrolyte research is tailored by compromises between all these properties. Moreover, despite the extensive research for enlarging the ESW, liquid electrolytes are in majority unstable at low and high potentials, *i.e.* at potentials at which the negative (< 1 V vs Li^+/Li) and positive electrodes (> 4 V vs Li^+/Li) operate. Therefore, the stability of the LIB relies on the formation of a passivating layer on the electrodes that prevents further electrolyte degradation by being electronically insulating while preserving Li^+ cations conduction. Hence, at the negative electrode/electrolyte interface, a solid electrolyte interphase (SEI) is formed following the electrolyte reduction²⁹. The first SEI model was developed in 1979 by Peled *et al.*³⁰. Then, Aurbach *et al.*³¹ developed a 2D SEI model based on one inorganic inner-layer close to the electrode surface, containing LiF compounds among others, and a porous organic outer-layer based on polymeric species. At the positive electrode/electrolyte interface, a cathode-solid interphase (CEI) was also reported for some electrode/electrolyte combinations^{32–34}. Besides, these interphases must ideally have a uniform morphology as well as being able to accommodate volume changes upon Li^+ insertion/deinsertion to be efficient.

In order to rationalize the SEI/CEI formation and thus to select the best electrolyte composition, HOMO/LUMO energy diagrams are widely used. Indeed, a HOMO/LUMO energy diagram describes the energy level of the highest occupied molecular orbital (HOMO) and the lowest unoccupied molecular orbital (LUMO) calculated for isolated molecules, as shown in Figure 1. 4. Thus, one can potentially correlate the energy levels to oxidation or reduction potentials of the electrolyte that can form the CEI (see yellow color in Figure 1. 4) or the SEI (see red color in Figure 1. 4), respectively. Following this framework, the band gap E_g defined by $E_{\text{LUMO}} - E_{\text{HOMO}}$ would be directly related to the ESW³⁵. However, the HOMO and LUMO energy levels are calculated for isolated molecules (solvent molecules or anions). Such calculations do not take into consideration the interactions between all the molecules contained in the electrolyte and the solvation structure that will undoubtedly change the electrolyte reactivity, as discussed in greater details in section 1.3 and 2. Therefore, as mentioned by Peljo *et al.*³⁶, the ESW is more accurately defined by the redox potentials of the electrolyte, which can only be inferred knowing the exact oxidation and reduction reactions and their associated Gibbs free energies. To illustrate this point (Figure 1. 4 in blue), taking water as an example, the band gap of water is calculated to be 8.9 eV³⁷ whereas the thermodynamic ESW is known to be 1.23 V.

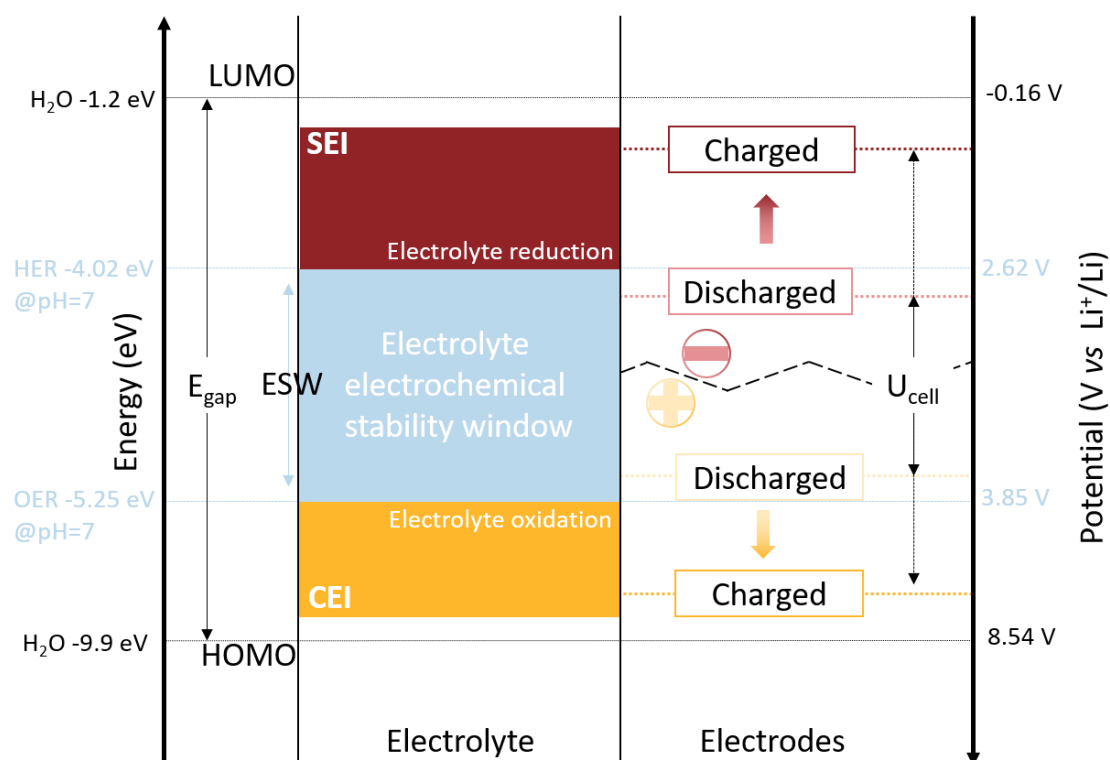


Figure 1. 4 Energy diagram (in eV, on the left) and corresponding potentials (in V vs Li⁺/Li, on the right) of the solid electrolyte interphase (SEI in red) and the cathode electrolyte interphase (CEI in yellow) formation at the surface of negative and positive electrodes during battery charge. Adapted from Ref^{35,36}.

1.3 From diluted to organic superconcentrated electrolyte: performances improvement

In commercial LIB, diluted electrolytes are generally employed, with concentrations close to ≈ 1 M. This “optimal” concentration reflects a compromise between viscosity (ionic mobility) and conductivity (dissociated charge carrier number) to ensure good transport properties^{38,39}, as shown in Figure 1. 5a.

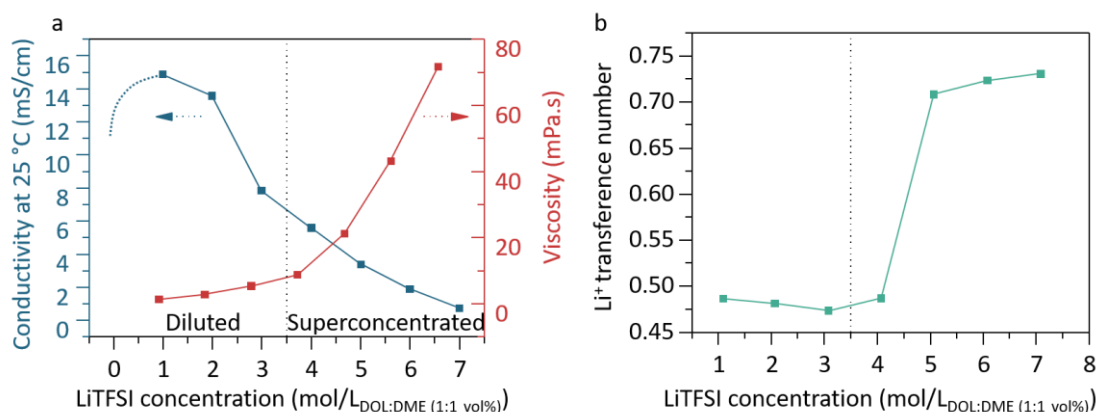


Figure 1. 5 (a) Ionic conductivity (blue) and viscosity (red) at 25 °C as function of the electrolyte concentration (1 mol/L (M), 2 M, 3 M, 4 M, 5 M, 6 M and 7 M LiTFSI in DOL:DME (1:1 vol%)). (b) Li⁺ transference number as function of the electrolyte concentration. Adapted from Ref⁴⁰.

Nonetheless, upon increase in concentration and when reaching superconcentration regime (leading to mass and volume of salt greater than the solvent ones), the solvation structure of ions changes, thus modifying bulk and interfacial electrolyte properties. Indeed, a competition takes place for Li⁺ solvation between scarce organic solvent molecules and anions, both being Lewis bases (*i.e.* capable of solvating Li⁺). Therefore, ionic association switches from solvent-separated ion pairs (SSIP) in diluted electrolytes to the formation of contact-ion pairs (CIP) or ionic aggregates (AGG) in superconcentrated ones, as shown in Figure 1. 6.

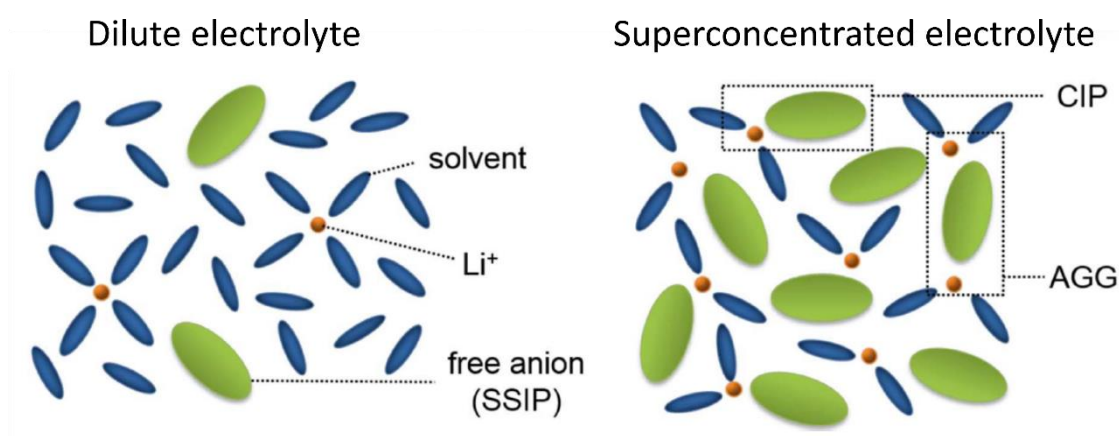


Figure 1. 6 Solvation structure from diluted to superconcentrated electrolyte. SSIP corresponds to solvent-separated ion pairs, CIP to contact-ion pairs, AGG to aggregate. Image taken from Ref³⁹.

Consequently, the solvation sheath of Li⁺ cation that is reported to be fourfold coordinated in diluted electrolytes^{41,42}, was found to be composed of two aprotic solvent molecules and two anion molecules in superconcentrated electrolytes⁴³.

Moreover, well-dissociated imide-based salts using anions such as TFSI⁻ anion, for example (see Table A.1. 1 at the end of the manuscript for anion structure), are preferred for the elaboration of superconcentrated electrolytes as they can be dissolved in greater amount in all polar solvents, thus reducing the number of free solvent molecule in the bulk. Regarding the solvent, it must be selected for its strong ability to solvate Li⁺ cations.

Looking at bulk properties, in superconcentrated electrolytes, although the overall conductivity -that is related to the capability of the electrolyte to carry the ionic current- is lower than in diluted ones, the transference number of Li⁺ -that considers the proportion of ionic current taking by each ionic species- can be greater than in diluted electrolyte, as illustrated in Figure 1. 5b. Indeed, a change in cation motion from vehicular (related to cation motion with its solvation sheath) to partially structural (when cations hop via a serial of ion association/dissociation from one anion or solvent molecule to another) was proposed to explain the increase in transference number^{39,44}. However, full understanding of ionic transport in superconcentrated electrolyte remains unclear⁴⁴. Besides, for superconcentrated electrolytes, the solvent volatility diminishes and the thermal stability is enhanced⁴⁴ since the energy needed to desolvate the solvent molecules becomes greater due to the diminution of free solvent molecules. The later effect also kinetically prevents electrode and SEI dissolution mechanism to occur⁴⁵, thus reducing side reactions. However, the high viscosity of the electrolyte remains a major drawback as it increases the cell impedance. In addition, from a practical point of view, the wetting of the electrodes/separators during battery assembly requires a much longer pre-treatment for this class of electrolytes.

Furthermore, superconcentration modifies the interfacial organization and thus the reactivity at both the positive and the negative electrodes. At the positive, anions populate the interface sufficiently to repulse solvent molecules to reach the inner-Helmholtz layer and thus prevent their oxidation when compared to dilute electrolytes for which solvent molecules are present in this layer (see Figure 1. 7a and b)^{46,47}. Moreover, anions are stable enough at high potential not to be oxidized prior to Li⁺ deintercalation, thus expanding the ESW (≈ 5.2 V vs Li⁺/Li for TFSI⁻ oxidation⁴⁸). Besides, the aforementioned double layer effect coupled with the lower amount of free solvent molecules reduce the corrosion of the aluminum current collector. Hence, unlike for diluted imide-based electrolyte that cannot form AlF₃ passivating layer that stops the corrosion, as PF₆⁻ does,⁴⁹ switching to superconcentrated regime allows for using aluminum current collector. Indeed, the few Al³⁺ cations formed upon oxidation of the

current collector will preferentially interact with the anions to form $[\text{Al}(\text{anion})_x]^{3-x}$ complexes. Since the viscosity is high, the complexes diffusion through the bulk electrolyte is reduced stabilizing the interface⁴⁶.

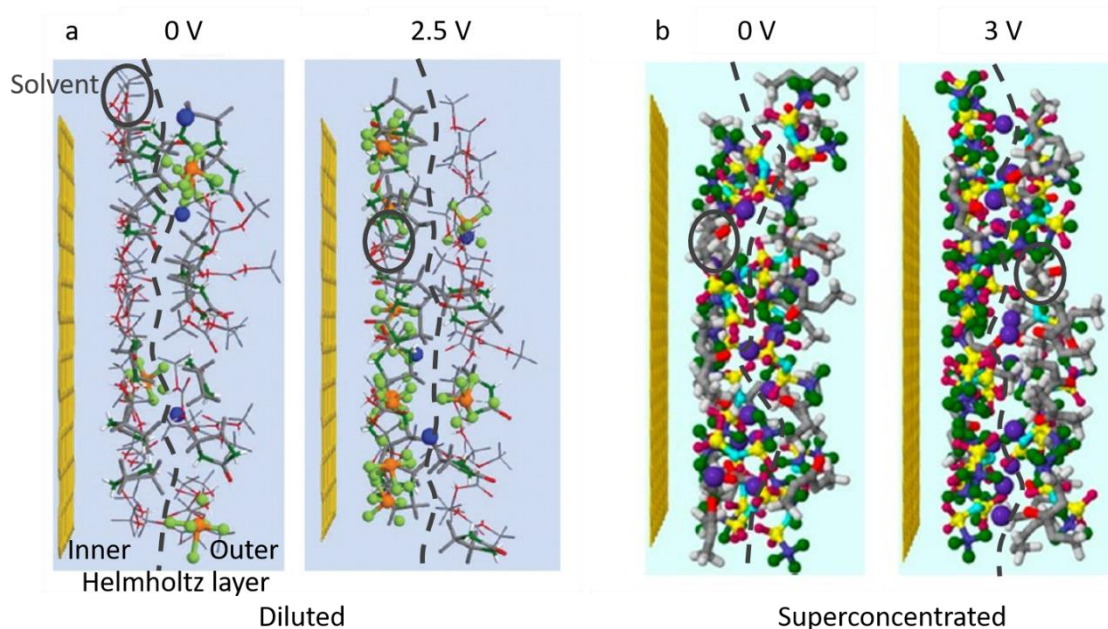


Figure 1. 7 Snapshots of the interfacial structure positively polarized from molecular dynamic (MD) simulations of (a) diluted electrolyte based on 1 M LiPF₆ in EC:DMC⁵⁰ (b) superconcentrated electrolyte based on LiTFSI(DMC)_{1.2}⁵¹. Adapted from Ref^{50,51}.

At the negative electrode, upon charge, the inner-Helmholtz layer of superconcentrated electrolyte is compacted and the anions coordinated to Li⁺ cations come closer to the electrode surface, as illustrated in Figure 1. 8a and b. Owing to this specific double layer structure, a direct reduction mechanism of the anions was proposed following density functional theory (DFT) calculations. Indeed, a shift of the anions LUMO to greater energies than the solvent LUMO was calculated. Therefore, a salt-derived anion-rich SEI was found to be formed at the negative electrode, as illustrated in Figure 1. 8c. Spectroscopy analysis such as X-ray photoelectron spectroscopy (XPS) and Fourier-transform infrared spectroscopy (FTIR) show that the SEI is majorly composed of inorganic compounds such as LiF, SO₂ or SO_x^{43,45,52–55} or Li₂O⁵⁶. Some CF₃ compounds were also identified as SEI contributor⁴³. However, as pointed out by Wang *et al.*⁵⁷ and Yamada *et al.*⁵⁸, imide-based salts tend to decompose upon Ar⁺ sputtering or X-ray radiation, thus caution must be exercised when performing SEI surface analysis. Besides, scanning electron microscopy (SEM), transmission electron microscopy (TEM) and atomic force microscopy (AFM) observations show a dense and uniform passivation film^{53–55}.

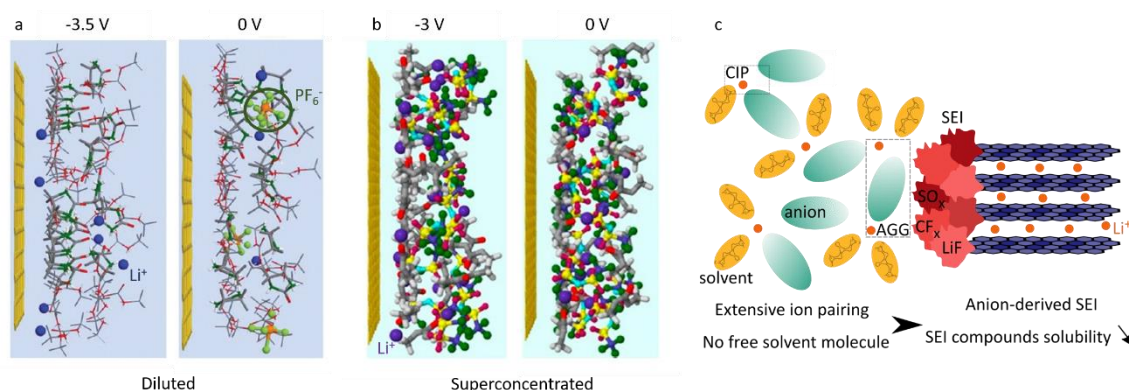


Figure 1. 8 Snapshots of the interfacial structure negatively polarized from molecular dynamic (MD) simulations of (a) a diluted electrolyte based on 1 M LiPF₆ in EC:DMC⁵⁰ (b) a superconcentrated electrolyte based on LiTFSI(DMC)_{1.2}⁵¹. Adapted from Ref^{50,51}. (c) Scheme of the SEI formed in superconcentrated electrolyte. Adapted from Ref⁵⁴. CIP: contact ion pair. AGG: aggregated cation-anion pairs.

Overall, both changes in bulk properties and interfacial reactivity impact the battery performances when switching from diluted to superconcentrated electrolytes. Major contributions have been made in this field, and are summarized in Figure 1. 9. Finally, one should recall that this topic is not recent. Indeed, more than thirty years ago, the pioneering work of McKinnon and Dahn⁵⁹ introduced a propylene carbonate (PC)-based electrolyte saturated with LiAsF₆ salt, enabling to cycle layered electrodes such as Li_xZrS₂ without PC co-intercalation. Subsequent works on superconcentrated electrolytes were shown to enable cycling graphite electrode while preventing solvent co-intercalation^{43,52,53,56,57,60–65}. Besides, polymer-in-salt electrolytes, as introduced by Angell *et al.*⁶⁶ in 1993, paved the way for reaching good transport properties in superconcentrated electrolytes ($\sigma > 0.1$ mS/cm at 25 °C in a 9:1 Li salt:polyethylene oxide (PEO) molar ratio electrolyte). In addition, high charging rates could be reached while preventing Li dendrites to be formed due to reduction of the cell polarization, thus greater cycling stability is obtained. Altogether, based on the bulk and interfacial properties of superconcentrated electrolyte, 5 V-class operation battery were assembled.

Despite all these advances, the use of organic superconcentrated electrolyte faces two major issues: the price and the sustainability. Indeed, knowing that in diluted LiPF₆-based electrolyte, the salt represents 10 % of the weight but 70 % of the price of the electrolyte, one can easily imagine that the cost of superconcentrated electrolytes will be critical for applications. Additionally, imide-based salts often employed to reach supersaturation are toxic and corrosive.

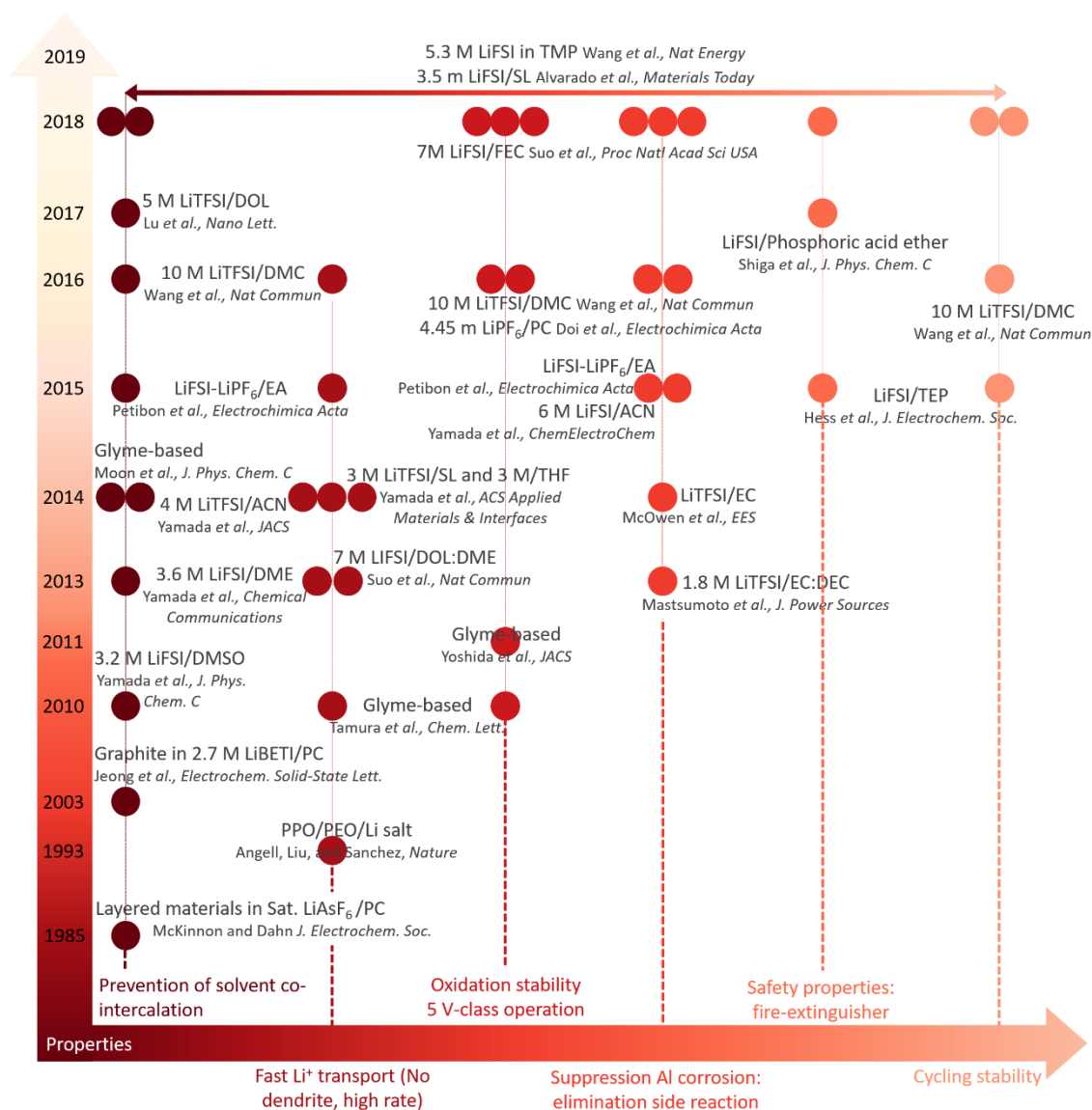


Figure 1. 9 Historical timeline of organic-based superconcentrated electrolyte highlighting some of their main properties. All references (Ref^{43,46,52,53,56,57,59–74}) are given in Section References at the end of this manuscript. Adapted from Ref⁴⁴. Abbreviation of salts and solvents are given at the end of the manuscript.

1.4 Aqueous rechargeable Li-ion battery (ARLIB) using diluted electrolyte: safety, cost and environmental friendliness at the expense of performances

The development of aqueous rechargeable Li-ion battery (ARLIB) relies on the compromise between electrode material performances (specific capacity, intercalation potential and material stability) and the aqueous electrolyte stability. Though ARLIB are theoretically cheaper, safer, and less toxic than their organic counterparts. Moreover, they provide high electrolyte conductivity ($\sigma \approx 100 \text{ mS/cm}^{75}$) and fast reaction kinetics, thus reducing the overall cell impedance⁷⁶. Indeed, the activation energy for charge transfer in aqueous electrolyte was found to be between 23 and 25 kJ/mol, compared to $\approx 50 \text{ kJ/mol}$ in organic electrolyte⁷⁵. Thus, high rate capabilities⁷⁷ are achievable, as well as good cycling stability⁷⁸ and greater specific capacity⁷⁹. Besides, despite a decrease of conductivity in saturated electrolyte due to lower amount of dissociated charge carriers, the increase in concentration reduces the water activity, as previously discussed in LiNO_3 -^{80–89} and Li_2SO_4 -based electrolyte^{77,78,90–96}, thus kinetically expanding the ESW^{89,92} and promoting Li^+ intercalation compared to proton intercalation⁹⁷ (even though the later has been recently qualified⁹⁸).

Positive electrodes for ARLIB must operate in a 3 to 4 V vs Li^+/Li potential window to avoid OER, as shown in Figure 1. 10. Therefore, LMO^{77,78,80,81,90,91,97,99–103} was extensively used as well as the well-known LCO^{82–84,92}, LFP^{85,86,93,104,105} or NCM⁹⁴. Carbon coating was reported to improve electrode stability^{91,104} while oxygen removal was shown to decrease polarization, cell resistance^{87,106} and self-discharge¹⁰⁷. However, proton intercalation may occur and compete with Li^+ intercalation -though depending on the electrode structure (favorable in layered structure such as LCO and NCM¹⁰⁸ compared to LFP). Proton and lithium co-intercalation is detrimental to cell performances as it blocks the Li^+ diffusion, thus off-balancing the intercalation of Li^+ in the electrodes and decreasing its related capacity. To avoid proton co-intercalation, adjusting pH to values greater than pH = 9 was shown to improve cell performances^{109,110}.

Though, the negative electrode is even more challenging as the HER potential ($E_{\text{HER}} = -0.06 \text{ pH V vs ESH}$, 2.62 V vs Li^+/Li at pH = 7) and the absence of SEI formation in inorganic-based electrolyte^{58,76,80,111} prevents the use of low potential negative electrodes such as graphite or metallic Li (see Figure 1. 10). Thus, vanadium-based (LiV_3O_8 ^{82,85,99}, VO_2 ⁸⁰, V_2O_5 ⁸⁸) or NASICON polyanionic compounds ($\text{LiTi}_2(\text{PO}_4)_3$ ^{91,96,112}, LTP) were majorly reported. As a consequence, the specific energy of ARLIB remains

limited to ≈ 50 Wh/kg with a nominal voltage of 1.5 V, far below that of organic-based LIB (≈ 200 Wh/kg_{cell} and ≈ 4 V). Also problematic, active materials such as vanadium-based¹⁰⁹ negative electrodes (or LMO⁹⁵ positive one) are prone to dissolution in aqueous electrolyte. Moreover, passive components (current collectors for instance) can suffer from corrosion. Titanium and stainless steel were reported to be the most appropriate ones¹⁰⁹ even though stainless steel still suffer from corrosion in acidic media¹¹³. Therefore, ARLIB as introduced as early as 1994 by Jeff Dahn *et al.*⁸⁰ using LiMn_2O_4 as positive and VO_2 as negative electrode and a saturated LiNO_3 electrolyte was never commercialized.

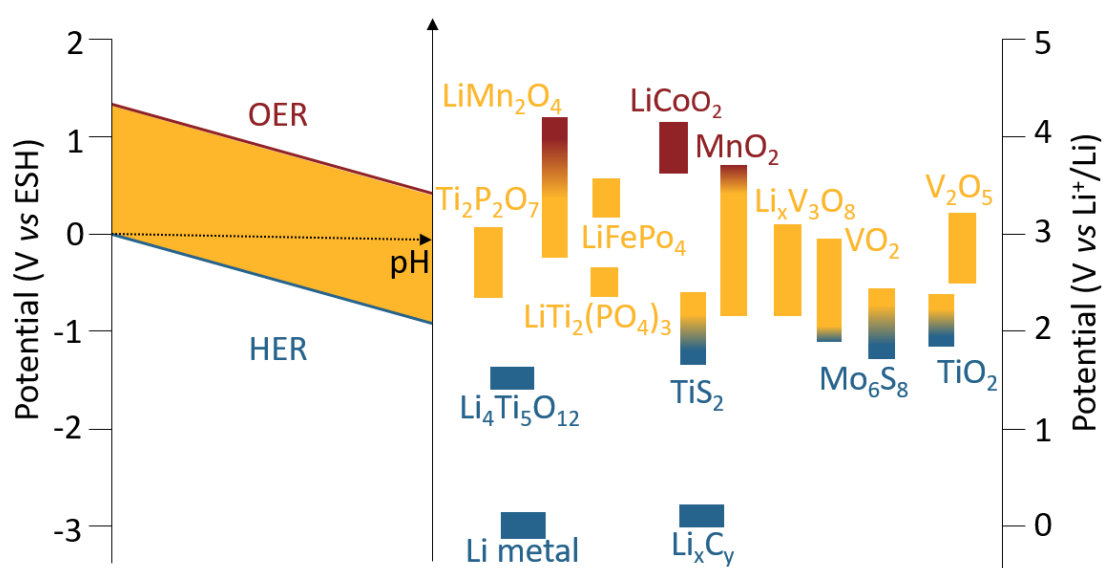


Figure 1. 10 Pourbaix diagram and intercalation potential of some electrodes used in LIB devices. Adapted from Ref⁸³.

In order to overcome voltage limitation, research efforts were focused on the development of electrode coating to physically impede water to reach the negative electrode. To do so, a combination of Li-based gel polymer and ionic conductive ceramic (LISICON) were used to enable cycling metallic Li in aqueous electrolyte^{112,114–119}, as illustrated in Figure 1. 11a. Diazonium grafting methods were also developed to covalently bond polyether-moieties known for their ability to conduct Li^+ cations to the negative electrode material¹²⁰. The nature of the ether group bounded to the phenyl ring have a great influence on the electrochemical properties by allowing Li^+ transport while preventing water access to the interface¹²¹. However, none of the above-mentioned strategies were commercially successful.

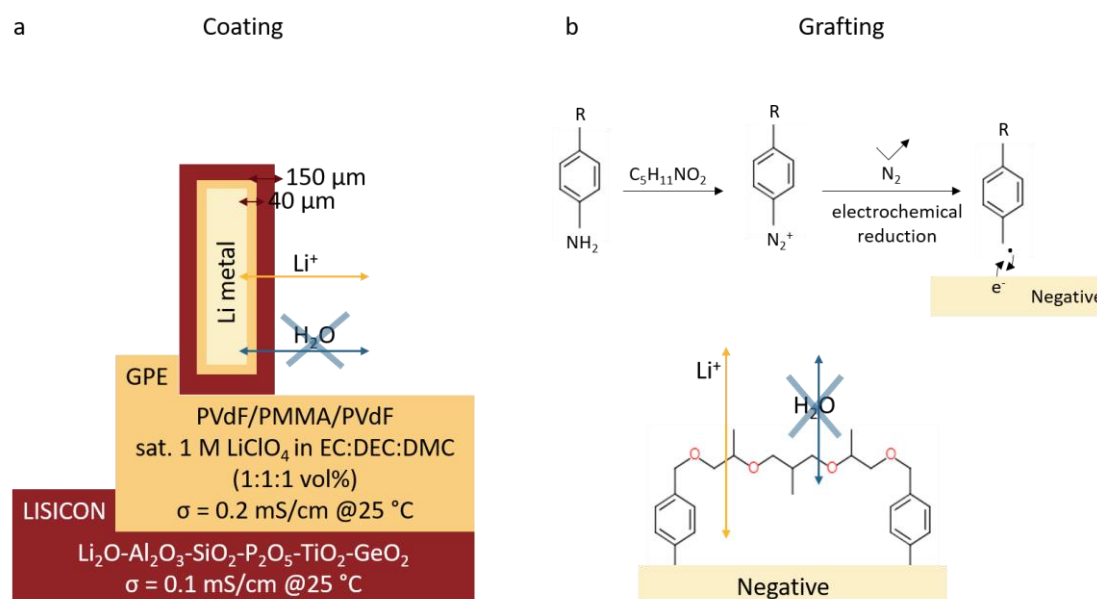


Figure 1. 11 (a) Scheme of metallic Li coated with a gel polymer electrolyte (GPE) (PVdF: polyvinylidene fluoride, PMMA: poly(methyl methacrylate) and ceramic layer (LISICON). (b) Principle of grafting consisting of the electrochemical reduction of a diazonium salt produced by nitrosylation of an amine by isoamyl nitrite. Adapted from Ref^{117,120}.

2 Aqueous superconcentrated electrolyte: can the modification of the physico-chemical properties and the interfacial reactivity unlock the competitiveness of aqueous Li-ion batteries?

Developing stable SEIs in aqueous media has been at the forefront of research for aqueous Li-ion batteries. Indeed, while limitations are found regarding the cathodic stability (corresponding to the negative electrode side) of classical diluted organic electrolytes, no stable SEI components are formed in diluted aqueous electrolytes⁷⁹. Therefore, based on the promising properties of superconcentrated electrolyte, Suo *et al.*¹¹¹ developed in 2015 an aqueous superconcentrated electrolyte referred to as *Water-in-salt electrolyte* (WiSE), quickly followed by the introduction of *Water-in-bisalt* (WiBS) in 2016 by Yamada *et al.*⁵⁸ and Suo *et al.*¹²². The use of superconcentration in aqueous based electrolyte was shown to enable enlarging the operating potential window of aqueous systems up to 3 V thanks to the formation of a SEI at the negative electrode and double layer effect at the positive electrode, while preserving good physico-chemical properties due to modification of the electrolyte structure, as discussed in the following section.

Prior to look into greater details to the electrolyte solvation structure, one must mention that for aqueous superconcentrated electrolyte the salt concentration is usually express in term of molalities (mol/kg) rather than molarities (mol/L). The Figure 1. 12 shows the corresponding molarities and molalities as function of LiTFSI amount (the mole and the mass fraction are shown). For instance, 20 mol/kg of LiTFSI corresponds to ≈ 5 mol/L. Moreover, organic imide-based salts such as LiTFSI are generally preferred¹²³ as LiTFSI is known to have good electrochemical and chemical stabilities (towards hydrolysis and in temperature) in aqueous environment¹²⁴ as well as keeping good dissociation properties. However, LiFSI is usually avoided as it is prone to hydrolysis in aqueous environment¹²⁵.

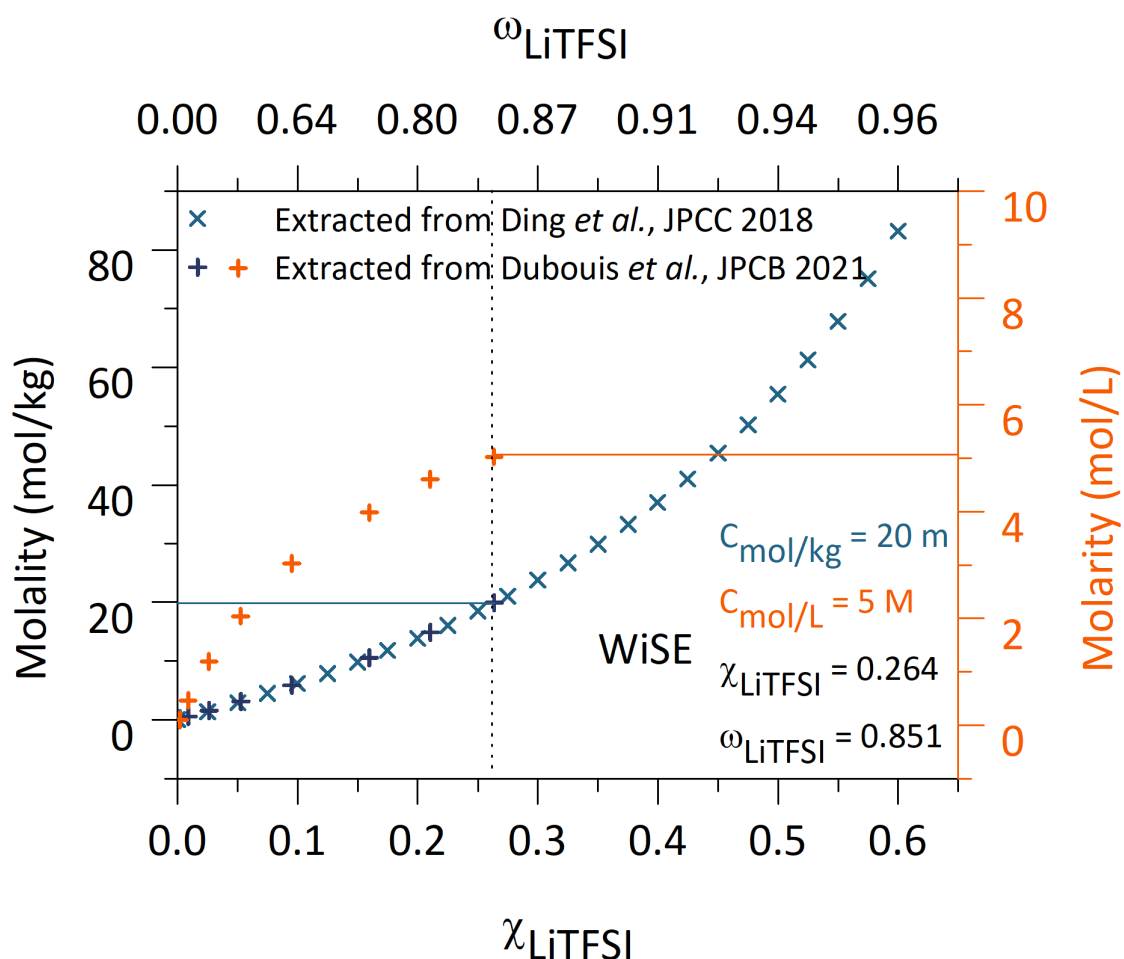


Figure 1. 12 Molality (mol/kg) (blue crosses) and molarity (orange crosses) as function of mole (bottom x axis) or mass fraction (top x axis). Data extracted from Ref^{126,127}.

2.1 Structure and dynamics of LiTFSI-based aqueous superconcentrated electrolyte

In a diluted electrolyte (≈ 1 M), ions are almost fully dissociated and water exists as “free” water, *i.e.* as non-ion-bounded molecules forming hydrogen-bonding (H-bond) network¹²⁸ (see Figure 1. 13a). When concentration increases, the ion-ion interactions increase as CIP are formed above 3 M (≈ 10 m), leading to 50 % of the TFSI⁻ anions being directly in contact with Li⁺ (see Figure 1. 13b)¹²⁹. Aggregate structure are observed at superconcentration above 5 M (≈ 20 m)¹³⁰, as illustrated in Figure 1. 13 and shown by Raman spectroscopy in Figure 1. 14a.

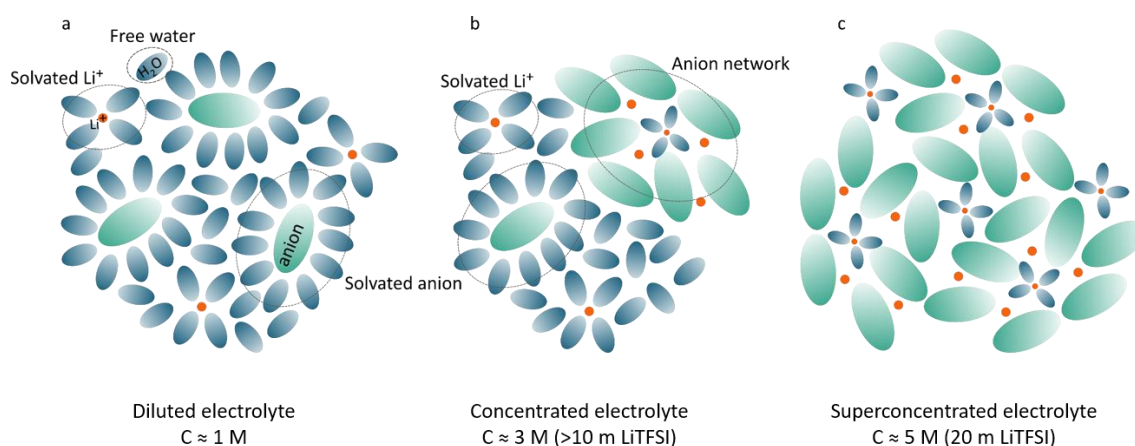


Figure 1. 13 Scheme of solvation structure of the electrolyte in (a) diluted electrolyte, (b) concentrated electrolyte and (c) superconcentrated electrolyte. Adapted from Ref¹³¹.

As shown in Figure 1. 14a, the intensities attributed to H-bond network and related to OH stretching at 3255.5 cm^{-1} and 3403 cm^{-1} diminish when the concentration increases from 0 to 5 M (> 20 m). This diminution is concomitant with the appearance of a sharp peak at 3565 cm^{-1} suggesting the disruption of the H-bond network and the absence of free water cluster^{58,123,132}, also determined by molecular dynamic (MD) calculations^{128,133}. Moreover, ⁷Li and ¹⁹F nuclear magnetic resonance spectroscopy (NMR) analysis showed changes in ionic structure, as shown in Figure 1. 14b and c. The lowering of the ⁷Li chemical shift observed upon increasing salt concentration results from an increase of the electronic density around Li⁺, suggesting greater amount of Li⁺-anions interactions. A shift of the ¹⁹F signal was also observed, suggesting greater anion-anion interactions¹³⁴.

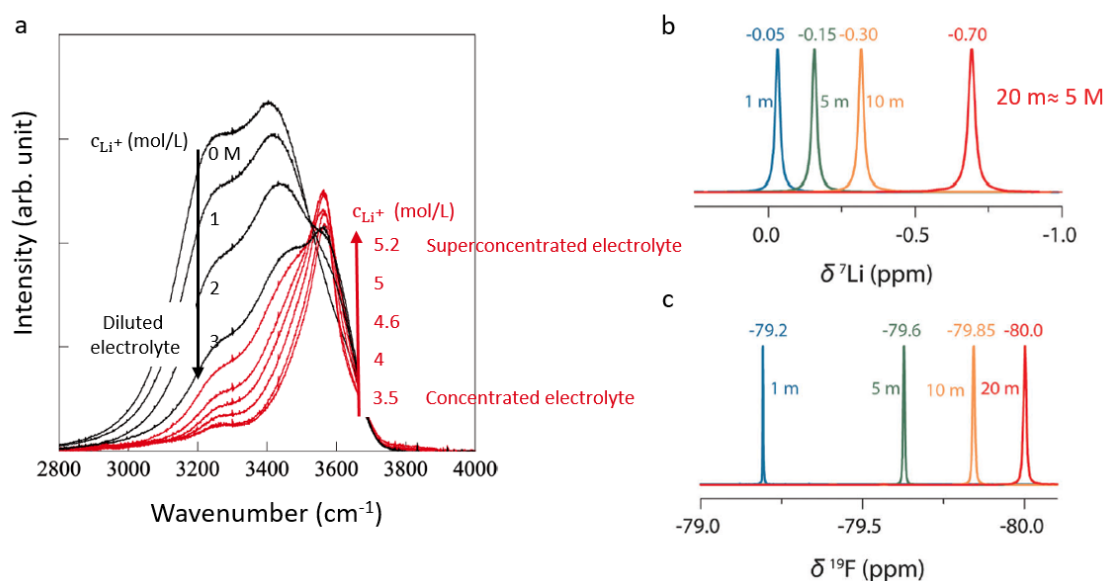


Figure 1. 14 (a) Raman spectra in the range 2800-4000 cm⁻¹ observed for LiTFSI aqueous solutions. 2800-4000 cm⁻¹ range corresponds to O-H stretching vibration restricted in a three-dimensional H-bond network structure. Adapted from Ref¹³⁰. Normalized NMR spectra of aqueous electrolytes showing the chemical shift of water molecules in the presence of LiTFSI at several molalities (1 m blue, 5 m green, 10 m orange and 20 m red). (b) ⁷Li (c) ¹⁹F. Adapted from Ref¹³⁴.

Moreover, the structure of aqueous superconcentrated electrolytes was reported to be an anion TFSI⁻-rich domain that behaves as an immobile matrix in which a water-rich domain (network domain¹³⁵ or cluster one¹³⁶) is interpenetrated, as depicted in Figure 1. 15. Fast Li⁺ transport is enabled through the water-rich domain thanks to bulk-like water structure, *i.e.* water which forms channels to support fast transport, intertwined in the porous TFSI⁻-rich skeleton¹³⁷ and interfacial water, *i.e.*, water bounded to Li⁺ cation that move through the water bulk-like channels. Though, Li⁺ transport may also take place through the TFSI⁻-rich domain¹³⁶. Altogether, these two networks give a heterogeneous structure with asymmetric clusters. Based on the identification of these two domains, the idea that upon increase in salt concentration water is not displaced from the first solvation sheath is strengthened, suggesting that all water molecules will preferentially bounds Li⁺ cation to form Li(H₂O)₄⁺ clusters rather than be involved in a mix first solvation sheath composed of TFSI⁻ anion and water.

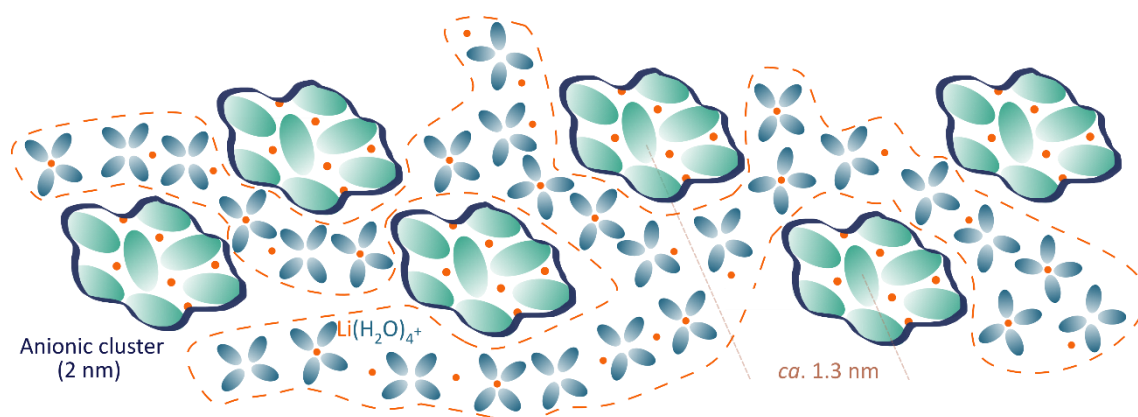


Figure 1. 15 Schematic diagram of Li⁺ cation transport in aqueous superconcentrated electrolyte composed of two interpenetrating network: a water-rich one (orange) and an anion-rich one (green/dark-blue). Li⁺ cationic transport mechanism remains unclear between vehicular mechanism and hopping-type one. Adapted from Ref¹³⁸.

2.2 Physico-chemical properties of bulk LiTFSI-based aqueous superconcentrated electrolyte

First, as ionic association is enhanced in superconcentrated electrolytes, the number of dissociated charge carriers decreases, thus the conductivity, as shown in Figure 1. 16a. However, conductivity values remain rather high (≈ 10 mS/cm in 21 m LiTFSI¹¹¹) thanks to the heterogeneous structure previously described that enables fast Li⁺ transport and provides high Li⁺ transference number¹³⁹ (> 0.6 ^{135,140,141} and found as high as 0.73¹³⁵ depending on the experimental or theoretical method of determination). The difference in transference number between Li⁺ and TFSI⁻, considered as immobile, is related to the asymmetry between anion and water clusters¹⁴⁰. Moreover, as viscosity is impacted by the concentration and the interaction between ions and solvent molecules¹⁴², its value is found to increase to values greater than 40 mPa.s in WiSE (see Figure 1. 16.b). Besides, as illustrated in Figure 1. 16c on the Walden plot, superconcentrated aqueous electrolytes reach the “ideal KCl line” and may even become superionic solution, *i.e.*, when conductivity and viscosity are decoupled, especially considering bi-salt media⁵⁸ which reach concentration above saturation, thus explaining that good transport properties are preserved.

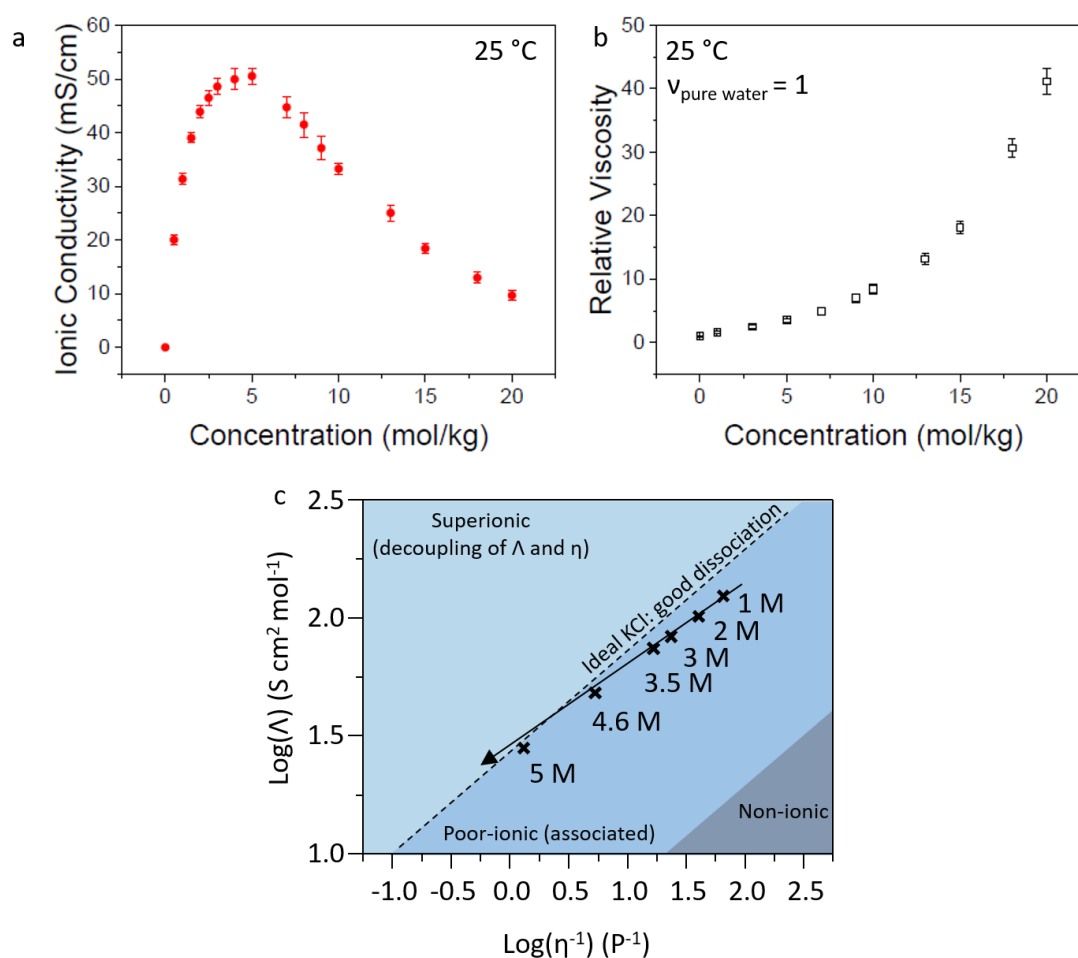


Figure 1. 16 (a) Conductivity measurements for LiTFSI aqueous solutions as function of concentration. (b) Relative viscosities measured for LiTFSI aqueous solutions as function of concentration. Adapted from Ref¹³⁹. (c) Walden plot for LiTFSI solutions as function of concentration. The Walden plot was generated from the molar conductivities (Λ) and the viscosity (η) of the electrolyte solutions. In a Walden plot, electrolyte solutions can be classified in terms of their performances as ionic conductors: superionic (upper left region above the ideal KCl line) which states a decoupling between viscosity and conductivity, good-ionic (on the ideal line), poor-ionic (bottom right region under the ideal line), or non-ionic (far below the ideal line) liquids. For the LiTFSI/H₂O solutions, the plot approaches the ideal line with increasing concentration, and finally joins with the ideal line at saturation. “Superionic” solution are reported for WiBS. Adapted from Ref^{58,130}.

Moreover, the increase of ESW, especially on the positive electrode side, was partially attributed to a diminution of water reactivity^{58,134} related to a decrease in water activity⁵⁸. Indeed, alike in organic superconcentrated electrolytes, as water is majorly bounded to ions, the energy required to desolvate water and thus to oxidize it is greater, thus pushing the onset potential of OER to higher potential¹⁴³. As an example, the vapor

pressure of water was measured to decrease from 4.25 kPa for pure water to 0.50 kPa at 30°C in $\text{Li}(\text{TFSI})_{0.7}(\text{BETI})_{0.3}$ electrolyte.

However, considering the negative electrode side and thus the HER parasitic reaction, water molecules bounded to Li^+ are more reactive than “free” water molecules upon reduction, as found by Dubouis *et al.*¹⁴⁴. Moreover, greater activity for protons was recently reported in superconcentrated electrolyte⁹⁸. These results suggest that the overall decrease of water activity is not sufficient to effectively increase the ESW, especially on the negative electrode side. Finally, upon increase of concentration, electrolytes become more acidic, thus shifting the onset potential of HER and OER to greater potential. Eventually, this increase was found to be similar to the increase in Li^+ insertion potential resulting from the increase in Li^+ activity as function of salt concentration⁵⁸. Therefore, shifting to WiSE does not favor Li^+ intercalation at the negative electrode relative to HER, for instance. One has to note that caution must be taken while conducting pH measurements in superconcentrated electrolyte as pH-meter with glass probe should be avoided¹²⁵. Acidification of the electrolyte was found with pH value as low as 2.8¹⁴⁵, even though a recent study determined that such drop was overestimated and that less than 1 mM of protons are formed in WiSE⁹⁸.

Eventually, WiSE cannot usually be used at low temperature due to their rapid crystallization¹³⁸. Indeed, as shown on the phase diagram (see Figure 1. 17, purple line for WiSE-region), the liquidus temperature of WiSEs is generally around 20 °C.

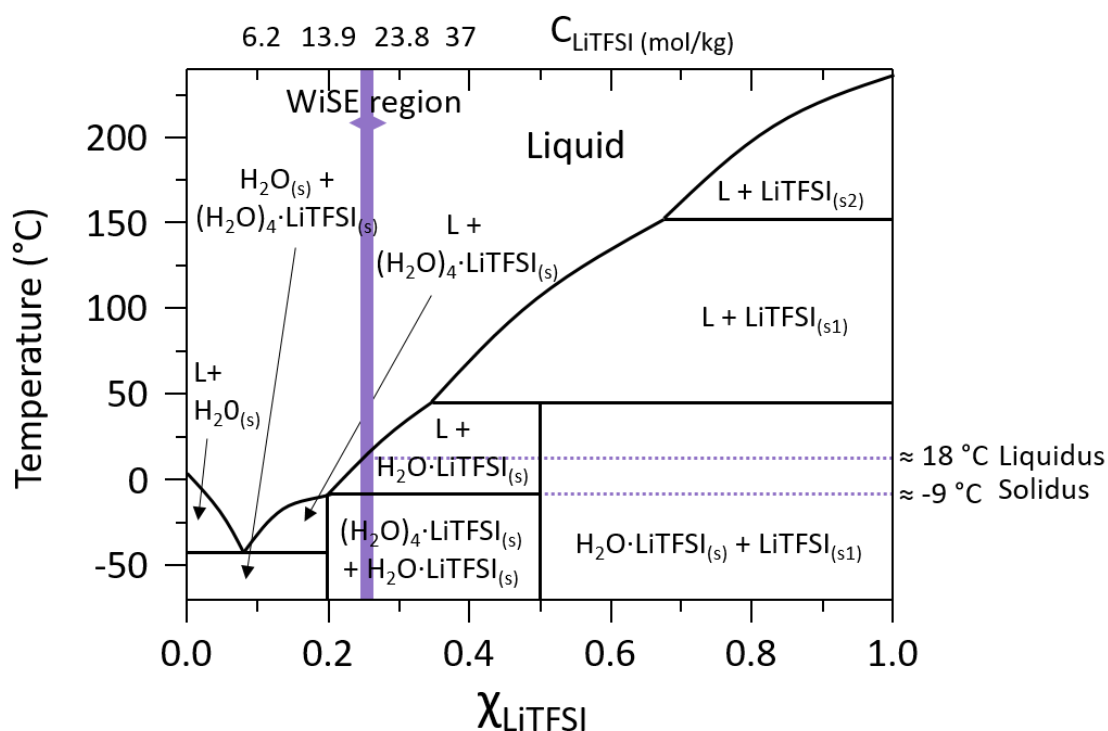


Figure 1. 17 Liquid-solid phase diagram of LiTFSI-H₂O binary system. Adapted from Ref¹²⁶. The purple line represents the 18.5-21 m LiTFSI concentration considered for aqueous superconcentrated electrolyte.

2.3 Interfacial reactivity at aqueous interfaces

At the negative electrode side, the origin for the enlarged electrochemical window (see Figure 1. 18) offered by aqueous superconcentrated electrolytes is ascribed to the anion degradation that forms a LiF-rich passivating SEI that pushes the HER onset potential from 2.62 V vs Li⁺/Li (at pH = 7) in 1 m LiTFSI to 1.9 V vs Li⁺/Li¹¹¹ in 21 m LiTFSI (see Figure 1. 18a). The exact mechanism for the SEI formation is still under debate, with three mechanisms being proposed, and further detailed in the appendix of the chapter: (i) the direct electrochemical reduction of anions or anion clusters such as Li₂(TFSI)⁺^{58,111,146–148}, (ii) the chemical degradation of anion by nucleophilic attack resulting from the HER reaction and the generation of hydroxyls^{134,149}, (iii) the precipitation/dissolution of LiTFSI salt¹⁴⁹. Besides, dissolved gases (O₂ or CO₂) were also reported to be involved in SEI formation. Though, despite the differences in SEI formation mechanism, all are combined with the lower solubility of SEI compounds in WiSE¹⁴⁸.

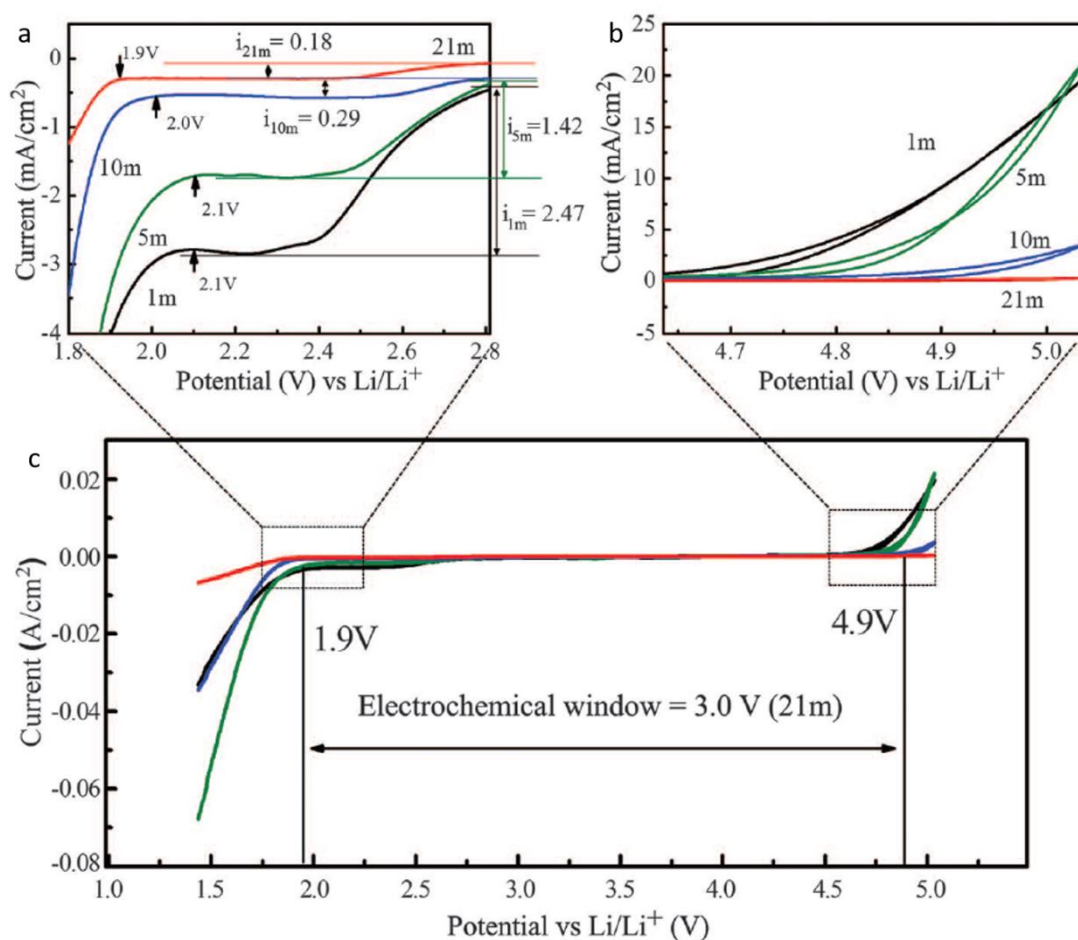


Figure 1. 18 Electrochemical stability window reported by Suo *et al.*¹¹¹ in 2015 for several electrolyte ranging from 1 m to 21 m LiTFSI on stainless steel. (a) Zoom on the cathodic stability at the negative electrode side. (b) Zoom on the anodic stability at the positive electrode side. (c) Overall ESW.

Nonetheless, water enrichment following the formation of hydrated cations ($[\text{Li}(\text{H}_2\text{O})_x]^+$) is still found below 1.5 V vs Li^+/Li ^{Ref 150,151} at the negatively charged interface, with hydrogen atoms oriented perpendicular to the surface, thus promoting the HER¹⁵⁰. Figure 1. 19 illustrates this enrichment near the negative electrode, often referred to as the cathodic challenge.

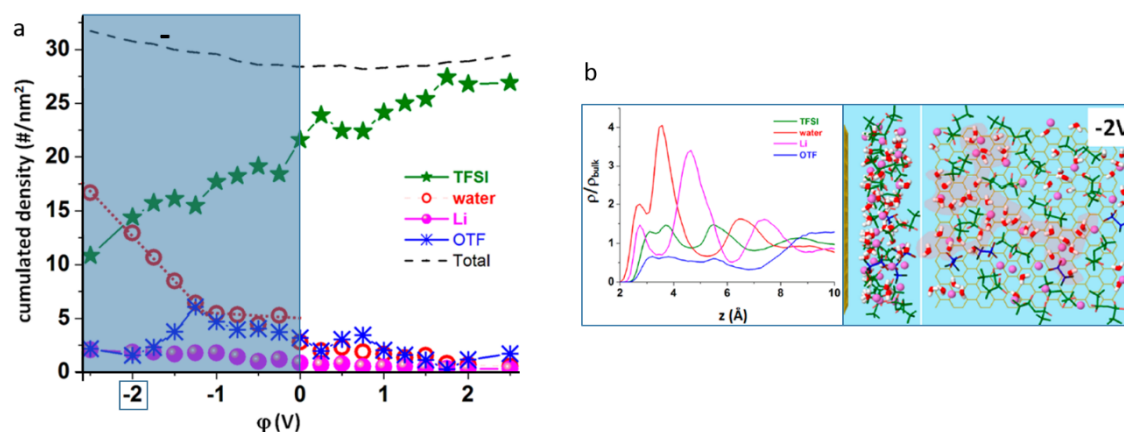


Figure 1. 19 (a) Contributions of ions and water to the atom density of the interfacial layer as a function of applied electrode potential assessed by classical molecular dynamics (MD). Blue region represents the interface of a negatively charged electrode mostly populated by water molecules. (b) Cumulative atom number density profiles normalized by bulk density as a function of distance from the electrode (z) and snapshots of the interfacial layer at -2 V vs the PZC (b). Adapted from Ref¹⁵⁰.

Moreover, the increase in ESW stability is in reverse order with the intrinsic HER electrocatalytic activity of the electrode material used to measure it^{152,153}, as illustrated in Figure 1. 20.

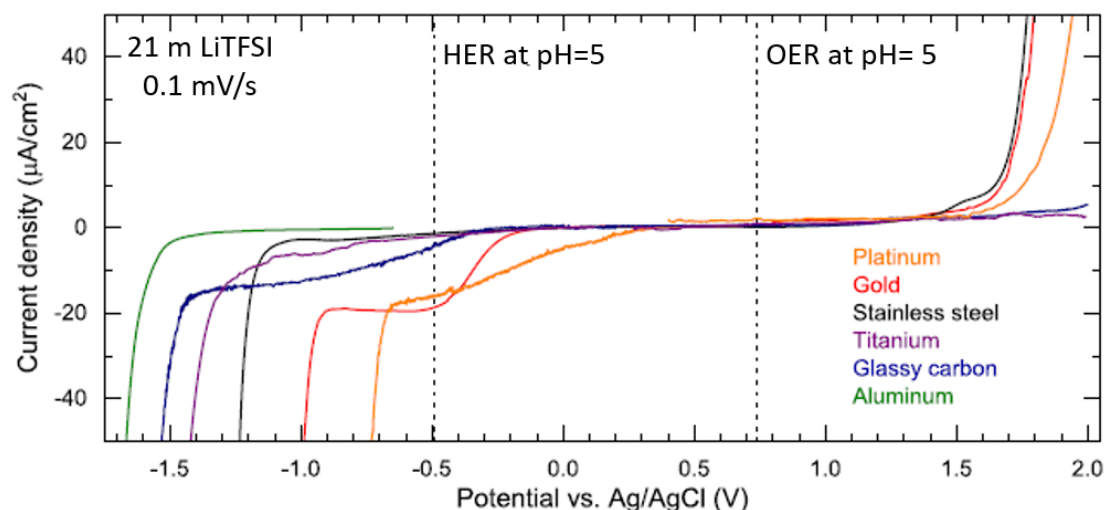


Figure 1. 20 Linear sweep voltammograms for 21 m LiTFSI on platinum, gold, stainless steel (SS), titanium, glassy carbon (GC), and aluminum. The pH of all solutions was adjusted to a value of ≈ 5 . Experiments were carried out at room temperature. Adapted from Ref¹⁵³.

As a conclusion, the SEI stability can be found highly dependent on the electrode material, the anion chosen and the applied potential^{148,152–154}. Last but not least, regarding the assessment of the ESW and thus the interfacial reactivity, the ESW can be

artificially increased by choosing a high threshold of current density ($i_{\text{threshold}}$). For example, the ESW increases from 2.1 V to 3.1 V by selecting a $i_{\text{threshold}}$ of $100 \mu\text{A}/\text{cm}^2$ rather than $2 \mu\text{A}/\text{cm}^2$ ¹⁵³.

Turning to the positive electrode, a double layer effect enables preventing the OER. Indeed, upon positive polarization and in superconcentrated electrolyte, the negatively charged anion species move towards the positive electrode to form an hydrophobic organic anion-rich double layer repelling water molecules, thus preventing their oxidation (through OER)^{150,152,155} (see Figure 1. 21). Hence, a shift in OER onset potential from 3.85 V vs Li^+/Li in 1 m LiTFSI at pH = 7 to 4.9 V vs Li^+/Li in 21 m LiTFSI was observed¹¹¹. The decrease of fraction of free water molecules was also proposed to diminish the amount of water that can be oxidized¹⁵⁰, though such consideration does not consider the strong impact of the electrocatalytic activity of the electrode material. Moreover, the anion choice impacts the interfacial reactivity at the positive electrode side. For instance, TFSI⁻ anion is preferentially adsorbed over Otf⁻ anion at the electrode/electrolyte interface¹⁵⁰ leading to a more effective screening even though Otf⁻ anions, that decompose at lower positive potentials, may form a partially insulating CEI¹⁵⁶.

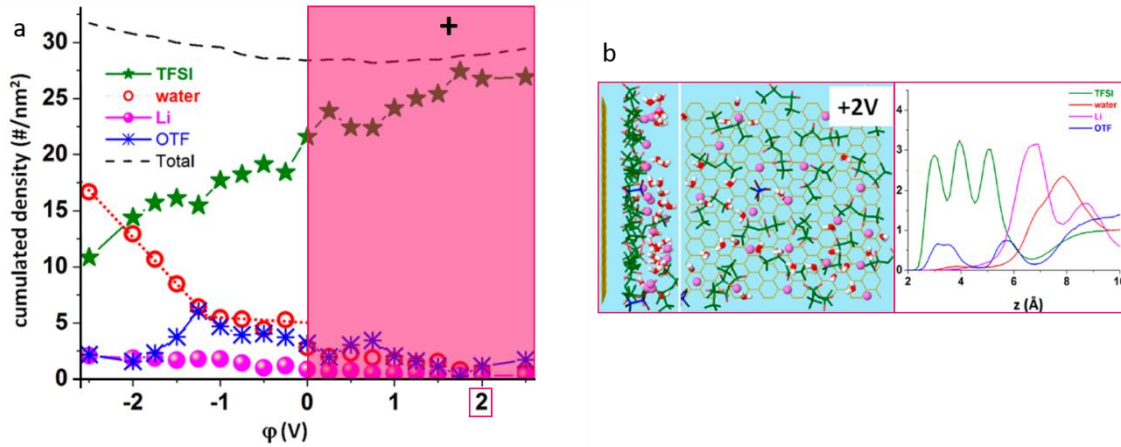


Figure 1. 21 (a) Contributions of ions and water to the atom density of the interfacial layer as a function of applied electrode potential assessed by classical molecular dynamics (MD). Pink region represents the interface of a positively charged electrode mostly populated by anions. (b) Cumulative atom number density profiles normalized by bulk density as a function of distance from the electrode (z) and snapshots of the interfacial layer at +2 V vs the PZC. Adapted from Ref¹⁵⁰.

2.4 Battery performances of *Water-in-salt* electrolyte

As described above, the electrolyte structure of WiSE impacts both bulk and interfacial properties, and thus the battery performances. Hence, the use of aqueous superconcentrated electrolyte was proposed to enable cycling negative electrode materials which Li^+ insertion potential lays outside the ESW of water or diluted aqueous electrolyte (LTO, Mo_6S_8 , TiO_2 , TiS_2 , see Figure 1. 10). In Figure 1. 22 is shown the discharge capacity and the Coulombic efficiency of WiSE-based batteries. As a proof of concept, a 2.3 V battery using Mo_6S_8 and LiMn_2O_4 as negative and positive electrodes, respectively, was first reported in 2015 by Suo *et al.*¹¹¹. Following this demonstration, Yamada *et al.*⁵⁸ then showed that mixing two organic lithium salts ($\text{Li}(\text{TFSI})_{0.7}(\text{BETI})_{0.3} \cdot 2\text{H}_2\text{O}$) increases further the concentration and enables assembling aqueous batteries with a working potential as high as 3.1 V using LTO in combination with $\text{LiNi}_{0.5}\text{Mn}_{1.5}\text{O}_4$ or LCO electrodes. Moreover, WiBS electrolyte (21 m LiTFSI : 7 m LiOtf) was also employed by Suo *et al.*¹²² to assemble a 2.5 V $\text{TiO}_2/\text{LiMn}_2\text{O}_4$ battery. Furthermore, using TiS_2 as negative, a 1.7 V $\text{TiS}_2/\text{LiMn}_2\text{O}_4$ cell using a 21 m LiTFSI electrolyte was reported¹⁵⁷. However, it was also observed that using LTO as negative electrode leads to drastic decrease in cell performances (see Figure 1. 22d, from cycle number 50).

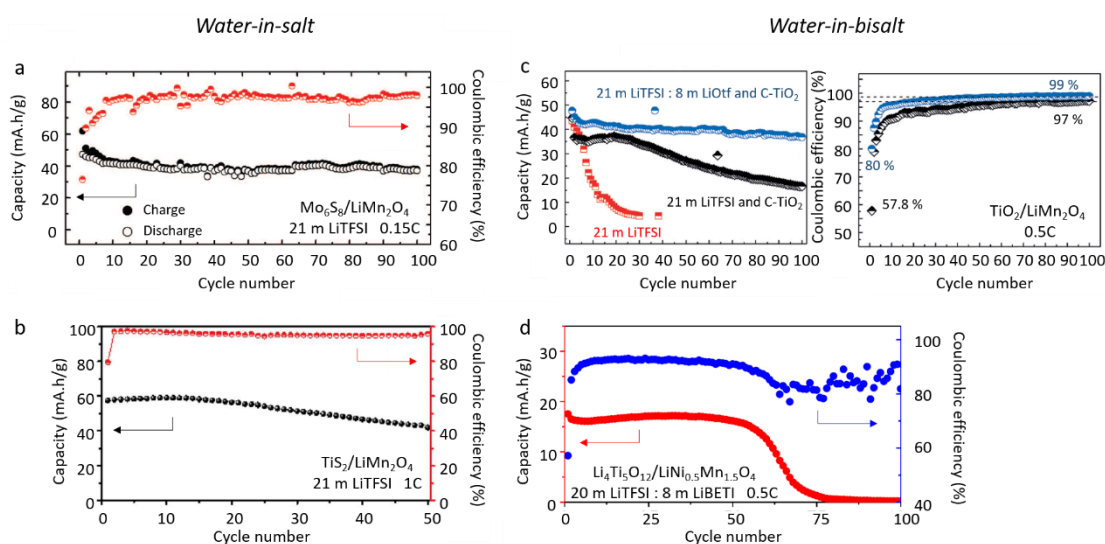


Figure 1. 22 Cycling stability of several aqueous superconcentrated electrolyte based on LiTFSI-salt. (a) $\text{Mo}_6\text{S}_8/\text{LiMn}_2\text{O}_4$ in 21 m LiTFSI at 0.15C. (b) $\text{TiS}_2/\text{LiMn}_2\text{O}_4$ in 21 m LiTFSI at 1C. (c) $\text{TiO}_2/\text{LiMn}_2\text{O}_4$ in 21 m LiTFSI and 21 m LiTFSI : 8 m LiOtf at 0.5C. (d) $\text{Li}_4\text{Ti}_5\text{O}_{12}/\text{LiNi}_{0.5}\text{Mn}_{1.5}\text{O}_4$ in 20 m LiTFSI : 8 m LiBETI at 0.5C. The cell capacity is calculated based on the total weight of the positive and negative active materials. Adapted from Ref^{58,111,122,157}.

Apart from improving capacity retention and Coulombic efficiency, the use of WiSE is said to impact solubility equilibrium of SEI or transition metal due to a decrease in water activity related to lower polar properties of water as most of water molecules are involved in the solvating sphere¹⁵⁸. Moreover, both SEI and electrode dissolution rates were reported to kinetically decrease as the increase in viscosity reduces the diffusion of dissolved species in the bulk and confine the dissolved species near the interface. At the positive electrode side, the smaller electrode area exposed to water due to the population of the double layer by anions¹⁵⁸ also kinetically reduce electrode dissolution rate. When formed by using Otf^- anions or additives such as tris(trimethylsilyl) borate (TMSB), CEI can also prevent transition metal dissolution such as Co or Mn at the positive^{156,159}.

Moreover, as pH of WiSE is neutral or mildly acidic, the use of Al current collector at the negative is enabled. Indeed, Al passivation domain is comprised between pH values of 4 to 8.5. At the positive electrode, the repulsion of water from the double layer, combined with the high TFSI^- oxidation potential, slows down the kinetics of Al dissolution¹⁶⁰, therefore enabling its use as current collector¹⁵⁰. Altogether, the possibility to use Al current collectors on both sides is of great interest as it has a low density (light weight), high electronic conductivity, low cost and great ability to process thin rolls.

As a conclusion, these studies have renewed interest for aqueous systems relying on the use of superconcentrated electrolytes, which was later on extended to aqueous Na-ion^{161–165}, K-ion^{166–169}, Zn-ion^{170,171} based on the promises of extending the ESW, Li-O_2 ¹⁷² in which reversible Li_2O_2 formation is observed unlike in diluted aqueous electrolytes, Li-S ^{173,174} in which WiSE prevents from polysulfide redox shuttle, Zn metal-based cell showing reversible Zn plating stripping^{170,175,176} or dual-ion battery including the halogen conversion-intercalation^{177–179}. However, several observations such as the fast capacity decay when using LTO as negative electrode call for further investigations to understand if the improved of ESW in WiSE is real in practice and to improve the overall performances of these systems, especially regarding instabilities at the negative electrode (*i.e.* the cathodic challenge).

3 Further improving aqueous superconcentrated-based LIB by expanding the ESW limit at the negative electrode side

Several strategies are employed to solve the cathodic challenge. On the one hand, the tuning of the electrolyte properties with the removal of free water molecules from the electrolyte¹⁴⁹, which would potentially open the path for increased ESW, or the use of additive to suppress water from Li^+ solvation sheath, as reports pointed towards the greater reactivity of water molecules participating to the Li^+ solvation sheath compared to free water molecules¹⁴⁴ are envisioned. On the other hand, several research groups focused their efforts on the use of coatings capable of preventing water to access the interface.

3.1 Increase in concentration to decrease the free water molecule amount and enhance thermal operation range

In binary mixtures, the electrolyte concentration is found to increase to greater values than the solubility limit of each of the two salts, thus reducing the amount of free water. Indeed, a hydrated salt can dissolve a non-hydrated salt which possess similar chemical properties. Mix-anions WiBS electrolytes^{58,122,180,181}, *i.e.* two salts based on the same cation but different anions, were first introduced in 2016 by Suo *et al.*¹²² and Yamada *et al.*⁵⁸, using 21 m LiTFSI : 7 m LiOTf and $\text{Li}(\text{TFSI})_{0.7}(\text{BETI})_{0.3} \cdot 2\text{H}_2\text{O}$, respectively. These systems are generally based on the use of stable chaotropic anions, *i.e.* disrupting the bulk-like water interactions, and good SEI-former anions, as rationalized by Reber *et al.*¹⁸². However, despite the decrease of free water molecule in the bulk, the increase in ESW for mix-anion systems is very limited, if not inexistent at the negative electrode (see Figure 1. 23).

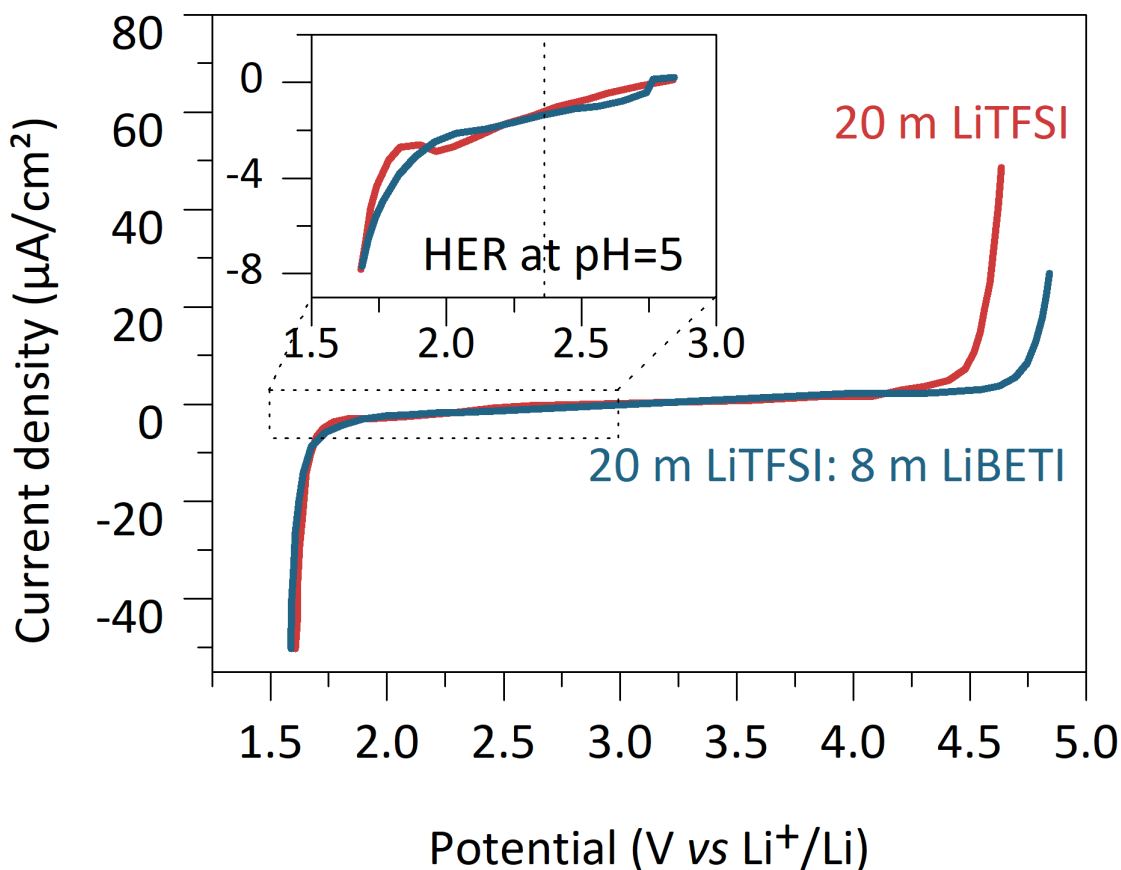


Figure 1. 23 Electrochemical stability window of 20 m LiTFSI and 20 m LiTFSI : 8 m LiBETI on stainless steel. Linear sweep voltamogram performed at 0.1 mV/s at room temperature. Adapted from Ref¹⁵³.

Mix-cation electrolytes^{183,184}, *i.e.* two salts based on one anion but using two different cations (Na-Li, K-Li or Na-K-based ones), enable to achieve greater solubility than mix-anion¹⁶², further minimizing the water to salt ratio. Nonetheless, a major drawback of this strategy is the co-intercalation¹⁸⁴ of both alkali cations that leads to fast performances decay. Thus, ammonium inert co-cations (such as tetraethylammonium (TEA⁺) or trimethylethylammonium (Me₃EtN⁺)) with larger radii were used^{162,183} (see Table 1. 1, for a comparison of cation radii).

Table 1. 1 Radii of different cations used in WiBS.

Alkali metal	Li ⁺	Na ⁺	K ⁺	TEA ⁺
Ionic radius (Å)	0.68	0.97	1.33	3.37

Besides, ternary electrolytes -based on the introduction of ionic liquid¹⁸⁵ (IL) for instance- have also been used to further increase the solubility of salts, as the entropy of mixing increases more in ternary than in binary mixtures. Eventually, to increase the

solubility limit and the thermal stability by shifting the liquidus temperature to lower temperature^{163,165,186}, the high vibrational mobility and flexibility of asymmetric moieties of ions is useful as they impede the formation of long range order^{165,180,181,187}. The asymmetry of the anion, such as FTFSI⁻ or PTFSI⁻, enable the formation of an asymmetrical solvation sheath of Li⁺ (see Figure 1. 24a, red circle). Hence, uncoordinated moieties, freer and more mobile, rotate and disturb the surrounding solvation structure preventing close packing of anions and cations (see Figure 1. 24a, purple circle). Furthermore, the asymmetry of the anion itself reduces the probability for specific rearrangement.

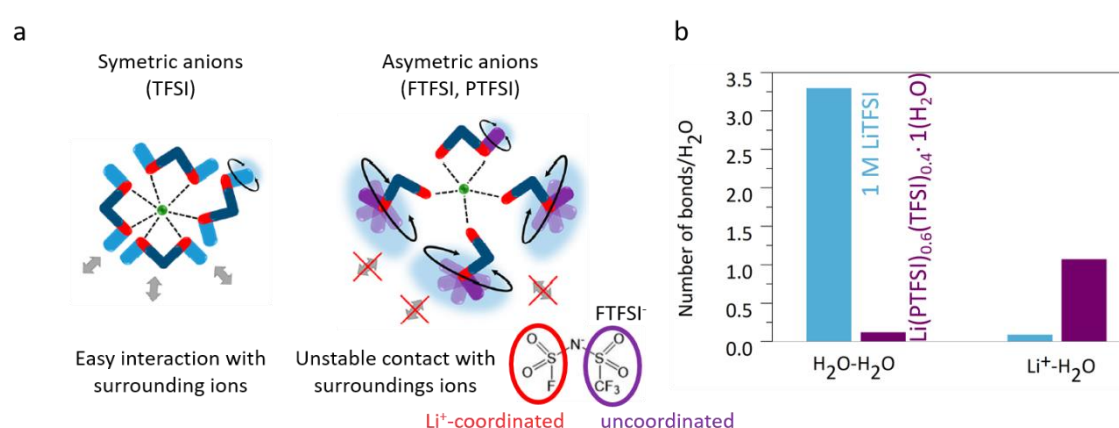


Figure 1. 24 (a) Schematic illustration of the difference in local coordination for symmetric TFSI⁻ and asymmetric FTFSI⁻ anion. (b) The numbers of hydrogen bond and coordination to cations around a water molecule, which were obtained by averaging three trajectories (The geometric criteria of hydrogen bonds were defined by the radial distance between the donor and acceptor oxygen atoms (< 3.5 Å) and the angle between the acceptor oxygen atoms and a donor-H-acceptor (135–180°) for a diluted 1 M LiTFSI and a WiBS electrolyte based on Li(PTFSI)_{0.6}(TFSI)_{0.4}). Adapted from Ref^{181,186}.

However, even though by using mix-anion, mix-cation or asymmetric ion-based electrolytes all water molecules are generally bounded to Li⁺ with negligible H-bonds, as calculated by MD simulation for mix-asymmetric anion electrolyte (see Figure 1. 24b), they generally leads to a decrease in conductivity and an increase in viscosity, as shown in Figure 1. 25 (bottom part) with limited thermal operating range (top part) and restricted increase in the cathodic limit of the ESW (middle part), restraining the use of negative electrode to LTO at best. Therefore, while research efforts dedicated to novel salts need to be continued to further improve electrolyte properties, other solutions are also investigated. Among them, tuning the solvation sheath of the Li⁺ cations by using hybrid organic/aqueous electrolyte to remove water from the first solvation sheath of Li⁺ and thus prevent water reduction was proposed.

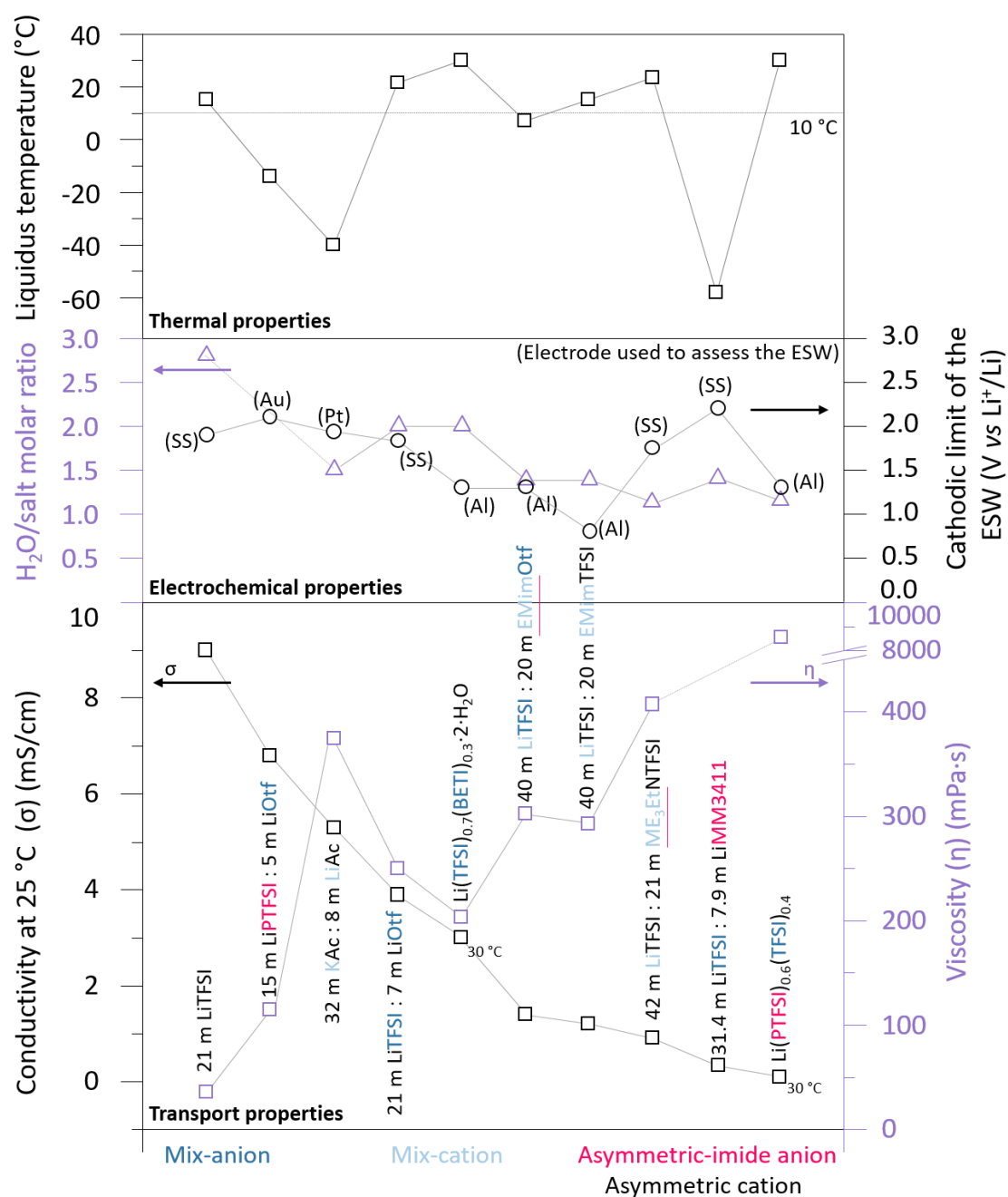


Figure 1. 25 Summary of some of the electrolyte properties (liquidus temperature, conductivity, viscosity, water to salt molar ratio, cathodic limit of the ESW (corresponding to the negative electrode side)) using mix-anion (dark blue), mix-cation (light blue), asymmetric-imide anion (pink) and asymmetric cation (underlined) in Li-ion battery. Adapted from Ref^{58,111,122,180,181,183–185,187}.

3.2 Electrolyte optimization: tuning the solvation sheath of Li^+ cation to change the reactivity

First, hybrid aqueous/non-aqueous electrolyte reduces water activity in the bulk by forming H-bonds between non-aqueous solvent and water, as observed in dimethylsulfoxide (DMSO)-based electrolyte^{188,189}. Moreover, the addition of co-solvent strongly coordinating Li^+ can promote the removal of water from the first solvation sheath of the alkali ion, or at least decrease its quantity (see Figure 1. 26a), thus preventing or slowing down water reduction. DMSO, dimethylformamide (DMF) and urea^{188–190} were identified as good candidates owing to their greater donor numbers than water (29.8 for DMSO vs 18 for water). On the contrary, DMC and acetonitrile addition^{191,192} impacts the solvation sheath by increasing the fraction of water in Li^+ first solvation sheath, thus promoting the nanophase separation leading to a water-rich domain and a TFSI-DMC-rich domain, as shown in Figure 1. 26b and c. This promoting effect will be detrimental for the cathodic stability of WiSE.

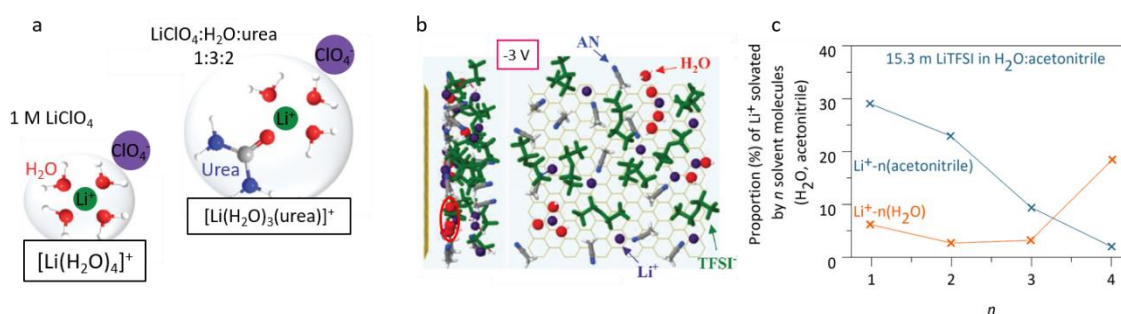


Figure 1. 26 (a) Modification of the solvation sheath of Li^+ cation upon addition of urea. Adapted from Ref¹⁹⁰. (b) Snapshots (including front and right side views) of inner-Helmholtz layer of negatively charged electrodes obtained from molecular dynamics (MD) simulation in 15.3 m LITFSI in water:acetonitrile (1:1 molar ratio). (d) Proportion of the Li^+ solvating with 1, 2, 3 and 4 solvent molecules (H_2O or DMC), obtained from molecular dynamic (MD) simulations. Adapted from Ref¹⁹².

Furthermore, not only the reduction potential of the co-solvent needs to be greater than the HER to promote the SEI formation, but the reduction product also has to be insoluble. Besides, as neutral solvents are less sensitive to negative repulsion, their reduction should be easier than TFSI-based clusters, thus leading to their participation to the SEI formation. DMC¹⁹², acetonitrile¹⁹², tetraethylene glycol dimethyl ether¹⁹³ (TEGDME), polyacrylamide¹⁹⁴ (PAM) reduction during first charges were reported to contribute to the presence of organic components in the SEI, thus enabling to expand the cathodic limit of ESW below 1 V vs Li^+/Li at the negative electrode while LiF is kept

in the inner layer due to TFSI⁻ degradation¹⁹² (see Figure 1. 27a and b). Upon urea, 1,5-pentanediol¹⁹⁵ or sulfolane¹⁹⁶ addition, an organic-inorganic SEI was also identified as illustrated by the dense SEI majorly composed of Li₂CO₃ and amorphous polyuria in urea-based electrolyte (see Figure 1. 27c) but without LiF participation and limited increase in the cathodic limit of the ESW (see Figure 1. 28).

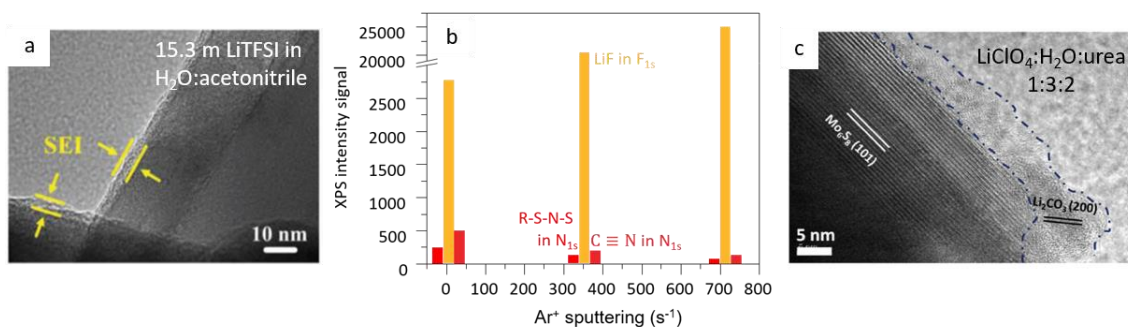


Figure 1. 27 (a) TEM images of LTO negative electrode after cycling showing the formation of a LiF-based SEI in 15.3 m LiTFSI in H₂O:acetonitrile. (b) Intensity changes of XPS analysis of LiF (yellow), C≡N (dark red), R-S-N-S (red) from F 1s and N 1s with various sputtering durations (c) TEM images of Mo₆S₈ negative electrode after 10 cycles showing the formation of a Li₂CO₃ SEI in 1:3:2 LiClO₄:H₂O:urea electrolyte.

Bulk properties, notably the conductivity, the cathodic limit of the ESW (corresponding to the negative electrode side) and the thermal properties are reported in Figure 1. 28. The expansion of the ESW enables to cycle LTO negative electrode in a mixture of water:acetonitrile at 0.2C¹⁹³, using LiTFSI:H₂O (1:2.8 molar ratio) and LiTFSI:TEGDME (1:0.41 molar ratio) in the proportion 1:1 (mass ratio), though only charging rates faster than 1C were tested¹⁹³ or in the sulfolane:water-based electrolyte¹⁹⁶. Other electrolytes are reported to cycle with negative electrode having greater intercalation potential, such as Mo₆S₈^{190,195} or TiO₂¹⁹⁴. Moreover, as observed in Figure 1. 28, the expansion of the ESW is in reverse order with the enhancement of conductivity (often lower than ≈ 3 mS/cm). Thus, tuning the solvation sheath by adding non-aqueous solvent, which can be related to the concept of diluted-concentrated electrolyte, may improve the cell performances by enabling the cycling of LTO electrode but this approach does not entirely overcome the cathodic challenge yet neither preserve good physico-chemical properties.

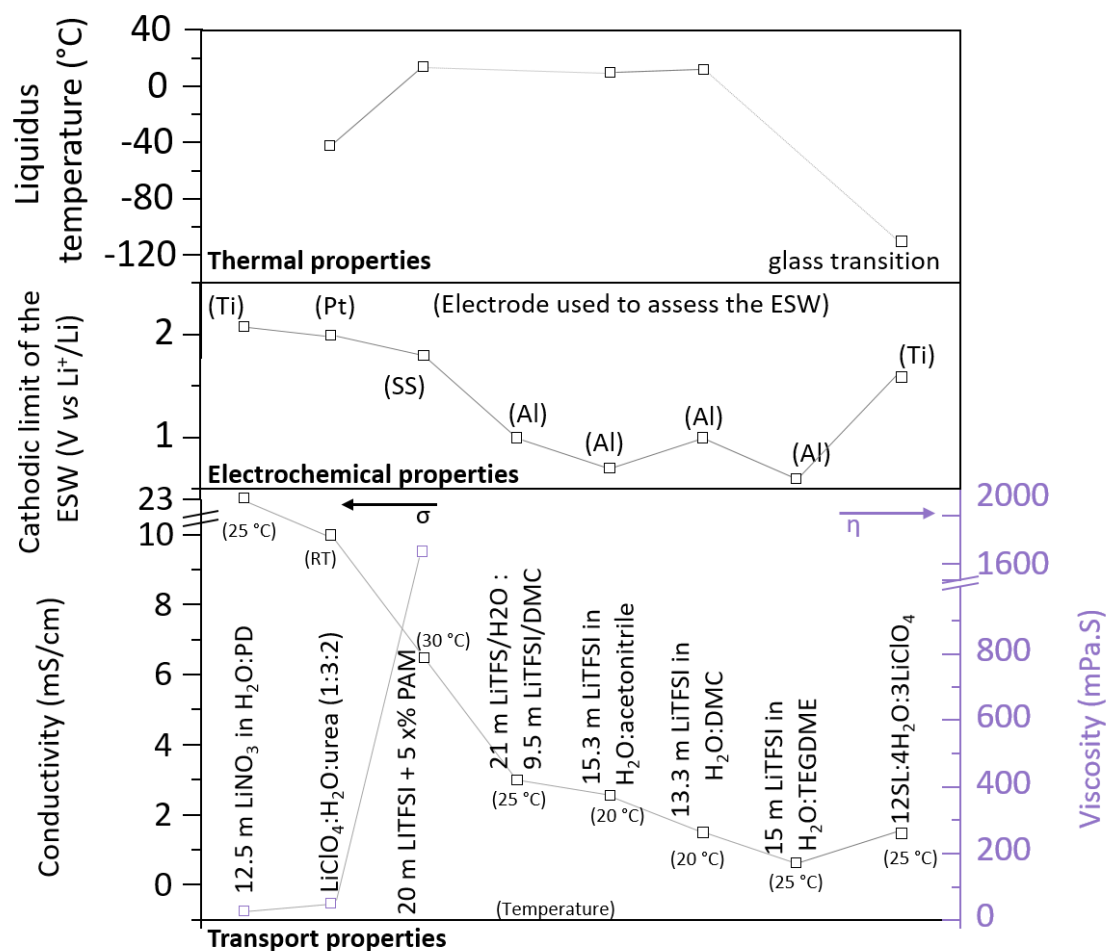


Figure 1. 28 Summary of some of the electrolyte properties (conductivity, viscosity, cathodic limit of the ESW and thermal stability) using solvation sheath tuning in Li-ion battery. Adapted from Ref^{190–196}.

3.3 Reducing water activity by using polymer electrolyte

The incorporation of WiBS in a polymer matrix enables to reduce water activity¹⁹⁷ by coordinating water with the polymer moieties. UV-curable gel-polymer electrolyte (GPE) (see Table A.1. 3, at the end of the chapter for details) using low viscosities polymers was proposed to enable good wetting of the porous electrodes^{197–199}. Moreover, in the spirit of suppressing the use of fluorinated salts and developing low-cost electrolyte, He *et al.*²⁰⁰ reported a *Water-in-ionomer* electrolyte based on 50 wt% LiPAA but constraining the negative material selection to the use of TiO₂. Furthermore, the suppression of the classical H₂O-H₂O H-bonds structure and the reduction of the amount of free water is promoted upon addition of PEG^{201,202} or PEO²⁰³. Such strategy enables decreasing the concentration of LiTFSI down to 2 m LiTFSI in a 2 m LiTFSI-PEG_x(H₂O)_(1-x),

$71 < x \text{ (wt\%)} < 94$, leading to a decrease in cost and toxicity, as reported by Xie *et al.*²⁰¹ and Li *et al.*²⁰².

However, alike for classical WiSE, a $\text{Li}(\text{H}_2\text{O})_4^+$ -rich domain and a polymer-LiTFSI-rich domain are found, suggesting that the cathodic challenge remains unsolved²⁰³. Besides, in these GPE, alike previously observed for organic/aqueous electrolytes, the ESW and the transport properties were found to be directly related to the water content^{201,203}. Indeed, increasing the water concentration from 6 wt% to 29 wt% in a LiTFSI-PEG-based GPE enhances the conductivity from 0.9 mS/cm to 3.4 mS/cm, while unfortunately reducing the ESW by $\approx 500 \text{ mV}$ ²⁰¹.

Eventually, in 2017, Yang *et al.*²⁰⁴ reported the assembly of batteries using metallic Li or graphite in combination with high potential positive electrode using a WiBS-gel polymer based on 21 m LiTFSI : 7 m LiOtf with 10 wt% of polyvinyl alcohol (PVA). Nonetheless, these outstanding performances rely more on an extra organic polymer coating layer used to protect the negative electrode from the HER, as shown in Figure 1. 29, than on the use of WiBS.

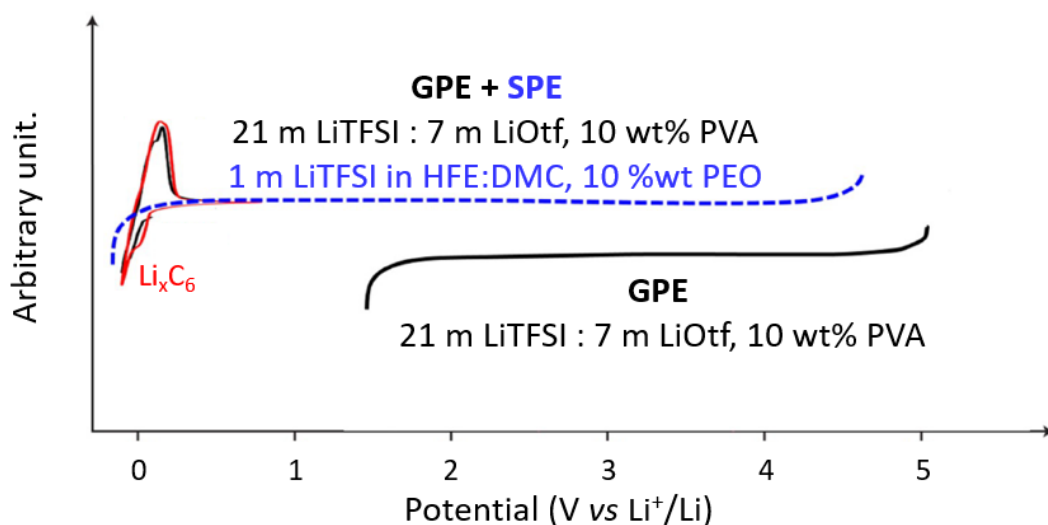


Figure 1. 29 Electrochemical stability window (ESW) of WiBS-gel polymer with or without an extra organic coating. Adapted from Ref¹⁹⁹.

3.4 Interface optimization: inorganic or organic coatings on the negative electrode to form artificial SEI

The use of metallic Li or graphite in WiSE-based electrolyte were shown to be enabled by the use of organic-coatings that (i) provides good mechanical properties, (ii) prevents

water from accessing the interface and (iii) may contribute to the SEI formation. The first type of organic coating integrates a GPE consisted of a HFE-LiTFSI-PEO GPE (HFE stands for highly fluorinated ether, here 1,1,2,2-Tetrafluoroethyl 2,2,2-Trifluoroethyl Ether)²⁰⁴. During first charges, the GPE undergoes reductive decomposition to form a LiF-based SEI which properties are enhanced by the contribution from organic-based compounds. Using this system, graphite and metallic Li electrodes were cycled 50 cycles at 0.3C with $\approx 99\%$ of Coulombic efficiency. Similarly, a UV-induced GPE coating using 1 m LiTFSI in fluoroethylene carbonate:trifluoroethyl methyl carbonate (FEC:FEMC, 1:1 vol%) was found to passivate the graphite electrode¹⁹⁹. However, the graphite/LCO cell performances show a rapid capacity decay (see Figure 1. 30). Besides, as proposed by Dubouis *et al.*¹³⁴, TFSI⁻ anions undergo a chemical degradation in presence of HO⁻ anion to form the SEI. Therefore, Zhang *et al.*¹⁹⁸ cycled a LTO-based cell for 200 cycles at 0.5C using a strongly basic solid polymer electrolyte (SPE), LiTFSI-PEO-KOH, to enable the formation of a LiF-Li₂CO₃-containing SEI that incorporates polymeric decomposition products.

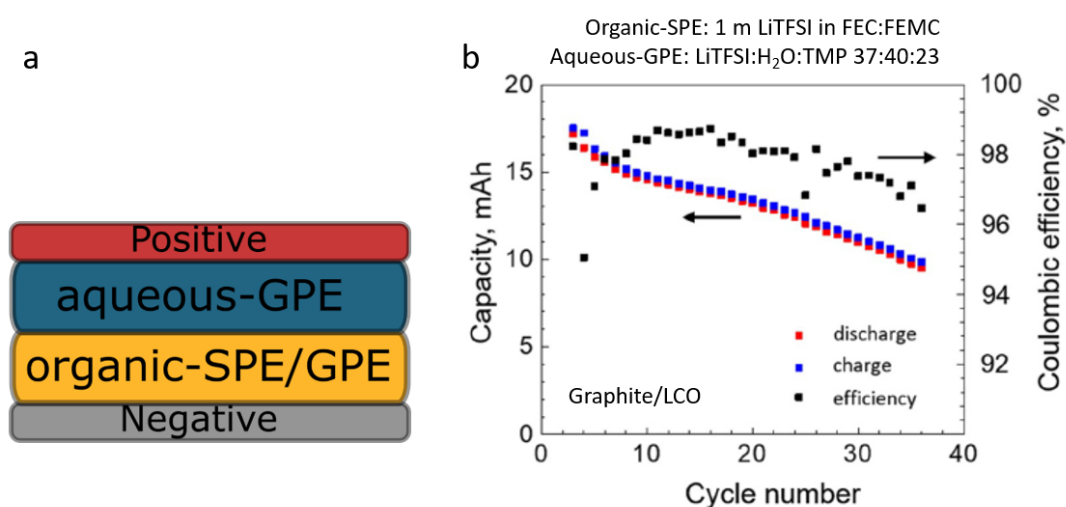


Figure 1. 30 (a) Scheme of a cell based on an organic coating. (b) Capacity and Coulombic efficiency as a function of cycle number for a graphite/LCO cell cycled in hybrid organic/aqueous electrolyte and using a polymer coating as a protection of the negative electrode. Adapted from Ref¹⁹⁹.

Inorganic coatings were also tested in WiSE. The propensity of a coating to suppress or, at least, reduce HER depends on its intrinsic electrocatalytic activity²⁰⁵. Aluminum oxide (Al₂O₃) coating was one of the most widely used^{205–207} as it shows the lower HER activity (see Figure 1. 31a.) and it is also known to be insoluble in water. However, LTO-Al₂O₃-coated electrodes were found to initially deliver 84.5 % of Coulombic efficiency in

a LTO- Al_2O_3 /LMO battery, suggesting that even though a conformal inorganic coating is deposited, some defects are present causing some electrolyte consumption. After 60 cycles, the LTO- Al_2O_3 /LMO cell could deliver 99 % of Coulombic efficiency even though a smooth capacity decay is observed (see Figure 1. 31b). The use of Al_2O_3 coating was also reported to suppress the oxygen reaction reduction (ORR)²⁰⁷ and thus enable the use of open-air cells (see Equation 1. 6 for ORR reactions) by suppressing self-discharge caused by the presence of dissolved O_2 ¹⁰⁷ (Figure 1. 31c). However, such design restricts the use of WISE to LTP-like negatives.

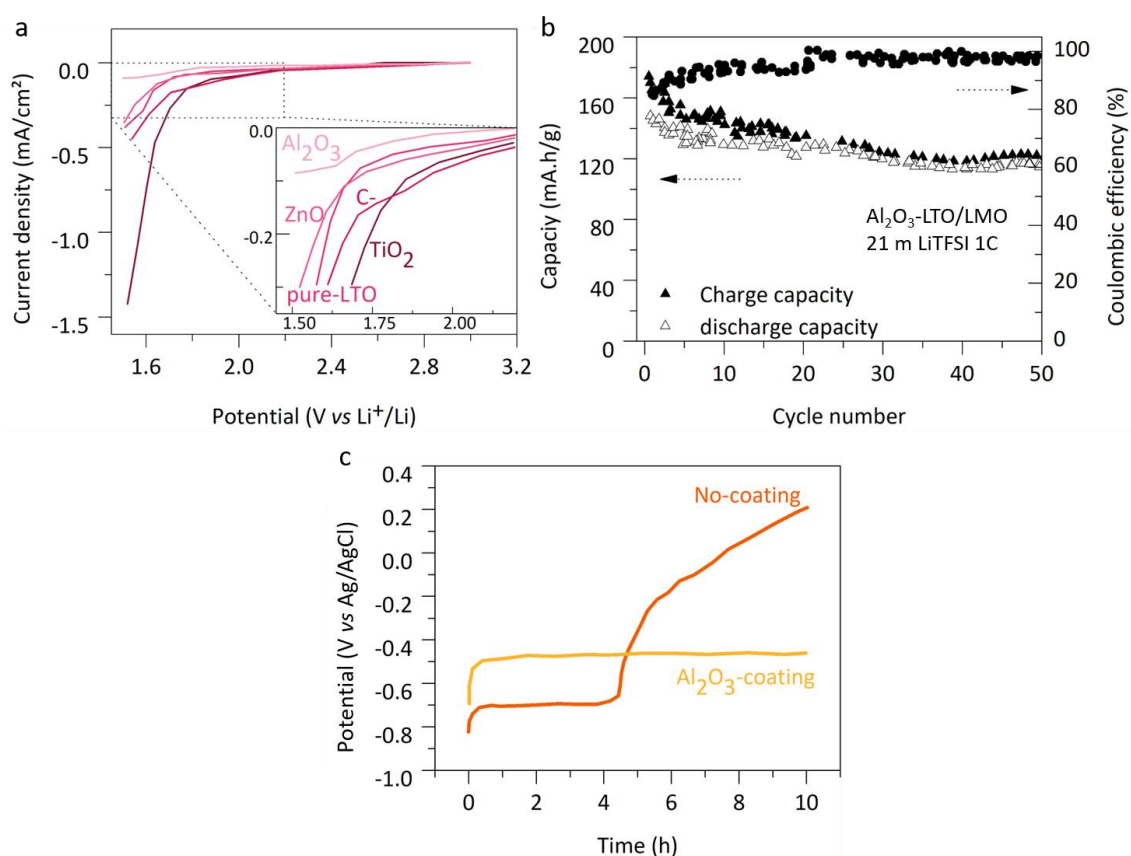
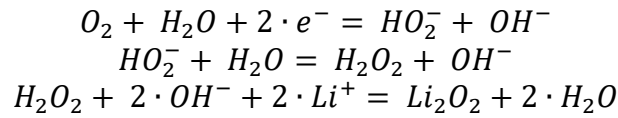


Figure 1. 31 (a) Cathodic limits evaluated by linear sweep voltammetry on LTO surfaces coated with different materials (inset shows the enlarged view). Counter electrode: activated carbon; reference electrode: Ag/AgCl, scan rate: 1 mV/s. (b) The cycling performance of the full cell using an Al_2O_3 -coated LTO negative and LMO positive in 21 m LiTFSI. Adapted from Ref²⁰⁵. (c) Effects of the ORR on the self-discharge of the lithiated $\text{Li}_3\text{Ti}_2(\text{PO}_4)_3$ electrodes in a three-electrodes open-cell configuration. The open-circuit potential curve of $\text{Li}_3\text{Ti}_2(\text{PO}_4)_3$ in the 1m Li_2SO_4 over 10 h of relaxation at open-circuit (orange). The open-circuit potential profile of the lithiated $\text{Al}_2\text{O}_3@ \text{Li}_3\text{Ti}_2(\text{PO}_4)_3$ electrode in 21 m LiTFSI : 8 m LiOtf (yellow) in the 28m WISE over 10 h of relaxation at open-circuit. These tests were conducted in an open-cell configuration with exposure to the ambient air. Adapted from Ref²⁰⁷.

Equation 1. 6:



Moreover, $AlF_3-Al_2O_3$ ²⁰⁶, LTP²⁰⁸ and carbon^{122,208,209} coatings were also reported but limiting the negative electrode choice to the use of TiO_2 electrode, far above graphite or even LTO ones.

Altogether, polymeric coating was reported to be the most efficient strategy as only this strategy enabled to cycle metallic Li or graphite negative electrodes.

Conclusion of the chapter

The introduction of superconcentrated aqueous electrolytes was proposed to overcome safety and environmental issues while keeping high performances. First, superconcentration enables to increase the ESW. Indeed, thanks to the formation of a SEI, majorly based on salt-derived compound LiF, negative electrodes with insertion potential laying outside the usual ESW (< 1.5 V) were implemented. Besides, WiSE-based battery enables to limit electrode and SEI dissolution while maintaining fast Li^+ transport owing to a high Li^+ transference number. As summarized in Figure 1. 32, many researches and advances have been done since the introduction of the seminal 21 m LiTFSI WiSE electrolyte developed by Suo *et al.*¹¹¹ in 2015, though achieving performances competitive with commercial-LIB still remains to be shown. Starting from binary or ternary liquid mixtures using mix-anion or mix-cation with asymmetrical ions, moving to hybrid aqueous/non-aqueous electrolyte to tune the first solvation sheath of Li^+ , using gel-polymer type electrolyte to reduce water activity or using artificial inorganic SEI on the negative electrode to prevent water to reach the electrode, all were proposed to partially overcome some limitations.

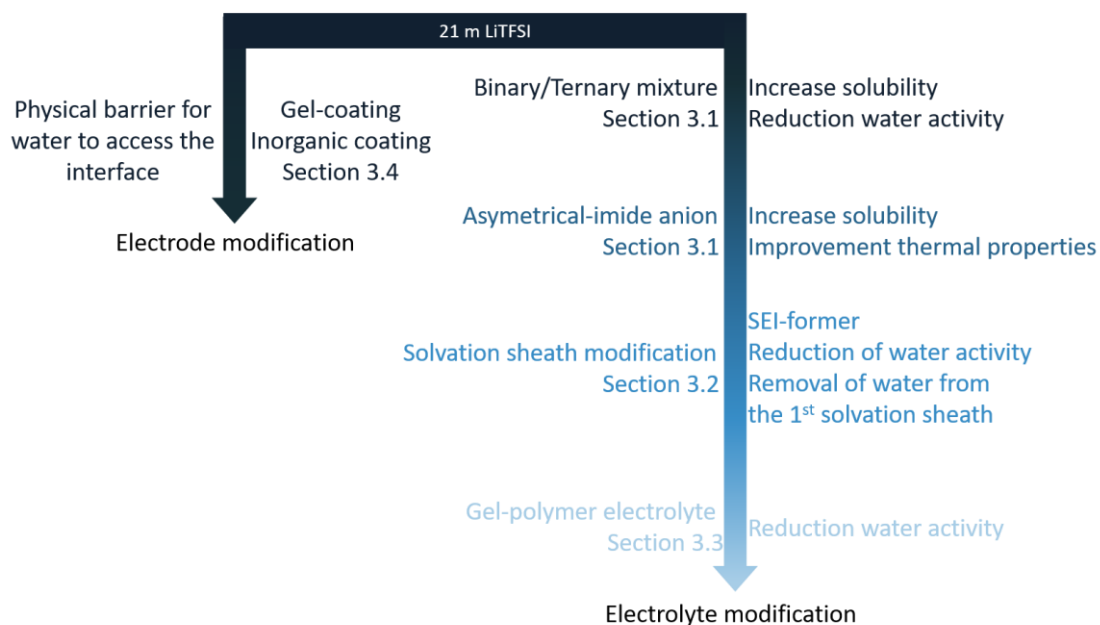


Figure 1. 32 Summary of the innovations developed to improve seminal-21 m LiTFSI aqueous superconcentrated electrolyte.

However, improvements previously observed cannot be directly transposed to practical devices as the increase of the ESW is strongly related (i) to the electrode material on which it is assessed and (ii) to the current threshold chosen. Eventually, one must look not only at the ESW but also at the physico-chemical properties to ensure high conductivity, low viscosity and wide thermal stability. As a conclusion, many parameters must be taken into account to assess the performances of one electrolyte. Therefore, the aim of this thesis is to explore the viability of 20 m LiTFSI as an example of aqueous superconcentrated electrolyte behavior by assessing key parameters representative of this chemistry to compete with classical LIB. Thus, Chapter 2 focuses on the performances obtained during cycling and self-discharge while monitoring parasitic reactions. Chapter 3 will investigate the instability of the native SEI and its ability to prevent the HER. Eventually, Chapter 4 will assess the use of LiF-based coating as artificial SEI for WiSE-based battery.

CHAPTER 2 – CYCLING VIABILITY OF AQUEOUS SUPERCONCENTRATED ELECTROLYTES BASED ON 20 MOL/KG LITFSI AND 20 MOL/KG LITFSI : 8 MOL/KG LIBETI ¹

¹ This chapter is based on the article that I co-authored: Droguet, L.; Grimaud, A.; Fontaine, O.; Tarascon, J. Water-in-Salt Electrolyte (WiSE) for Aqueous Batteries: A Long Way to Practicality. *Adv. Energy Mater.* **2020**, *10* (43), 2002440. <https://doi.org/10.1002/aenm.202002440>.

Introduction

As described in Chapter 1, the use of superconcentrated aqueous electrolytes was proposed to widen the electrochemical stability window (ESW) of aqueous-based electrolytes. Among them, 21 mol/kg (m) LiTFSI *Water-in-salt* (WiSE) has been widely used¹¹¹ since the seminal publication by Suo *et al.*¹¹¹ in 2015 reporting an increase in ESW up to 3 V. Besides, greater salts concentration -thus lesser water content- were reached by using *Water-in-bisalt* (WiBS) electrolyte such as $\text{Li}(\text{TFSI})_{0.7}(\text{BETI})_{0.3}$, potentially enlarging the ESW even more⁵⁸. Throughout this chapter, two similar electrolytes (20 m LiTFSI and 20 m LiTFSI : 8 m LiBETI) will be benchmarked as representative to study aqueous superconcentrated electrolytes practical viability in Li-ion battery (LIB).

Prior to study the effect of cycling parameters on performances of WiSEs-based aqueous batteries, proper current collectors must be selected. The ESW widening was previously assessed using metallic current collectors such as platinum, conductive glassy carbon or directly with current collectors materials (titanium, stainless steel or aluminum) with overpotential for the oxygen evolution reaction (OER) greater than 500 mV measured on the oxidation part^{58,152,160,161,184,210} using superconcentrated electrolytes. Instead, almost no change is observed for hydrogen evolution reaction (HER) overpotential (on the reduction part) as function of the metallic current collector^{152,210} when increasing the salt concentration, the exception being aluminum that passivates^{58,148,153,154,160}. However, these potential shifts are determined by cyclic voltammetry measurements rather than by potentio/galvano-static methods, hence departing from practical conditions. Indeed, by narrowing down the number of testing parameters, especially when the threshold current density is not taking into account, the influence of parasitic reactions such as the HER can be downplayed, as discussed by Kühnel *et al.*¹⁵³ Figure 2. 1 shows the ESW of 20 m LiTFSI on glassy carbon, aluminum, stainless steel and titanium current collectors. Aluminum and glassy carbon show an ESW reduction limit at 1.8 V vs Li^+/Li for HER (considering a $i_{\text{threshold}} = 0.25 \text{ mA/cm}^2$) followed by stainless steel at 2 V vs Li^+/Li and titanium reduction limit at 3 V vs Li^+/Li (Figure 2. 1b). On the oxidation limit, titanium passivation enables the increase of the ESW to potentials greater than 4.5 V vs Li^+/Li . Therefore, based on both these results and their relative ease-of-use, stainless steel current collectors were selected for electrodes which lithium insertion/de-insertion potential lays in the range 2 to 4 V vs

Li^+/Li , and titanium as current collector electrode materials which Li insertion/de-insertion potential is above 4 V vs Li^+/Li .

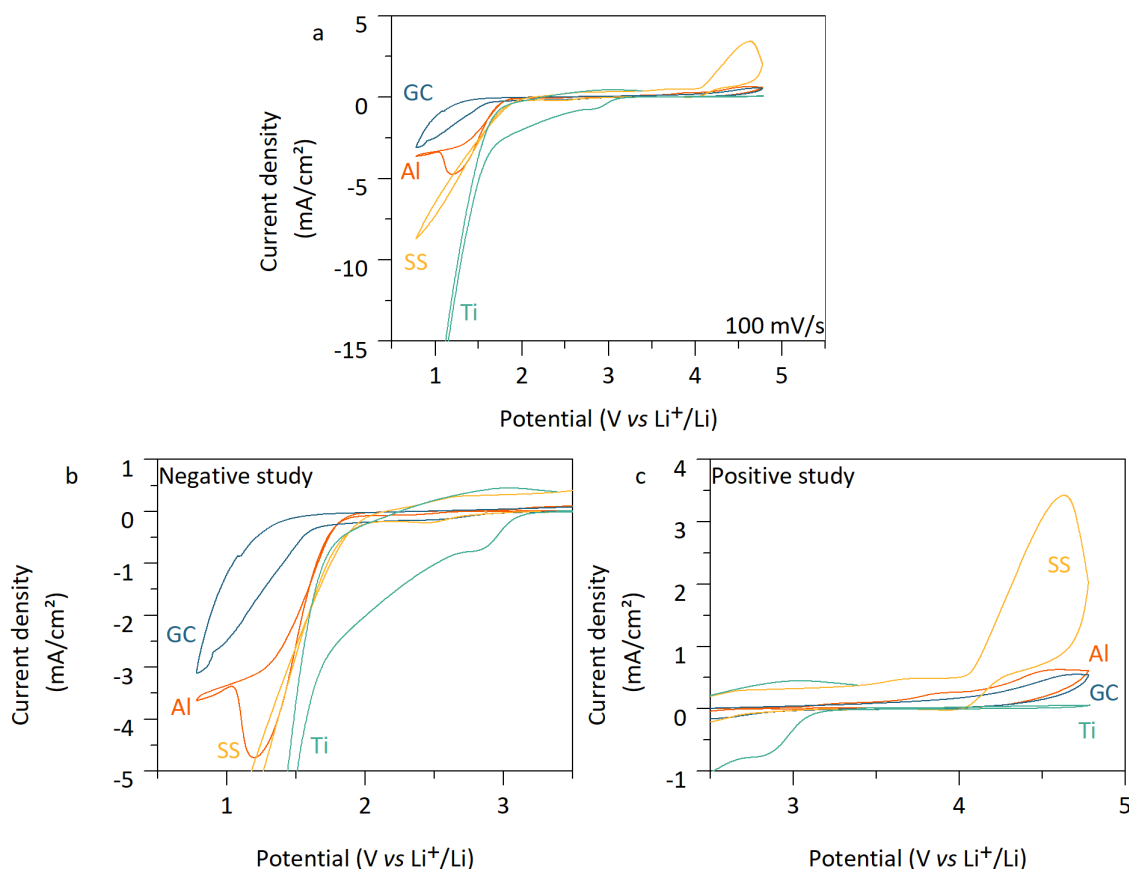


Figure 2. 1 Electrochemical stability window of 20 m LiTFSI electrolyte assessed at 100 mV/s on glassy carbon (blue), aluminum (orange), stainless steel (yellow) and titanium (green) as working electrodes (WE), Pt wire as counter electrodes (CE) and Ag/AgCl as reference. In (a) is display the full ESW and in (b) and (c) a zoom on the cathodic and anodic stability part, respectively, are provided.

To independently assess the parasitic reactions occurring at the negative electrode from those at the positive electrode, Mo_6S_8 negative electrode was chosen as cathode while NMC_{622} was chosen as anode to test the ESW. Mo_6S_8 and NMC_{622} electrochemical signatures are shown Figure 2. 2a. One can notice the classical electrochemical signature of Mo_6S_8 with four Li^+ ions being reversibly inserted, three at 2.3 V vs Li^+/Li and one at 2.7 V vs Li^+/Li . Moreover, LFP and LTP were selected as counter electrode for Mo_6S_8 and NMC_{622} , respectively. Indeed, using a 3-electrodes Swagelok cell with an Ag/AgCl reference electrode, both LFP and LTP counter electrodes, known to reversibly exchange Li^+ in aqueous electrolytes^{76,107,112}, were found to have their redox potential within the ESW of the WiSE electrolyte studied in this work (see Figure 2. 2b). Having defined the proper current collectors and active materials, full cells were thus assembled to study

the effect of WiSE on the redox properties of both active materials, Mo_6S_8 and NMC_{622} , measured against LFP and LTP, respectively (see Figure 2. 2a). Besides, to avoid that LFP and LTP counter electrodes limit the cell cycling, capacity ratio were set to 4:1 for LFP/ Mo_6S_8 and 1.1:1 for LTP/ NMC_{622} . Eventually, after checking the redox potentials for LFP and LTP versus the potential of Ag/AgCl reference electrode, the potentials for the working electrodes were rescaled versus Li^+/Li . Doing so, an upshift in ≈ 230 mV is observed when cycling Mo_6S_8 and NMC_{622} in WiSE compared to the organic electrolyte (1 M LiPF_6 in EC:DMC, *e.g.* LP30). This shift, previously observed, was assigned to the effect of the salt concentration on the redox potential of the intercalation electrodes⁵⁸. Such an upshift of the intercalation potential combined with the use of a fixed cutoff potential of 4.2 V defined vs Li^+/Li in charge explains the lower measured capacity for NMC_{622} in WiSE as opposed to non-aqueous electrolytes (see Figure 2. 2a, orange full and dash line). The importance of adequately selecting this cutoff potential will be discussed in greater detail in Section 4.

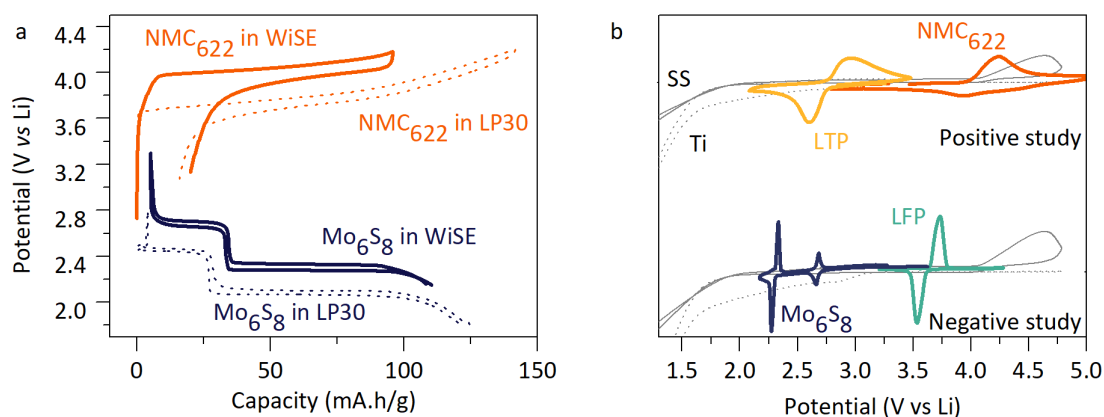


Figure 2. 2 (a) Galvanostatic charge and discharge signatures for electrode materials. Galvanostatic experiment performed at 1C with Mo_6S_8 measured in LP30 versus metallic Li and 20 m LiTFSI versus LFP on SS current collector (1st cycle). Galvanostatic experiment performed at 0.10C with $\text{LiNi}_{0.6}\text{Mn}_{0.2}\text{Co}_{0.2}\text{O}_2$ measured in LP30 versus metallic Li and 20 m LiTFSI versus LTP on Ti current collector (1st cycle). (b) Reversibility of Li^+ intercalation/de-intercalation of electrode materials in 20 m LiTFSI. Cyclic voltammograms performed at 1 mV/s on Mo_6S_8 (dark blue), LFP (light blue), LTP (yellow), NMC_{622} (orange) as WE, YP50 activated carbon as CE and Ag/AgCl as reference electrode. All experiments were performed at room temperature (RT).

1 Cycling performances in aqueous superconcentrated electrolyte on the negative electrode side: role of concentration, cycling rate and temperature

In this section, we will focus on the cycling performances of a $\text{Mo}_6\text{S}_8/\text{LFP}$ cell using either 20 m LiTFSI or 20 m LiTFSI : 8 m LiBETI to assess the viability of these aqueous superconcentrated electrolytes in practice. Cell performances were estimated with electrochemical tests upon varying concentrations, cycling rate (C-rate defined by 1C corresponding to one Li^+ inserted in one hour) and temperatures.

1.1 Use of Water-in-salt: 20 m LiTFSI as electrolyte

1.1.1 Influence of concentration and C-rate

The capacities in charge and discharge of a $\text{Mo}_6\text{S}_8/\text{LFP}$ cell were measured as a function of the salt concentration from 5 m up to 20 m, corresponding to *Water-in-salt* electrolyte. Cell capacity and Coulombic efficiency measured at 1C at room temperature are shown in Figure 2. 3a and b. The difference between charge and discharge capacities is becoming greater when lowering the salt concentration, *i.e.*, the Coulombic efficiency is decreasing. Furthermore, the capacity is found to fade over cycling much faster when lowering the salt concentration. These results can tentatively be interpreted either as the sign that no SEI is formed at lower concentrations or by invoking a greater solubility of inorganic compounds forming the SEI, such as $\text{LiF}^{134,146}$, $\text{Li}_2\text{O}^{146}$ or LiOH^{134} previously observed forming on the surface of negative electrodes, at lower concentrations. Either way, the continuous parasitic reactions occurring on the surface of Mo_6S_8 negative electrode consume Li^+ and cause the performances to decay over cycling at low concentration. Finally, and more interestingly, the initial capacity in charge is found, in Figure 2. 3a, similar for the different concentrations: 125 mA.h/g at 5 m, 120 mA.h/g at 10 m and 123 mA.h/g at 20 m, suggesting that the nature and the number of parasitic reactions are independent on the concentration during the first charge, before the formation of a SEI.

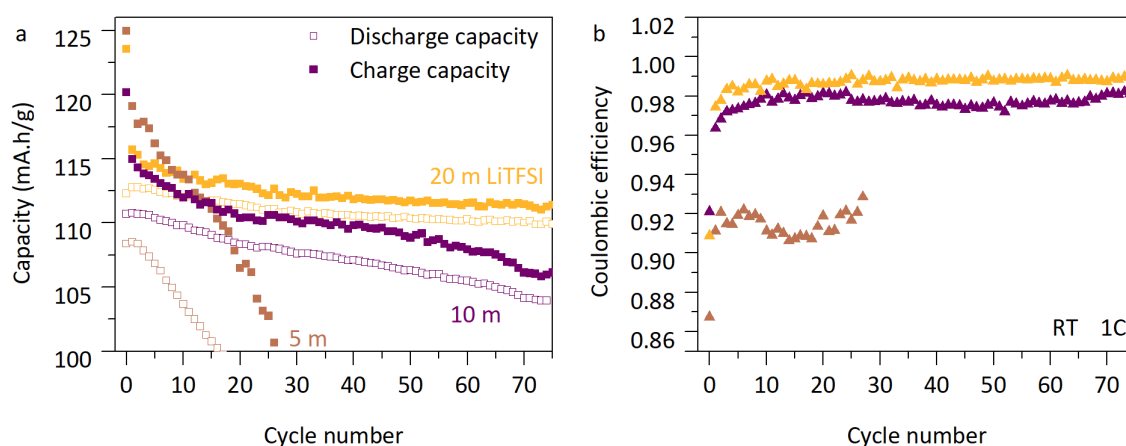


Figure 2. 3 Effect of concentration for Mo₆S₈/LFP full cells measured in LiTFSI-based aqueous electrolytes. (a) Capacities of charge and discharge and (b) Coulombic efficiency (CE) as function of cycle number for several concentrations: 5 m LiTFSI (brown square), 10 m LiTFSI (purple square), 20 m LiTFSI (yellow square). Constant current measurements were performed at 1C at room temperature (RT).

Even though the cycling performances improve with concentration, they are dependent on the C-rate, as shown in Figure 2. 4a and b where the evolution of the charge capacity (Figure 2. 4a) and the Coulombic efficiency (Figure 2. 4b) are reported for several C-rates at room temperature. Indeed, it clearly appears that the faster the cycling rate is, the higher the Coulombic efficiency. However, the absolute value for the charge capacity is slightly lower, hence leading to significant improvements in the cell capacity retention. This phenomenon can be related to greater amount of parasitic reactions occurring as time spent at potential close to the HER potential increases when lowering the C-rate, thus “artificially” increasing the charge capacity at the expense of the discharge capacity. As a result, and as often seen in the literature¹⁵³, one obvious way to increase the Coulombic efficiency and cycling performances of such systems is by increasing the C-rate. However, our work reveals that C-rate below 1C must be employed to accurately evaluate the performances of aqueous systems in this configuration.

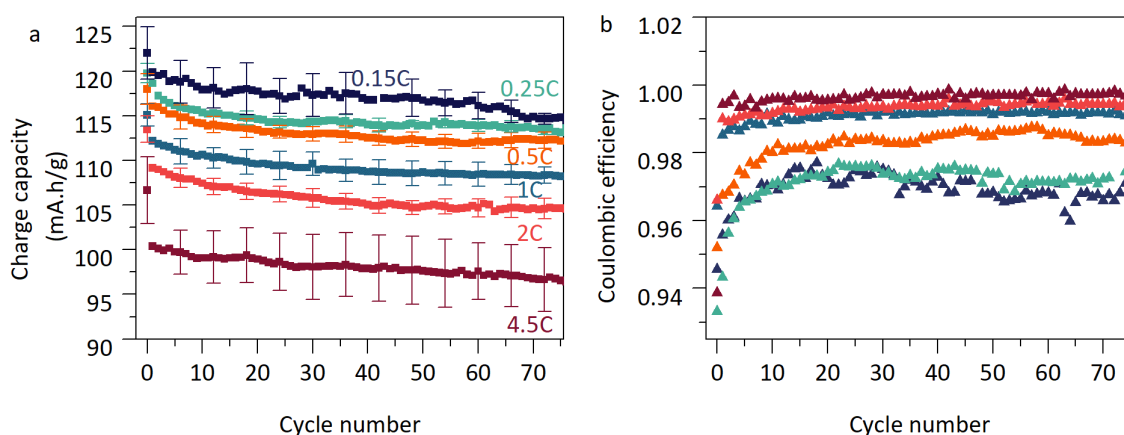


Figure 2. 4 Effect of C-rate for Mo₆S₈/LFP full cells measured in LiTFSI-based aqueous electrolytes. Capacity of charge (a) and Coulombic efficiency (b) as function of cycle number for several C-rate: 0.15C, 0.25C, 0.5C, 1C, 2C, 4.5C. Constant current measurements were performed in 20 m LiTFSI electrolyte at room temperature.

1.1.2 Influence of temperature

Figure 2. 5 reveals that the effect of temperature is more pronounced at low C-rate than at C-rate above 1C. Indeed, an operating temperature of 55 °C leads to a rapid decay of the reversible capacity and a drastic drop of the Coulombic efficiency, both leading to a shorter lifetime for the battery at low C-rate. Moreover, we can observe at 55 °C a larger charge capacity at the beginning of cycling associated with lower Coulombic efficiency (see Figure 2. 5a and Figure 2. 5b), demonstrating a greater amount of parasitic reactions at higher temperatures. Besides the enhancement of the global degradation of the cell (loss of electrical contact, faster aging of materials, etc.) at high temperatures, the origin for this phenomenon can be either kinetics or thermodynamics. On the kinetics side, a higher temperature will both enhance the HER kinetics, as well as the SEI degradation rate for SEI-components such as LiF, LiOH or Li₂O as reported in literature^{134,146}. On the thermodynamics side, note that the HER potential shifts towards lower potential by 160 mV between 25 °C and 55 °C ($E_{\text{HER}} @ 25\text{ °C}} = 2.16\text{ V vs Li}^+/\text{Li}$ and $E_{\text{HER}} @ 55\text{ °C}} = 2\text{ V vs Li}^+/\text{Li}$), while the Li insertion potential for Mo₆S₈ only shifts by 20 mV (see Figure 2. 5b). This difference leads to the appearance of a plateau attributed to the HER (as proved by gas monitoring) before the cell potential reaches the cut-off of 1.5 V, again artificially increasing the charge capacity of the LIB while reducing the lifetime.

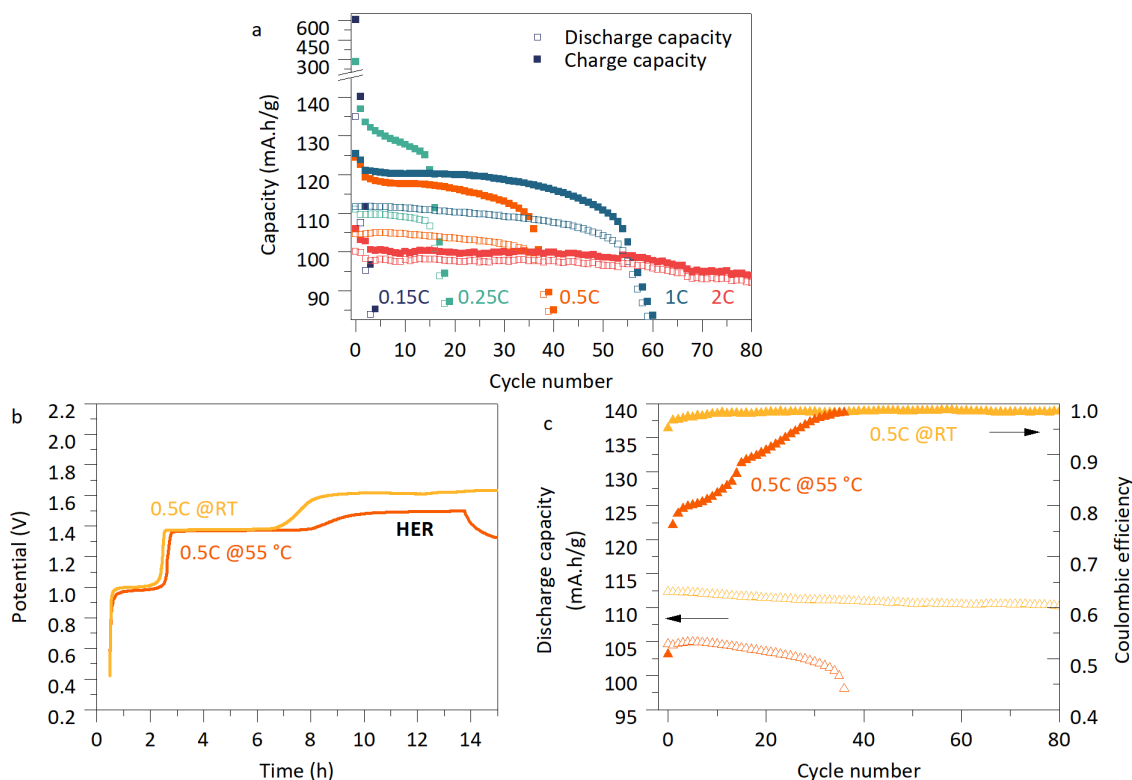


Figure 2. 5 Temperature impact for $\text{Mo}_6\text{S}_8/\text{LFP}$ full cells measured in 20 m LiTFSI. (a) Charge and discharge capacities as a function of cycle number at 55 °C for several C-rates: 0.15C, 0.25C, 0.5C, 1C, 2C. (b) Potential as function of time for cells cycled at 0.5C at 25 °C and at 55 °C showing the shift of the HER plateau depending on the temperature. (c) Comparison between discharge capacities and Coulombic efficiency as function of cycle number for cells cycled at 0.5C at 25 °C (yellow) and 55 °C (orange).

1.1.3 Reproducibility issue

During the temperature study using the 20 m LiTFSI electrolyte, we could observe for some cells cycled at 0.5C at 55 °C a large dispersion of charge and discharge capacities values (see Figure 2. 6a). Our results at 55 °C (capacity vs cycle number) for three different cells show charge capacity during the first charge ranging from 107 mA.h/g to 142 mA.h/g, far greater than the range for charge capacities determined at room temperature ($112 \text{ mA.h/g} < Q_{\text{charge @RT}} < 123 \text{ mA.h/g}$) (see Figure 2. 6a). This phenomenon is rooted in the effect of temperature that exacerbates small variations in the SEI formation and stability, which in turn leads to different microstructures (thickness and density) and thus damaging rate when cycled at 55 °C. Such variation is highlighted in Figure 2. 6b with the appearance of a HER plateau at 55 °C before the cell cut-off.

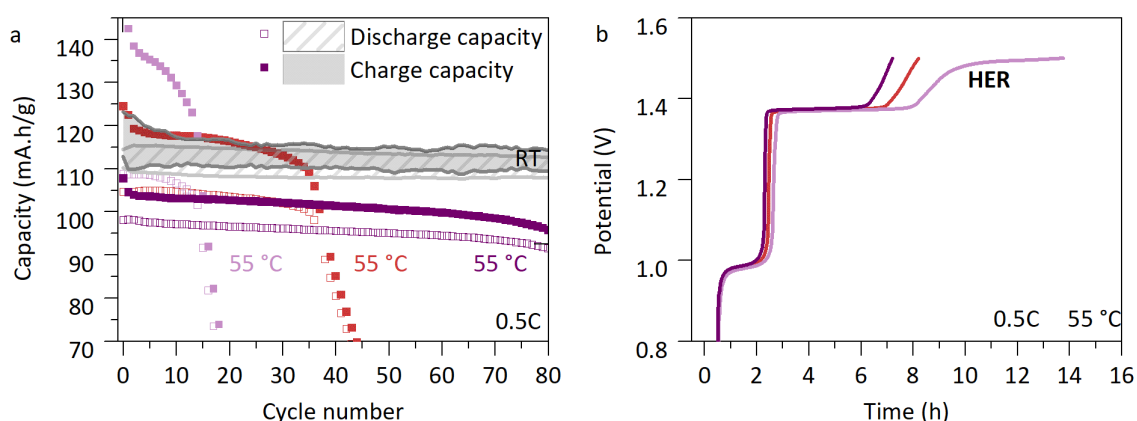


Figure 2. 6 (a) Charge and discharge capacities as function of cycle number for three $\text{Mo}_6\text{S}_8/\text{LFP}$ cells cycled at 0.5C at 55 °C and range of values for three cells cycled at 0.5C at room temperature that fall with the shaded grey area. (b) Potential as a function of time for three cells cycled in similar conditions, at 0.5C and 55 °C, showing the poor reproducibility of cell performances at elevated temperature.

1.2 Extension to Water-in-bisalt: 20m LiTFSI : 8 m LiBETI

To further study the viability of aqueous superconcentrated electrolytes, 20 m LiTFSI : 8 m LiBETI *Water-in-bisalt* electrolyte was then investigated. Indeed, such electrolyte, in which the water amount is even smaller (salt to water molar ratio is set to 1:2 in 20 m LiTFSI : 8 m LiBETI compared to 1:2.8 in 20 m LiTFSI), was previously propose to provide better cycling performances than classical 20 m LiTFSI electrolyte, thus enabling to cycle low potential negative electrode such as LTO⁵⁸.

1.2.1 Influence of the C-rate: 0.15C vs 1C at RT and temperature: RT vs 55 °C at 0.15C

Based on the results shown in section 2.1.1, the C-rate study was limited to C-rates no greater than 1C to accurately evaluate the performances of WiBS. Therefore, two C-rates of 1C and 0.15C were chosen to illustrate WiBS behavior with cycling rate. Figure 2. 7a shows the evolution of the charge capacity and the Coulombic efficiency with cycles. The influence of the C-rate for WiBS-based cell performances is in line with the results previously obtained in WiSE. Indeed, the faster the cycling rate is, the greater the Coulombic efficiency, the lower the charge capacity. Cycling performances were then tested at 55 °C (see Figure 2. 7b). Doing so, an increase of temperature was found to lead to greater capacity in charge (132 mA.h/g at 55 °C compared to 119 mA.h/g at RT) associated with lower Coulombic efficiency, in agreement with an increased amount of parasitic reactions occurring at high temperature due to faster HER kinetics, greater HER

onset potential and faster SEI degradation rate combined with an enhancement of the global degradation of the cell (loss of electrical contact, faster aging of materials, etc.), alike previously observed in WiSE.

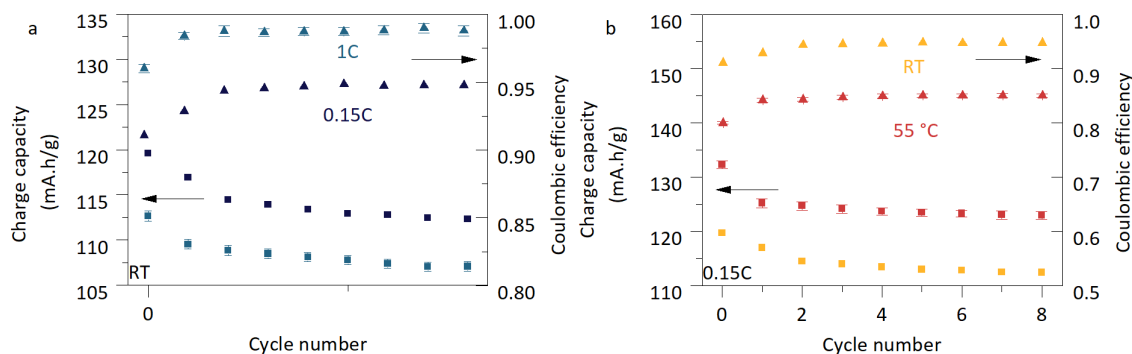


Figure 2. 7 Effect of C-rate and temperature for Mo₆S₈/LFP full cells cycled in 20 m LiTFSI : 8 m LiBETI LIB. (a) Capacity of charge and Coulombic efficiency as function of cycle number for two representative C-rates: 0.15C (dark blue) and 1C (light blue). Constant current measurements were performed in 20 m LiTFSI electrolyte at room temperature. (b) Temperature effect on WiBS-based LIB. Comparison between charge capacities and Coulombic efficiency as function of cycle number for cells cycled at 0.15C at room temperature (yellow) and 55°C (red).

1.2.2 Comparison with WiSE-based electrolyte at 55 °C at 0.15C

While all these measurements are very much in line with those previously obtained for WiSE, the capacity fading is nevertheless found to be much slower when using WiBS electrolyte than with WiSE (see Figure 2. 8), leading to longer shelf-life. Bearing in mind that the concentration of water in WiBS is 1.6 times smaller than in WiSE, this observation could at first be explained by a decrease of the number of water molecules available for the HER and a decrease of the dissolution rate of the SEI in WiBS^{148,211}. However, this explanation is contradicted by recent studies showing that water molecules reduced in the HER process are those solvating lithium cation²¹² and that the first solvation sheath of lithium cation is rather similar in WiSE and WiBS, therefore the reactivity of water in these two electrolytes should be alike. A more likely possibility is the viscosity difference between both electrolytes that is about 6 times greater for WiBS (203 mPa.s at 30°C⁵⁸) than for WiSE electrolyte (36.2 mPa.s at 25°C¹¹¹). Indeed, a greater viscosity would limit the HER kinetics and the degradation rate of the SEI, thus enabling better performances.

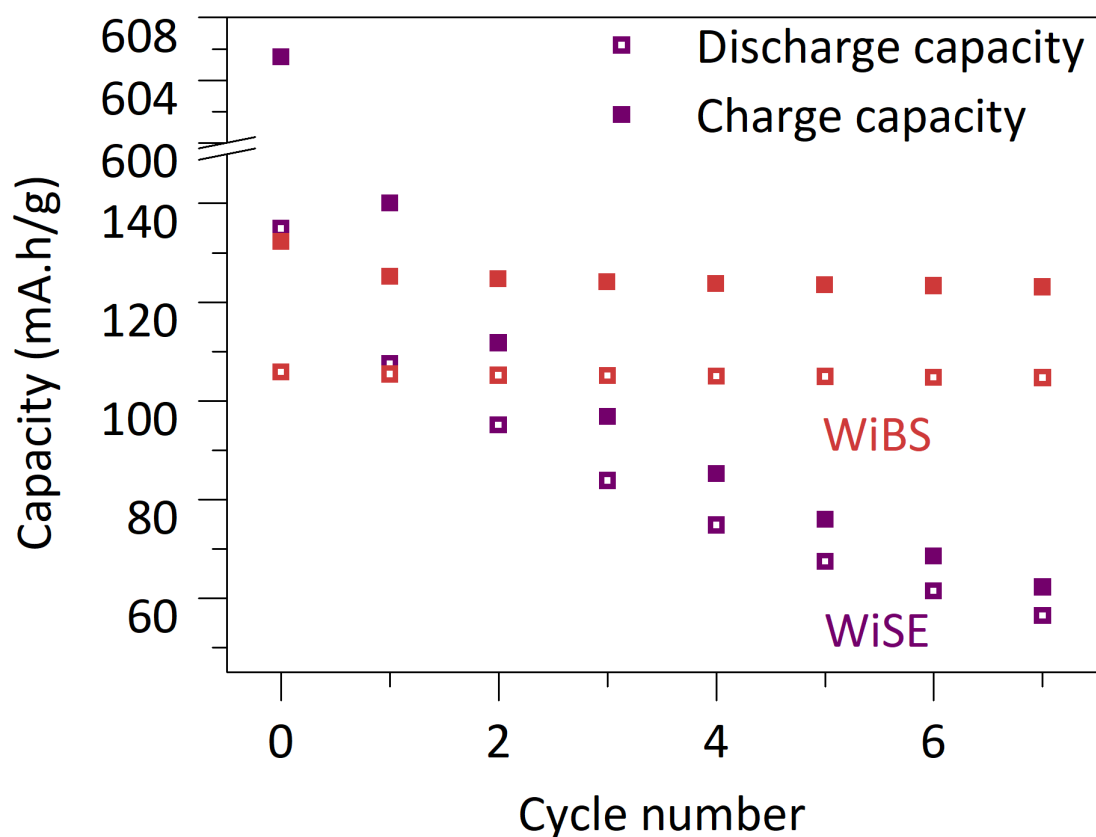


Figure 2. 8 Comparison of WiSE and WiBS performances with cycling. Charge and discharge capacity as function of cycle number for $\text{Mo}_6\text{S}_8/\text{LFP}$ full cells cycled at 0.15C at 55 °C.

Altogether, studies varying concentration, C-rate and temperature show that 20 m LiTFSI-based LIB still suffer from damaging parasitic reactions, which will be discussed in the following section dedicated to the water reduction reaction.

2 Origin of the performances decay: a gas monitoring study

Having demonstrated the effect of cycling conditions on parasitic reactions, we then performed *operando* gas monitoring using a combination of online electrochemical mass spectrometry (OEMS) and pressure cells (i) to highlight that water reduction takes place during cycling and (ii) to qualitatively and (iii) quantitatively interrogate the impact of gas evolution on the battery performances.

2.1 Pressure cells and Online electrochemical mass spectrometry (OEMS) results in Water-in-salt: 20 m LiTFSI

Figure 2. 9a shows the potential and pressure changes as a function of time during cycling for 20 m LiTFSI electrolyte. The cell pressure is found to increase when the potential reaches the 2nd lithium insertion plateau of Mo₆S₈ at 2.3 V vs Li⁺/Li (≈ 1.4 V in a complete Mo₆S₈/LFP cell, see Figure 2. 9b for the definition of the plateau). Strikingly, the pressure never stops increasing in this configuration during cycling, demonstrating that parasitic reactions keep occurring, consistent with the low Coulombic efficiency observed in Figure 2. 4b. Moreover, from OEMS measurements (Figure 2. 9b), we could deduce the formation of gaseous hydrogen as soon as Mo₆S₈ reaches its second lithium insertion plateau. Therefore, water reduction producing hydrogen is responsible for the pressure increase, and any SEI formed on the electrode at these potentials is not protective enough to prevent the continuous consumption of WiSE during cycling. Besides, it is important to notice that hydrogen evolution competes with lithium insertion, but the former does not prevent the latter. Hence, two rates for the electrochemical hydrogen evolution were observed in Figure 2. 9b. The first rate starts concomitantly with the 2nd insertion of lithium around 1.38 V. However, this first rate is slow compared to the one kicking in once the electrode is fully lithiated, when the potential goes above 1.4 V and where all electrons are consumed toward the HER. Moreover, as seen in Table 2. 1, the discharge capacity recorded with a pressure cell cycled at 0.10C remains stable at ≈ 107.5 mA.h/g during the four first cycles, unlike the charge capacity which is always greater and varies from 126 to 117 mA.h/g. This result indicates that lithium insertion into Mo₆S₈ is not affected by the HER during charge, as the cell provides the same discharge capacity over the first cycles. However, the continuous consumption of water *via* the HER may eventually lead to the crystallization of the salt and ultimately the drying out of the cell, that will be prejudicial for practical application¹⁵³.

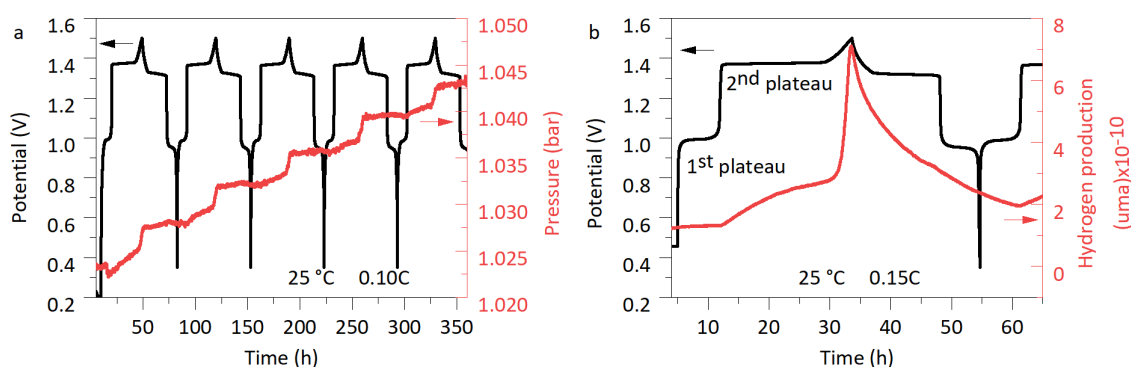


Figure 2. 9 Gas monitoring for a Mo₆S₈/LFP full cell measured in 20 m LiTFSI. (a) Potential (black line) and pressure (red line) as function of time at 0.10C monitored in a pressure cell. (b) Potential (black line) and hydrogen evolution (red line) as function of time at 0.15C monitored using an *online* electrochemical mass spectrometry (OEMS) cell. Experiments performed at 25 °C.

Table 2. 1 Discharge and charge capacities and Coulombic efficiency for a Mo₆S₈/LFP pressure cell cycled at 0.10C and 25 °C in 20 m LiTFSI.

Cycle number	Discharge capacity [mA.h/g]	Charge capacity [mA.h/g]	CE [%]
1	107.66	126.25	85.2
2	107.62	119.88	89.8
3	107.47	118.53	90.7
4	107.44	117.84	91.2

Figure 2. 10 shows the hydrogen evolution recorded during cycling at 0.15C and 55 °C by OEMS. First, these results indicate that, as already observed at 25 °C, hydrogen production starts on the 2nd Li insertion plateau at 1.37 V at 55 °C. Then, the hydrogen production is greater as the temperature increase, due to the enhancement of both the HER kinetics and SEI degradation rate. Indeed, an approximate linear fit of the first slope -corresponding to hydrogen production during 2nd insertion plateau- is four times greater at 55 °C than at 25 °C ($\approx 3.4 \cdot 10^{-11}$ uma/h at 55 °C compared to $\approx 0.81 \cdot 10^{-11}$ uma/h at 25 °C). Eventually, as shown in Figure 2. 5, increasing the temperature to 55 °C may lead to the apparition of a 3rd plateau around 1.46 V that can be attributed to pure HER.

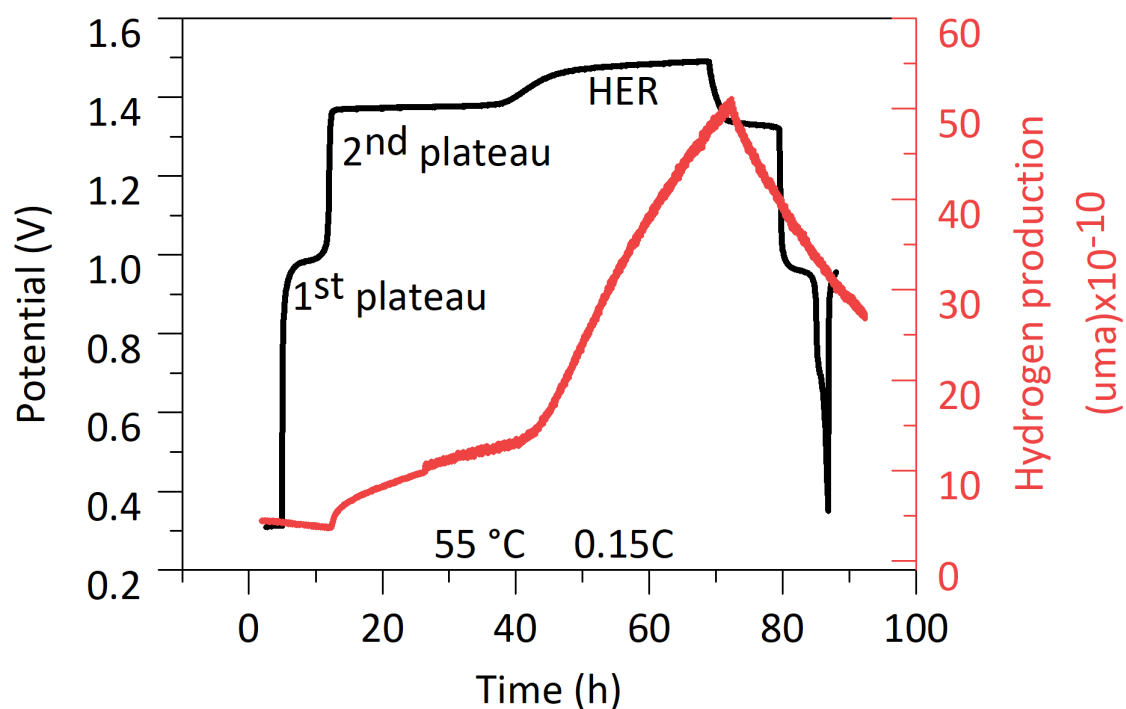


Figure 2. 10 Online electrochemical mass spectrometry (OEMS) performed in 20 m LiTFSI for a $\text{Mo}_6\text{S}_8/\text{LFP}$ full cell at 55 °C. Potential (black line) and hydrogen evolution (red line) as function of time at 0.15C.

2.2 Use of Water-in-bisalt: 20 m LiTFSI : 8 m LiBETI

The potential and the pressure changes plotted as function of time during cycling in 20 m LiTFSI : 8 m LiBETI (see Figure 2. 11a) show that the cell pressure continuously increases during cycling, as the result of the evolution of H_2 spotted by OEMS measurement (see Figure 2. 11b). Hence, alike for WiSE electrolyte, continuous water consumption occurs in parallel with lithium insertion for WiBS electrolyte.

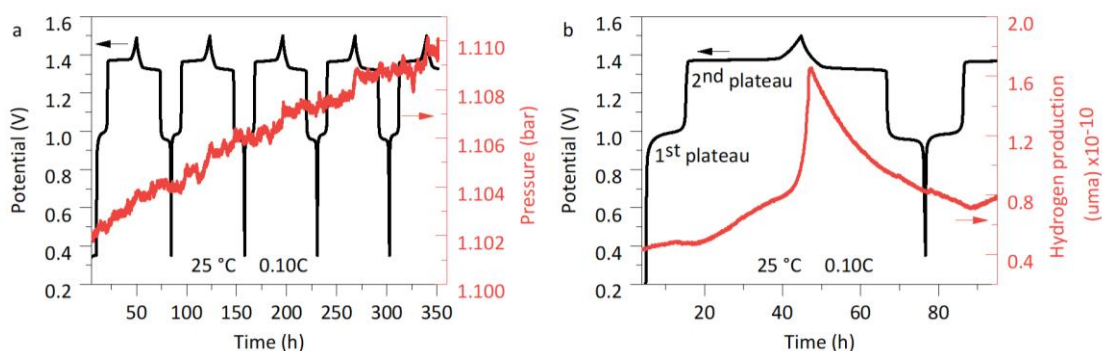


Figure 2. 11 Gas monitoring for a $\text{Mo}_6\text{S}_8/\text{LFP}$ cell measured in 20 m LiTFSI : 8 m LiBETI WiBS. (a) Potential (black line) and pressure (red line) as function of time at 0.10C monitored using a pressure cell. (b) Potential (black line) and hydrogen (red line)

evolution as function of time at 0.10C monitored using an *online* electrochemical mass spectrometry OEMS cell.

When comparing the relative pressure increase for two pressure cells during cycling in 20 m LiTFSI and 20 m LiTFSI : 8 m LiBETI (see Figure 2. 12), one can observe that alike for cycling performances, WiBS-based battery gives better results, *i.e.*, less gas production. However, the use of WiBS does not prevent water reduction to occur.

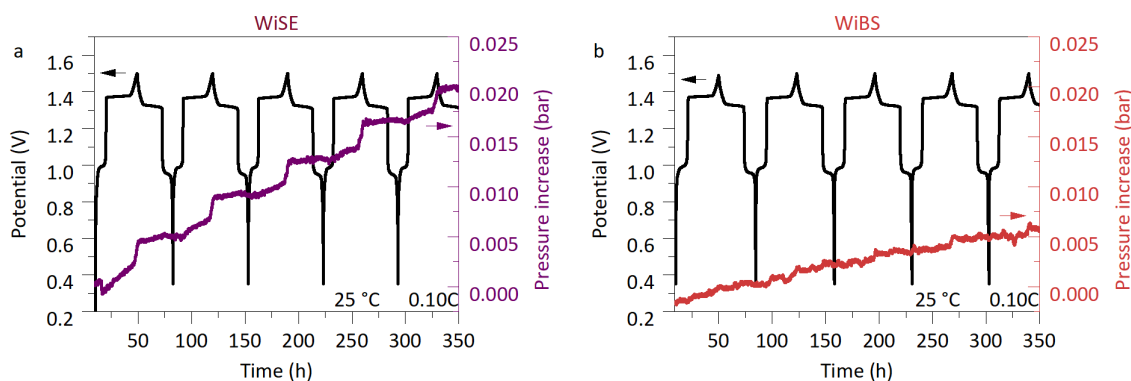


Figure 2. 12 Comparison of gas evolution and cycling performances at high temperature in $\text{Mo}_6\text{S}_8/\text{LFP}$ cells using either WiSE or WiBS. (a) Potential (black line) and relative pressure increase (purple line) as function of time at 0.10C monitored using a pressure cell in 20 m LiTFSI electrolyte. (b) Potential (black line) and relative pressure increase (red line) as function of time at 0.10C monitored using a pressure cell in 20 m LiTFSI : 8 m LiBETI electrolyte.

2.3 Link between irreversible capacity and gas production

To evaluate further the importance of hydrogen gas release in the total parasitic reactions, we plotted its amount as a function of irreversible capacity per cycle for several C-rates (see Figure 2. 13) and note a nearly linear trend with, at 0.1C, an irreversible capacity of 12 mA.h/g that corresponds mainly to a gas release of 1.4 μmol in addition to the contribution of other side reactions.

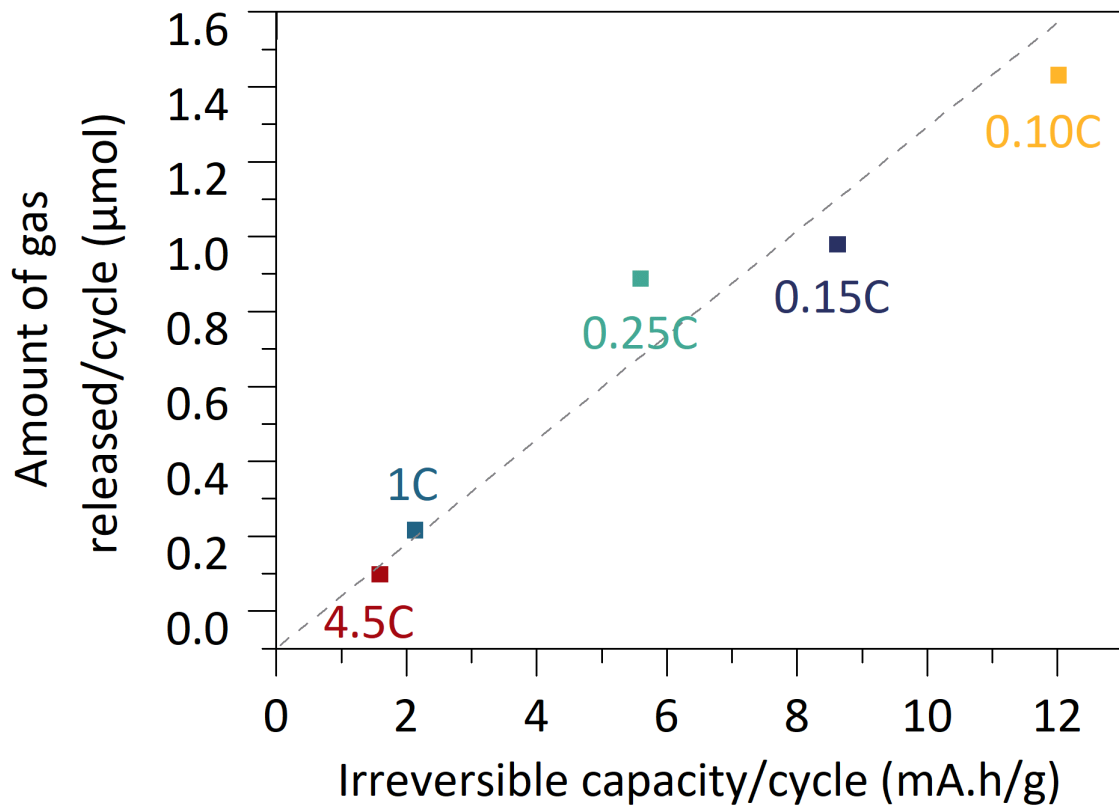
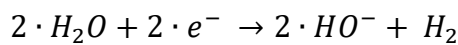


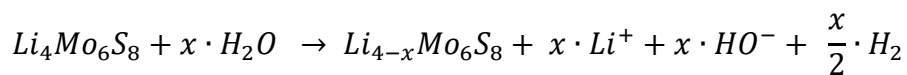
Figure 2. 13 Amount of gas released per cycle as function of irreversible capacity (dash line is a guide to the eyes). Experiments performed at room temperature using $\text{Mo}_6\text{S}_8/\text{LFP}$ full cells in 20 m LiTFSI WiSE.

Such an hydrogen evolution originates from the decomposition of H_2O that could proceed either via a direct or indirect process according to Equation 2. 1 and Equation 2. 2, respectively.

Equation 2. 1: Direct HER



Equation 2. 2: Indirect HER



On the basis of the direct mechanism (Equation 2. 1), we can from simple calculations (based on the ideal gas law) nearly account for the amount of H_2 released either during pressure cells or OEMS experiments (see Table 2. 2 and Table 2. 3 for listed results and Figure M.M. 11, Figure M.M. 12 and Figure M.M. 13, in Chapter Materials and Methods for calculation details). The results implies that Equation 2. 1 is by far majority in the total irreversible capacity (70 % of the irreversible capacity per cycle) regardless the use

of WiSE or WiBS and the C-rate, suggesting that the nature of parasitic reactions taking place in WiBS electrolyte is identical to the one in WiSE. Therefore, such a system will certainly face similar issues to WiSE electrolyte, with nevertheless a decreased amount of hydrogen evolution (as shown in Figure 2. 12).

Table 2. 2 Coulombic efficiency and gas quantification by operando pressure cells (average value on the first five cycles) as function of C-rate for a $\text{Mo}_6\text{S}_8/\text{LFP}$ full cell cycled in WiSE or WiBS electrolyte.

Electrolyte	C-rate	1 st Coulombic efficiency [%]	$\frac{Q_{HER}}{Q_{irr}}$ [%]
WiSE	0.10C	89.2	67
WiSE	0.15C	92.7	78
WiSE	0.25C	95.8	79
WiSE	1C	98	67
WiBS	0.10C	90.2	71

Table 2. 3 Coulombic efficiency and gas quantification by OEMS (1st cycle) for a $\text{Mo}_6\text{S}_8/\text{LFP}$ cell cycled in WiSE or WiBS electrolyte.

Electrolyte	C-rate	Coulombic efficiency [%]	$\frac{Q_{HER}}{Q_{irr}}$ [%]
WiSE	0.15C	73.2	79.4
WiBS	0.10C	79.9	86.9

As a conclusion, the study of the impact of concentration, cycling rate and temperature on the cell performances combined with *operando* gas monitoring highlight that water reduction is not prevented during cycling in aqueous superconcentrated electrolytes. To further explore the practical viability of WiSE and WiBS, the following section will focus on self-discharge protocol assessing the cell performances during resting period.

3 Self-discharge protocol to assess aqueous superconcentrated electrolytes viability during resting period

3.1 Monitoring the SEI formation time: self-discharge protocol reaching 25 % state-of-charge (SOC) at room temperature

The impact of self-discharge on cell performances was estimated using coin cells. Two cycling protocols were used to assess the cell open circuit voltage (OCV) decay during self-discharge and thus the SEI stability. The first one, depicted in Figure 2. 14a, corresponds to a single full charge followed by an OCV period until the cell voltage gets to 1.31 V (2.34 V vs Li^+/Li) where the 2nd plateau is entirely over, *i.e.* the cell state-of-charge reaches 25 %. Indeed, as mentioned in the introduction of the chapter, the 2nd insertion plateau -corresponding to a cell voltage of 1.32 V in discharge- accounts for three Li^+ cations over the four that Mo_6S_8 can insert/de-insert. Moreover, to be able to extend the SEI formation time during the first few charges, a second protocol employing a pre-cycling step consisting of five consecutive charge/discharge cycles followed by one last charge was used, as displayed in Figure 2. 14b. Alike for the single-charge protocol, the cell was then discharge at 25 % SOC and several C-rates, from 0.15C to 4.5C, were tested to vary the SEI formation time.

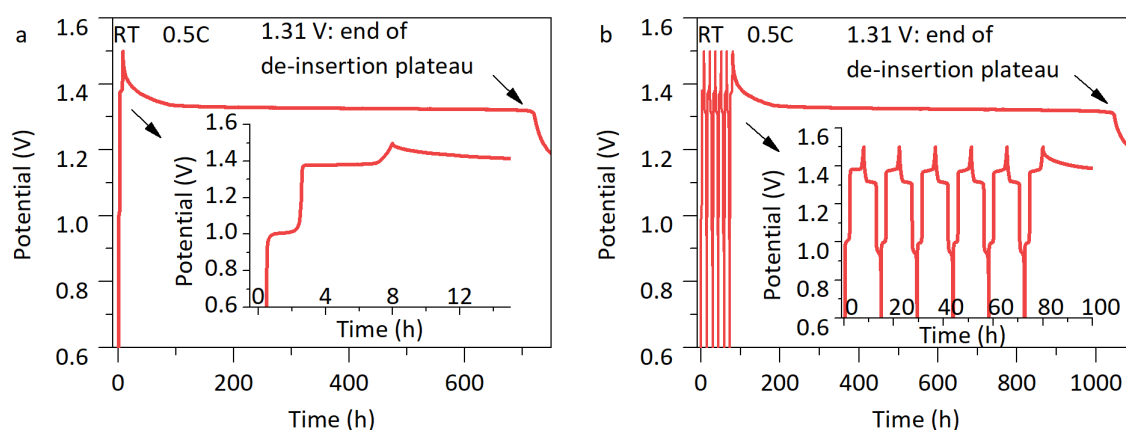


Figure 2. 14 Illustration of the self-discharge protocols performed in this study. (a) Open circuit voltage (OCV) decay measured upon rest for a cell fully charged at 0.5C. (b) OCV decay measured for a fully charged cell after five pre-cycles at 0.5C at room temperature.

In Figure 2. 15 is compared the time needed to reach 25 % state-of-charge (SOC) during self-discharge with the time spent to form the SEI during charge. As discussed in Chapter 1, the SEI formation either through the direct reduction of TFSI⁻ anions or their chemical reaction with hydroxide anions produced by HER occurs at cell voltage above 1.3 V (i.e. 2.34 V vs Li⁺/Li at the negative electrode). Thus, the stability of the SEI must be dependent on the cycling rate and/or the number of consecutive charges, both defining its thickness and density. Indeed, one can notice in Figure 2. 15 that the longer the time spent to form the SEI, the slowest the self-discharge. Moreover, when more than 20 h are used to form the SEI, the time needed to discharge the cell to 25 % SOC remains roughly stable (≈ 900 h needed) and no further improvement in the SEI stability is observed. However, we must acknowledge that reproducibility tests were not performed. Furthermore, the number of parameters tested is far from being exhaustive. Therefore, an in-depth study would be needed to draw a solid trend regarding the SEI stability and identify and optimize the key parameters (absolute time spent on charge or repeated cycles, temperature etc.) controlling the SEI formation step in aqueous superconcentrated electrolytes.

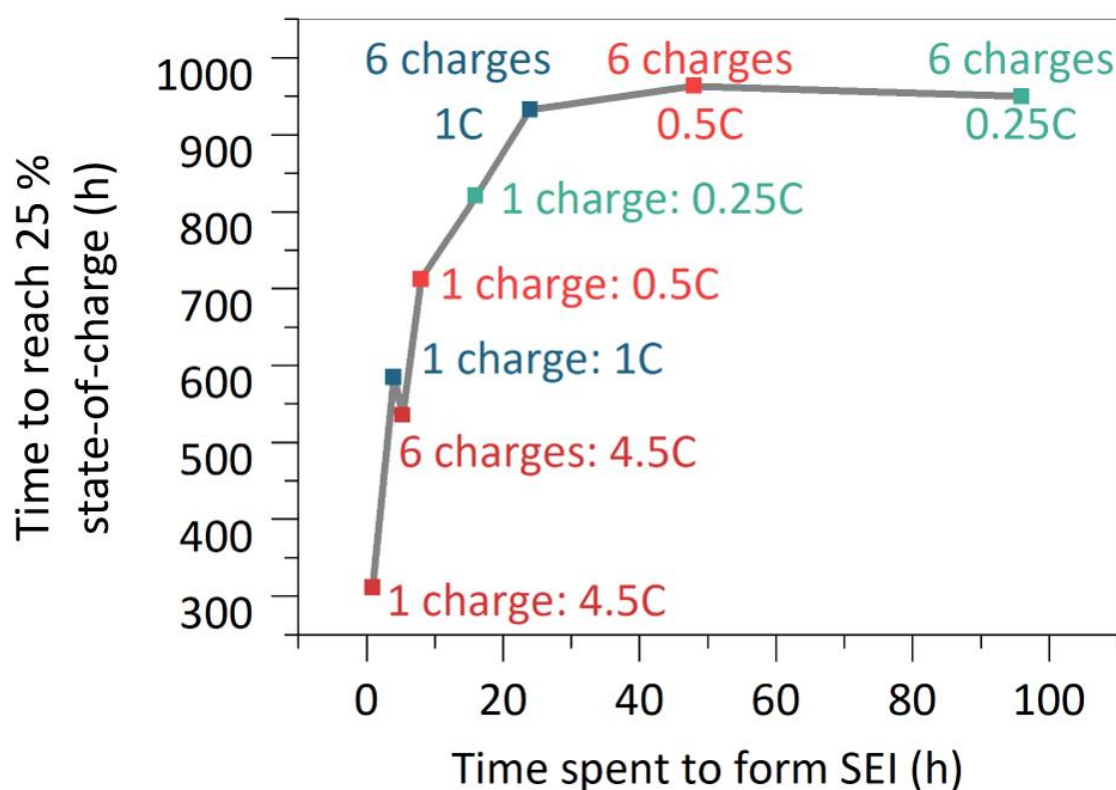


Figure 2. 15 Assessment of the SEI stability. Time needed to reach 25 % state-of-charge by resting period as function of the time spent to form SEI during charge at room temperature. Mo₆S₈/LFP full cells using 20 m LiTFSI were used.

3.2 Impact of self-discharge protocol using 20 m LiTFSI on the LIB performances

3.2.1 Long cycling impact on cell performances at room temperature

To assess the battery performances when the cell faces self-discharge period, long cycling with self-discharge protocol was performed. 0.5C C-rate was chosen as a compromise between fast experiments to quickly assess the cell performances and sufficiently slow C-rate to highlight parasitic reactions.

In Figure 2. 16a is shown the protocol, called 20 h OCV protocol, using a 20 h OCV step at the end of each charge after one cycle of charge/discharge/charge. The second protocol, called 10 cycles -10 h OCV protocol, (see Figure 2. 16b) consists of a pre-cycling step of 10 cycles to form the SEI. After that, the cell is let to rest for 10 h every 10 cycles. Cycling with or without self-discharge step are compared in terms of discharge capacity, normalized discharge capacity and Coulombic efficiency.

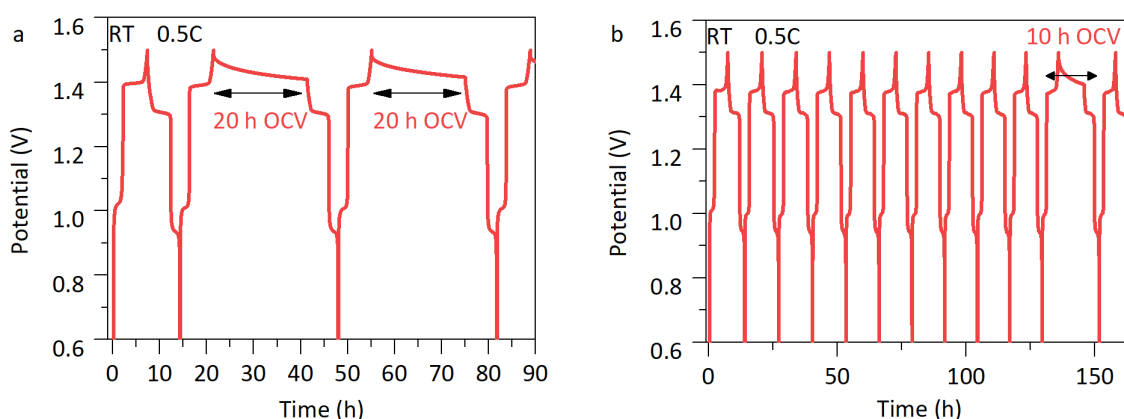


Figure 2. 16 Illustration of the self-discharge protocols performed in this study. (a) 20 h OCV protocol using a 20 h OCV period after each charge. (b) 10 cycles-10 h OCV protocol using a 10 h OCV period after 10 cycles of charge/discharge. All Mo₆S₈/LFP cells were cycled at 0.5C at room temperature in 20 m LiTFSI.

Clear conclusions can be drawn comparing results obtained with a continuous cycling protocol, the 20 h OCV protocol and the 10 cycles-10 h OCV protocol. Figure 2. 17 shows the mean values and the standard deviation (over 3 cells) of discharge capacity, normalized discharge capacity by the first discharge capacity and the Coulombic efficiency for each protocol.

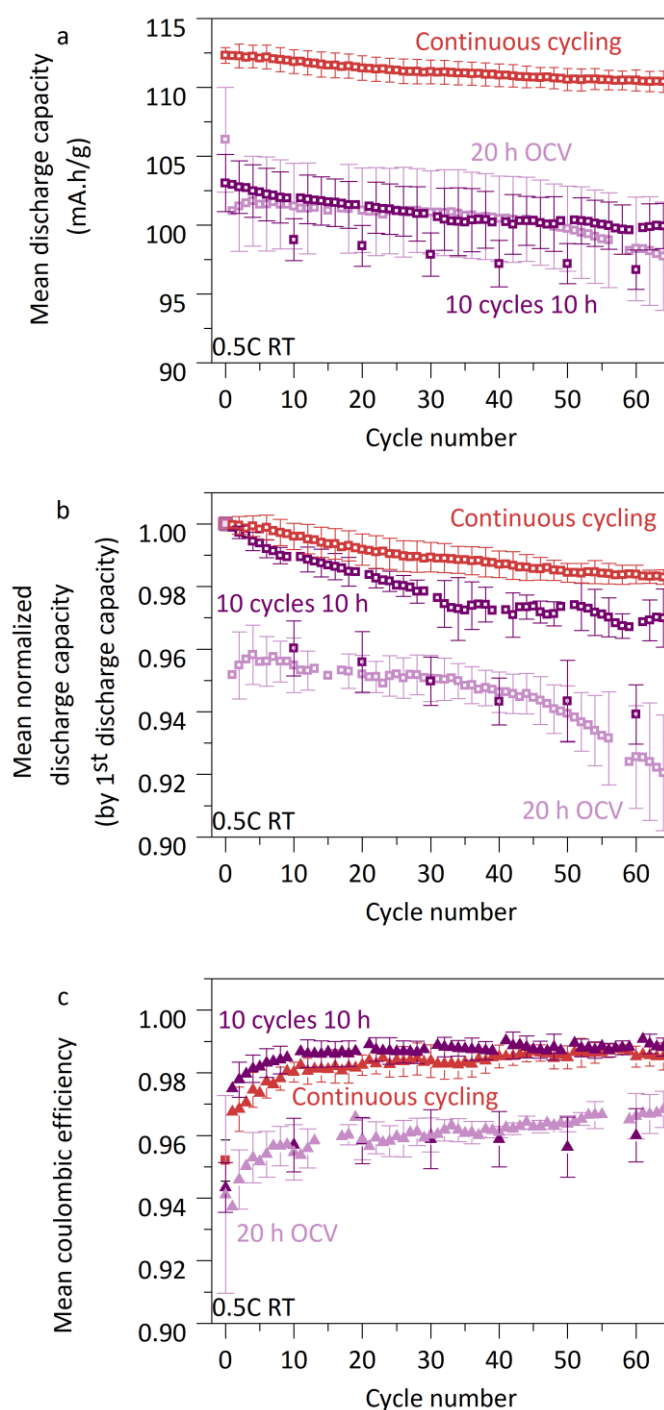


Figure 2. 17 Impact of the self-discharge protocol on the cell performances. Continuous cycling (red), 20 h OCV protocol (light purple), 10 cycles-10 h OCV (dark purple). (a) Mean discharge capacity obtained at 0.5C at room temperature as function of cycle number. (b) Mean normalized discharge capacity by the first discharge capacity obtained as function of cycle number. (c) Mean Coulombic efficiency as function of cycle number. All $\text{Mo}_6\text{S}_8/\text{LFP}$ cells were cycled at 0.5C at room temperature in 20 m LiTFSI. Three cells were used for each protocol.

First looking at the discharge capacities (see Figure 2. 17a), a drop of capacity of about 4 mA.h/g is observed for both self-discharge protocols after resting period. Thus, the use of a resting period leads to a drop of discharge capacity of 4 % (see Figure 2. 17b) compared to a continuous cycling, regardless the resting protocol. Moreover, for the 20h OCV protocol, after resting both the Coulombic efficiency and the discharge capacity drop from the first cycle and stabilize at around 96 % and 100 mA.h/g, respectively (see Figure 2. 17a and c). Hence, while the parasitic reactions occurring during the first charge are similar (the Coulombic efficiencies being around 95 % during the first cycle for both), when performing the 20 h OCV protocol, the cell degradation is enhanced as a result of the extended period spent at OCV. These observations are further confirmed with the 10 cycles-10 h OCV protocol where each resting period is followed by a decrease of capacity in discharge, normalized capacity of discharge and Coulombic efficiency close from the values obtained with the 20 h OCV protocol. Altogether, these data suggest a partial degradation of the SEI or a partially porous SEI. Thus, the SEI cannot fully prevent the HER, therefore explaining that 98 % Coulombic efficiency cannot be passed with this system.

Besides, the coupling of self-discharge protocol (as described in Figure 2. 16a) with pressure cell experiments enable to show that water reduction also happen during resting period.

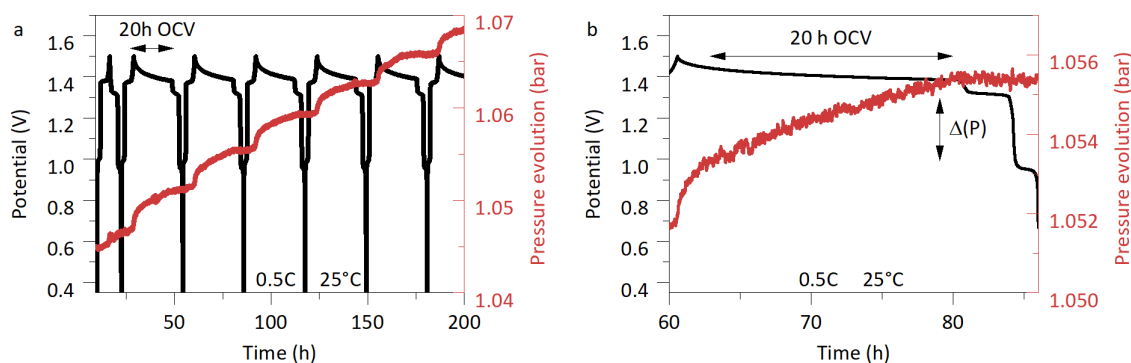


Figure 2. 18 Pressure cell assessing gas evolution during 20 h OCV protocol illustrating self-discharge. (a) Potential (black line) and pressure (red line) as function of time for a $\text{Mo}_6\text{S}_8/\text{LFP}$ cell cycled at 0.5C and 25 °C. (b) Zoom of the pressure evolution (red line) as function of time during resting period.

As shown in Figure 2. 18, when a cell is stored at 100 % SOC, pressure increase takes place during resting. As described in Chapter Materials and Methods, the application of the ideal gas law enables to determine a water consumption of $0.13 \mu\text{mol}_{\text{water}}/\text{h}_{\text{self-discharge}}$ (mean value for two pressure cells, cycled at 0.5C, 25 °C with a similar mass of

active material). Assuming a two electrons reaction for water reduction, one can calculate the capacity related to such water consumption and compare it to the discharge capacity loss due to 20h OCV period (as described in Chapter Materials and Methods). Thus, the proportion of water reduction related to self-discharge is found to be between 75 % and 100 % of the discharge capacity loss for two pressure cells cycled in the same conditions.

Nonetheless, these observations contrast with a report published in 2016 by Suo *et al.*²¹³ in which self-discharge was assessed using the 10 cycles-10 h OCV protocol at 0.5C. There, a steady increase of the Coulombic efficiency following each of the 10 hours resting period was observed, as reproduced in Table 2. 4. First, when reproducing this protocol, Coulombic efficiency obtained in this work was found to stabilize after 3-4 cycles at values of 98 %, while 30 cycles were required to reach the same Coulombic efficiency as reported by Suo *et al.*²¹³. Bearing in mind that cycling protocols are identical, the SEI stability is expected to be similar. Such differences thus most likely arise from the morphology of the electrode materials and/or the cell assembly (ratio mass of active material vs volume of electrolyte, etc.). Second, we found a constant loss of capacity of about 4 mA.h/g upon rest at room temperature while this capacity loss, initially of 6 mA.h/g after the first resting period, decreases on the subsequent resting periods in Suo's report. In conclusion, our results evidence a continuous loss of capacity upon subsequent resting highlighted by the discharge capacity that smoothly decays upon cycling.

Table 2. 4 Comparison of the Coulombic efficiencies and discharge capacities obtained after each 10h resting period at OCV in Ref²¹³ with those experimentally obtained in this work.

Cycle number (following the 10h OCV period)	CE as reported by Suo ²¹³ [%]	CE (obtained in this work) [%]	Discharge Capacity (obtained in this work) [mA.h/g]
0	82	94.3	103 ± 2
11 th	80.6	95.7	98.9 ± 1.5
21 th	84.7	95.8	98.5 ± 1.5
31 th	87.6	95.9	97.9 ± 1.6
41 th	89.1	95.9	97.2 ± 1.7

Importantly, one can notice that the self-discharge is reversible in terms of lithium balance. Indeed, both the Coulombic efficiency and the discharge capacity are recovered upon cycling after a resting time. Indeed, by comparing the discharge capacity obtained

before and after the 10h OCV period, one can find that discharge capacity recovers from 99.7 % to 100 % even after 13 repetition of the 10 cycles-10 h OCV protocol.

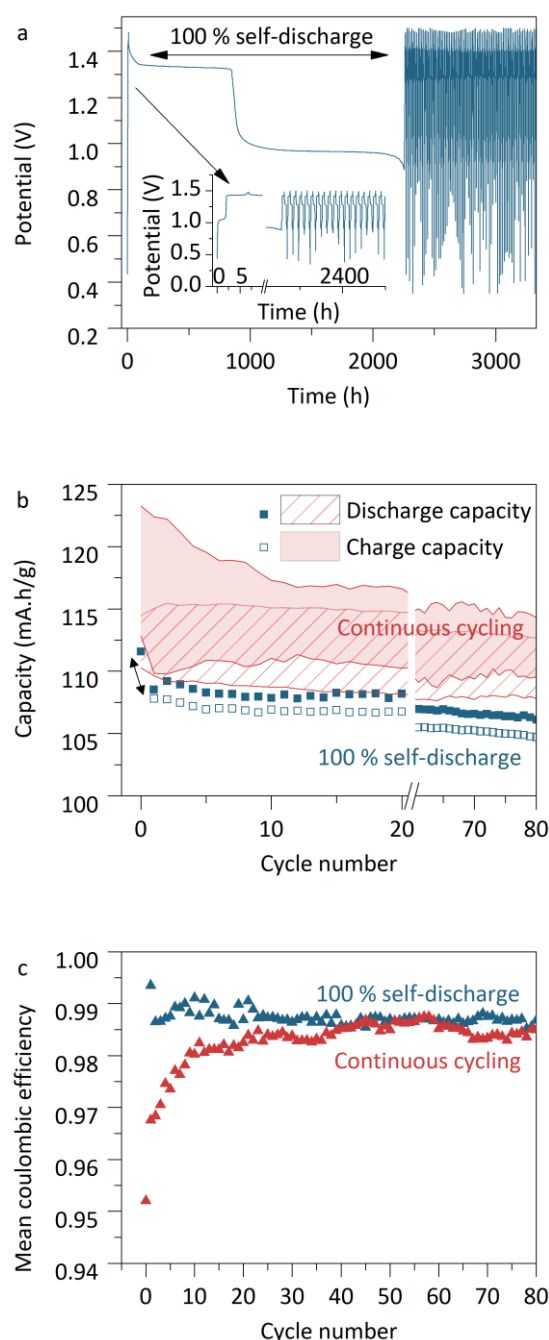


Figure 2. 19 Reversibility of Lithium loss during self-discharge. (a) Illustration of protocol reaching 100 % self-discharge for a $\text{Mo}_6\text{S}_8/\text{LFP}$ cell fully charged at 0.5C followed by continuous cycling at 0.5C. (b) Charge and discharge capacities as function of cycle number (mean value over three cells for continuous cycling protocol), (c) Coulombic efficiency as function of cycle number capacity obtained for three cells continuously cycled and one cell which endured 100 % self-discharge after the first charge. All $\text{Mo}_6\text{S}_8/\text{LFP}$ cells were cycled at 0.5C at room temperature in 20 m LiTFSI.

To confirm that the self-discharge is mostly reversible in terms of Li balance, a unique charge was performed at 0.5C followed by a complete self-discharge. Once the cell reaches 0 % SOC, continuous cycling was done at 0.5C. First of all, one can observe in Figure 2. 19a that the self-discharge process follows the electrochemical signature of Mo_6S_8 . However, the first plateau (at 0.97 V *i.e.* 2.7 V vs Li^+/Li) is longer than the second one (at 1.33 V *i.e.* 2.3 V vs Li^+/Li), ≈ 1400 h and 900 h, respectively. This is in contrast with the fact that the first plateau accounts for $\frac{1}{4}$ and the second plateau for $\frac{3}{4}$ of the Li insertion/de-insertion. Indeed, during self-discharge, the removal of Li from the electrode material depends on the kinetics of the reaction (Equation 2. 2), thus the length of the plateaus may be modified if the water reduction kinetics is different for each plateau, which will be discussed in greater details in Chapter 3. However, one can already note that self-discharge is relatively slow since more than three months are needed to fully self-discharge the cell. Regarding the charge and discharge capacities, Figure 2. 19b and c compare the performances for 3 cells cycled continuously at 0.5C with that of a cell that first underwent a 100 % self-discharge after the first charge. Doing so, one can first observe that the cell which endured a 100 % self-discharge exhibit lower charge and discharge capacity, the difference being however limited. Moreover, the Coulombic efficiency is found to stabilize to similar values (between 0.98 and 0.99) after 10 cycles for both protocols (Figure 2. 19c). This confirms that the Li loss underwent during self-discharge is reversible.

3.2.2 Temperature effect on self-discharge

Acknowledging that temperature will enhance the SEI instability, 55 °C cycling tests were performed with the 10 cycles-10 h OCV protocol where SEI is expected to be stable. In Figure 2. 20 is plotted the discharge capacity and Coulombic efficiency as function of cycles for experiments carried out at room temperature and 55 °C. First, one can observe that applying 10 h resting period leads to a similar behavior regardless of the temperature. Indeed, both discharge capacity and Coulombic efficiency fall after the OCV period. However, as shown in at 0.5C.

Table 2. 5, the drop in capacity is enhanced at 55 °C. This result is consistent with a faster SEI degradation and an enhanced HER kinetics at 55 °C, both leading to an increased drop in cell performances.

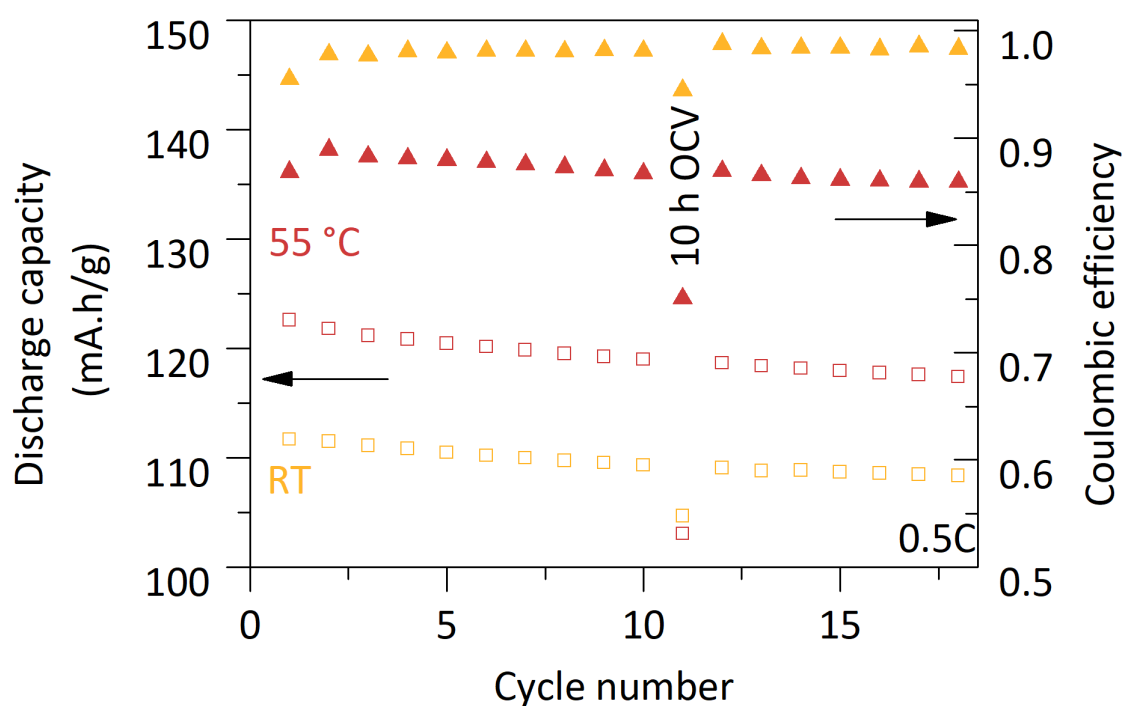


Figure 2. 20 Impact of temperature on self-discharge performances using a 10 cycles-10 h OCV protocol. Discharge capacity and Coulombic efficiency as function of cycle number for $\text{Mo}_6\text{S}_8/\text{LFP}$ full cells cycled at room temperature (yellow) and 55 °C (red) at 0.5C.

Table 2. 5 Capacity loss after 20h OCV resting period for $\text{Mo}_6\text{S}_8/\text{LFP}$ cells. Comparison at 25 °C and 55 °C.

Temperature	RT	55°C
Capacity loss [mA.h/g]	4	16

Having investigating in depth the 20 m LiTFSI WiSE system, our attention then turned to the stability of the SEI formed in WiBS 20 m LiTFSI : 8 m LiBETI. For that, the same methodology as previously used for WiSE was employed and similar behavior was observed for the 20 h OCV protocol. Hence, the loss in discharge capacity observed after a 20 hours OCV period applied after a first cycle performed at 1C is found identical to the discharge capacity loss measured in WiSE for the same C-rate, *i.e.* $\approx 9 \text{ mA.h/g}$.

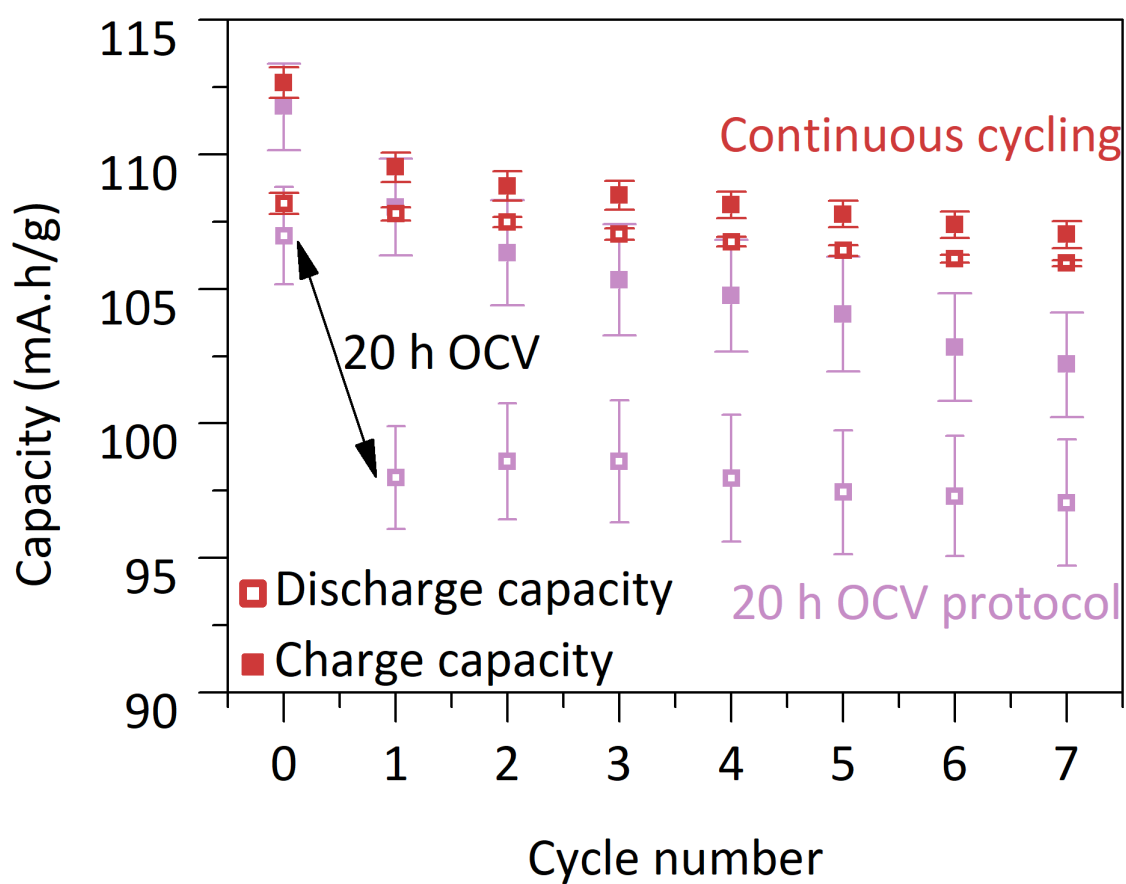


Figure 2. 21 Impact of the 20 h OCV protocol on cell performances using WiBS electrolyte. Charge and discharge capacity as function of cycle number for continuous cycling (red) and 20 h OCV protocol (light purple) for $\text{Mo}_6\text{S}_8/\text{LFP}$ full cells cycled at 1C at room temperature.

As a conclusion, the use of self-discharge protocols enabled us to highlight the instability and/or the lack of protective power of the SEI formed in aqueous superconcentrated electrolytes. Therefore, while optimizing the formatting conditions can help delaying the degradation of the SEI, as intensively experimented in non-aqueous Li-ion batteries, this certainly will not prevent the drying out of the cell over prolonged time, especially at temperature greater than room temperature as it will be discussed in Chapter 3.

4 Cycling viability on the positive side: a gas monitoring study

Besides the SEI forming at the negative electrode, another important aspect in selecting electrolytes regards their stability at the positive electrode under highly oxidizing potentials. Having established that the cycling performances for WiSE-based

aqueous batteries will certainly be limited by the absence of passivating SEI at the negative electrode, we focused our attention on gassing experiments rather than on cycling performances for the positive electrode.

Figure 2. 22a shows the evolution of pressure and potential as a function of time for a LTP/NMC₆₂₂ cell using WiSE electrolyte at 25 °C. There, even when pushing the potential cut-off up to 2 V (4.78 V vs Li⁺/Li for NMC₆₂₂), any pressure increase can hardly be detected, with only a pressure increase of 0.6 mbar (0.22 μmol of gas) being observed, this amount being within the detection limit of this technique. This absence of gassing is consistent with the previously reported formation of a TFSI-rich double layer, preventing water to access the interface, as described in Chapter 1. Furthermore, this observation is also consistent with the OER kinetics being very sluggish when compared to the HER, as widely discussed in the electrocatalysis field²¹¹. Hence, at 25 °C, WiSE electrolyte seems to be stable and not to face any drastic degradation, in agreement with the electrochemical stability of superconcentrated aqueous electrolytes under anodic polarization reported in previous studies^{58,214}.

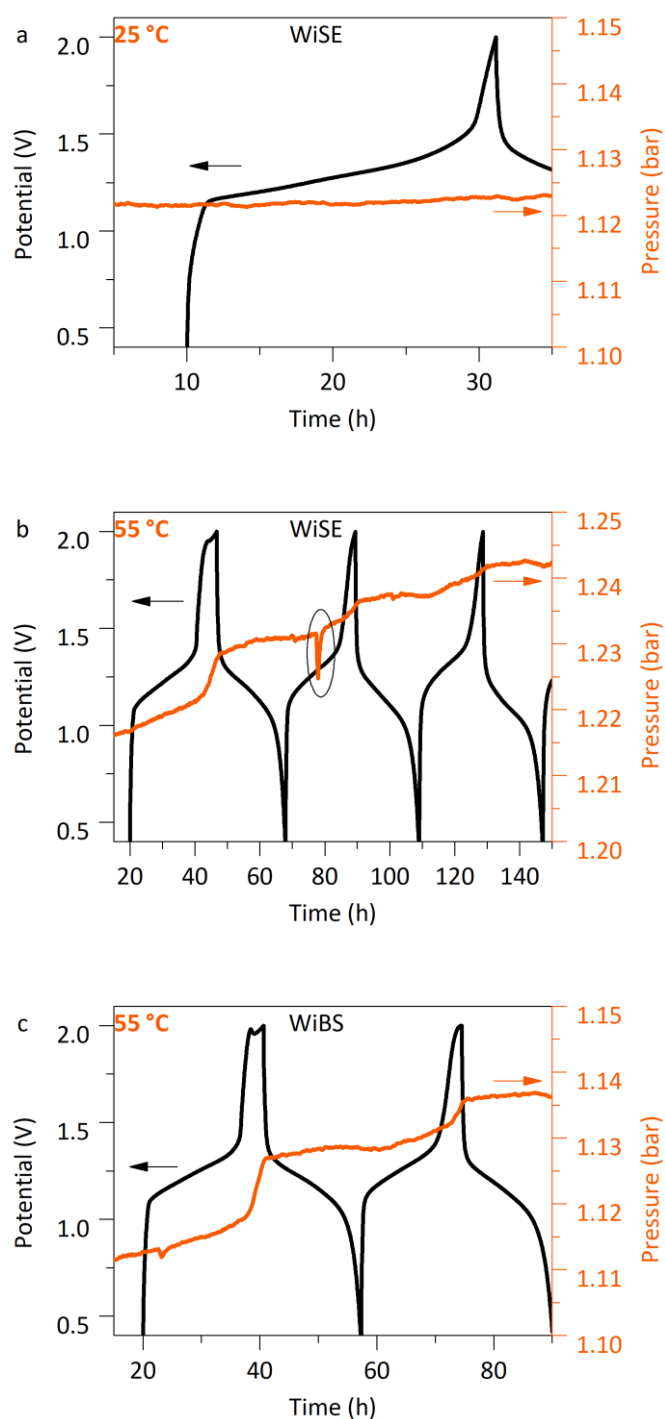


Figure 2. 22 Potential (black line) and pressure (orange line) measured as a function of time for NMC₆₂₂/LTP full cells cycled in (a) *Water-in-salt* 20 m LiTFSI electrolyte at 25 °C, (b) at 55 °C (*note that the peak observed below 80 hours for the pressure is due to an opening of the oven) and (c) *Water-in-bisalt* 20 m LiTFSI : 8 m LiBETI at 55 °C.

Following these measurements at 25 °C, the anodic stability of WiSE was assessed at higher temperature by cycling pressure cells at 55 °C. The evolution of pressure and potential as a function of time are reported in Figure 2. 22b. Compared to the results

obtained at room temperature, a significant gas evolution could be spotted during delithiation/oxidation of NMC_{622} with two slopes being observed. The first one that leads to a pressure increase of 4.3 mbar ($1.59 \mu\text{mol}$) occurs between 1.1 V and 1.4 V, and can be explained by the competition between the electrochemical Li^+ de-intercalation and the slow parasitic reactions, either direct (OER) or indirect (self-discharge)²¹⁵. The second one starting above 1.4 V (4.2 V vs Li^+/Li) leads to a greater production of gases of ≈ 7 mbar ($2.59 \mu\text{mol}$) and can be mainly attributed to parasitic reactions, which can also be responsible for the appearance of a plateau at high potential (≈ 2 V) which is solely present during the first charge. Indeed, NMC is known to face greater degradation at high temperatures and high potential cut-off^{216–218}. However, the origin of the gas production certainly arises from the corrosion of the carbon additive at high potential in aqueous media, as spotted by OEMS measurements during which CO_2 is detected (see Figure 2. 23)^{219,220}. Nonetheless, the detection of more than one gas, during these measurements, prevents us from performing quantification to determine the amount of mole produced by each gases. For sake of completion, the stability of WiBS-based electrolyte was also tested using pressure cells at 55 °C (see Figure 2. 22c), and similar behavior is observed as for WiSE. Hence, the pressure increase recorded during the de-insertion plateau between 1.1 V and 1.4 V is ≈ 3 mbar ($1.11 \mu\text{mol}$) in WiBS, compared to 4 mbar in WiSE. This first gas release is followed by an additional pressure increase of 8 mbar ($2.96 \mu\text{mol}$) at greater potential, compared to 7 mbar previously measured for WiSE. Differences in pressure variations were considered to be within the same ranges. To conclude, at elevated temperature, the stability of the NMC_{622} self-standing electrode/superconcentrated aqueous electrolyte assembly is compromised under anodic polarization when compared to room temperature.

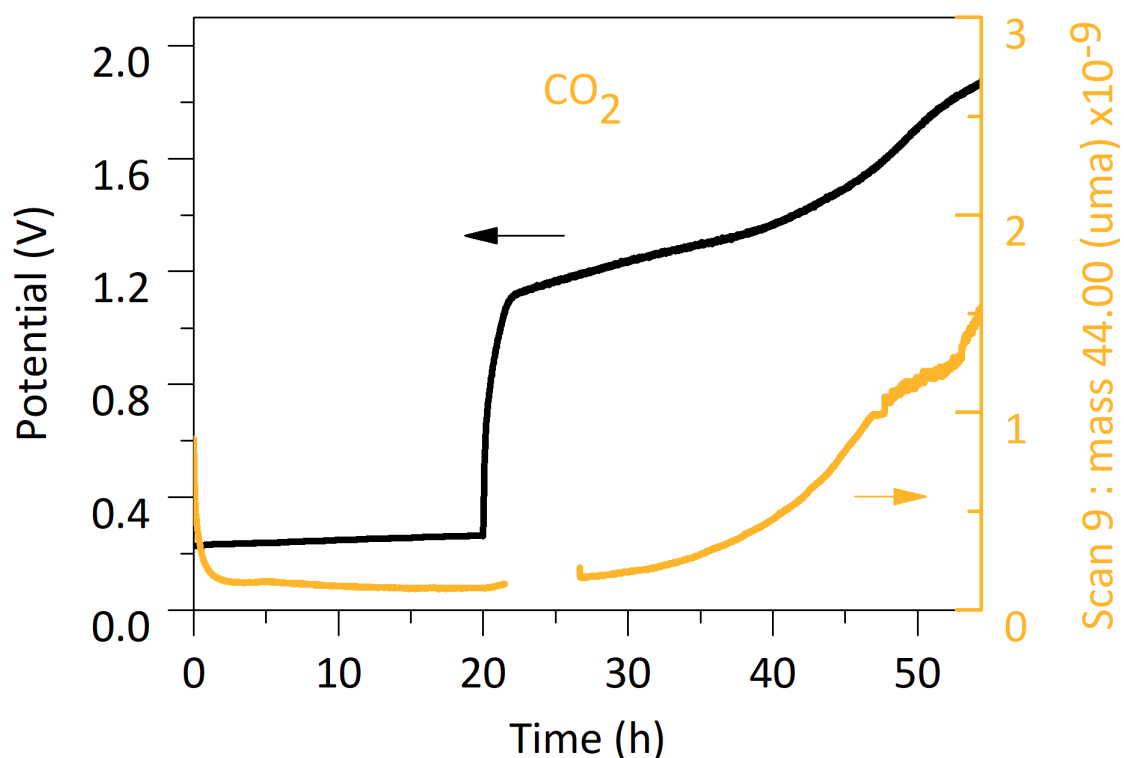


Figure 2. 23 Online electrochemical mass spectrometry performed on NMC₆₂₂/LTP full cell using WiSE electrolyte. Potential (black line) and gas evolution (yellow line) as function of time are plotted for carbon dioxide (CO₂: m/z=44). Experiment performed at 55 °C, at C/40. Note the gap is attributed to a partial stop of the experiment.

Conclusion of the chapter

In this chapter, an in-depth study of the cathodic and anodic stability of superconcentrated aqueous electrolytes as function of the operating conditions was carried out. First, the assessment of the capacity retention and Coulombic efficiency with increased LiTFSI concentration shows the benefic influence of superconcentration on cycling performances. However, such improvement was quickly nuanced when performing tests at different C-rate. Indeed, when cycled at low C-rate (below 1C), the damaging effect of parasitic reactions such as hydrogen evolution reaction are brought to light. Their detrimental impact is exacerbated at higher temperature. To determine the origin of the performances decay, we then performed *operando* gas monitoring. Combining pressure cell tests with online electrochemical mass spectrometry, hydrogen production was detected to start concomitantly with Li insertion at a cell voltage of ≈ 1.38 V (2.3 V vs Li⁺/Li at the negative electrode). This gas evolution never stops during cycling, testifying of the poor SEI protective power against HER. Eventually, the practical viability of WiSE electrolyte in LIB was assessed by self-discharge protocols. Several self-

discharge protocols were thus applied to both assess the SEI stability as a function of its formation time and the impact of self-discharge during long cycling. Altogether, these results show that even though self-discharge is partially reversible in terms of lithium balance, cell life is limited when self-discharge protocols are applied. Furthermore, to assess the behavior of aqueous superconcentrated electrolyte in LIB, a non-exhaustive but representative study was performed using 20 m LiTFSI : 8 m LiBETI WiBS electrolyte. Even though the ESW is larger in WiBS electrolyte, HER was found to occur during cycling, although less intense. Moreover, discharge capacity loss was observed after resting period, showing the weak passivation of the SEI. Therefore, WiBS-based LIB faces critical limitations identical to the ones encountered in WiSE. Finally, studying parasitic reactions at the positive electrode side show limited evolution of oxygen and only at elevated temperature damageable parasitic reactions were observed.

Altogether, the results presented in this chapter on the practical viability of aqueous superconcentrated electrolyte on the negative electrode call for the design of a stable SEI that will effectively passivate the negative electrode and prevent water reduction. Indeed, the major drawback of aqueous superconcentrated electrolytes lays in the continuous water consumption during both cycling and self-discharge, eventually leading to the drying out of the cell. Therefore, Chapter 3 will first discuss the instability of the SEI in WiSE. Then the irreversible consumption of water that may cause the crystallization of the electrolyte, thus the drying out, will be presented. Finally, the kinetics of water reduction during both self-discharge and cycling will be determined.

CHAPTER 3 – INSTABILITY
OF NATIVE SEI LEADS TO
THE DRYING OUT OF
AQUEOUS
SUPERCONCENTRATED LI-
ION BATTERY

Introduction

As evidenced in Chapter 2, practical viability of *Water-in-salt* electrolyte (WiSE) is limited by continuous parasitic reactions occurring at the negative electrode during cycling and resting period. Online electrochemical mass spectrometry measurements and pressure cells tests identified water reduction as the major parasitic reaction limiting the cell viability. SEI instability and/or specific morphology may explain that water reaches the electrode interface. Therefore, Chapter 3 will focus on the assessment of the native SEI stability by electrochemical characterizations, cyclic voltammetry (CV) and electrochemical impedance spectroscopy (EIS), before to focus on the effect of water consumption on the cell life by using differential scanning calorimetry (DSC). Besides, kinetics of water consumption through direct HER ($2 \cdot H_2O + 2 \cdot e^- \rightarrow 2 \cdot HO^- + H_2$) or indirect self-discharge ($Li_4Mo_6S_8 + x \cdot H_2O \rightarrow Li_{4-x}Mo_6S_8 + x \cdot Li^+ + x \cdot HO^- + \frac{x}{2} \cdot H_2$) mechanisms are assessed by electrochemical measurements using CV, continuous cycling protocols and self-discharge tests as function of temperature. Hence, based on the Arrhenius law, the activation energies of both mechanisms can be extracted. Figure 3. 1 illustrates the outline of the chapter based on the results discussed in Chapter 2.

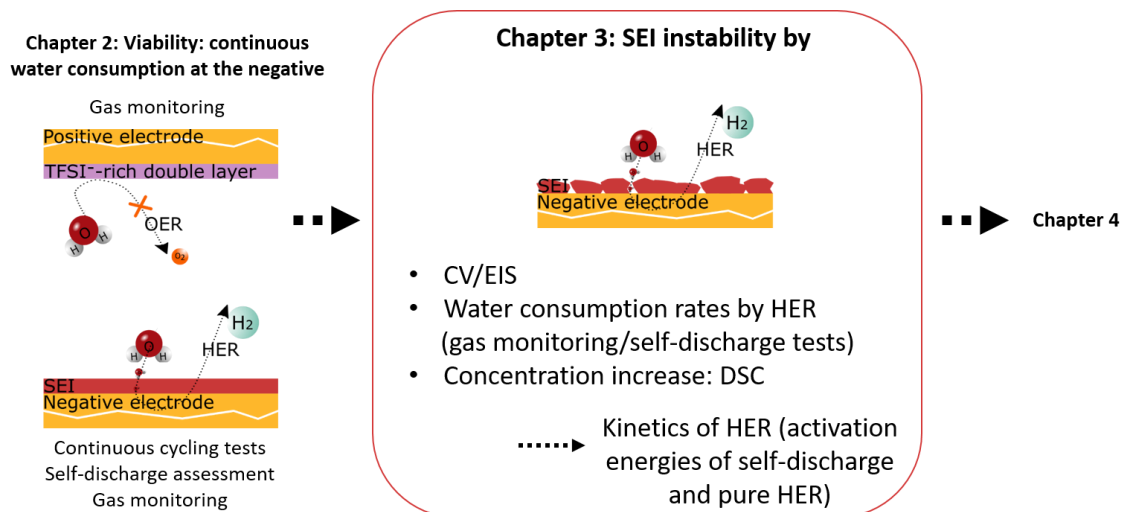


Figure 3. 1 Scheme of the outline of Chapter 3 based on the results discussed in Chapter 2.

Eventually, the figure of merits for WiSE-based aqueous Li-ion batteries is provided and compared with existing aqueous technologies (Lead-acid, Ni-Cd, Ni-MH) and aprotic Li-ion batteries to assess the viability of this technology.

1 Probing the SEI instability in aqueous superconcentrated electrolytes

1.1 Use of an inert glassy carbon to assess passivation of the electrode surface

As shown in Chapter 2, the amount of irreversible capacity upon cycling associated to HER (70 %) demonstrates that the SEI forming in WiSE is not passivating enough, nor stable. To check the protective power of native SEI, SEI formation was mimicked by cycling a glassy carbon working electrode in a 3-electrodes cell before applying a resting period of one-hour and perform another CV measurement to measure the cathodic current corresponding to the HER (see Figure 3. 2). Both 20 m LiTFSI and 20 m LiTFSI : 8 m LiBETI electrolytes were tested at 25 °C and 35 °C, respectively (see Figure 3. 2). Moreover, the influence of temperature on the passivating abilities of aqueous superconcentrated electrolyte was assessed using 20 m LiTFSI (see Figure 3. 3).

During the first CV scan, a peak at 0.8 V vs Li^+/Li is observed in WiSE (see Figure 3. 2a), and is attributed to HER on the surface of the glassy carbon working electrode^{134,149}. Upon cycling, the intensity of this peak decreases before to eventually almost vanish after 15 cycles (see green line). This phenomenon is explained by the gradual passivation of the glassy carbon electrode as a result of the SEI formation, as proposed by Dubouis *et al.*¹³⁴ and schematized in Figure 3. 2c. However, after applying a one-hour resting period, the subsequent CV recorded (see purple line) attests that the passivation is lifted as the peak intensity corresponding to the HER is back to that recorded during the very first cycle. A similar behavior is found when performing the experiment in 20 m LiTFSI : 8 m LiBETI, although the reductive peak observed during first scan is shifted to lower potential (0.5 V vs Li^+/Li) (see Figure 3. 2b).

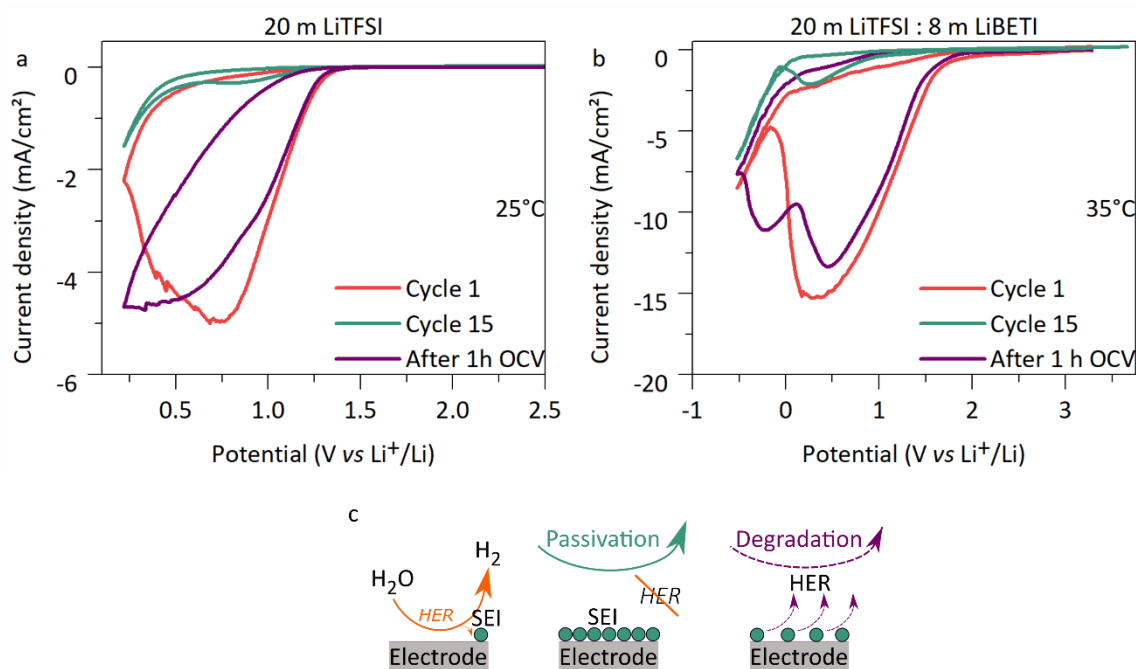


Figure 3. 2 Assessment of the SEI stability over time by mimicking its formation on inert material. (a) Cyclic voltammetry performed at 50 mV/s in 20 m LiTFSI in a 3-electrodes cell using glassy carbon as working electrode, Pt wire as counter electrode and silver wire as pseudo-reference. (b) Cyclic voltammetry performed at 35 °C (to avoid crystallization) at 50 mV/s in 20 m LiTFSI : 8 m LiBETI in a 3-electrodes cell using glassy carbon as working electrode, Pt wire as counter electrode and saturated calomel electrode as reference. (a-b) The first (red) and the fifteenth (green) voltammograms are shown, as well as the one recorded after one-hour open circuit voltage (OCV) (purple). (c) Illustration of the SEI formation and its partial degradation after a resting period of 1 h.

Besides, similar experiments were also performed as function of temperature (at 35 °C, 45 °C and 55 °C) in WiSE, as shown in Figure 3. 3, and similar trends were observed with the passivation of glassy carbon. Thus, the passivating layer is deteriorated during resting period, further confirming our self-discharge measurements discussed in Chapter 2. The presence of two peaks in the cyclic voltammetry performed after the resting period at 35 °C in WiBS (see Figure 3. 2b) and at 55 °C in WiSE (see Figure 3. 3d) may be attributed to shifts in potential due to the presence of bubbles at the electrode interface. Moreover, a competition between the precipitation of LiTFSI, as recently proposed¹⁴⁹, and the dissolution of LiF can contribute to this dynamic SEI behavior. Indeed, bearing in mind that the ratio volume of the electrolyte/active material (several mL vs 4 mm diameter of glassy carbon) is greater in this experience than in a practical battery, more than one-hour OCV would certainly be needed to partially dissolve the SEI and suppress its passivation in a full cell.

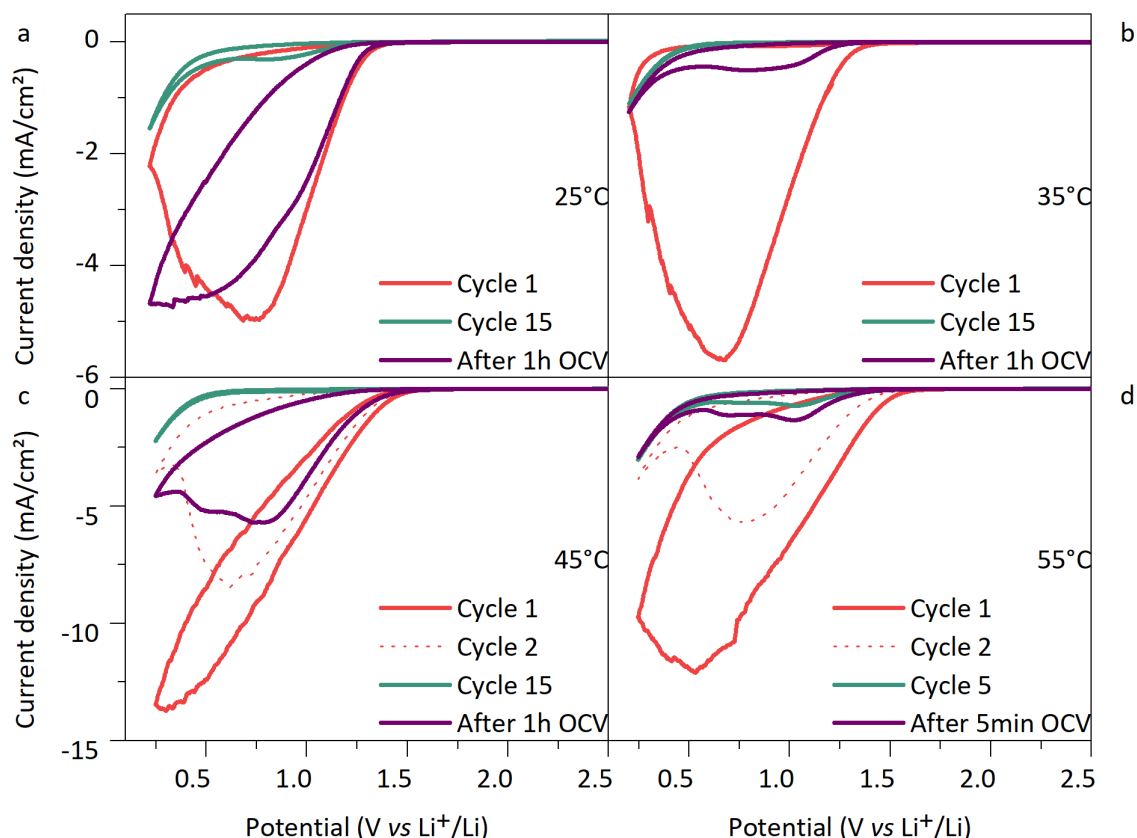


Figure 3. 3 Assessment of the SEI stability as function of temperature over time by mimicking its formation on inert material by cyclic voltammetry performed at 50 mV/s in 20 m LiTFSI in a 3-electrodes cell using glassy carbon as working electrode, Pt wire as counter electrode and silver wire as pseudo-reference. (a) 25 °C, (b) 35 °C, (c) 45 °C, (d) 55 °C.

1.2 SEI instability in battery cell

Hence, prior to study the effect of resting period on the SEI degradation in battery set-up, the impact of the electrolyte volume on the SEI dissolution was determined by assessing discharge capacity losses during resting period. To do so, the protocol illustrated in Figure 3. 4 was applied to check the effect of the initial volume of electrolyte on the discharge capacity lost during resting period. Normalized discharge capacity loss as function of electrolyte volume is shown in Figure 3. 5.

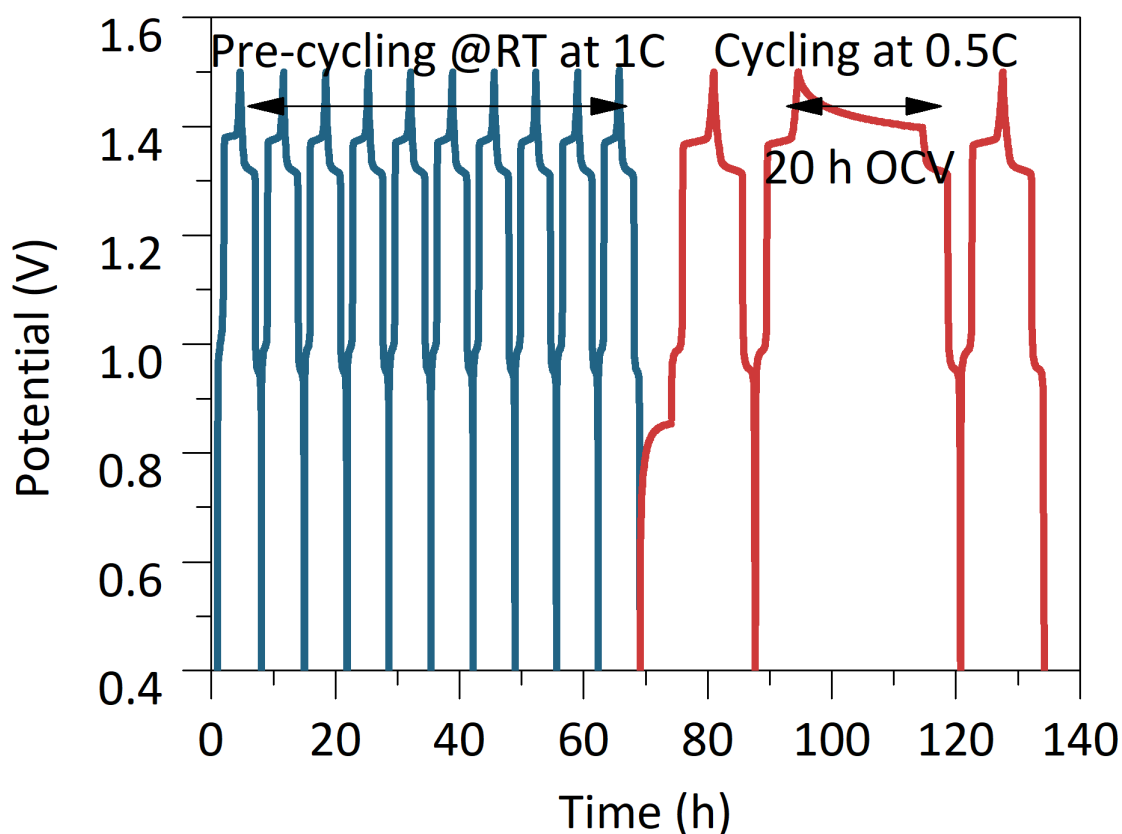


Figure 3. 4 Illustration of the protocol performed to assess the electrolyte volume influence on the SEI stability in a $\text{Mo}_6\text{S}_8/\text{LFP}$ cell in 20 m LiTFSI. A pre-cycling step of 10 cycles at 1C is applied at room temperature followed by a cycling step at 0.5C with 20 h of open circuit voltage (OCV) after the second charge at room temperature.

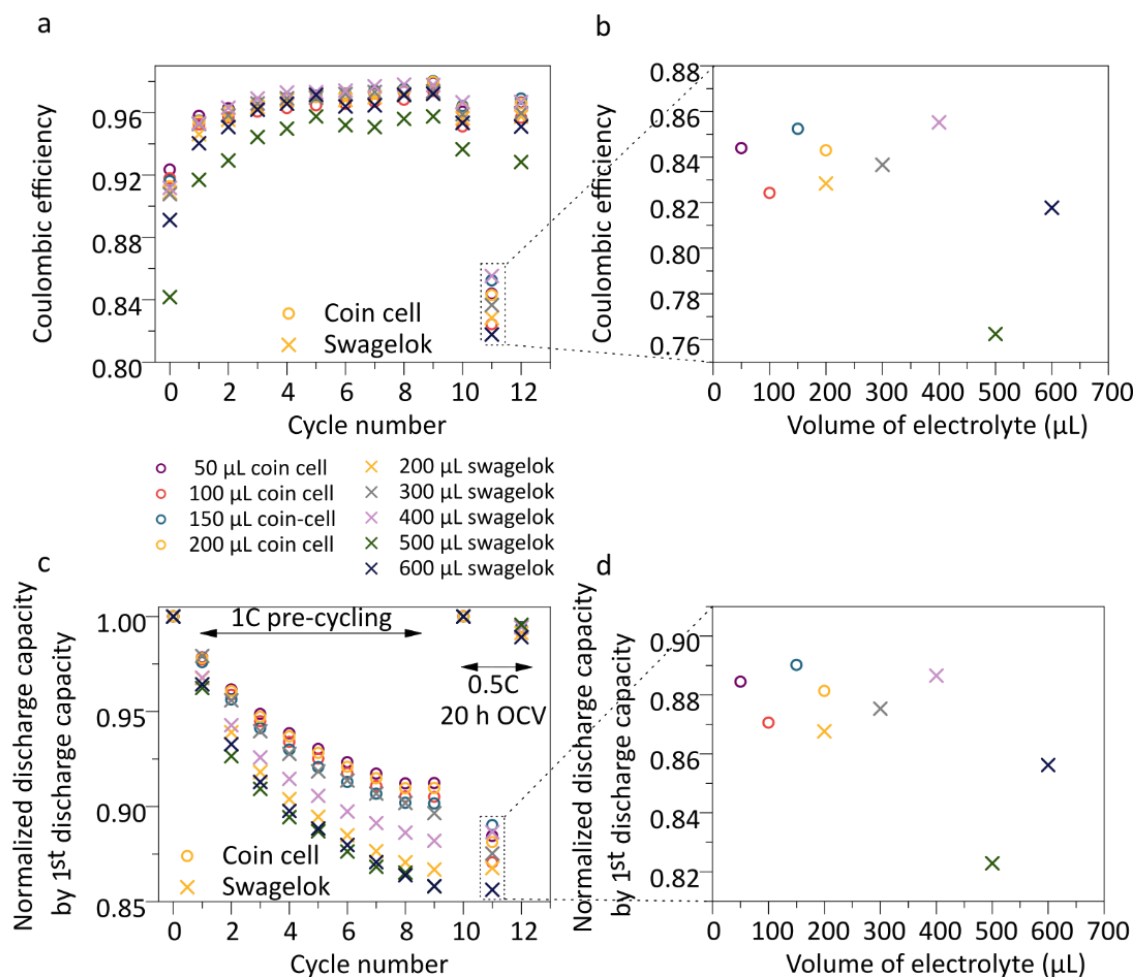


Figure 3.5 Influence of the electrolyte volume on the SEI stability in a $\text{Mo}_6\text{S}_8/\text{LFP}$ full cell in 20 m LiTFSI. (a) Coulombic efficiency as function of cycle number. (b) Zoom on the Coulombic efficiency obtained after 20 h open circuit voltage (OCV) as function of the volume of electrolyte. (c) Normalized discharge capacity as function of the cycle number. Normalization by the 1st discharge capacity obtained at 0.5C during cycling step. (d) Zoom on the normalized discharge capacity as function of the volume of electrolyte after 20 h OCV.

While the electrolyte volume is increased from 50 μL up to 600 μL , all cells components and parameters are kept constant, *i.e.*, the electrode diameter and number of glass fiber separators. Coin cells were used for electrolyte volume below 200 μL to ensure good reproducibility of the results as the pressure applied is controlled to 0.8 T. However, when testing greater electrolyte volumes (above 200 μL), coin cells cannot be used since the electrolyte overflows in the crimping machine. Thus, Swagelok® design was used despite lower performances and poorer reproducible results due to the hand-applied pressure, as highlighted when comparing the results obtained for 500 μL volume of electrolyte (Figure 3.5a and c, green crosses).

First, as shown in Figure 3. 5, Coulombic efficiencies measured throughout the pre-cycling step show a similar behavior with a steady increase from 0.91 up to 0.98 after 8 cycles, attesting the formation of the SEI regardless of the electrolyte volume. In contrast, greater disparities are noticed for normalized discharge capacities (see Figure 3. 5c and d). Considering the limited differences observed for the values of capacity retention obtained for coin cells and the dispersion of values in the case of Swagelok, one can conclude that these disparities certainly originate from the difference of results obtained between coin cell and Swagelok formats, rather than from the electrolyte volume. This assumption is further confirmed by looking at the similar Coulombic efficiency and normalized discharge capacity estimated after 20 h of OCV regardless of the electrolyte volume. Moreover, considering a 10 nm thick LiF-based SEI¹¹¹ forming on a 1.27 cm diameter electrode, one can estimate the concentration of LiF expected if the SEI dissolves as function of the electrolyte volume, as shown in Figure 3. 6a (LiF solubility limit will be discussed in greater details in the next Chapter). Thus, even for a large volume of electrolyte $\approx 600 \mu\text{L}$, the solubility limit is reached and the LiF-based SEI should not dissolve as a whole.

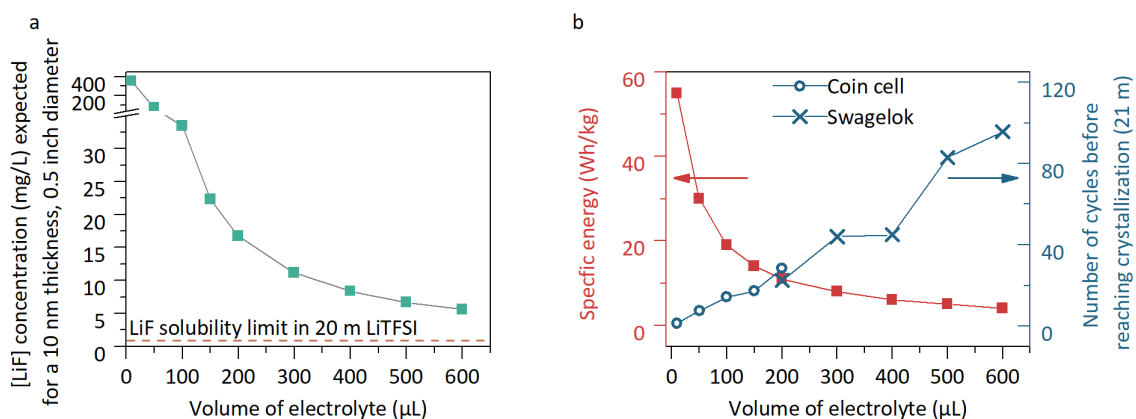


Figure 3. 6 (a) Estimated LiF concentration for a 10 nm LiF layer as function of the electrolyte volume (from 9.4 μL to 600 μL) considering an electrode surface of 1.27 cm² (details of calculation are given in Chapter Material and Methods). Dash line corresponds to the solubility limit determined using an ion selective electrode to fluoride, as detailed in Chapter 4. (b) Specific energy (red) and maximum number of repeated cycles (blue) (one cycle is defined by one pre-cycling step of 10 cycles performed at 1C followed by a cycling step of charge/discharge and 20 h OCV at 0.5C, as described in Figure 3. 4) before crystallization at 21 m LiTFSI as function of the electrolyte volume (from 9.4 μL to 600 μL). Energy density and specific energy correspond to calculations made with the model developed by Betz *et al.*²²¹ by changing the electrolyte volume from optimized amount (9.4 μL) up to 600 μL (see Figure A3.1). Details for the calculation are given in the Appendix of this Chapter (see Table A3.6-11).

The number of repeated cycles (each cycle being composed of 10 pre-cycles at 1C followed by 20 h OCV at 0.5C) that can be made before reaching 21 m, concentration at which LiTFSI crystallizes at RT, are estimated as a function of the electrolyte volume. For this calculation, two hypotheses were made to assess the amount of water consumed during one cycle, based on the results presented in Chapter 2. First, the HER is responsible for 70 % of the irreversible capacity during continuous cycling (see Table 2.2 in Chapter 2). Second, 100 % of the capacity loss during OCV period is due to the HER (see Figure 2.18 in Chapter 2). Thus, the amount of water available in the cell after each cycle can be compared to the amount of water expected for a concentration of 21 m. Obviously, these calculations do not consider the consumption of salt during cycling to form the SEI. Nonetheless, as shown in Figure 3.6b, the lower the amount of electrolyte, the faster the 21 m LiTFSI concentration is reached and thus the faster the cell dies, as expected. Moreover, to estimate the energy density and the specific energy as function of the electrolyte volume, the model developed by Betz *et al.*²²¹ was used. In this protocol, values are estimated for Li-ion battery based on lab-scale measurements (in Swagelok or coin cells) by extrapolation of the electrode materials loading and the electrolyte volume usually employed for 18650 cells. The details for these calculations are given in the appendix of this Chapter. Hence, increasing the electrolyte volume obviously lowers the specific energy and the energy density due to the weight and volume added, as shown in Figure 3.6b and in Figure A.3.1. One can observe that using an optimized volume of electrolyte of $\approx 10 \mu\text{L}$ (based on the electrodes porosity), 55 Wh/kg (161 Wh/L) are estimated for the battery performances. However, the cell would reach the saturation limit after only one unique protocol of 10 charges/discharges at 1C followed by 0.5C cycling with 20 h of resting period.

Electrochemical impedance spectroscopy (EIS) was then performed to assess the formation of the SEI, as proposed by Suo *et al.*¹⁴⁶. Indeed, by fitting the experimental data with an equivalent circuit taking into account the electrolyte resistance, the impedances related to the SEI, the double layer and the diffusion contribution, the authors found an effect of cycling on the SEI formation on Mo_6S_8 in a 2-electrode full cell based on $\text{Mo}_6\text{S}_8/\text{LMO}$. Unlike Suo *et al.*¹⁴⁶, we used a 3-electrode Swagelok to decouple contributions from both the negative and the positive electrodes. The protocol illustrated in Figure 3.7 was employed, using Mo_6S_8 as counter electrode, LFP as working electrode and a ring of partially delithiated $\text{Li}_{0.5}\text{FePO}_4$ deposited on a stainless steel gauze as reference. The electrochemical signature of the cell is given in Figure 3.7. Before analyzing the EIS data, one must acknowledge that faster self-discharge is measured in this configuration when compared to the coin cell one. Observing that the

performances obtained during the pre-cycling steps is poor (see Figure 3. 7b), this behavior certainly originates from a poorly passivating SEI formed in this configuration which combines more separators and a lower pressure. However, despite these experimental limitations, this protocol was used to assess the SEI stability. First, we found that the contribution of the LFP counter electrode to the cell impedance barely varies throughout the experiment, thus confirming that the influence of high capacity loading of LFP versus Mo_6S_8 (4:1) is enough to neglect the impact of the cell state-of-charge (SOC) on LFP impedance. Moreover, the electrochemical signature and performances of the 3-electrode cell, despite not being optimized, are reproducible, as shown in Figure A.3. 2 in the Appendix of Chapter 3.

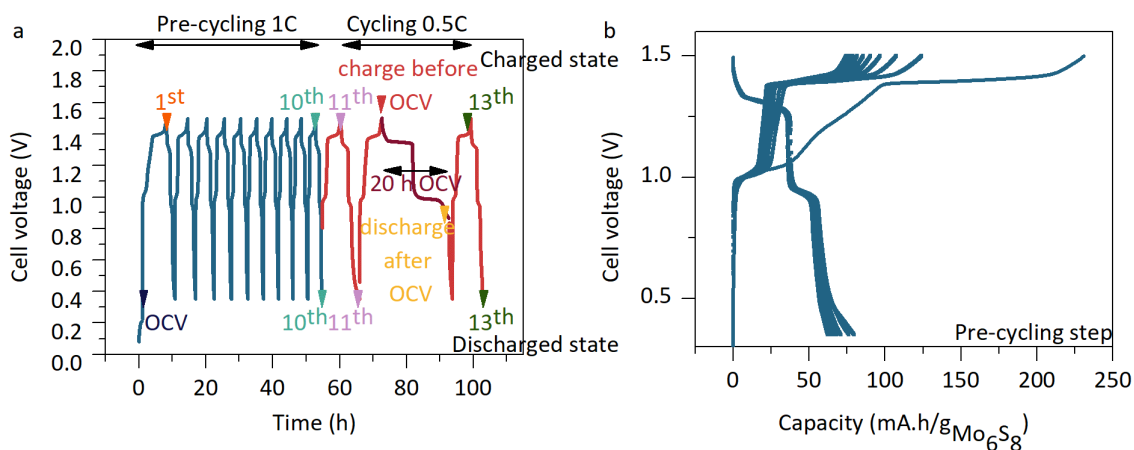


Figure 3. 7 (a) Illustration of the protocol used to assess SEI stability over self-discharge cycling in a 3-electrodes cell based on Mo_6S_8 as counter electrode, LFP as working electrode and a ring of electrochemically delithiated $\text{Li}_{0.5}\text{FePO}_4$ on a stainless steel gauze as reference in 20 m LiTFSI. Cell voltage, *i.e.* $E_{\text{LFP}} - E_{\text{Mo}_6\text{S}_8}$, is shown. (b) Cell voltage as function of capacity (based on Mo_6S_8 electrode mass).

Figure 3. 8 shows the impedance spectra obtained for Mo_6S_8 during cycling. First, one can notice that Mo_6S_8 impedance spectra are affected by the state-of-charge at low frequency (see Figure 3. 8b and d), which might be related to changes in diffusion in the electrode material, among other phenomena. Moreover, the two semi-circles at middle frequency, defined by the arrows in Figure 3. 8b, could be attributed to SEI and charge transfer contribution¹⁴⁶. Considering either a charged or discharged state, no changes are visible upon cycling, as shown in Figure 3. 8b and 3. 7c for charged state and in Figure 3. 8d and e for discharged state. Besides, the resting period of 20 h does not seem to have an influence on the response of the system, as the spectra obtained before and after the OCV period are similar (yellow and light purple crosses in Figure 3. 8e). Therefore, using our 3-electrode cell configuration, we conclude that EIS is not an

appropriate tool to study the SEI formation and its degradation upon cycling, unless further optimization regarding the cell set up and reference position are made at the negative electrode. Thus, rather than EIS, we then investigated the SEI stability by monitoring the impact of water consumption on the electrolyte concentration.

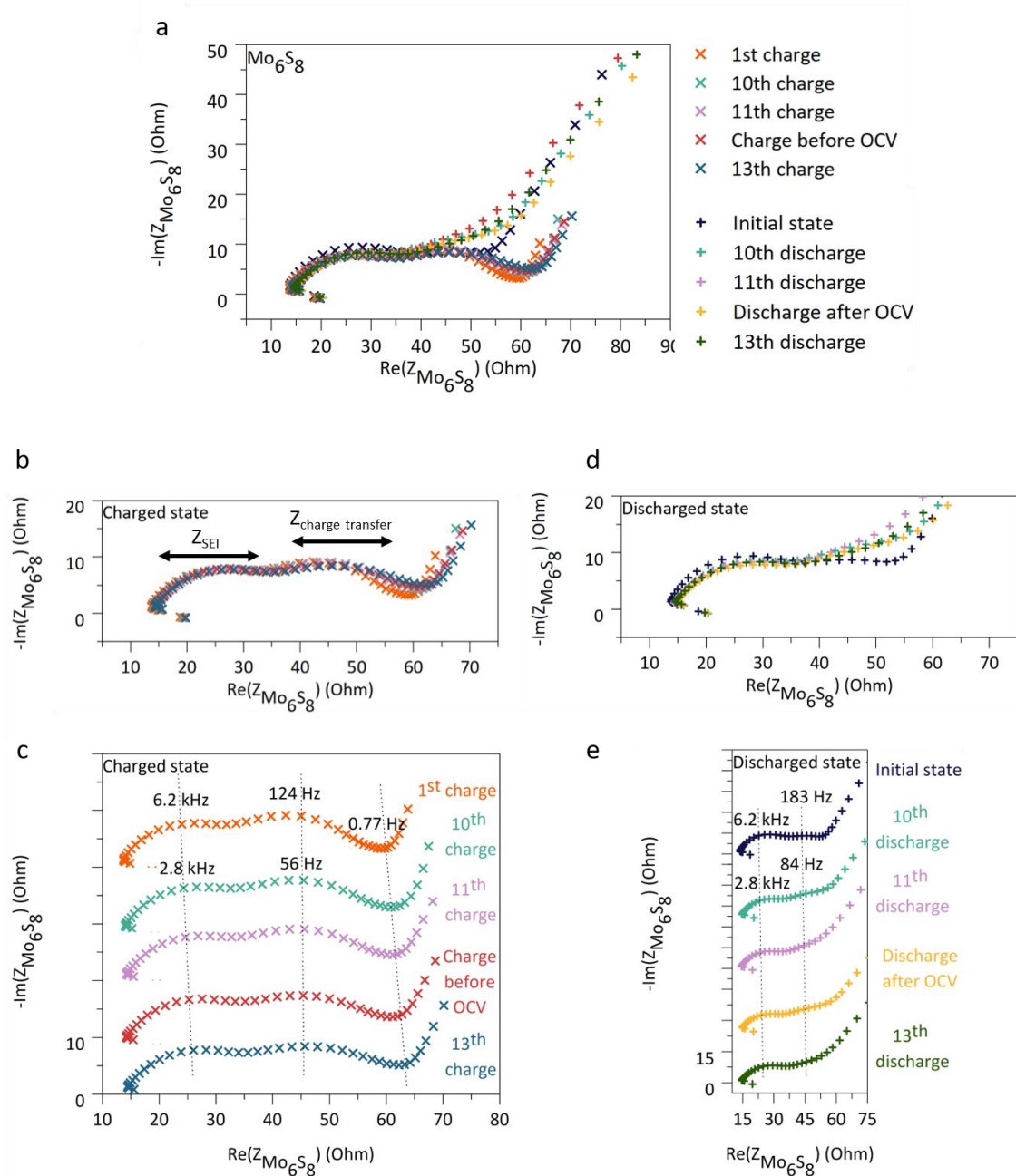


Figure 3. 8 Nyquist plot obtained by electrochemical impedance spectroscopy (EIS) recorded for Mo_6S_8 upon cycling. (a) Summary of all impedance spectra. (b, c) Impedance spectra obtained in charged state. (d, e) Impedance spectra obtained in discharged state. EIS study was performed with a 20 mV amplitude signal between 1

MHz and 50 mHz of frequency range using Mo_6S_8 as counter electrode, LFP as working electrode and $\text{Li}_{0.5}\text{FePO}_4$ as reference electrode in 20 m LiTFSI.

2 Impact of water consumption on electrolyte crystallization

To compare and rationalize the importance of water consumption during cycling and self-discharge to electrolyte concentration, the rate of water consumption associated with each reaction (direct and indirect HER) was calculated taking into account the time, the mass of active material and the hydrogen release. A volume of electrolyte of 200 $\mu\text{L}/\text{cell}$ that corresponds to an initial quantity of water of 2.79 mmol (based on the 20 m LiTFSI physico-chemical properties) was used as a baseline.

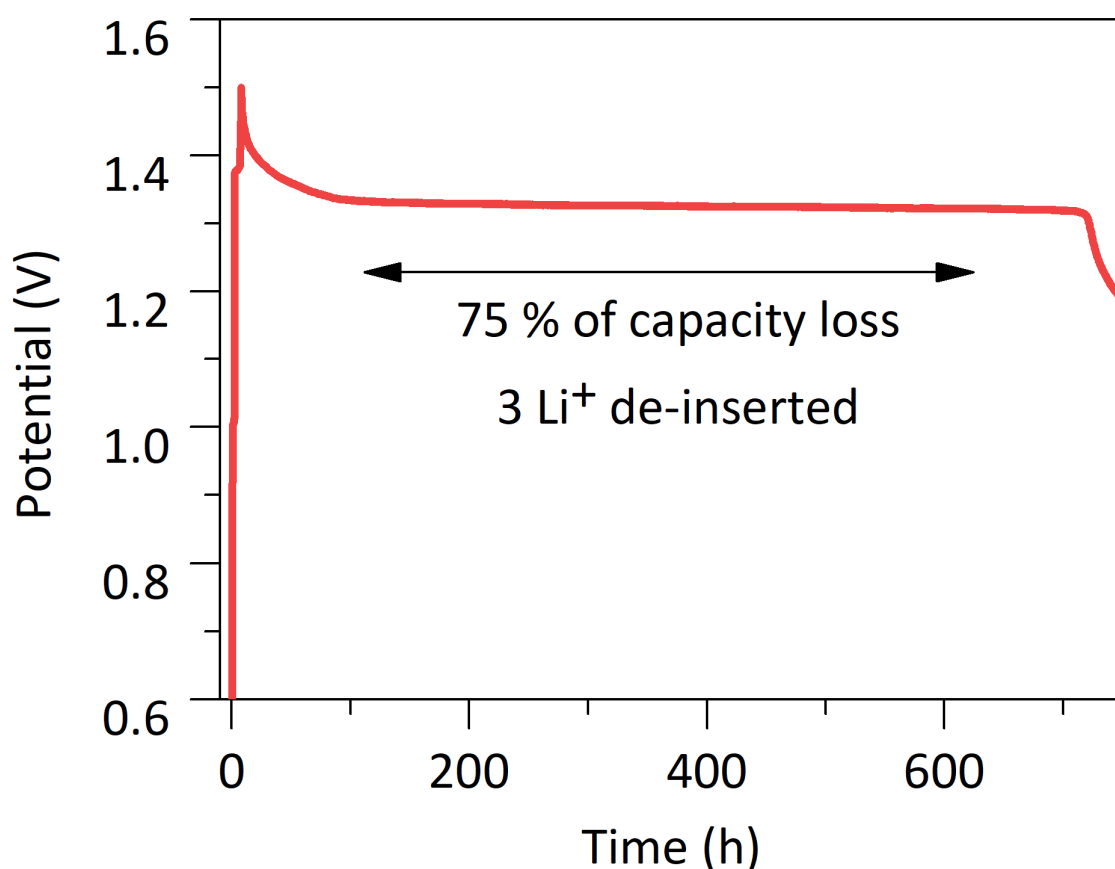
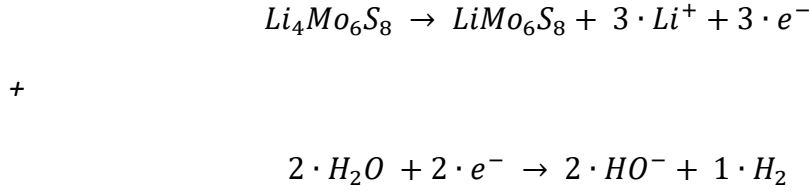


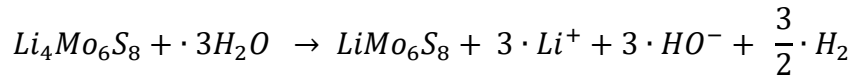
Figure 3. 9 Illustration of self-discharge under open circuit voltage (OCV) happening for $\text{Mo}_6\text{S}_8/\text{LFP}$ cells using 20 m LiTFSI electrolyte after being charged to 100 % state-of-charge (SOC).

Based on the cycling curve shown in Figure 3. 9, one can consider that 75 % of the initial capacity is lost during this self-discharge protocol, bearing in mind that three

electrons are exchanged to de-insert three Li^+ from $\text{Li}_4\text{Mo}_6\text{S}_8$ as described by Equation 3. 1. Thus, the self-discharge mechanism can be written as follow.



Equation 3. 1:



Moreover, the amount of water consumed (in mole) can be written as function of the amount of electrode material (see Equation 3. 2 and Equation 3. 3)

Equation 3. 2:

$$n_{\text{H}_2\text{O consumed by self-discharge}} = 3 \cdot n_{\text{Li}_4\text{Mo}_6\text{S}_8}$$

Equation 3. 3:

$$n_{\text{H}_2\text{O consumed by self-discharge}} (\text{mol}) = 3 \cdot \frac{0.75 \cdot Q (\text{C})_{\text{cell}}^{\text{intial}}}{z \cdot F}$$

with $Q_{\text{cell}}^{\text{intial}} (\text{C})$ the initial cell capacity calculated according to the limiting material, *i.e.* Mo_6S_8 ; z the number of electron transfer to reach 75 % of delithiation, *i.e.* 3; F the Faraday constant equal to 96500 C/mol.

Besides, for the direct mechanism, the rate of water consumption can be determined by calculating the number of moles of water consumed during cycling thanks to pressure cell experiments. As detailed in Chapter 2, the amount of mole of gas produced during cycling is determined thanks to the Faraday law. Then, the amount of mole of water consumed is correlated to the amount of mole of hydrogen through the Equation 3. 4.

Equation 3. 4:

$$n_{\text{H}_2\text{O consumed by cycling}} (\text{mol}) = 2 \cdot n_{\text{gas}}$$

with $n_{\text{gas}} (\text{mol})$, defined by the ideal gas law and 2, the stoichiometric coefficient between H_2 and H_2O considering direct HER.

Finally, the quantity of water consumed during self-discharge or cycling can be normalized by n_{water} , the initial amount of water in the electrolyte, $t_{self-discharge/cycling}$, the duration of self-discharge to lose 75 % of the capacity or the charge time and $m_{active\ material}$, the mass of active material, as described in Equation 3. 5.

Equation 3. 5:

$$\text{Rate of water consumed during self – discharge or cycling} = \frac{n_{H_2O\ consumed\ by\ self-discharge/cycling}}{n_{water} \cdot m_{active\ material} \cdot t_{self-discharge/cycling}}$$

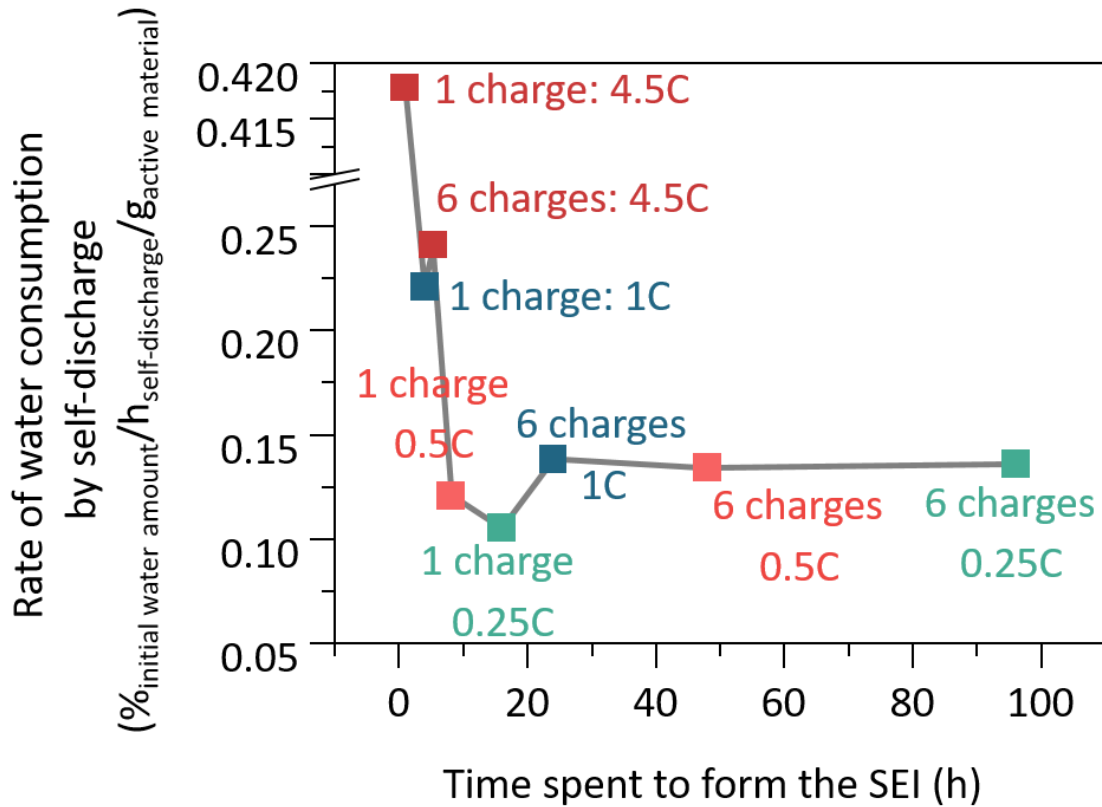


Figure 3. 10 Rate of water consumed by self-discharge as function of the time spent to form the SEI.

Figure 3. 10 summarizes the rate of water consumption for cells that underwent self-discharge protocol until 25 % SOC. One can observe that when sufficient time is spent to form a stable SEI, *i.e.* at low rate and/or with multiple formation steps, the rate for the indirect HER mechanism is constant at ≈ 0.15 %initial water amount/(hself-discharge·gactive material). Hence, this protocol highlights the conditions under which a passivating SEI is formed and assesses the rate of water consumption during self-discharge. Furthermore, this rate (indirect mechanism) is within the same order of magnitude, though smaller, than the rate of water consumption during cycling (direct mechanism, considering SEI

formation time greater than 20 h, see Table 3. 1), suggesting that its irreversible impact cannot be neglected when assessing the practicability of WiSE. Bearing in mind that a 20 m LiTFSI electrolyte operates close to the limit of solubility of the salt, the combine direct and indirect water consumption rates can lead to changes in concentration and eventually to severe drying out of the cell upon cycling and/or storage. Hence, despite the fact that most of capacity lost during self-discharge is reversible (regarding Li⁺ balance, see Chapter 2), it will lead to early cell death.

Table 3. 1 Ratio of water consumed during cycling in % initial water amount /(h·g) assessed by pressure cell measurements.

Cycling (results based on pressure cells)	0.1C	0.15C
Mass of active material [mg]	9.63	7.88
Amount of hydrogen produced/cycle [μmol]	1.43	0.978
Duration of cycling (related to SEI formation) [h]	40	26.7
Amount of water consumed during cycling/cycle [μmol]	2.86	1.96
Rate of water consumption [%/h/g]	0.27	0.33

Moreover, to assess the impact of water consumption, we recorded the evolution of water content in the electrolyte as function of cycle number and self-discharge period experienced by a WiSE-based cell. In the literature, NMR, IR or Raman spectroscopy results were shown to be sensitive to the salt concentration in WiSE. Though, in this study, the use of differential scanning calorimetry (DSC) was preferred for practical reasons. Indeed, DSC enables to limit the contamination by moisture before carrying out the experiments (when no operando spectroscopical cells are available, as it is the case of us) while showing great sensitivity to changes in concentration, as shown in Figure A.3. 4.)

First, a calibration curve is determined using reference electrolytes with concentration of 19.803 m, 20.591 m, 20.910 m, 21.992 m and 22.9983 m. Using the first crystallization peak of the reference electrolytes (described by the arrow in Figure A.3. 4b), the following fit $T_{crystallization\ peak} = 4.68 \cdot C_{LiTFSI}^{mol/kg} - 91.5$ (see Figure 3. 11c) is obtained.

Then, DSC experiments were performed on separators collected from aged cells, as shown in Figure 3. 11c and d. Looking at the exothermic peak corresponding to the hydrated LiTFSI phase (H₂O·LiTFSI) crystallization, cells can be split into two groups: 1) those that underwent continuous cycling (yellow and orange curve) at lower

temperature and 2) the cells that underwent a 20 h OCV step after each charge (pink and purple line). Based on these results, one can hypothesize that, upon repeated resting period, the electrolyte salt concentration increases, originating from a non-negligible amount of water consumed, thus confirming our previous calculation of the water consumption rate. Eventually, a greater salt concentration is deduced for cells cycled during 15 cycles suggesting a greater water consumption than in the case of cells cycled during 100 cycles (see Figure 3. 11c). This observation could originate from partial water recombination during cycling, however, reproducibility must be verified before drawing any definitive conclusion. Calibration curves and additional measurements on cells aged are currently under investigation. To complement these results and accurately reflect the cell drying off, further measurements can be done by fixing the overall time of experiment while changing the cycling or self-discharge cycle number.

Finally, one has to acknowledge that assessing water consumption in coin cell devices still remain far from 18650 or pouch cells in which the design will drastically modify the electrolyte/electrode ratio and so, the influence of the parasitic reactions.

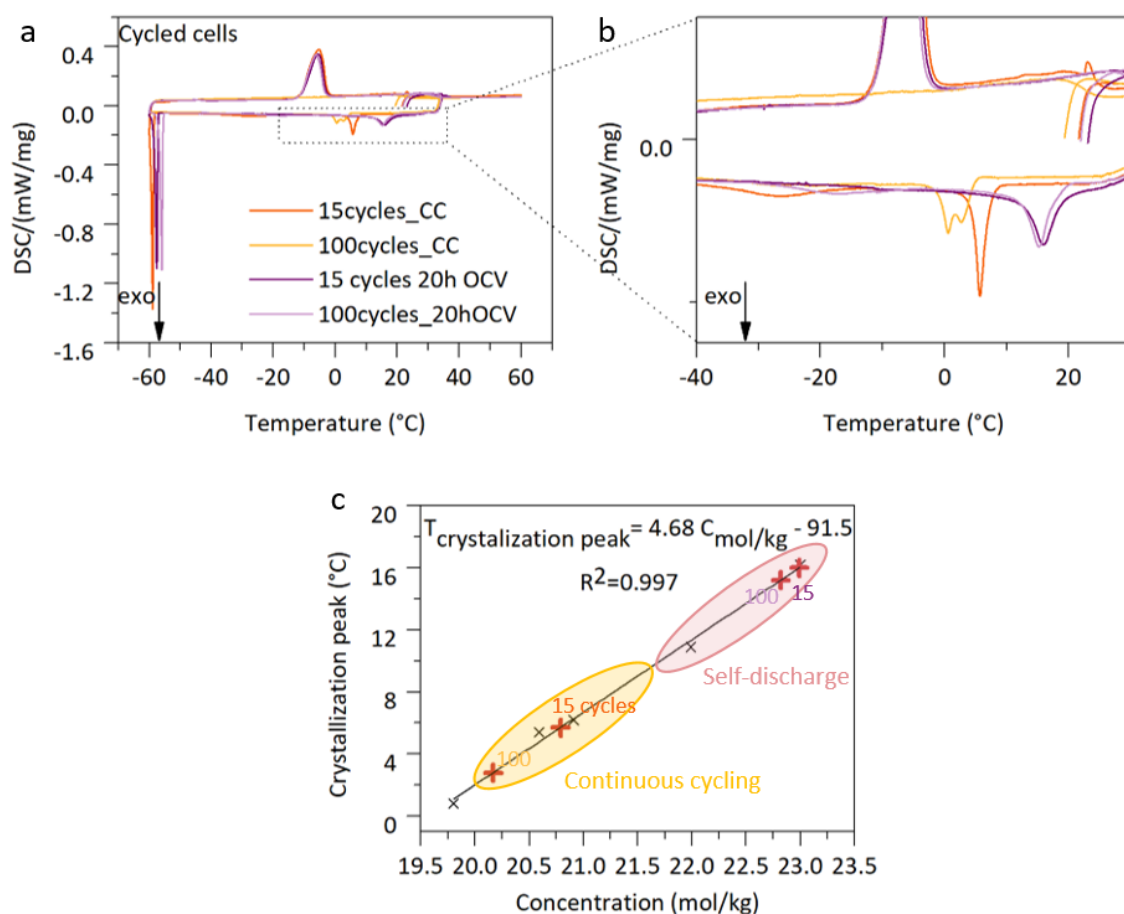


Figure 3. 11 Differential scanning calorimetry (DSC) experiments performed at 2 °C/min between 35 °C and -60 °C upon cooling and back to 60 °C on heating. (a) Cells aged for 15 and 100 cycles with continuous cycling protocol or with a 20 h OCV resting period at the end of each charge (b) zoom on the crystallization peak of aged cells. (c) Crystallization peak measured as function of electrolyte concentration obtained from the calibration data (black cross) and linear fit (black line) enabling the calculation of the aged cells concentration (red cross).

3 Activation energy of direct and indirect HER in WiSE

As shown by self-discharge measurements, the SEI formed upon cycling in WiSE-based electrolyte does not prevent water to access the interface where it is reduced. Our results suggest a much higher HER onset potential than the one previously determined (1.9 V vs Li⁺/Li)¹¹¹ by linear scan voltammetry on stainless steel current collectors. Knowing that the potential for de-intercalation of Li₄Mo₆S₈ is ≈ 2.7 V vs Li⁺/Li, the reversible potential for water reduction must be greater than this value to explain self-discharge observed in this work (see Figure 3. 12a). This conclusion is in line with the results published by Kühnel *et al.*¹⁵³ assessing the ESW as function of the current density threshold with an onset potential for HER at 2.48 V vs Li⁺/Li ($i_{\text{threshold}} = 2 \mu\text{A}/\text{cm}^2$)

on stainless steel. Besides, HER potential also depends on the electrode material¹⁵³. Naik *et al.*²²² reported a HER onset potential on Mo_6S_8 to be around -0.2 V vs NHE, *i.e.* ≈ 2.8 V vs Li^+/Li in diluted media, barely dependent on the pH of the electrolyte.

Furthermore, by normalizing the time needed to fully de-insert $\text{Li}_4\text{Mo}_6\text{S}_8$ by constant-current de-insertion or by de-insertion through self-discharge, two de-insertion distinct rates can be seen (see Figure 3. 12b). Indeed, during self-discharge, three Li^+ are de-inserted in $\approx 1/3$ of the overall time during the 2nd plateau while one Li^+ is de-inserted in $\approx 2/3$ of the time during the first plateau, indicating that the de-intercalation of Li^+ is faster during the second plateau when driven by self-discharge. To explain this observation, one must first keep in mind that the driving force for de-intercalation is different between the two plateaus. Hence, the driving force defined by $\Delta E = E_{\text{HER}} - E_{\text{de-intercalation}}$ is greater for the second plateau at 2.3 V than the first plateau at 2.7 V vs Li^+/Li (see Figure 3. 12a), which eventually lowers the activation barrier for the indirect HER associated with the second plateau.

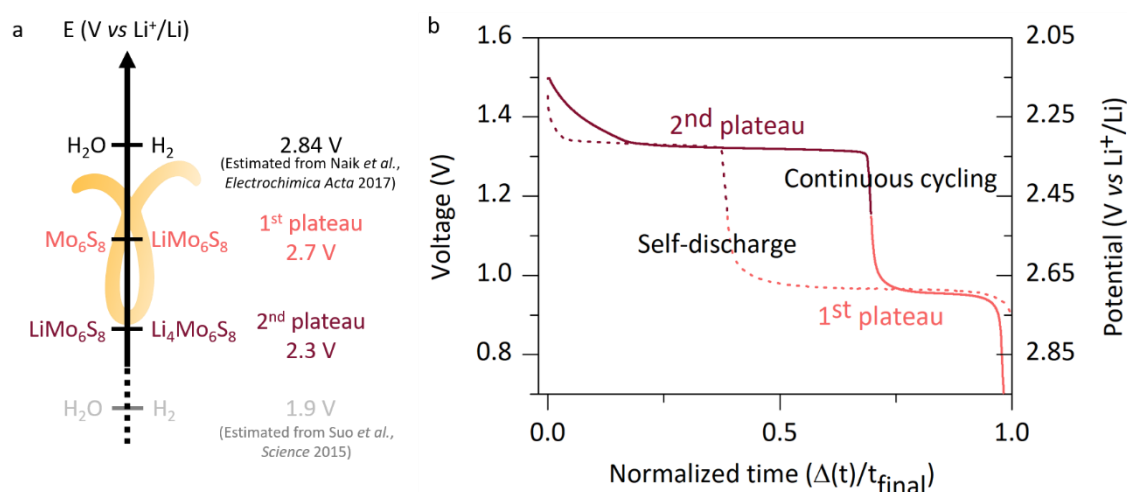


Figure 3. 12 (a) Redox potentials for Mo_6S_8 and the HER, extracted from the literature^{111,222}. (b) Voltage as function of normalized time for a $\text{Mo}_6\text{S}_8/\text{LFP}$ cell in 20 m LiTFSI undergoing self-discharge (dotted line) or constant-current continuous cycling (full line). Normalized time is defined by the ratio between evolution of time during discharge and the end of discharge time.

In order to clarify these observations, activation energies for self-discharge associated with the first and the second intercalation plateau of Mo_6S_8 in WiSE were determined using a $\text{Mo}_6\text{S}_8/\text{LFP}$ cell based on 20 m LiTFSI electrolyte. To perform this study, (i) the LFP electrode is in large excess compared to the Mo_6S_8 one, (ii) oxygen is purged from the electrolyte before assembly and (iii) the contribution of LFP to the self-discharge is considered negligible, as demonstrated in Chapter 2 where water oxidation

potential was shown to occur above 4 V vs Li⁺/Li. In addition, we considered that the reaction between charged (delithiated) FePO₄ and hydrogen produced at the negative electrode is negligible, as it is controlled by the diffusion of hydrogen across the cell.

To determine these activation energies, the protocol described in Figure 3. 13a and c was used. First, a pre-cycling step of 10 cycles performed at 1C, 25 °C, was applied to form a sufficiently stable SEI (as concluded from Figure 3. 10). The cell was then cycled at 0.5C at different temperatures (15 °C, 25 °C, 35 °C, 45 °C, 55 °C) using a charge/discharge/charge protocol followed by 20 h OCV. Capacity retention was calculated by normalizing the discharge capacity obtained after 20 h of resting period to the one obtained during full cycling. For the 1st plateau of Mo₆S₈ (2.7 V vs Li⁺/Li), a cut off of 1.2 V was set during the cycling step, while a cut off of 1.5 V was used for the 2nd plateau. Then, following the Arrhenius equation, the normalized loss of discharge capacity upon self-discharge is plotted as function of the inverse of temperature (Figure 3. 13.b and d), allowing the extraction of the activation energies from Equation 3.6.

Equation 3. 6:

$$k = A \cdot e^{\frac{-E_a}{RT}}$$

with k , the reaction rate (the unit depends on the reaction considered, no unit for self-discharge, h⁻¹ for pressure cell and A for CC-CV 2-electrodes coin cell); A the pre-exponential factor (the unit is defined by the unit of the reaction rate); E_a , the activation energy (J/mol); R , the universal gas constant (8.314 J/mol/K) and T , the temperature (K).

Almost identical activation energies are extracted following this protocol (19 kJ/mol for the 2nd plateau and 25 kJ/mol for the 1st plateau), regardless of the potential of the intercalation plateau (Figure 3. 13), suggesting that self-discharge mechanism is similar between these two insertion plateaus, the difference of reaction rates being attributed to difference in driving force ($\Delta E = E_{\text{HER}} - E_{\text{de-intercalation}}$).

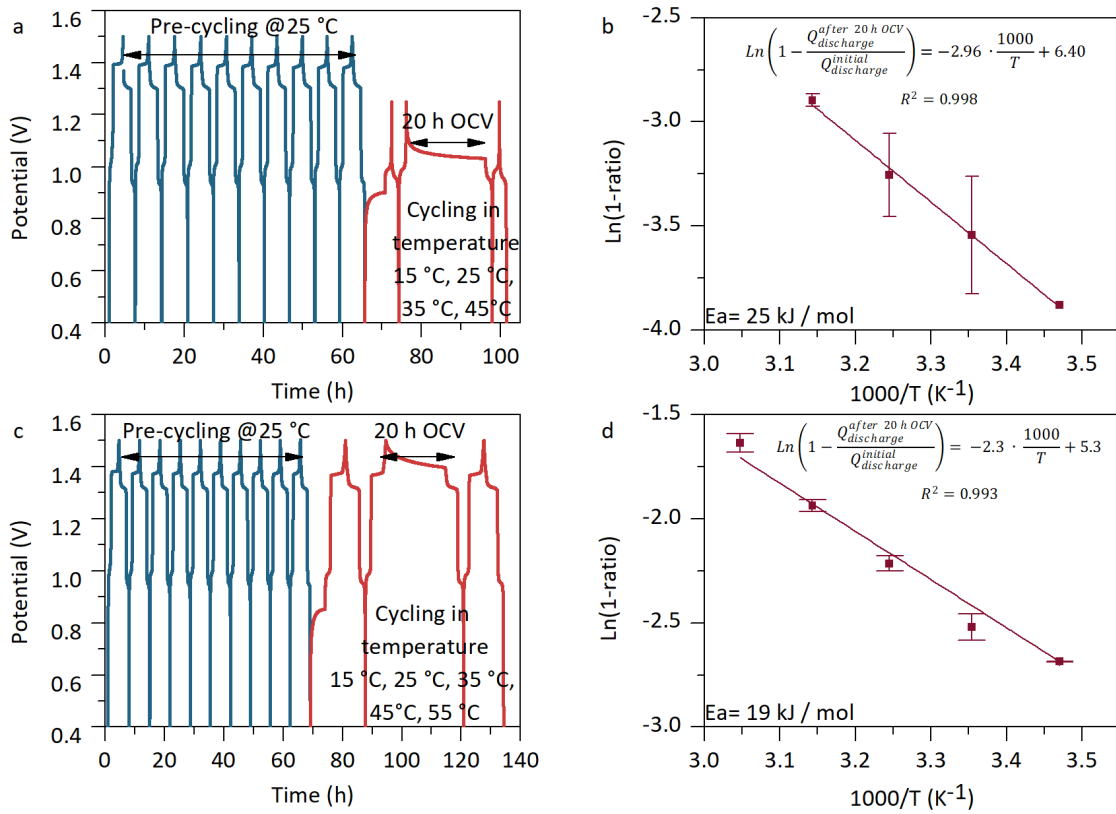
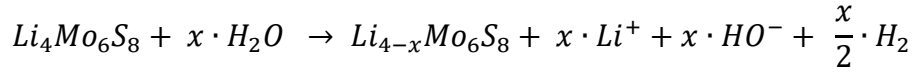


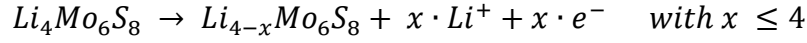
Figure 3. 13 Determination of the activation energy of the indirect HER taking place during self-discharge. (a) Potential as function of time for self-discharge experiment performed on the first plateau of Mo_6S_8 (2.7 V vs Li^+/Li). Ten cycles are performed at 1C, 25 °C, followed by cycling at 0.5C at different temperature (15 °C, 25 °C, 35 °C and 45 °C). (b) Arrhenius plot of the normalized discharge capacity loss by indirect HER during self-discharge as function of temperature. Unfortunately, no value was determined at 55 °C for the first plateau, since changes in the electrochemical signature are observed and are currently investigated. (c) Potential as function of time for self-discharge experiment performed on the second plateau of Mo_6S_8 (2.3 V vs Li^+/Li). Ten cycles are performed at 1C, 25 °C, followed by cycling at 0.5C at different temperature (15 °C, 25 °C, 35 °C, 45 °C and 55 °C) (d) Arrhenius plot of the normalized discharge capacity loss by indirect HER during self-discharge as function of temperature. (b, d) Data points represent the mean of three cells, the exception being only one cell at 15 °C during 1st plateau experiment. All cells are based on $\text{Mo}_6\text{S}_8/\text{LFP}$ cell with 20 m LiTFSI electrolyte.

Moreover, self-discharge reaction (see Equation 3. 7) is a combination of two redox reactions (see Equation 3. 8 and Equation 3. 9) that comprised multiple steps, as more than one electron is transferred. Besides, ions exchange (HO^- and Li^+) can lead to mass transport limitation in the bulk of the electrolyte, across the SEI and/or in the electrode material. Therefore, comparison between the activation energy obtained for self-discharge should be confronted with activation energies for these phenomena.

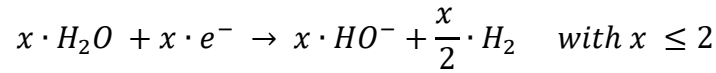
Equation 3. 7:



Equation 3. 8:



Equation 3. 9:



Considering the redox reaction associated with lithium de-intercalation (Equation 3. 8), mass transport is usually not considered as rate determining step (for moderate C-rate such as those used in this study) since Li^+ diffusion in Mo_6S_8 material was reported to be fast enough during intercalation/de-intercalation process with an activation energy comprised between 10 to 17 kJ/mol in Mo_6S_8 ^{223,224}. Furthermore, diffusion in the SEI is often considered as fast compared to charge transfer²²⁵. Eventually, bulk diffusion in the electrolyte is generally not limiting the intercalation mechanism at moderate C-rate due to a rather high conductivity of the electrolyte (≈ 10 mS/cm at 25 °C for 21 m LiTFSI). Therefore, the rate-determining step for intercalation reaction in LIB is generally considered to be the de-solvation step during charge transfer²²⁶, which activation energy largely varies with the solvent. Indeed, it was reported to be much faster in diluted aqueous-based electrolyte^{75,227} than in organic based one^{225,228}. Unfortunately, the impact of superconcentration and thus of solvation sheath on the activation energy of the de-solvation process is barely studied, with the exception of Hu *et al.*²²⁹ who recently reported an activation energy for solvation of 20 kJ/mol in 20 m LiTFSI. Nonetheless, such value is highly debatable due to questionable experimental methods that include measurements at 0 °C, temperature at which the electrolyte is crystallized. Altogether, one can hypothesize that the solvation/desolvation process should limit, alike in organic based LIB, the intercalation reaction in WiSE-based LIB systems. However, the determination of the rate-determining step in the overall self-discharge reaction is not straightforward since both half-redox reactions (see Equation 3. 8 and Equation 3. 9) may interplay.

Attempts were thus made to determine the activation energy of the HER in a battery device. To do so, Mo_6S_8 /LFP pressure cells were assembled using 20 m LiTFSI electrolyte. The SEI was first formed by performing 10 cycles at 1C, 25 °C. The activation energy for the HER was then extracted by measuring the pressure increase at different temperatures (25 °C, 35 °C, 45 °C and 55 °C) during the four subsequent continuous

cycles performed at low C-rate (0.15C), as illustrated in Figure 3. 14a. To determine the activation energy of the direct/electrochemical HER, the rate of hydrogen production was determined considering that gas is generated only during charge (see Figure A.3. 5 of the Appendix of this chapter). Such experiments are inspired from the work done by Ayeb *et al.*²³⁰ who determined by gases measurements the HER activation energy during overdischarge conditions in Ni-MH battery to be in the range from 50 to 70 kJ/mol. Figure 3. 14b shows the Arrhenius plot obtained for the direct HER on the surface of Mo₆S₈, from which an activation energy of 72 kJ/mol is determined. Unfortunately, no values for the HER activation energy on Mo₆S₈ was reported for comparison, to the best of our knowledge. However, Mo₆S₈ is reported to be a very promising HER catalyst in acid^{222,231,232} with activity reaching the one of Pt -which is known to have an activation energy of about 10 kJ/mol in acid -, albeit the HER is known to be much slower at pH higher than 2, corresponding to our experimental conditions²³³. Thus, one can hypothesize that the activation energy obtained in this study is rather high and surprising. This can be explained by the use of pressure cell-type devices, in which the activation energy extracted from pressure measurements are obtained in a regime in which with mass transport limitations occur. Moreover, experimentally speaking, due to the low C-rate used (0.15C), a plateau corresponding to pure direct HER is visible above 1.4 V (and before the 1.5 V cut off) at 45 °C and 55 °C, as shown in the appendix of this chapter. Finally, and more importantly, as both HER and intercalation reaction take place simultaneously, the total current is not entirely directed toward the HER.

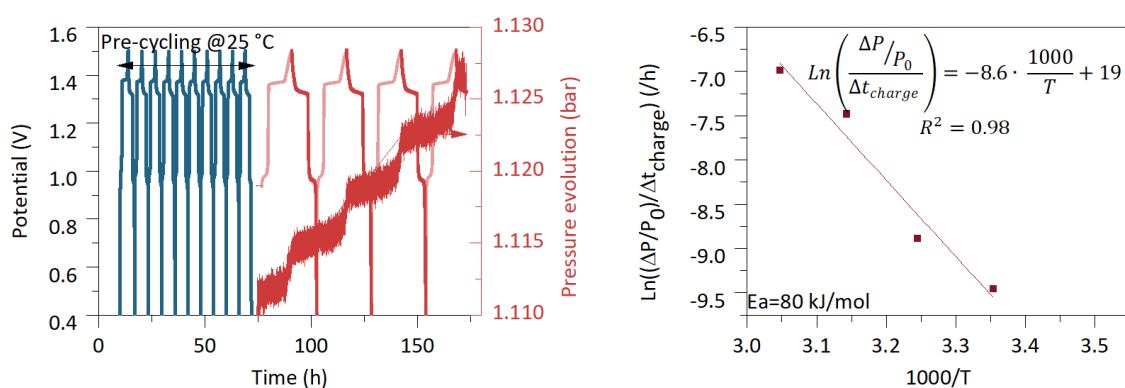


Figure 3. 14 (a) Illustration of the protocol used to assess the activation energy of direct HER on Mo₆S₈ in 20 m LiTFSI by pressure cell tests. Potential and pressure as function of time. (b) Arrhenius plot showing the pressure increase as function of temperature.

To circumvent all these uncertainties related to the experimental conditions, we completed by measuring the activation energy for direct HER in practical conditions applying a constant current - constant voltage (CCCV) protocol to reach the HER

potential after full charging of the cell, as illustrated in Figure 3. 15a. In details, 2-electrodes coin cells were assembled and pre-cycled at 25 °C during 10 cycles at 1C to form the SEI. The cell was then charged to 100 % SOC with a voltage cut off fixed to 1.4 V, to avoid any pure HER plateau starting below 1.5 V above 45 °C. Once 100 % SOC is reached, the cell voltage is set to 1.5 V for 20 h. The current density was then measured as function of temperature (25 °C, 35 °C and 45 °C and 55 °C). The corresponding Arrhenius plot is shown in Figure 3. 15b and the activation energy for pure HER on Mo₆S₈ in 20 m LiTFSI in battery set up is found to be 25.5 kJ/mol.

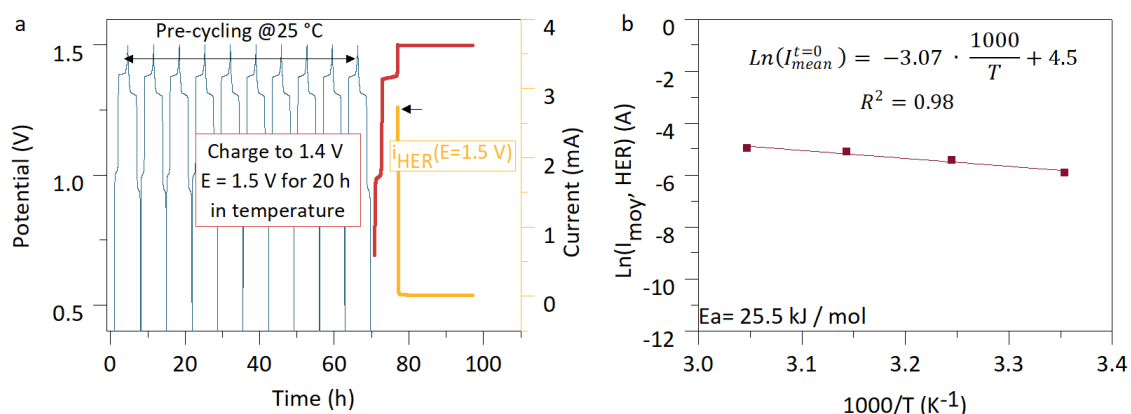


Figure 3. 15 (a) Protocol used to assess the activation energy of direct HER for Mo₆S₈ in 20 m LiTFSI in coin cells. Potential as function of time with pre-cycling step performed at 1C at 25 °C in blue, and cycling step based on full charge at 0.5C up to 1.4 V followed by the application of 1.5 V during 20 h as function of temperature (25 °C, 35 °C, 45 °C and 55 °C) in red as well as current response to a 1.5 V voltage applied (in yellow). (b) Arrhenius plot for the current measured at 1.5 V and 100 % state-of-charge as function of temperature (each point is the mean of two cells).

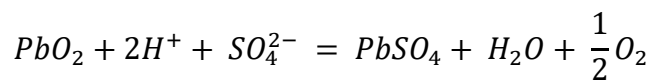
Although the value measured in this study has some uncertainty and the self-discharge experiments measure a global phenomenon, it represents the actual activation energies in practical conditions. Comparing the activation energy found for self-discharge occurring during both plateau with that measured during the CCCV measurements, values are found very similar ($\approx 20 \text{ kJ/mol}$). Therefore, we can conclude that the kinetics for the self-discharge mechanism is presumably governed by the HER rate. For the sake of comparison, activation energies determined for self-discharge for Lead-acid battery and Ni-MH battery (considering self-discharge driven by water reacting with the positive electrode, see Equation 3. 10: and Equation 3. 11:) or organic-electrolyte-based LIB, are listed in Table 3. 2 and compared to the experimental value obtained in this study, regardless of the operating conditions used.

Table 3. 2 Summary of activation energy corresponding to the overall self-discharge mechanism. Considering Ni-MH and Lead-acid, the reaction taken into account is the reaction with water of the positive electrode at 100 % SOC, as described in Equation 3. 10 and Equation 3. 11. Considering LIB, the positive electrode or the negative electrode are considered as limiting electrode.

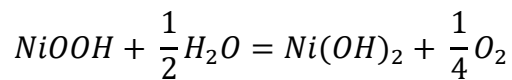
Technology	This work	Organic LIB	Ni-MH	Lead-acid
Activation energy (kJ/mol)	≈ 20	20^{234} to $80^{235,236}$	$67^{ref\ 237}$	$40-70^{ref\ 238}$

Considering lead-acid and Ni-MH devices, the positive electrode is the capacity-limiting one, unlike in our system where the limiting electrode is the negative. This technological choice is made such that oxygen is evolved preferentially instead of hydrogen upon overcharges or self-discharges (see Equation 3. 10 and Equation 3. 11). Having the OER as the rate-determining step^{238,239} reduces the self-discharge rate compared to an HER-driven one since OER kinetics is more sluggish. Hence, the activation energies measured for WiSE (20 kJ/mol) is much lower than those reported for Ni-MH and Lead-acid (67 and 40-70 kJ/mol, respectively).

Equation 3. 10:



Equation 3. 11:



For the LIB technology, two ranges of values were reported for the activation energy related to self-discharge: low values of ≈ 20 kJ/mol and greater values up to 80 kJ/mol. Activation energy of 20 kJ/mol is observed at the negative electrode (synthetic flake graphite)²³⁴ and linked to self-discharge governed by Li^+ de-intercalation and SEI growth, both associated to electrolyte reduction (1.2 M $LiPF_6$ in EC:DEC (1:3 vol%)). The greater values are related to Li^+ intercalation occurring at the positive electrode (LCO) and associated with electrolyte oxidation. These comparisons have a direct impact on practicality of the WiSE technology, as it traduces that the shelf-life of systems for which the self-discharge is governed by reactions at the negative electrode will be greatly limited. To summarize, for WiSE-based LIB, the self-discharge mechanism seems to be controlled by fast kinetics reaction occurring at the negative. However, the strategies employed in other aqueous-based batteries in which the positive produces oxygen and

prevents hydrogen evolution, *i.e.* Lead-acid and Ni-MH, cannot be transposed as discussed in the following section.

Discussion and conclusion of the chapter

In this chapter, we monitored the instability of the native SEI formed on negative electrode when cycled in aqueous superconcentrated electrolyte (20 m LiTFSI). First, as shown on a model-electrode (glassy carbon) and further confirmed by self-discharge experiments, parasitic reactions are not prevented during resting period by the protective passivating layer initially formed. DSC experiments also attest the irreversible consumption of water during both cycling and self-discharge experiments. In addition, based on self-discharge and continuous cycling experiments, one can determine that the rate of water consumption is in the same order of magnitude (in terms of $\frac{\%_{\text{initial water amount consumed}}}{(h \cdot g_{\text{AM}})})$ during self-discharge at 2.3 V vs Li^+/Li than during constant current continuous cycling, though smaller. Besides, as shown by normalizing the time of Li^+ de-insertion either during cycling or by self-discharge, reaction rates are found different. To understand this observation, we designed electrochemical protocols to assess the activation energies associated with self-discharge and direct HER. Experimental results confirm a similar activation energy for self-discharge on both Mo_6S_8 plateau, the difference in reaction rate being explained by differences in driving force. Despite difficulties in accurately estimating the activation energy for direct HER, our results suggest that the rate for self-discharge is governed by the generation of hydrogen, and not by delithiation of Mo_6S_8 , explaining the difference in de-intercalation rate. Altogether, we highlight the dramatic impact of self-discharge that is driven by parasitic reactions occurring at the negative electrode on the practicality of this technology.

To conclude on the viability of WiSE-based LIB, the figure of merits for WiSE-based aqueous Li-ion system is compared to those for classical organic Li-ion (NMC₁₁₁ / LP30 / graphite) as well as other aqueous systems (see Figure 3. 16). As evidenced in our study, WiSE-based aqueous batteries can only safely operate within a ≈ 2 V operating window to avoid parasitic side reactions, unlike organic LIB. To be able to compare our WiSE or WiBS-based battery to classical Li-ion or commercial aqueous systems, we estimated both the energy density and the specific energy for WiSE and WiBS following the protocol proposed by Betz *et al.*²²¹. In conclusion, both the specific energy and the energy density at a cell level are twice smaller than for aprotic Li-ion batteries and eventually similar to the ones achieved by Ni-MH batteries, while being above those for Ni-Cd or Lead-acid batteries. However, the energy efficiency is

similar/close to the one obtained for Li-ion ($> 90\%$), unlike Lead-acid, Ni-Cd, and Ni-MH batteries that show energy efficiency closer to 80-85 %.

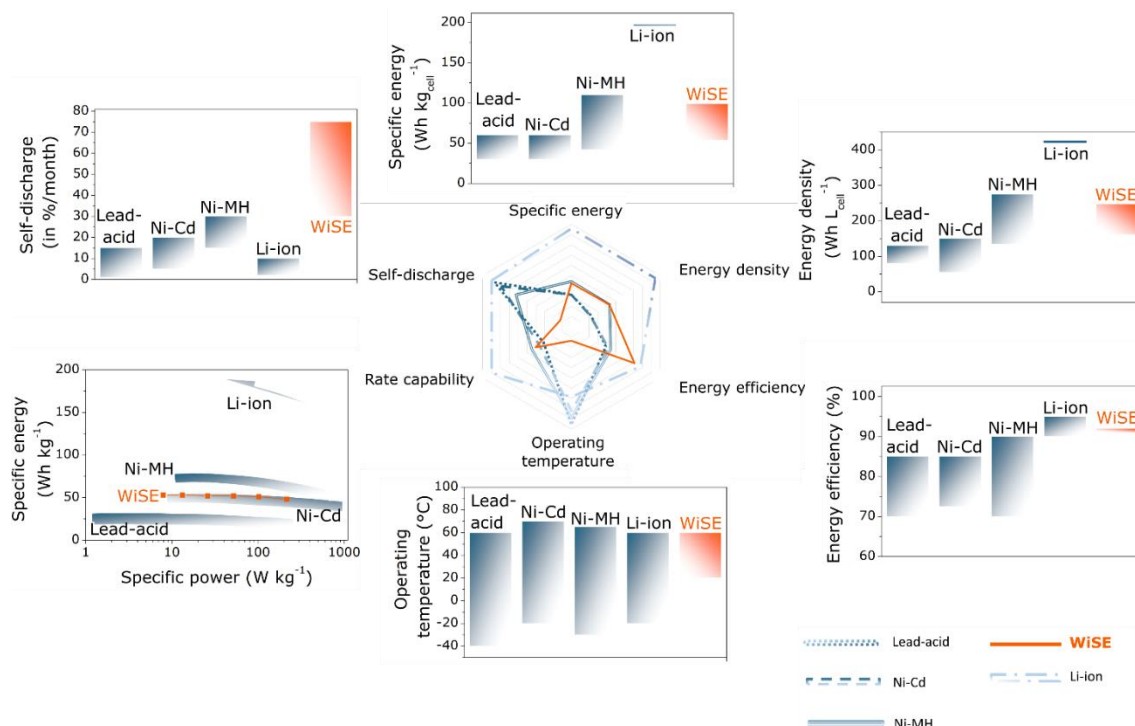


Figure 3. 16 Benchmarking WiSE-based and WiBS-based aqueous batteries against other aqueous systems, namely Lead-acid, Ni-Cd and Ni metal hydrides (Ni-MH) batteries as well as against aprotic Li-ion batteries. The spider-chart at the center compares these systems in terms of six parameters defining the overall performances of these systems. On top is compared the specific energy for these systems, on the left the self-discharge for these systems, on the right the energy density, on the bottom left is represented the specific energy as a function of specific power, on the bottom right is reported the energy efficiency for these systems while on the bottom the operating temperature window for the different technologies. All references are given in the Appendix of the Chapter.

Evidently, cycling batteries within the practical thermodynamically stable potential window of WiSE (≈ 2 V) drastically limits the energy density, which cannot reach the one achieved by LIB. The obvious way to increase the energy density would be to further extend the operating window, by finding chemical-engineering means to handle the gas generated during cycling, alike in other aqueous batteries (Lead-acid, Ni-Cd or Ni-MH).

To do so, two cell designs are generally considered for the aqueous technologies: flooded batteries and sealed ones (that can be vented or not). For flooded batteries, gases are evacuated away from the electrodes prior to be recombined ($\text{H}_2 + \frac{1}{2} \text{O}_2 = \text{H}_2\text{O}$). Furthermore, electrolyte (or water) can be added to compensate water consumption. Regarding vented-sealed batteries, thanks to a pressure valve, the pressure increase resulting from the HER and/or OER can be regulated by outflowing the gases from the cell without allowing oxygen to come in. This strategy reduces the pressure build up during the battery operation. For example, for Lead-acid batteries, the so-called Valve Regulated Lead Acid (VRLA) sealed batteries were developed. Moreover, a catalyst such as Pd can be added in the form of a battery plug to catalyze the gas recombination reaction ($\text{H}_2 + \frac{1}{2} \text{O}_2 = \text{H}_2\text{O}$) and minimize the electrolyte loss and thus the drying-out of the cell. Hence, vented-WiSE batteries could be envisioned, providing that the salt crystallization issue discussed by Kühnel *et al.*¹⁵³ can be solved for superconcentrated electrolytes, as upon continuous consumption of water the battery lifetime will rapidly reduce.

An alternative approach to circumvent the electrolyte drying-out can be the design of sealed WiSE-based batteries using the oxygen recombination strategy. Indeed, another mean to control water decomposition is by adjusting the capacity balance to promote OER compared to HER. For a capacity ratio of negative to positive (N/P) equal to one, both the OER and the HER take place on the positive electrode and the negative one, respectively, upon overcharge. In order to limit the hydrogen production, the positive electrode is set to be the limiting one ($\text{N/P} > 1$), reaching full charge before the negative faces HER. Hence, only O_2 is produced and diffuses through the electrolyte to recombine into water by reacting with the negative electrode (as described in Figure 3.17), thus forming the “oxygen cycle”⁷ that prevents the cell drying off. Altogether, one should keep in mind that such solution can only be efficient if the O_2 production rate is not faster than the recombination one. In definitive, if no care about the dimensionality of the electrodes is taken, aqueous-based batteries face an unbalanced generation of gases and poor recombination efficiency. Eventually, in order to (i) reduce electrolyte evaporation, (ii) to enhance safety by limiting electrolyte creepage and (iii) to promote oxygen diffusion to the negative electrode, electrolyte properties can separately be improved. Porous gel-type electrolytes were implemented to promote the diffusion of O_2 to the negative electrode as gases diffuse faster in gel-type electrolyte than in liquid aqueous electrolytes. Indeed, water consumption taking place in the electrolyte induces the formation of cracks thus creating a network for O_2 diffusion. Another alternative was

the use of electrolyte absorptive glass fiber separators, to avoid having excess of electrolyte in the cells.

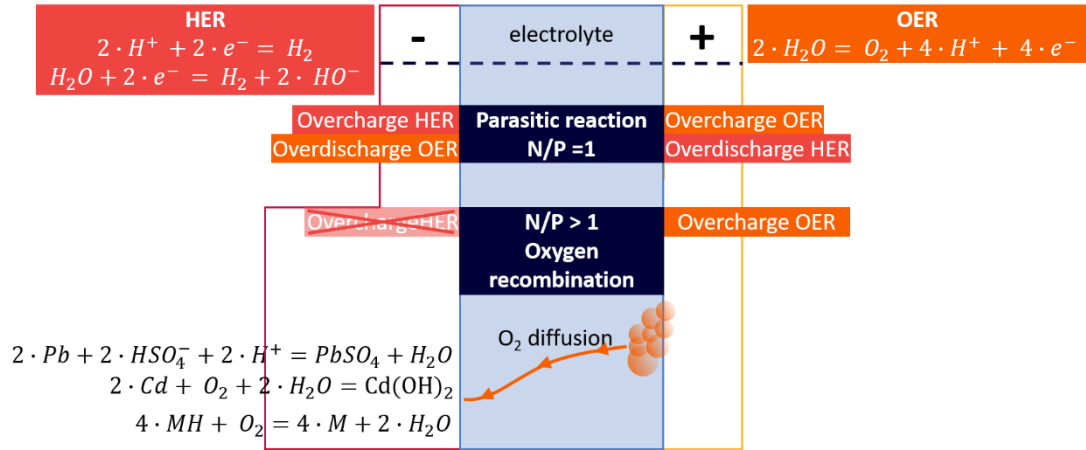


Figure 3. 17 Some parasitic reactions taking place in lead-acid, Ni-Cd and Ni-MH batteries. N/P ratio correspond to the capacity balance between the positive and the negative electrode.

However, altogether the development of these different concepts would (i) need electrolyte refill to avoid drying-out of the cell or (ii) require the use of catalysts to recombine water from O_{2(g)} and H_{2(g)} and/or (iii) of a gelified electrolyte to improve gas diffusion. Therefore, these constraints would impose drastic limitations regarding both the operating voltage as well as the charging rate for WiSE-based aqueous batteries. Indeed, both increasing the operating voltage and increasing the charging rate would lead to increased kinetics for gas generation. For instance, as observed for Ni-Cd batteries, water recombination catalysts can only handle a certain amount of gas, which limits the charging to 0.1C. Moreover, the water recombination in these aqueous devices requires a sufficient amount of oxygen to allow recombination. Indeed, these systems rely on the paradox that a too good positive electrode for which no oxygen is released would not allow for the water recombination at the negative electrode. However, as evidenced in our study, while hydrogen is produced in parallel with Li⁺ intercalation at the negative electrode during charge, almost no oxygen is released at the positive electrode at room temperature. This unbalanced generation of gases between the positive and the negative electrode towards the generation of hydrogen, which is not encountered for other aqueous devices, drastically limits the possibility of water recombination in WiSE-based aqueous batteries, eventually leading to severe drying-out issues for the battery.

Furthermore, another major drawback of WiSE-based batteries is the narrow operating temperature range. Indeed, crystallization of the electrolyte may occur at room temperature. Even though several anions have been considered to downshift the crystallization point^{180,181,183,187}, as discussed in chapter 1, the question of the cost, scalability and the competitiveness of the superconcentrated aqueous electrolyte will be raised. With this in mind, reducing further the amount of water by increasing the amount of lithium salt in the electrolyte does not appear as a viable solution for applications competing with Li-ion batteries since the SEI instability is not suppressed by the use of bisalt superconcentrated electrolytes.

Finally, for grid applications, the capacity fading of WiSE-based batteries must be limited over time. However, as shown in our work, the second intercalation plateau of Mo_6S_8 corresponding to 75 % of the total capacity of the material is completely lost after a resting period of 300 to 800 hours, depending on the C-rate employed during cycling. Thus, capacity fading in the order of 30 to 75% per month is deduced for this specific configuration, which must be compared with capacity fading of 2-10 % measured for aprotic Li-ion batteries, 1-15 % for Lead-acid batteries, 15-30 % for Ni-MH and 10-20 % for Ni-Cd, bearing in mind that some can be recovered for commercial Ni-Cd and Ni-MH aqueous systems as well as for WiSE-based system. Thus, without further improvement to the current technology and the finding of optimized pre-cycling conditions, WiSE-based aqueous batteries cannot currently be regarded as a viable option for grid electricity storage.

As a summary, the SEI formed in these superconcentrated electrolytes is not protective enough to prevent the electrolyte degradation during cycling and resting period, more specifically to avoid water reduction and hydrogen generation. Based on these experimental results, we provide the figure of merit for WiSE-based Li-ion battery that we compared to that of classical Li-ion battery and commercial aqueous system such as Lead-acid, Ni-Cd or Ni-MH. Doing so, it clearly appears that while WiSE-based batteries share the energy efficiency of aprotic Li-ion batteries, owing to similar intercalation reactions, it only offers the energy density and the specific energy of Ni-MH batteries. However, WiSE-based batteries show poorer temperature stability than either systems. Furthermore, the continuous electrolyte consumption occurring both on charge and upon self-discharge for WiSE-based batteries may lead to the drying-out of the cell. Our analysis further revealed that owing to the lack of oxygen generation upon charge, the implementation of a gas recombination cycle in WiSE-based cells as used for other aqueous battery applications might be complex. Therefore, superconcentrated

aqueous electrolyte are currently not able to compete with commercialized aqueous systems for grid storage application until means to prevent the HER at the negative electrode can be found and benchmarked in practical conditions. This calls for the design of stable SEI as reported. Toward this goal, Chapter 4 will focus on the stability of artificial SEI based either on inorganic coatings while the perspectives of this thesis will tackle polymeric ones.

CHAPTER 4 –MIMICKING INORGANIC-BASED SEI WITH LIF-COATING. UNDERSTANDING OF INORGANIC SEI LIMITATIONS IN *WATER- IN-SALT* ELECTROLYTE².

² This chapter is based on the article that I co-authored: Droguet, L.; Hobold, G. M.; Lagadec, M. F.; Guo, R.; Lethien, C.; Hallot, M.; Fontaine, O.; Tarascon, J.-M.; Gallant, B. M.; Grimaud, A. Can an Inorganic Coating Serve as Stable SEI for Aqueous Superconcentrated Electrolytes? *ACS Energy Lett.* **2021**, 6 (7), 2575–2583. <https://doi.org/10.1021/acsenergylett.1c01097>.

Introduction

Developing stable SEIs in aqueous media has been at the forefront of research for aqueous Li-ion batteries (LIB) and other aqueous technologies such as electrochemical capacitors (based on carbon or pseudocapacitive electrodes) or Na-ion batteries^{58,111,117,164}. As described in Chapter 1, one major advance was the introduction of superconcentrated aqueous electrolytes in which salt molecules exceed water molecules both in volume and in mass. Indeed, in these so-called WiSE or WiBS^{58,122}, almost all water molecules contribute to the solvation sphere of Li^+ , allowing for a strong ion-pair interaction between solvated Li^+ cations and organic anions such as TFSI⁻ or its derivatives. However, as shown in Chapter 2 and 3 of this manuscript, the atypical solvation structure does not suppress the reduction of water at the negative electrode. Nonetheless, the reactivity of the $-\text{CF}_3$ terminal groups of TFSI⁻ anions present at the interface is unlocked, which triggers the formation of LiF and passivate, at least partially, the negative electrode^{134,146–148}. Therefore, contrary to organic LIB electrolytes, where the decomposition of both the solvent molecules and salt anions results in a native SEI layer containing both inorganic (LiF, Li_2CO_3 , Li_2O , etc.) and organic/oligomeric species^{240,241}, for superconcentrated aqueous electrolytes, the passivation predominantly relies on LiF.

The SEI thickness and density generally vary with the formation step (cycling rate, duration, temperature etc.). Moreover, part of the SEI can be dissolved. This raises the question of whether the water reduction observed in the previous chapters upon rest originates from the morphology and porosity of the deposited LiF layer or from its intrinsic solubility and/or instability in aqueous superconcentrated electrolyte. To decide between these two options, in this Chapter, we first assessed the LiF solubility limit in aqueous electrolytes as a function of LiTFSI salt concentration. Then, we studied the stability of a conformal LiF layer deposited onto metallic Li anode as a proxy to mimic the formation of a native SEI. First, by using environmental scanning electron microscopy (E-SEM), we tested LiF protection against moisture. Second, we assessed its stability against two aqueous superconcentrated electrolytes (20 m LiTFSI and 20 m LiTFSI : 8 m LiBETI) using gas chromatography and compared it to insoluble Al_2O_3 coating prepared onto metallic Li. Eventually, by using presoaking step in organic solvent/electrolyte, we analyzed the importance of salt/solvent-derived species to ensure self-passivation and maintain stable the SEI. The outline of this chapter is illustrated in Figure 4. 1.

Throughout this Chapter, because of practical considerations in terms of energy density gain, we focused our attention on metallic Li anode rather than on the classically used Mo_6S_8 anodes, bearing in mind that the kinetics for electrolyte reduction will be greatly enhanced together with accompanied gas generation. Hence, it provides an accelerated approach to pinpoint the weaknesses of any SEI layer composed of LiF which will eventually appear during cycling of anode materials.

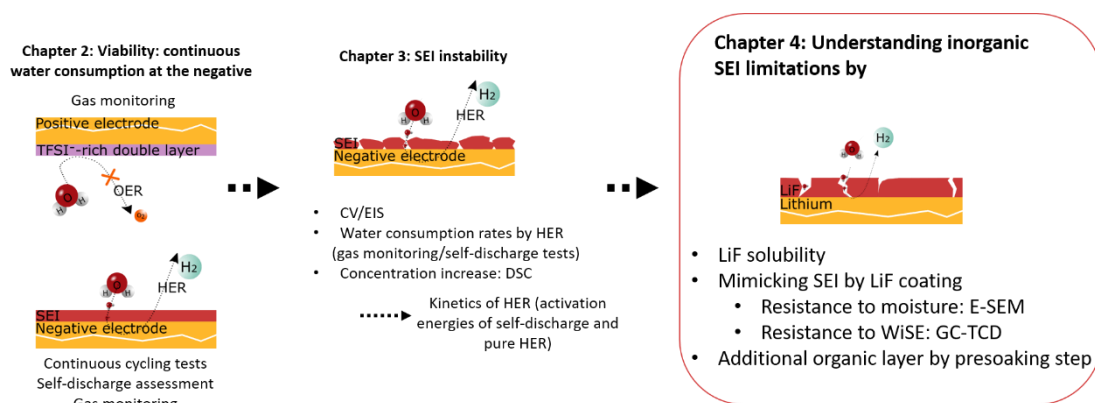


Figure 4. 1 Illustration of the outline of Chapter 4 based on the results discussed in chapter 2 and 3.

1 LiF solubility limit in aqueous superconcentrated electrolyte

The solubility limit of lithium fluoride is well-known in pure solvents (note that solubility limit measurements are performed at thermodynamic equilibrium). It is notably greater in water than in most carbonate solvents, with the exception of EC (see Table 4. 1).

Table 4. 1 LiF solubility limit found in literature in various solvents: water, ethylene carbonate (EC), dimethyl carbonate (DMC), propylene carbonate (PC). One can note that the difference in solubility limit of two orders of magnitude in DMC was explained by differences in the protocol, especially regarding the filtration technique as detailed in Chapter Materials and Methods.

Solvent	LiF solubility at 25 °C (g/L)	LiF solubility at 40 °C (g/L)
H ₂ O	1.11 ²⁴²	1.20 ²⁴²
DMC	0.57 ²⁴² $4 \cdot 10^{-3}$ ²⁴³	
PC	0.14 ²⁴²	0.21 ²⁴²
EC		5.52 ²⁴²

Nonetheless, very little is known regarding the solubility limit of LiF as a function of salt concentration. The common-ion effect arising from the dissolved Li-salt is believed to lower the solubility of LiF in superconcentrated aqueous electrolytes. In order to probe this effect, the solubility limit of LiF was directly measured in aqueous electrolytes as a function of the LiTFSI salt concentration using a fluoride ion selective electrode (ISE) and following the protocol developed by Strmcnik et al.²⁴⁴ illustrated in Figure 4. 2a (details are given in Chapter Materials and Methods). As shown in Figure 4. 2b, the LiF solubility limit was observed to decrease from pure water (0.93 g/L) down to $1.9 \cdot 10^{-3}$ and $1.5 \cdot 10^{-3}$ g/L for 20 m LiTFSI and 20 m LiTFSI : 8 m LiBETI aqueous electrolytes at 23 °C, respectively.

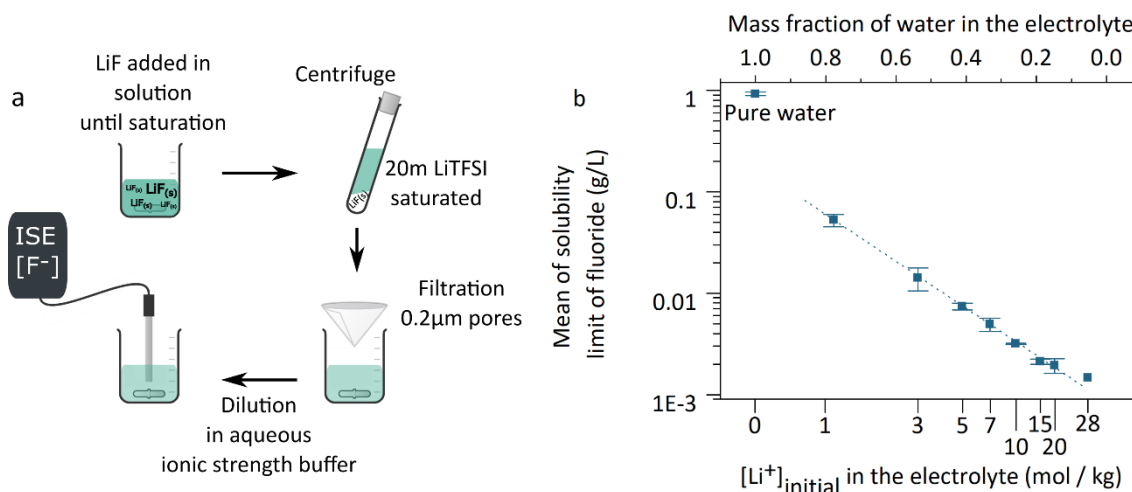
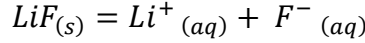


Figure 4. 2 (a) Schematic explanation of the protocol used to measure LiF solubility, further details are provided in the chapter Materials and Methods. (b) Solubility limit of LiF in saturated aqueous solutions measured in pure water and at different LiTFSI concentration ranging from 1m to 20m (WiSE) as well as for 20 m LiTFSI : 8 m LiBETI (WiBS). The dashed line is a guide to the eyes.

Considering the reaction described in Equation 4. 1, the constant of dissolution of LiF –K_s– in an aqueous solution can be expressed following Equation 4. 2.

Equation 4. 1:



Equation 4. 2:

$$K_s = a_{Li^{+}} a_{F^{-}} = \gamma_{Li^{+}} [Li^{+}] \cdot \gamma_{F^{-}} [F^{-}] = \gamma_{Li^{+}} \gamma_{F^{-}} \cdot [Li^{+}] [F^{-}]$$

Due to LiF stoichiometry, the product of the activity coefficients of ions in solution – $\gamma_{Li^{+}} \gamma_{F^{-}}$ can be defined as the square of the mean ionic activity coefficient of the salt²⁴⁵ *i.e.* $\bar{\gamma}_{Li^{+}F^{-}}^{-2}$ as expressed in Equation 4. 3. Therefore, Equation 4. 2 becomes Equation 4. 4.

Equation 4. 3:

$$\gamma_{Li^{+}} \gamma_{F^{-}} = \bar{\gamma}_{Li^{+}F^{-}}^{-2}$$

Equation 4. 4:

$$K_s = \bar{\gamma}_{Li^{+}F^{-}}^{-2} \cdot [Li^{+}] [F^{-}]$$

Besides, the fluoride and lithium ions concentration can be expressed according to Equation 4. 5.

Equation 4. 5

$$[Li^{+}] = [Li^{+}]_{electrolyte} + [Li^{+}]_{lim} \text{ and } [F^{-}] = [F^{-}]_{lim} \\ \text{with } [Li^{+}]_{lim} = [F^{-}]_{lim}$$

where $[Li^{+}]_{electrolyte}$ (mol/L) is the initial concentration of Li⁺ cation due to the LiTFSI concentration in solution (*i.e.* the molarities corresponding to the following molalities: 1 m, 3 m, 5 m, 7 m, 10 m, 15 m, 20 m), $[F^{-}]_{lim}$ (mol/L) is the solubility limit of fluoride measured by the ISE electrode and $[Li^{+}]_{lim}$ (mol/L) is the concentration of Li⁺ cation added during the LiF dissolution in the electrolyte. Considering the high initial $[Li^{+}]_{electrolyte}$ in the bulk electrolyte (> 1 m *i.e.* 0.87 M) and the measured fluoride solubility limit (< 1 g / L *i.e.* 0.05 mol / L), $[Li^{+}]$ can be simplified as follow:

Equation 4. 6:

$$[Li^{+}] = [Li^{+}]_{electrolyte}$$

Therefore, Equation 4. 4 is simplified in Equation 4. 7.

Equation 4. 7:

$$[F^-]_{lim} = \frac{K_s}{\bar{\gamma}_{Li^+F^-} \cdot [Li^+]_{electrolyte}}$$

with K_s the constant of solubility, $\bar{\gamma}_{Li^+F^-}$ the mean activity coefficient of the LiF salt and $[Li^+]_{electrolyte}$ (mol/L) the initial concentration of lithium in the electrolyte.

As theoretically described by McEldrew *et al.*²⁴⁶, the logarithm of the mean activity coefficient $\log(\bar{\gamma}_{Li^+F^-})$ increases with the molality. Therefore, even without knowing the effect of the molality and thus of the solvation structure on K_s , the decrease of solubility limit observed in Figure 4. 2b is consistent with the common ion effect and the increase of activity coefficient, which are both related to the increase of molality. Moreover, taking into consideration these theoretical results by McEldrew *et al.*²⁴⁶, one can rescale the logarithm of the activity coefficient as function of the molarity rather than the molality. Doing so, a linear trend is obtained, as shown in Figure 4. 3.

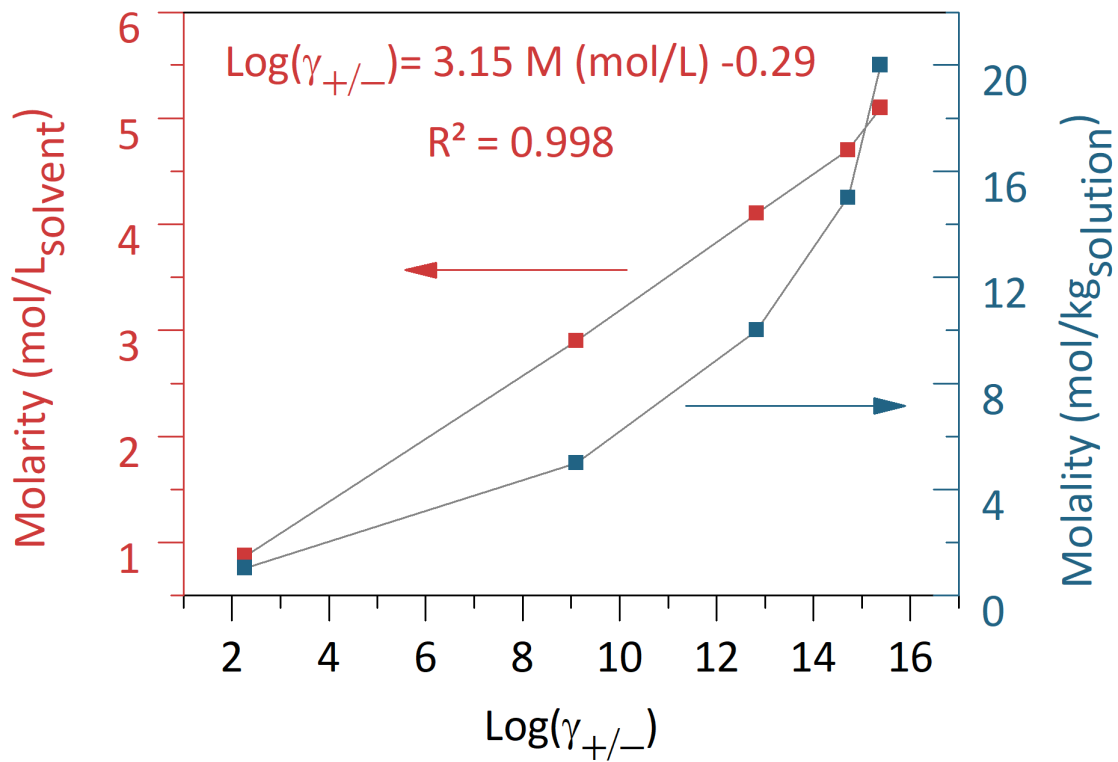


Figure 4. 3 Molarity (mol/L_{solvent}) (red line) and molality (mol/kg_{solution}) (blue line) as function of the logarithm of the activity coefficient of a salt. Data extracted from Ref²⁴⁶ and rescaled vs molarity.

$\text{Log}(\bar{\gamma}_{Li^+F^-})$ can thus be expressed according to Equation 4. 8.

Equation 4. 8:

$$\text{Log}(\bar{\gamma}_{Li^+F^-}) = 3.15 \cdot [Li^+]_{electrolyte}^{mol/L} - 0.29$$

with $R^2 = 0.998$

Besides, applying $_{10}\log$ function to Equation 4. 7, one can obtain Equation 4. 9.

Equation 4. 9:

$$\log([F^-]_{lim}) = \log(K_s) - 2 \log(\bar{\gamma}_{Li^+F^-}) - \log([Li^+]_{electrolyte})$$

In Equation 4. 9, considering K_s as a constant and replacing $\log(\bar{\gamma}_{Li^+F^-})$ by its expression described in Equation 4. 8, one can find Equation 4. 10.

Equation 4. 10:

$$\log([F^-]_{lim}) = C - A \cdot [Li^+]_{electrolyte} - B \cdot \log([Li^+]_{electrolyte})$$

where $[Li^+]_{electrolyte}$ is the initial concentration of Li^+ in the electrolyte, A, B and C constant values, C being proportional to K_s .

Thus, comparison between experimental data and fitted ones can be done as shown in Figure 4. 4a and described in Equation 4. 11. Details of fitted parameters are given in Chapter Materials and Methods.

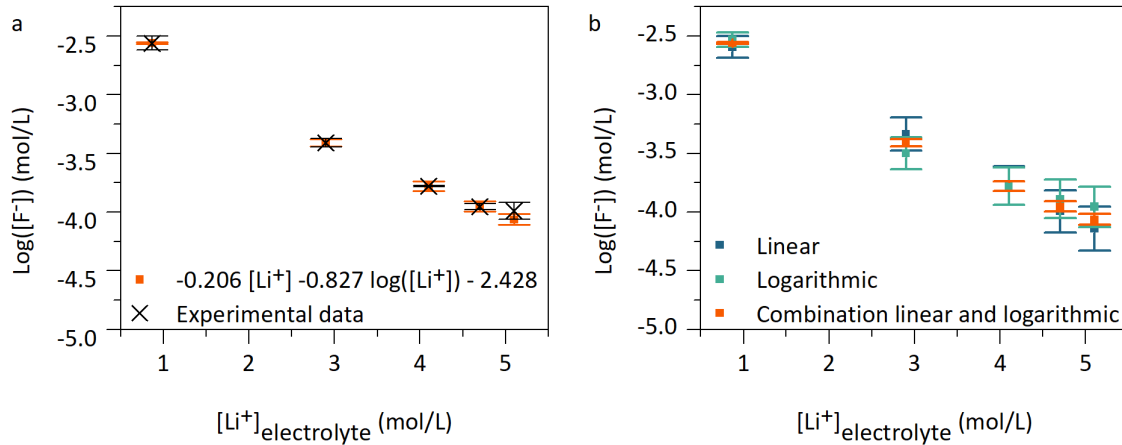


Figure 4. 4 Logarithm of the limit of solubility of fluoride as function of initial concentration $[Li^+]_{electrolyte}$ (mol/L) in the electrolyte. (a) Comparison between experimental data (black cross) and combination fit (orange). (b) Comparison between three fits: linear fitting (blue), logarithmic fitting (green), combination (orange).

Equation 4. 11:

$$\text{Log}([F^-]_{lim}) = -0.206 \cdot [Li^+]_{electrolyte} - 0.827 \log([Li^+]_{electrolyte}) - 2.428$$

First, fitted values and experimental data are in good agreement, with interception of their standard deviation range. Besides, K_s that is related to the intercept of the equation can be determined to be: $K_{s_{fit}} = 10^{-2.428} = 3.7 \cdot 10^{-3}$. This value is consistent with K_s calculated by approximating the activity coefficients (a_{Li^+} and a_{F^-}) by $[Li^+]_{lim}$ and $[F^-]_{lim}$ and taking into account LiF solubility in pure water (0.93 g/mol *i.e.* $3.7 \cdot 10^{-2}$ mol /L) *i.e.* $K_{s_{dilute\ solution}} = [F^-]_{lim}^2 \approx 1.4 \cdot 10^{-3}$.

Nonetheless, although the theoretical relationships can be simplified as a combination of $[Li^+]_{electrolyte}$ and $\log[Li^+]_{electrolyte}$, pure linear (see Equation 4. 12) or pure logarithmic fits (see Equation 4. 13) as shown in Figure 4. 4b also give good results with the interception of their standard deviation range and good assessment of K_s value. Therefore, we must acknowledge that determining an accurate equation for the expression of the solubility limit as a function of the electrolyte molarity must be trickier than these simple calculations.

Equation 4. 12:

$$\begin{aligned} \text{Log}([F^-]_{lim}) &= -0.366 \cdot [Li^+]_{electrolyte} - 2.274 \\ K_{s_{linear\ fit}} &= 10^{-2.274} = 5.3 \cdot 10^{-3} \end{aligned}$$

Equation 4. 13:

$$\begin{aligned} \text{Log}([F^-]_{lim}) &= -1.854 \cdot \log([Li^+]_{electrolyte}) - 2.6426 \\ K_{s_{logarithmic\ fit}} &= 10^{-2.6426} = 2.3 \cdot 10^{-3} \end{aligned}$$

2 Using Li/LiF-coating to mimic inorganic-based SEI. Exposure to atmosphere environment, aqueous superconcentrated electrolyte and comparison with the behavior observed in organic electrolyte³

Having established that the LiF solubility limit is drastically decreased in WiSE, we focused our attention on the ability for LiF to protect a negative electrode against

³ E-SEM images were performed by Marie-Francine Lagadec from Chaire chimie du solide et de l'énergie, Collège de France, Paris. Gustavo M. Hobold and Betar Gallant from the Department of mechanical engineering, MIT, Cambridge, carried out Li/LiF SEM images and GC-TCD/FID experiments.

reacting with water. To do so, a LiF artificial coating was prepared to mimic the native LiF-rich SEI formed on the surface of anode materials in WiSE. Briefly, during the Li/LiF sample preparation, the metallic Li is rolled on a current collector and then exposed to NF_3 gas at 175 °C, just below the melting temperature of Li, under mild conditions (further details are provided in Chapter Materials and Methods). As shown in Figure 4. 5a by cross section view, the LiF layer thickness is estimated to be ≈ 30 nm. Such a LiF thickness may be considered as representative of a native SEI. Indeed, as observed by SEM and TEM experiments^{111,122,247,248}, the thickness of a native LiF-based SEI is ≈ 10 nm. Moreover, as previously demonstrated²⁴⁹ and observed in Figure 4. 5b and c, homogenous and conformal deposits are realized. Thus a complete LiF coating is formed and protects the metallic Li when further exposed to moisture or electrolytes.

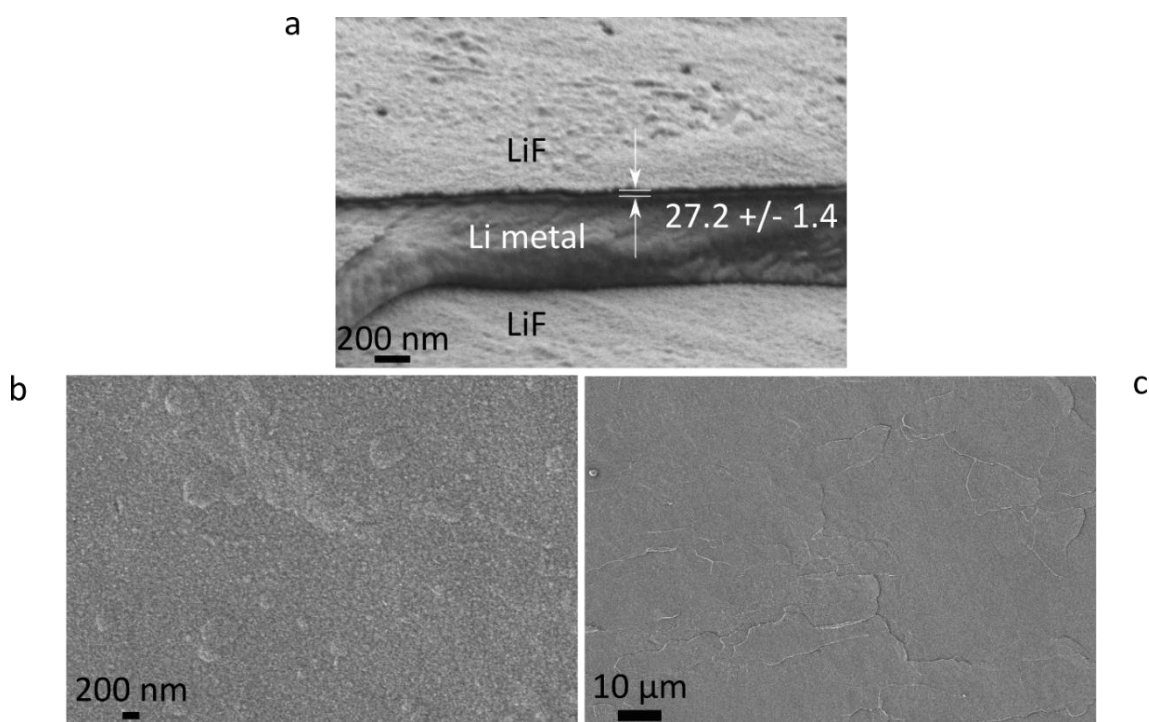


Figure 4. 5 Scanning electron microscopy (SEM) images (a) Cross section SEM image of a Li/LiF pristine sample. Top-view SEM images of a Li/LiF pristine sample, (b) high magnification, (c) low magnification.

The thickness of the LiF coating layer as observed by SEM was compared with the amount of $[\text{F}^-]$ measured after full dissolution of the LiF layer. Doing so, agreement is met with a thickness of 30 nm, with a deviation of less than 1 %, as described in Table 4.2 (Calculation and protocol details are provided in Chapter Materials and Methods).

Table 4. 2 Fluoride concentration measurement after complete dissolution of a Li/LiF sample. Comparison with expected concentration based on SEM observation. Assumptions are the following: Li/LiF sample with 30 nm thickness, 1.27 cm diameter.

Volume of the solution in which sample is dissolved (mL)	[F ⁻] expected (mg/L)	[F ⁻] measured by ISE (mg/L)	Relative deviation (%)	Temperature (°C)	pH of the solution
125	0.0803	0.0805	0.25	19	5.79
150	0.0669	0.0671	0.3	19.3	5.74

Eventually, owing to this nanoscale thickness, the LiF layer cannot be detected by laboratory XRD. However, previous demonstration was made by our collaborators (see He *et al.*²⁴⁹) that thicker layers grown using a similar methodology but with longer reaction times are polycrystalline.

Besides, Figure 4. 6 compares the solubility limit of LiF in aqueous and organic electrolytes with the concentration of fluoride calculated for the complete dissolution of the 30 nm conformal LiF-layer in 250 μ L of electrolyte, *i.e.* a concentration of $2.02 \cdot 10^{-2}$ g/L. Doing so, one can infer that in diluted aqueous electrolytes, the conformal LiF-layer would be able to dissolve, unlike in superconcentrated aqueous electrolyte and (1,3-dioxolane:dimethoxyethane) DOL:DME or EC:DMC-based electrolyte. This trend is also preserved at 55°C since the LiF solubility increases by less than a factor of 2 ($3.7 \pm 0.4 \cdot 10^{-3}$ g/L in WiSE and $2.9 \cdot 10^{-3}$ g/L in WiBS at 55 °C), so the very limited dissolution still enables practical cycling conditions. This implies that the instability of the LiF-based SEI -either native or artificial- in WiSE should not arise from the complete dissolution of the passivating layer.

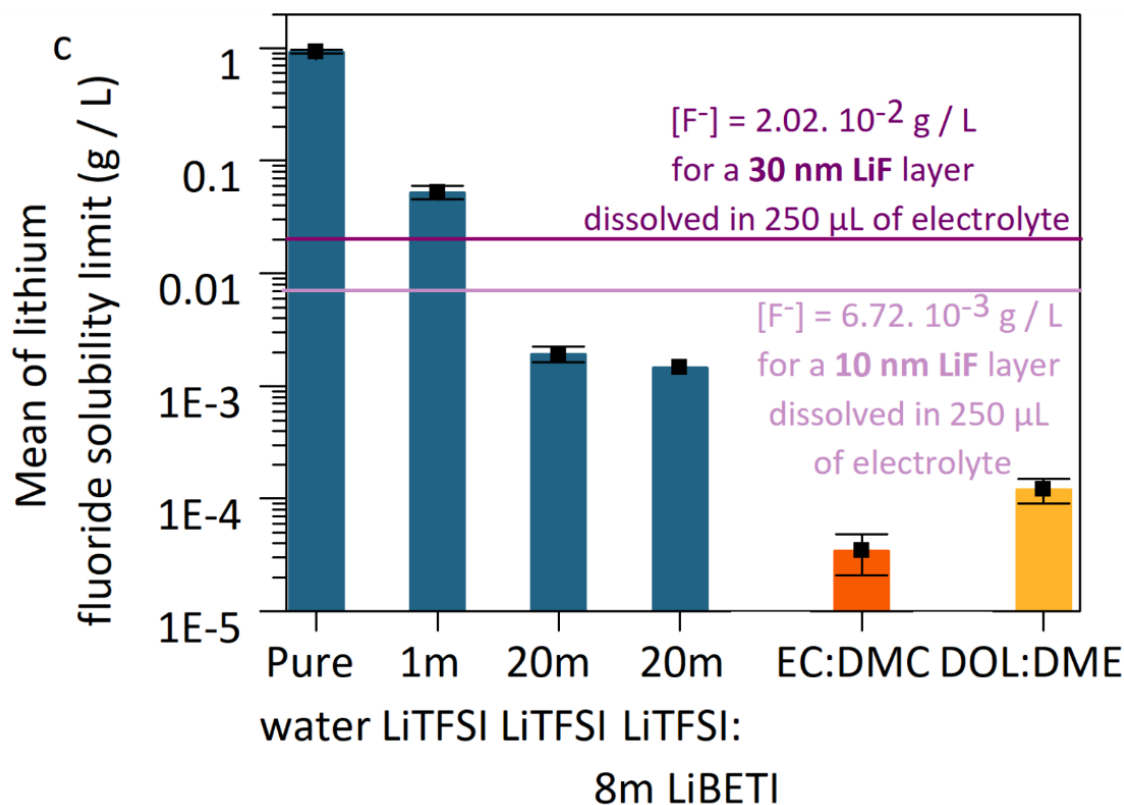


Figure 4. 6 Comparison of the LiF solubility limits measured in different electrolytes: water, 1 m LiTFSI, 20 m LiTFSI, 20 m LiTFSI : 8 m LiBETI, EC:DMC (1:1 vol%), DOL:DME (1:1 vol%). The reference lines indicate the fluoride concentration expected from the complete dissolution of a 0.9 cm diameter and 30 nm thickness layer (dark purple) or a 10 nm thickness (light purple) LiF layer dissolved in 250 µL of electrolyte.

Having established that LiF solubility drastically decreased in WiSE, environmental scanning electron microscopy (E-SEM) was used to assess the protective power of the LiF layer against moisture (see Figure 4. 7). In this experiment, the sample is kept at 20 °C while gradually increasing the relative humidity (RH) of the atmosphere in the chamber from 0 to 90 % RH as illustrated in Figure 4. 7b.

As depicted in Figure 4. 7a, round-shaped particles start forming on the surface of a metallic Li sample as the chamber's RH exceeds 0 %, their occurrence increasing with the increasing RH. On the contrary the LiF-conformal layer protects the metallic Li from reacting with gaseous water below a threshold of 60 % RH. However, approaching water condensation (RH \approx 90 %), the LiF-conformal layer no longer plays a protective role and similar (but larger) round-shaped particles are observed alike for bare metallic Li. Interestingly, as observed in Figure 4. 7a and illustrated in Figure 4. 7c, reactivity can first be observed at cracks and pits formed in the LiF layer, suggesting that microstructural defects inherently present in the artificial SEI lead to reactions of the

underlying Li layer with moisture. However, testing Li/LiF samples resistance to moisture is still far from the potential impact of aqueous superconcentrated electrolyte when in contact with Li/LiF, therefore Li/LiF behavior in aqueous superconcentrated electrolyte was then studied.

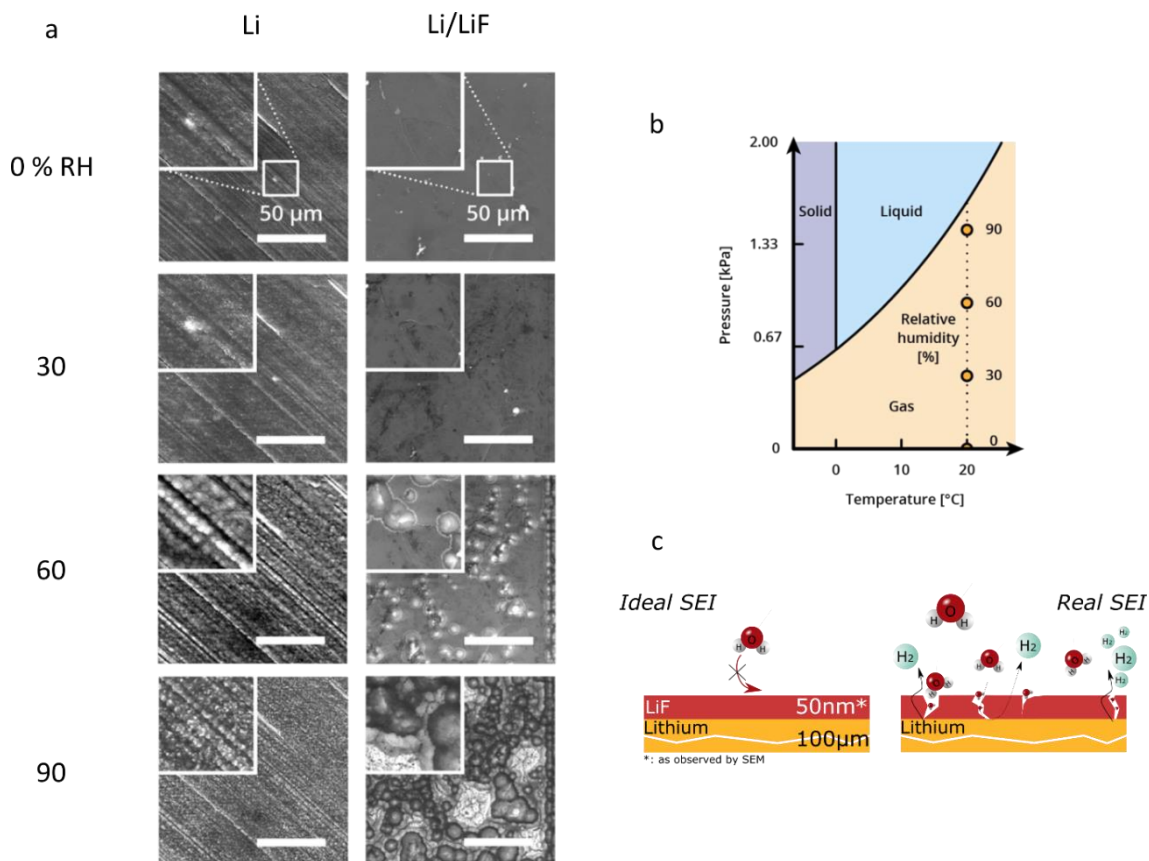


Figure 4. 7 (a) E-SEM images of bare Li and Li/LiF samples exposed to moisture. (b) Phase diagram for pure water, illustrative scheme of the E-SEM operation. (c) Scheme of an ideal and a real SEI exposed to moisture.

Our attention then turned to the chemical stability of the LiF-coated metallic Li samples in both superconcentrated electrolytes, 20 m LiTFSI and 20 m LiTFSI : 8 m LiBETI. For that, Li/LiF samples were exposed to various electrolytes while monitoring the gas evolution by gas chromatography with thermal conductivity/flame ionization detectors (GC-TCD/FID), as shown in Figure 4. 8.

First, for comparative purposes, we determine the gas evolution when a Li/LiF sample is exposed to organic LP30 electrolyte for which the total amount of gas released (Figure 4. 8a) originates from the decomposition of carbonates, *i.e.* CO, CO₂, C₂H₄ and CH₄ as shown in Figure 4. 8b. It stabilizes after 30 minutes at a very low value of approximately $0.5 \cdot 10^{-2} \%$ in the headspace (the rest being argon), which is close to the detection limit

of the GC-FID instrumentation. Hence, even though minute cracks exist in the LiF-conformal layer, the exposition of bare Li to LP30 eventually leads to the formation of some polymeric/oligomeric structures that passivate the electrode^{250,251} and prevent further gas evolution, explaining the decrease of gas detected over time (inset in Figure 4. 8a).

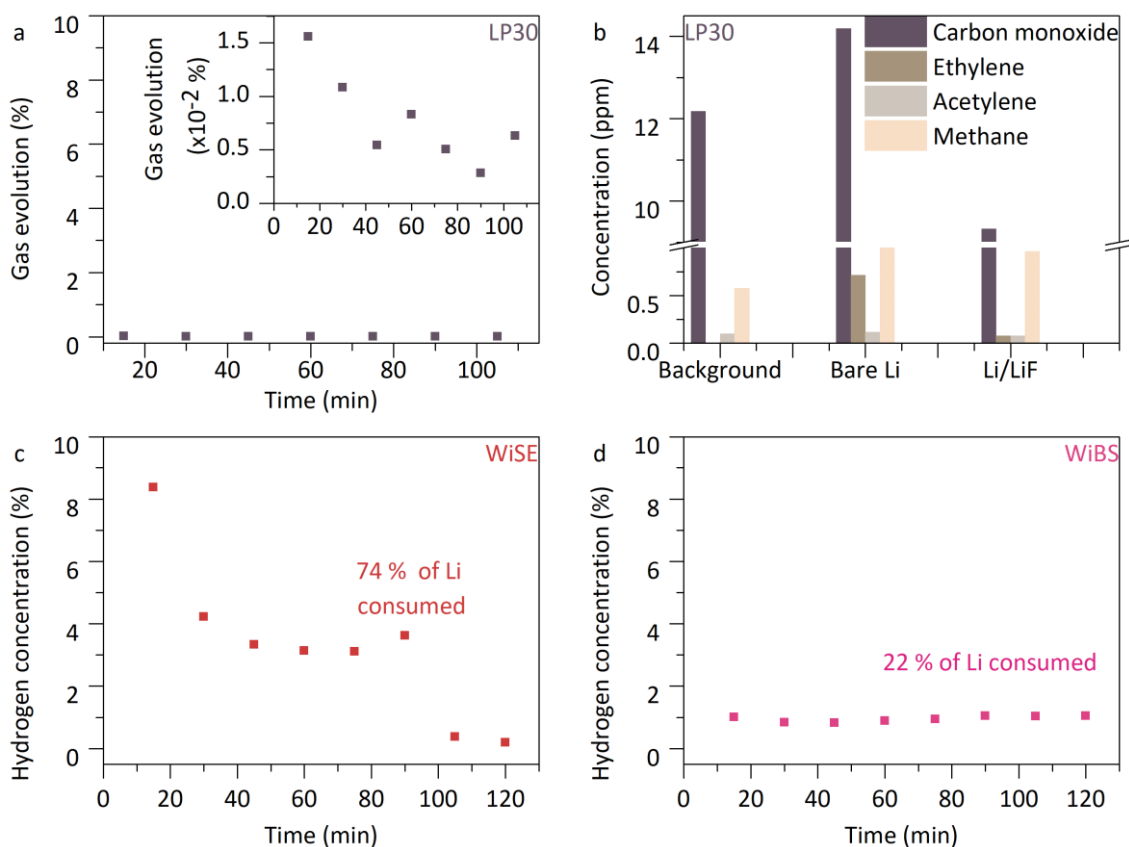


Figure 4. 8 (a) Gas evolution as a function of time for Li/LiF samples during exposure to 1M LiPF₆ in EC:DMC (LP30). The gas evolution is the sum of all gases detected in (b). (b) Concentration in Carbon monoxide (dark brown), ethylene (light brown), acetylene (grey) and methane (flesh color) when exposing Li/LiF or bare metallic Li samples to LP30 electrolyte during 15 min. Hydrogen evolution as a function of time for Li/LiF samples upon exposure to (c) 20 m LiTFSI and (d) 20 m LiTFSI : 8 m LiBETI.

In contrast, a large amount of hydrogen ($\approx 8\%$) of the sampled gas is detected with a LiF-protected metallic Li sample exposed to 20 m LiTFSI electrolyte (see Figure 4. 8c). This amount then stabilizes at $\approx 4\%$ before vanishing after 100 minutes when almost all the metallic Li is consumed. Indeed, as described in Table 4. 3, a hydrogen molar ratio of 26.35 % is detected after 120 min, which corresponds to 182 μmol of hydrogen produced and thus $\approx 80\%$ of total Li consumption (calculation parameters are given in Table M.M. 5 in Chapter Materials and Methods). Similarly, when exposing the Li/LiF sample to 20 m LiTFSI : 8 m LiBETI, hydrogen is detected with a concentration of $\approx 1\%$.

Unlike for the 20 m LiTFSI solution, this concentration remains constant throughout the measurement, leading to a consumption of $\approx 22\%$ of metallic Li after 2 hours. Eventually, such continuous hydrogen evolution indicates that, unlike for carbonate-based electrolytes, no self-passivation occurs in superconcentrated aqueous electrolytes.

Table 4. 3 Consumption of Li after exposure to 20 m LiTFSI (WiSE) or 20 m LiTFSI : 8 m LiBETI for the Li/LiF samples.

Li/LiF pristine exposed to	Molar ratio of H ₂ (after 120 min) $x_{\text{Hydrogen}}(\%)$	Amount of H ₂ released (after 120 min) $n_{\text{Hydrogen}}(\mu\text{mol})$	Ratio of Li consumed (after 120 min) (%)
20 m LiTFSI	26.35	182	74
20 m LiTFSI : 8 m LiBETI	7.63	53	22

Altogether these GC-TCD results indicate that aqueous electrolyte reaches the underlying metallic Li electrode through microstructural defects, *i.e.* cracks or grain boundaries, which have previously being observed for native SEI formed in superconcentrated aqueous electrolytes by SEM and TEM experiments^{111,122,247,248}. Moreover, kinetics for water reduction is not drastically impacted by the salt concentration⁷ and the amount of water contained in 250 μL of aqueous superconcentrated electrolytes does not limit the reaction (0.489 mmol of metallic Li available per Li/LiF sample compared to 3.49 mmol of water, see Chapter Material and Methods for detailed calculations). Thus, one can hypothesize that the greater the viscosity of the electrolyte, ($\eta_{\text{WiBS}} = 203 \text{ mPa}$ at 30 °C⁵⁸ and $\eta_{\text{WiSE}} = 36.2 \text{ mPa}$ at 25 °C¹¹¹), the slower the electrolyte penetrates through minute cracks present in the LiF layer, thus explaining the differences of Li-water reactivity between the two superconcentrated aqueous electrolytes.

3 Comparison of LiF behavior with Al₂O₃-coated Li sample⁴

One legitimate question arising from this study regards the quality of the LiF layer. We thus compared the protective power of our LiF layer with that of a conformal Al₂O₃ layer prepared by atomic layer deposition (ALD), previously proposed to allow for

⁴ Li/Al₂O₃ coatings were provided by Christophe Lethien and Maxime Hallot from the University of Lille. GC-TCD experiments were done by Gustavo M. Hobold and Betar Gallant from the Department of mechanical engineering, MIT, Cambridge.

passivation of anode materials in WiSE as Al_2O_3 is not soluble in water^{205,207}. Using a similar approach combining E-SEM (see Figure 4. 9) and GC-TCD (see Figure 4. 10), evolution of hydrogen upon consumption of the underlying Li electrode is once again observed as summarized in Table 4. 4.

Table 4. 4 Consumption of Li after exposure of Al_2O_3 -coated metallic Li exposed to 20 m LiTFSI or 20m LiTFSI : 8 m LiBETI.

	Molar ratio of H_2 (after 120min) $x_{\text{Hydrogen}}(\%)$	Amount of H_2 released (after 120min) $n_{\text{Hydrogen}} (\mu\text{mol})$	Ratio of Li consumed (after 120min) (%)
Al_2O_3 -coated metallic Li exposed to 20m LiTFSI	1.15	7.933	18
Al_2O_3 -coated metallic Li exposed to 20m LiTFSI : 8m LiBETI	0.416	2.867	6.4

Environmental-SEM observations were first performed on 2 nm and 10 nm thick Al_2O_3 layers prepared by ALD on the surface of metallic Li, bearing in mind that the native-SEI growing in WiSE is itself in the 10 nm thickness range. Figure 4. 9 shows the images obtained with increasing RH. As seen before exposure to moisture, Al_2O_3 layers prepared by ALD forms a granular and textured coating on the surface of Li, alike the microstructure previously reported elsewhere for a similar coating²⁰⁷. Nevertheless, when gradually increasing the water partial pressure from 0 to 90 % RH, obvious degradations are observed starting at 30 % RH for the 2 nm thick coating (see Figure 4. 9, top row). Bearing in mind that Al_2O_3 does not dissolve in pure water, this change in microstructure from granular to a cauliflower-like may arise from two effects. First, Al_2O_3 can gradually transform to $\text{Al}(\text{OH})_3$, this phase transformation inducing a change in molar volume (from 403 mol/cm³ for Al_2O_3 to 188.8 mol/cm³ for $\text{Al}(\text{OH})_3$, *i.e.* a contraction of 7 % in volume). Second, the granular morphology of the Al_2O_3 coating itself can induce reactivity of the underlying Li electrode associated with the formation of LiOH and/or $\text{LiOH} \cdot \text{H}_2\text{O}$ upon reaction with water. In other words, the granular morphology of the 2 nm Al_2O_3 coating prepared by ALD may not prevent water from accessing Li. Therefore, a thicker coating of 10 nm was then prepared, but similar degradation was observed, with a cauliflower-like structure being formed upon increased relative humidity (see Figure 4. 9, bottom row).

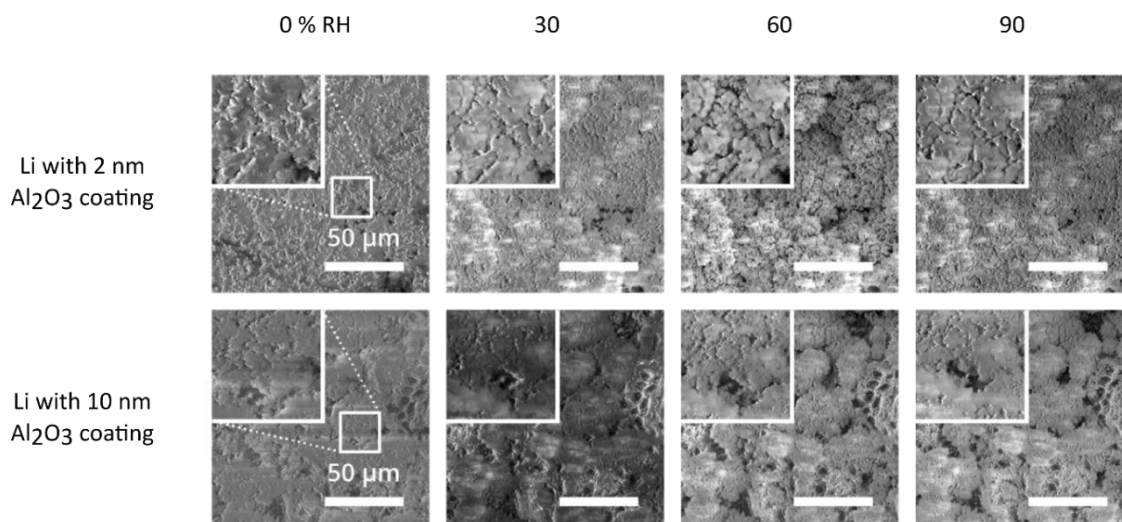


Figure 4. 9 E-SEM images for 2 nm (top) and 10 nm (bottom) Al_2O_3 coated metallic Li taken successively at 0, 30, 60 and 90 % RH with zoom-ins.

To further understand the reactivity of Al_2O_3 -coated metallic Li in contact with superconcentrated aqueous electrolytes, GC-TCD measurements were performed alike the ones carried out for the Li/LiF-protected samples. Upon exposure to 20 m LiTFSI, a constant evolution of hydrogen is observed during two hours with a concentration of ≈ 0.15 % of hydrogen in the headspace (see Figure 4. 10). While this concentration is much smaller than the one previously observed with the Li/LiF sample (see Figure 4. 8c), once normalized by the amount of Li -taking into account the surface and the thickness of the metallic Li electrode- one can estimate that 18 % of the metallic Li was consumed by the reaction. Thus, as observed by environmental-SEM, the conformal coating of Al_2O_3 does not prevent metallic Li from reacting with WiSE aqueous electrolyte but slows down the reaction. Finally, alike for Li/LiF samples, upon exposure to 20 m LiTFSI : 8 m LiBETI electrolyte, the concentration of hydrogen measured by GC-TCD is two to three times lower than that measured in 20 m LiTFSI electrolyte. Nevertheless, the concentration of gas keeps increasing upon measurement, indicating a continuous degradation of the coating and a greater reactivity of the underlying Li electrode. Eventually, 6.4 % of metallic Li is estimated to be consumed after two hours, as summarized in Table 4. 4.

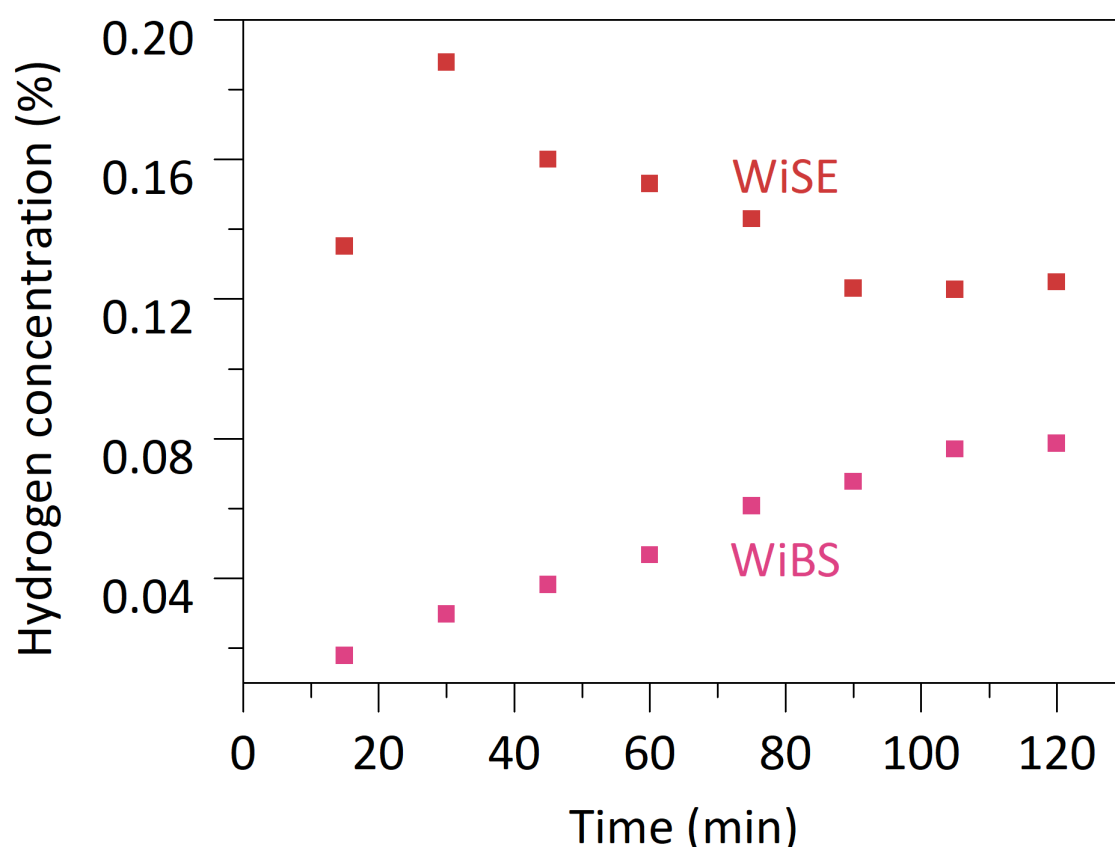


Figure 4. 10 Gas evolution as a function of time for 10 nm Al_2O_3 -coated metallic Li samples after exposure to 20m LiTFSI (red) and 20m LiTFSI : 8m LiBETI (pink) aqueous superconcentrated electrolytes.

To summarize, acknowledging that the high-quality LiF layer prepared in this work, as well as Al_2O_3 prepared by ALD deposition method, will always exhibit some degree of structural defects (cracks, microporosity or else) alike a native SEI which consists of a mosaic of LiF grains^{111,240}, our study highlights that even if the use of superconcentrated aqueous electrolytes prevents the dissolution of the inorganic SEI compounds, these electrolytes are deprived of self-passivating ability through the formation of an organic-inorganic SEI outer layer required to stabilize anode materials.

4 Filling the structural defects by presoaking in organic electrolyte: assessment of the importance of an organic-inorganic based SEI⁵

To overcome the absence of self-passivation, Li/LiF samples were soaked in three organic-based solutions: pure fluoro-ethylene carbonate (FEC) solvent and two electrolytes, namely 7 M LiFSI in FEC and 2 M LiFSI : 1 M LiTFSI in DOL:DME (1:1 %vol) with 3 % LiNO₃ additive, both known for forming good elastomeric passivating SEI with a LiF-rich inner layer and enabling very high Coulombic efficiencies for Li plating/stripping^{252–254}. After soaking, during which any possible defects within the LiF layer may be further passivated by the formation of an additional organic-inorganic layer derived from a non-aqueous electrolyte, the samples are exposed to superconcentrated aqueous electrolyte and hydrogen evolution is measured by GC-TCD (Figure 4. 11).

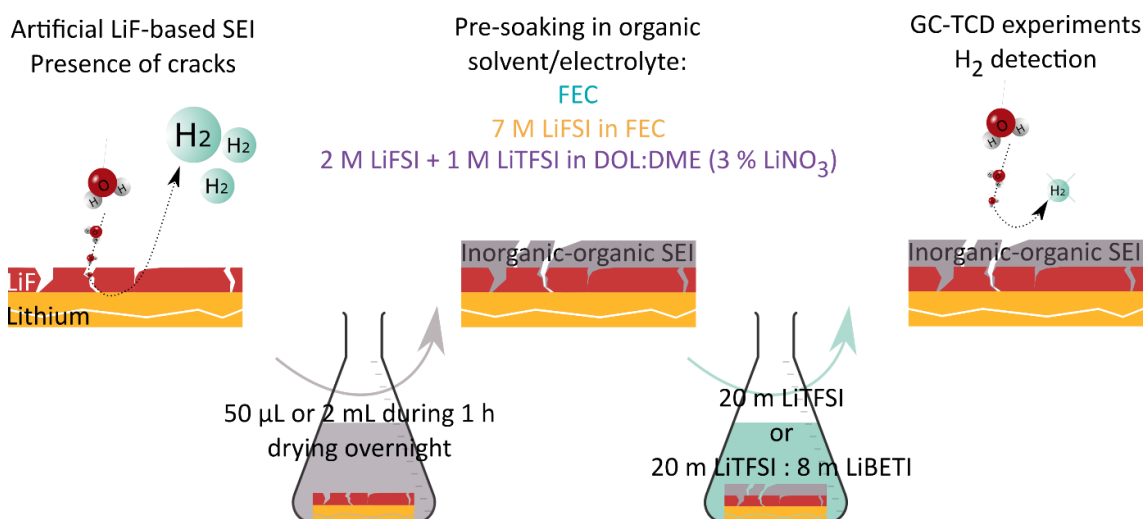


Figure 4. 11 Illustration of the presoaking step in organic solvent/electrolyte, further exposed to aqueous superconcentrated electrolyte.

4.1 Solubility of LiF layer in pure FEC: influence of FEC volume

Hydrogen concentration is measured over time for pristine Li/LiF sample and samples presoaked in 50 µL or 2 mL of FEC further exposed to WiBS (see Figure 4. 12a). First, the

⁵ Gustavo M. Hobold did GC-TCD experiments from the Department of mechanical engineering, MIT, Cambridge. Rui Guo, Gustavo M. Hobold and Betar Gallant from the Department of mechanical engineering, MIT, Cambridge, carried out XPS analysis.

hydrogen concentration measured after presoaking the sample in 50 μL of pure FEC is similar than for the pristine LiF-protected Li sample (22 % of metallic Li consumption for pristine sample vs 19 % for the sample presoaked in 50 μL FEC, see Table 4. 5). Interestingly, when increasing the volume of FEC during the soaking step (from 50 μL to 2 mL), we observe an increase of hydrogen evolution ($\approx 3\%$ after 15 min compared to $\approx 1\%$ for the pristine Li/LiF as shown in Figure 4. 12a) which is translated into an increased metallic Li consumption from 22 % to 55 % (see Table 4. 5). Combining this observation with post soaking XPS analysis (see Figure 4. 12b and c), one can attribute it to the partial dissolution of the LiF layer in FEC as the intensity of both the F 1s and the Li 1s signals decreases for the sample presoaked in 2 mL FEC (see signal [1] on Figure 4. 12b and c).

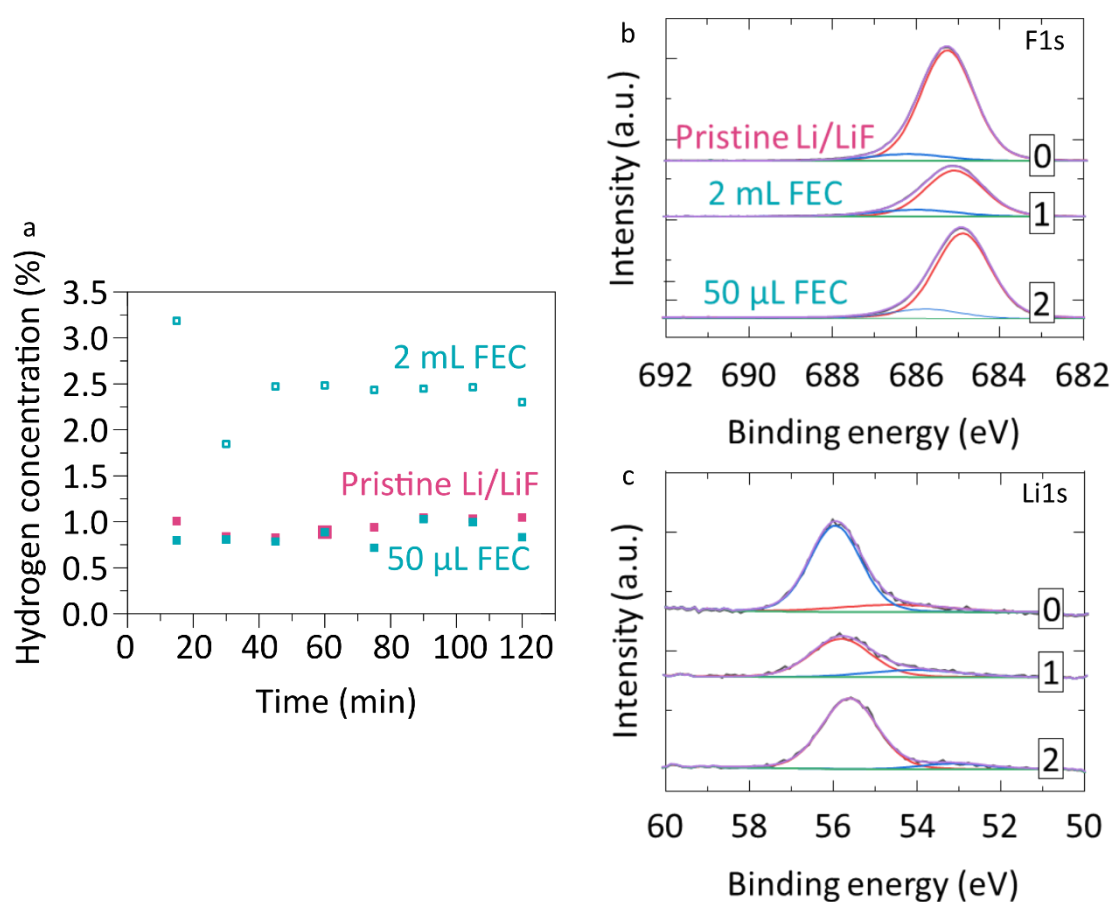


Figure 4. 12 (a) Hydrogen evolution as function of time for pristine Li/LiF sample (pink), presoaked in 2 mL FEC (light blue, empty square), presoaked in 50 μL FEC (light blue, full square) prior to exposure to 20 m LiTFSI : 8 m LiBETI. X-ray photoelectron spectroscopy (XPS) spectrum of (b) F 1s and (c) Li 1s of pristine Li/LiF [0], presoaked Li/LiF sample in 2 mL FEC [1], presoaked Li/LiF sample in 50 μL FEC [2].

Table 4. 5 Consumption of metallic Li after exposure to 20 m LiTFSI : 8 m LiBETI for the Li/LiF sample: pristine, presoaked in 2 mL FEC, presoaked in 50 μ L FEC assuming hydrogen evolution only caused by HER in Li consumption ratio calculation.

Exposure to 20 m LiTFSI : 8 m LiBETI	Molar ratio of H ₂ (after 120min) $x_{\text{Hydrogen}}(\%)$	Amount of H ₂ released (after 120min) $n_{\text{Hydrogen}} (\mu\text{mol})$	Ratio of Li consumed (after 120min) (%)
Li/LiF pristine	7.63	53	22
Li/LiF presoaked in 2 mL pure FEC	19.6	135	55
Li/LiF presoaked in 50 μ L pure FEC	6.85	47	19

Unfortunately, the solubility of the LiF layer in FEC as observed during these experiments could not be correlated with a greater solubility limit for LiF in FEC, as determined in Section 0 by ISE methods for other solvents. Indeed, the main advantage of the fluoride ion selective electrode technique lies in its ability to measure fluoride concentration in organic solvent/electrolyte diluted in an aqueous ionic strength buffer. Hence, Strmcnik *et al.*²⁴⁴ showed that by diluting LP57 (EC/EMC/LiPF₆) in ionic aqueous strength buffer by a factor 100, the hydrolysis of PF₆⁻ anions was quenched. Nonetheless, despite this approach shows good results in LP57, continuous hydrolysis of FEC was observed in the ionic aqueous strength buffer with a continuous increase of the probed [F⁻] concentration for over a week (from ≈ 3 g / L at 23 °C to ≈ 180 g / L at 23 °C for both LiF-saturated or non-LiF-saturated FEC solution after one week). This effect prevented us to determine the solubility limit of fluoride in pure FEC.

4.2 Beneficial impact of presoaking in organic electrolyte

To overcome the dissolution of the LiF coating, samples were then soaked in an ether-based electrolyte (1 M LiTFSI : 2 M LiFSI in DOL:DME + 3 % LiNO₃). As mentioned in section 4.1 and shown in Figure 4. 2, DOL:DME-based electrolyte should not dissolve LiF layer. When exposing this sample to WiBS (see Figure 4. 13a, purple dots), the hydrogen evolution is greater after 15 min (≈ 1.6 %) than for the pristine Li/LiF sample. Nevertheless, the signal rapidly decreases and stabilizes below 1 % of hydrogen detected in the headspace. Overall, after this equilibration period, soaking the Li/LiF anode in 1 M LiTFSI : 2 M LiFSI in DOL:DME + 3% LiNO₃ has a slight positive impact on the gassing, decreasing the metallic Li consumption through hydrogen evolution by 4 % when compared with the pristine Li/LiF sample (see Table 4. 6).

To further study the impact of presoaking in organic electrolyte, we then soaked a Li/LiF sample in an organic superconcentrated electrolyte, namely 7 M LiFSI in FEC, before exposing it to WiBS (see Figure 4. 13a, yellow dots). This soaking step is found to have a beneficial impact and diminishes the hydrogen evolution upon exposure to WiBS, which approaches the detection limit even at the earlier stage of exposure (0.035 % of the total headspace after 15 min). Furthermore, even if the amount of hydrogen detected slightly increases with time, it corresponds to a consumption of metallic Li of only 4 % after two hours considering HER as the sole source for H₂ evolution, compared to 22 % for the pristine Li/LiF sample as described in Table 4. 6.

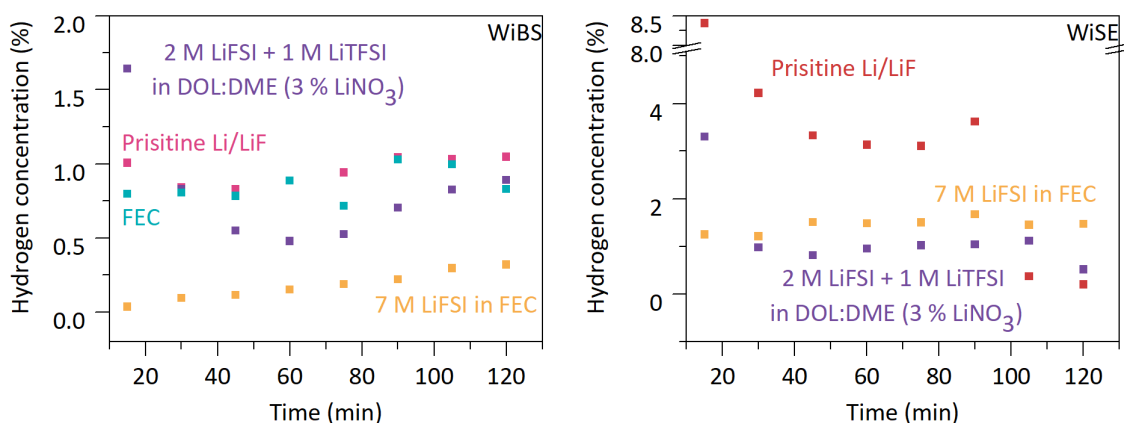


Figure 4. 13 Hydrogen evolution as function of time for Li/LiF samples. Li/LiF presoaked in pure FEC (light blue), Li/LiF presoaked in 7 M LiFSI in FEC (yellow) or presoaked in 2 M LiFSI : 1 M LiTFSI in DOL:DME (purple) prior to exposure to (a) 20 m LiTFSI : 8 m LiBETI with pristine Li/LiF in pink, (b) 20 m LiTFSI, with pristine Li/LiF in red.

Table 4. 6 Consumption of Li after exposure to 20 m LiTFSI : 8 m LiBETI for the Li/LiF pristine, presoaked in 2 mL FEC, presoaked in 50 μ L FEC, presoaked in 7 M LiFSI in FEC or 2 M LiFSI : 1 M LiTFSI in DOL:DME, 3 % LiNO₃ assuming hydrogen evolution only caused by HER in metallic Li consumption ratio calculation.

Exposure to 20 m LiTFSI : 8 m LiBETI	Molar ratio of H ₂ (after 120min) $x_{\text{Hydrogen}}(\%)$	Amount of H ₂ released (after 120min) $n_{\text{Hydrogen}} (\mu\text{mol})$	Ratio of Li consumed (after 120min) (%)
Li/LiF pristine	7.63	53	22
Li/LiF presoaked in 50 μ L of 2 M LiFSI + 1 M LiTFSI in DOL:DME, 3 % LiNO ₃	6.44	44	18
Li/LiF presoaked in 50 μ L of 7 M LiFSI in FEC	1.41	10	4

Besides, similar experiments have been performed in WiSE (see Figure 4. 13b). As in WiBS, the presoaking in 1 M LiTFSI : 2 M LiFSI in DOL:DME + 3 % LiNO₃ and in 7 M LiFSI

FEC has a beneficial, but reduced, impact on the hydrogen gassing. The metallic Li consumption of LiF-coated Li samples exposed to WiSE fades from 74 % for the pristine sample to 27 % in 1 M LiTFSI : 2 M LiFSI in DOL:DME and 33 % in 7 M LiFSI in FEC, respectively, as described in Table 4. 7. Furthermore, trends observed for both organic electrolytes are similar than in WiBS. In details, after 15 min exposure to WiSE, the hydrogen concentration measured for the sample soaked in 1 M LiTFSI : 2 M LiFSI in DOL:DME increases to ≈ 3 % then stabilizes at ≈ 1 % while it is mostly constant during the two hours experiment after soaking in 7 M LiFSI in FEC. However, one can notice that although the decrease of metallic Li consumption is significant, the differences recorded between these two soaking steps is less remarkable than in WiBS and the metallic Li consumption is still greater than the one of the sample exposed to WiBS. One possible explanation would be the difference of kinetics for such electrolyte penetration being dependent on its viscosity and the mass transport across the microporosity and/or cracks leading to a faster access of water in the case of WiSE and preventing from greater performances.

Table 4. 7 Consumption of metallic Li after exposure to 20 m LiTFSI for the Li/LiF samples: pristine, presoaked in 7 M LiFSI in FEC or 2 M LiFSI : 1 M LiTFSI in DOL:DME, 3 % LiNO₃ assuming HER as sole source for hydrogen evolution in metallic Li consumption ratio calculation.

Exposure to 20 m LiTFSI	Molar ratio of H ₂ (after 120 min) $x_{\text{Hydrogen}}(\%)$	Amount of H ₂ released (after 120 min) $n_{\text{Hydrogen}}(\mu\text{mol})$	Ratio of Li consumed (after 120 min) (%)
Li/LiF pristine	26.35	182	74
Li/LiF presoaked in 7 M LiFSI in FEC	11.53	80	33
Li/LiF presoaked in 2 M LiFSI : 1 M LiTFSI in DOL:DME, 3 % LiNO ₃	7.94	67	27

Based on the decrease of hydrogen gassing observed during GC-TCD measurements, XPS analysis were performed to analyze the surface of the Li/LiF samples after the presoaking step. XPS spectrum of C 1s, O 1s, F 1s, Li 1s, N 1s and S 2p are shown in Figure 4. 14. First of all, presoaking step in DOL:DME-based electrolyte or FEC-based electrolyte almost fully covered the Li/LiF layer with another layer. Indeed, the signal intensity of LiF is barely visible in F 1s and Li 1S spectrum (Figure 4. 14c and d). Moreover, the nature of the additional covering layer formed during presoaking step may be attributed to the formation of a salt-derived layer as shown by LiTFSI or LiFSI signals in Figure 4. 14b, c, e

and f. Regarding presoaking step in DOL:DME-based electrolyte, C 1s spectra gives a greater amount of carbonaceous compounds, *i.e.* more organic-based species deposited on the Li/LiF sample that can be due to the presence of C-F bound in TFSI salt. Therefore, one can suspect that the beneficial impact of 7 M LiFSI in FEC and 1 M LiTFSI : 2 M LiFSI in DOL:DME + 3 % LiNO₃ arises from their ability to form an inorganic-organic SEI upon decomposition on the surface of Li, ^{71,249} both being able to partially compensate the microstructural defects of the *ex-situ* LiF interface. Hence, post-soaking XPS analysis reveal the formation of a salt-derived inorganic SEI for both electrolytes with an organic contribution for the DOL:DME-based electrolyte.

Consequently, the beneficial impact on hydrogen gassing when a Li/LiF sample is exposed to WiBS ranks as follows: pristine Li/LiF < pure FEC < 1 M LiTFSI : 2 M LiFSI in DOL:DME + 3% LiNO₃ < 7 M LiFSI in FEC. From this trend, one can conclude that the ability of the electrolyte to form and maintain stable a LiF-rich SEI inner layer is of prime importance to positively stabilize the interface. Additionally, having an organic contribution to the SEI, as we observe for DOL:DME tends to be beneficial. All of this without promoting the partial dissolution of the SEI.

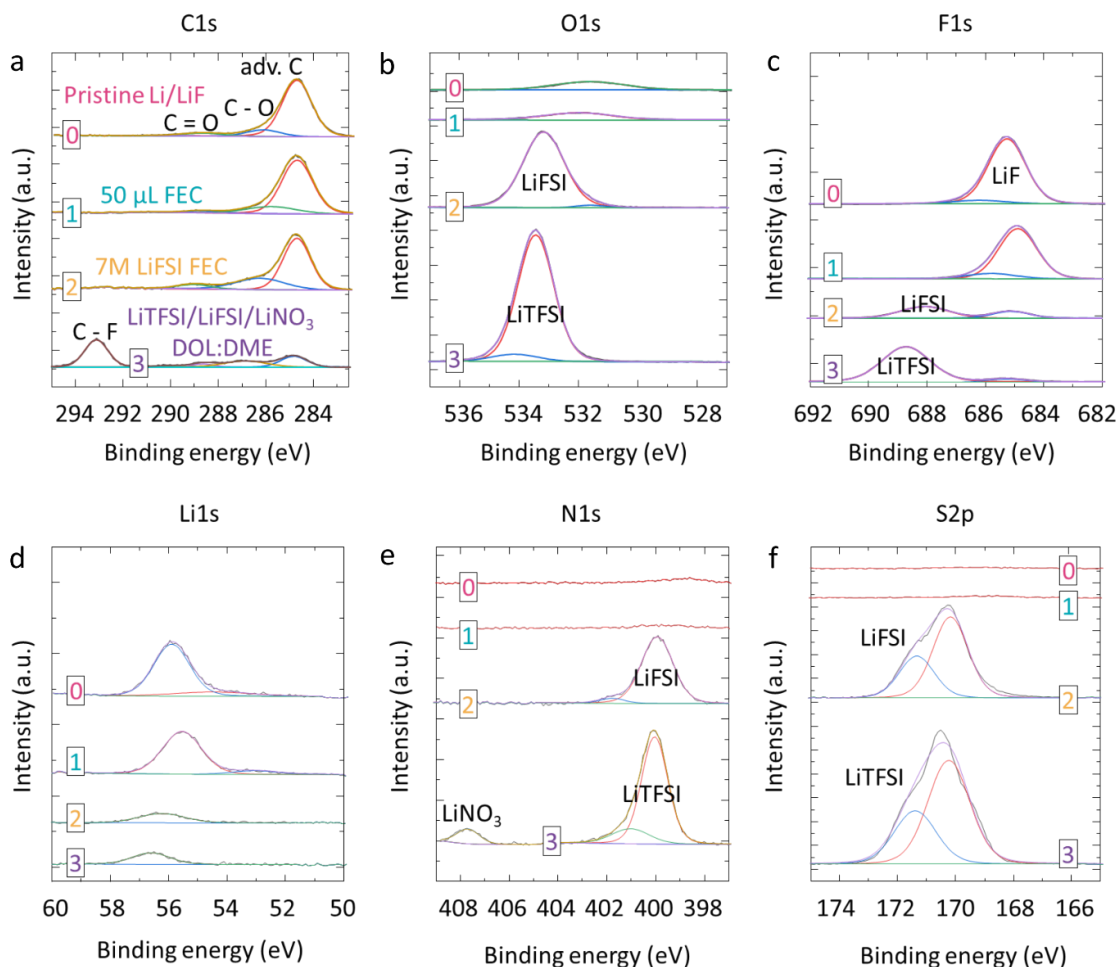


Figure 4. 14 X-ray photoelectron spectroscopy (XPS) spectrum of (a) C 1s, (b) O 1s, (c) F 1s, (d) Li 1s, (e) N 1s, (f) S 2p of pristine Li/LiF [0], presoaked in 50 µL FEC [1], presoaked in 7 M LiFSI [2] and presoaked in 2 M LiFSI : 1 M LiTFSI in DOL:DME, 3% LiNO₃ [3].

Conclusion of the chapter

In this Chapter, we first determined the fluoride solubility limit of LiF salt as function of LiTFSI salt concentration from diluted aqueous media to aqueous superconcentrated electrolyte. Based on these measurements, one can conclude that LiF-based SEIs is non-soluble in both 20 m LiTFSI and 20 m LiTFSI : 8 m LiBETI. Therefore, LiF coatings onto metallic Li were used to mimic LiF-based SEI in aqueous superconcentrated electrolyte. Combining E-SEM with GC-TCD measurements during Li/LiF samples exposition to moisture or WiSE/WiBS, respectively, enable to find that unlike in classical organic electrolyte, aqueous superconcentrated electrolyte cannot self-passivate the interface. These results are further confirmed by testing insoluble Al₂O₃ coating resistance to WiSE/WiBS exposure. Indeed, hydrogen production is also found even though less intense. Therefore, a presoaking step in organic electrolyte known to form good

passivating SEI with LiF-rich inner layer and organic outer layer was employed to analyze the importance of organic-inorganic species in the SEI to maintain it stable. To do so, 1 M LiTFSI : 2 M LiFSI in DOL:DME + 3 % LiNO₃ or 7 M LiFSI in FEC were tested. GC-TCD results show that hydrogen evolution is diminished. This may be explained by the formation of a salt-derived SEI, as shown by XPS post-soaking analysis, as well as the presence of organic compounds in the case of the DOL:DME-based electrolyte. Moreover, combining these analysis and comparing them with those obtained in organic electrolytes, we conclude on the partially-protective role of both native and artificial LiF-rich SEI for superconcentrated aqueous electrolytes. More importantly, we demonstrate that a salt-derived inorganic and solvent-derived organic layers play a crucial role in the SEI's ability to self-repair and allow for cycling anode material outside of the thermodynamic stability window of the electrolyte.

Indeed, as recently demonstrated with the use of organic co-solvents such as acetonitrile¹⁹², DMC^{191,255} or ether-based one (TEGDME)¹⁹³, organic SEI outer layer seems to be beneficial. Similarly, additives such as urea^{190,256} were also shown to have positive effects on the cycling behavior of Li₄Ti₅O₁₂ anode (1.7 V vs Li⁺/Li) in WiSE-based batteries owing to its decomposition in both inorganic (Li₂CO₃) and amorphous organic (polyuria) layers. Nevertheless, bearing in mind that in these electrolytes, the first solvation sheath of Li⁺ contains both water and organic species, it is tempting to conclude that both should be simultaneously present at the interface, leading to the detrimental reduction of water simultaneously to the SEI formation (knowing that solvating water molecules are more reactive than non-solvating ones¹⁴⁴). Moreover, despite the diminished hydrogen evolution with an artificial inorganic LiF layer presoaked in 7 M LiFSI in FEC, these *ex-situ* protections are not sufficient to envision practical applications. Indeed, considering the electrolyte's water content as the limiting factor, in the best-case scenario, fewer than 50 cycles in WiSE and 250 cycles in WiBS would be achieved before the drying out of a cell cycled at 1C rate (see Table 4. 8). Furthermore, taking into account the quantity of metallic Li used in this study (489 μmol), only six hours would be needed to fully consume the metallic Li in WiSE, and less than fifty hours in WiBS. These simple calculations do not take into account electrolyte crystallization but merely the full consumption of water, thus providing grossly underestimated numbers that would be even worse in practice. Evidently, using metallic Li as an anode leads to harsh degradation which could be partially alleviated, or at least slowed down, by the use of an anode material with a greater redox potential (LTO, TiO₂, Mo₆S₈, LTP or else). Indeed, around 8750 cycles could be performed using unprotected

Mo₆S₈ as negative electrode before the complete drying out of the cell as shown in Table 4. 8, this gain in cycling life coming at the expense of energy density.

Table 4. 8 Estimation of water and metallic Li consumption according to the gassing measured by GC-TCD.

Case	Li/LiF, cracks filled with 7M LiFSI in FEC, exposure to WiSE	Li/LiF, cracks filled with 7M LiFSI in FEC, exposure to WiBS	Mo ₆ S ₈ electrode used in WiSE (based on Chapter 2 and 3)
Water consumption $\mu\text{mol}_{\text{H}_2\text{O}}/\text{h}$	80	10	*0.14
Water amount in 250 μL of electrolyte (mmol)	3.49	2.48	3.49
Time (h) needed to consume water	44	248	25000
Number of cycle considering 1C C-rate (1 Li ⁺ inserted / h)	<50	<250	<6300
Li amount used in the study (μmol)	489	489	
Time (h) needed to consume Li	6.1	48.9	

*based on Chapter 2 and 3, rate of water consumption is calculated to be ≈ 0.0005 %initial water amount/h_{self-discharge} for a stable SEI formed and ≈ 0.004 %initial water amount/h_{cycling} at 1C during cycling. Therefore, in this calculation, we only consider cycling data.

As a conclusion, altogether, this work evidences that 1) the use of superconcentrated aqueous electrolytes does not allow for the self-passivation of the SEI at the anode; 2) the solubility is not the predominant factor governing the poor stability of such inorganic coatings. These results are in good agreement with the performances obtained with self-discharge protocol (drop of discharge capacity and Coulombic efficiency after resting period) in Chapter 2 and 3. Eventually, while inorganic-rich interphases can physically impede the reaction and allow for a certain stability over a short period, the aqueous electrolyte will inherently reaches the underlying anode material owing to extrinsic defects, which will be present in any practical the SEI. Furthermore, bearing in mind that cracks and/or microporosity may continuously form upon cycling, triggering their self-passivation is necessary to protect the underlying electrode. Towards that goal, two strategies can be envisioned, either with additives or with organic coatings. Regarding

the use of additives, they must be targeted following their ability to preferentially solvate Li^+ and thus displace water from its solvation sheath. Organic coatings can also be developed by a grafting strategy or by laminating polymer protective layers, as previously reported^{120,204}. Towards these goals, the perspectives of this thesis will be dedicated to polymer layer as artificial SEI for aqueous superconcentrated electrolyte LIB application.

GENERAL CONCLUSION AND PERSPECTIVES

Through this phd thesis, the use of aqueous superconcentrated electrolyte, namely *Water-in-salt*, was investigated in LIB. The attraction towards WiSE is explained by structural and physical modifications arising from the formation of two interpenetrated networks in these electrolytes, a water-rich network and an anion-rich one. This peculiar solvation structure was shown to enable fast transport with high Li^+ cation transference number while promoting the formation of a salt-derived inorganic-rich SEI at the negative interface and preventing water oxidation on the positive side thanks to the formation of an hydrophobic double-layer. Therefore, the electrochemical stability window of these electrolytes was reported to increase above 2 V. These changes in physico-chemical properties and in interfacial reactivity, and the influence of superconcentrated aqueous electrolytes on LIB performances are described in the first chapter.

Besides, the set-up of a systematic study on both the anodic and cathodic stability of 20 m LiTFSI was performed as function of the operating conditions to assess the viability of WiSE electrolyte in LIB. Although the impact of the increase in concentration was shown to positively impact cell performances at room temperature, by changing the C-rate, the presence of parasitic reaction is brought to light. These parasitic reactions were found to be even further damaging at higher temperature. Therefore, *operando* gas monitoring experiments were carried out to determine the nature of the parasitic reactions causing performances decay. Combining pressure cell and online electrochemical mass spectrometry, hydrogen evolution (HER) was found to occur both during cycling and resting period, triggering a so-called self-discharge. However, one must note that self-discharge appears partially reversible in terms of lithium balance, the major drawback being the irreversible water consumption. Eventually, this study was completed with the use of 20 m LiTFSI : 8 m LiBETI to illustrate that the aforementioned limitations are general to aqueous superconcentrated electrolytes used in LIB. Indeed, alike what was observed in 20 m LiTFSI, this study show that the HER takes place during cycling and resting period, suggesting a weak passivation of the SEI formed in these WiSEs, though HER intensity was found much decreased in 20 m LiTFSI : 8 m LiBETI when compared to 20 m LiTFSI. Besides, on the anodic side, the oxygen evolution impact was shown to be non-existent at room temperature, and to have limited impact at higher temperature. Altogether, the results found in Chapter 2 show that the main issue regarding the use of WiSE regards the negative electrode and the SEI stability.

To understand these limitations, the native SEI stability was investigated by electrochemical characterizations (cyclic voltammetry and electrochemical impedance spectroscopy), showing the passivating power of the SEI but its poor efficiency towards preventing water consumption. The later was further highlighted by differential scanning calorimetry showing a shift in crystallization peak attesting of an increase in salt concentration after cycling and resting period. Besides, rate of water consumption during resting was found in the same order of magnitude than the rate of water consumption albeit smaller. Moreover, the de-intercalation rates of Li^+ during self-discharge and cycling were found to largely differ. To comprehend this observation, the activation energy of self-discharge phenomenon occurring during resting was determined and compared to the activation energy of the HER taking place during cycling. Experimental results confirmed a similar activation energy (≈ 20 kJ/mol), suggesting that self-discharge is governed by HER rather than by delithiation of the negative electrode. Altogether, in Chapter 3 the dramatic impact of water reduction during self-discharge and cycling is highlighted when relying on the formation of a native SEI.

To understand the relative instability of the native SEI, the solubility of LiF (the major contributor to the SEI) was studied in several media, from pure water, 1 m LiTFSI to 20 m LiTFSI and 20 m LiTFSI : 8 m LiBETI WiSEs. Experimental results demonstrate that a ≈ 10 nm LiF thickness (comparable to a native SEI one) should not completely dissolve in aqueous superconcentrated electrolyte, showing that solubility is not the issue. To probe if the microstructure of the native SEI is limiting its stability, an artificial LiF SEI was prepared onto metallic Li (Li/LiF) to assess the efficiency of an inorganic coating to protect the negative electrode from water reduction. Combining E-SEM and GC-TCD measurements, the exposure to moisture or aqueous superconcentrated electrolyte was found to enable water to react with Li, despite the presence of a conformal LiF coating. More impactful, WiSE or WiBS do not allow for self-passivation unlike what is observed in organic electrolyte (here, in LP30). The absence of self-passivation was confirmed using Al_2O_3 coating, known to be insoluble in water, demonstrating that in the absence of self-passivation water reacts with the underlying electrode through surface defects such as micro-porosity or cracks in the SEI. In order to overcome this limitation, a presoaking step was performed in organic electrolyte known to form good passivating SEI with LiF-rich inner layer and organic outer layer: 1 M LiTFSI : 2 M LiFSI in DOL:DME + 3 % LiNO_3 or 7 M LiFSI in FEC. GC-TCD measurements show that hydrogen evolution is diminished when further exposing the electrode to WiSE or WiBS, owing to the deposition of salt-derived compounds as shown by XPS. As a consequence, the use

of artificial inorganic SEI coupled with presoaking in organic electrolyte demonstrates the need for the SEI to be able to self-repair. It further suggests that the presence of organic component further promote SEI stability, and that negative electrode may operate at low potential far below the ESW limit if coated with such organic layer.

The figure-of-merits, as detailed in Chapter 3, compare the performances of WiSE-based LIB with that of other rechargeable battery technologies such as Lead-acid, Ni-Cd, Ni-MH and commercial LIB (using diluted organic electrolyte). Evidently, WiSE-based batteries can only operate within a ≈ 2 V operating window to avoid parasitic reactions, thus drastically limiting the energy density and specific energy compared to Ni-MH batteries. Moreover, while the use of chemical-engineering means to handle gas generated during cycling could be envisioned, alike what is done for other aqueous secondary battery (Lead-acid, etc.), the superconcentration may cause rapid crystallization of the electrolyte for vented or flooded-type cells that evacuate gases produced without compensating water consumption. However, paradoxically, too few oxygen is produced at the positive while hydrogen production happens concomitantly with Li^+ insertion at the negative, thus preventing the implementation of the “oxygen cycle” used in sealed-type batteries. Apart from energy consideration, a major drawback of most of the aqueous superconcentrated electrolytes is their narrow thermal stability range. Indeed, they often crystallize near room temperature. Several strategies were previously shown to overcome the operating temperature range limitation by the use of asymmetric anion and/or the introduction of organic co-solvent that downshift the melting point, as detailed in the first chapter. Finally, and more critically, while self-discharge is found reversible in terms of Li^+ balance, it is responsible for irreversible water consumption. Therefore, means need to be found to reduce capacity fading and prevent electrolyte crystallization for large-scale commercialization.

As a summary, WiSE-based batteries still face many drawbacks that must be overcome before to attain satisfactory performance when compared with commercial LIB batteries. Many strategies are envisioned to improve these systems. As detailed in the first chapter, the introduction of organic-solvent was brought to tune the first solvation sheath of Li^+ promoting the organic co-solvent reduction and thus its participation to SEI formation while (i) reducing the amount of water in the first solvation sheath and (ii) disrupting the water H-bonds network. Nonetheless, bearing in mind that water is still partially involved in the solvation sheath, it is tempting to conclude that both the organic co-solvent and water will be reduce at low potential, thus not fully addressing the cathodic challenge. Based on the performances first

reported in 2017 by Yang *et al.*²⁰⁴, the use of organic polymer coating could be seen as a promising path to develop. Therefore, we tried to reproduce their results and to assemble a battery, as described in Figure Conclusion. 1. The polymer coating is based on 0.5 M LiTFSI dissolved in a highly fluorinated ether solvent (HFE): DMC mixture (95:5 vol%) with 10 wt% PEO. Here, DMC is used as a co-solvent to promote LiTFSI and PEO dissolution in HFE. It is then removed during the fabrication process and does not participate to the final coating layer. However, during our trials, difficulties to dissolve LiTFSI and PEO in such low quantity of DMC were encountered, forcing us to move to acetonitrile as co-solvent to enable the dissolution²⁰¹. Once the gel is obtained, the deposition on the negative electrode was found tricky/hard to reproduce. Indeed, the gel is sticky and need to be heated up to flow in liquid state during coating procedure. Therefore, no success in cycling such polymer-protected WiSE batteries was obtained yet, but trials are being performed. As a summary, even though the use of polymer coating was reported to enable the cycling of metallic Li or graphite, to the best of my knowledge, its technical implementation requires improvement.

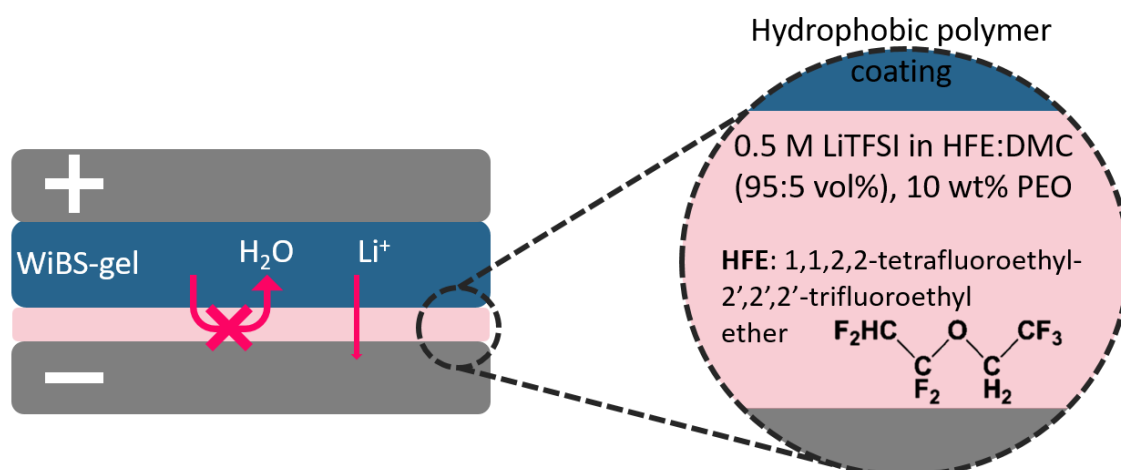


Figure Conclusion. 1 Scheme of a Li-ion battery relying on the use of a polymer coating on the negative electrode. The polymer coating is based on 0.5 M LiTFSI in a highly fluorinated ether (HFE):DMC (95:5 vol%) mixture with 10 wt% polyethylene oxide (PEO).

REFERENCES

- (1) International energy agency. World Energy Outlook 2020. **2020**.
- (2) International energy agency. World Energy Outlook 2021. **2021**, 386.
- (3) Bloomberg New Energy Finance, “Electric Vehicle Outlook 2020”, BloombergNEF, New-York. **2020**.
- (4) Avicenne. Avicenne Energy Report: EU Battery Demand and Supply (2019-2030) in a Global Context.
- (5) Cano, Z. P.; Banham, D.; Ye, S.; Hintennach, A.; Lu, J.; Fowler, M.; Chen, Z. Batteries and Fuel Cells for Emerging Electric Vehicle Markets. *Nat Energy* **2018**, 3 (4), 279–289. <https://doi.org/10.1038/s41560-018-0108-1>.
- (6) May, G. J.; Davidson, A.; Monahov, B. Lead Batteries for Utility Energy Storage: A Review. *Journal of Energy Storage* **2018**, 15, 145–157. <https://doi.org/10.1016/j.est.2017.11.008>.
- (7) Reddy, T.; Linden, D. *Linden’s Handbook of Batteries (4th Edition)*; McGraw-Hill Professional Publishing: New York, USA, 2010.
- (8) Van den Bossche, P.; Vergels, F.; Van Mierlo, J.; Matheys, J.; Van Autenboer, W. SUBAT: An Assessment of Sustainable Battery Technology. *Journal of Power Sources* **2006**, 162 (2), 913–919. <https://doi.org/10.1016/j.jpowsour.2005.07.039>.
- (9) Beck, F.; Rüetschi, P. Rechargeable Batteries with Aqueous Electrolytes. *Electrochimica Acta* **2000**, 45 (15–16), 2467–2482. [https://doi.org/10.1016/S0013-4686\(00\)00344-3](https://doi.org/10.1016/S0013-4686(00)00344-3).
- (10) Rouxel, J.; Danot, M.; Bichon, M. Les Composites Intercalaires Na_xTiS_2 . Etude Générale Des Phases Na_xTiS_2 et K_xTiS_2 . *Bulletin de la Société Chimique de France* **1971**, 11, 3930–3936.
- (11) Whittingham, M. S. Intercalation Chemistry and Energy Storage. *Journal of Solid State Chemistry* **1979**, 29 (3), 303–310. [https://doi.org/10.1016/0022-4596\(79\)90187-7](https://doi.org/10.1016/0022-4596(79)90187-7).
- (12) Whittingham, M. S. Electrical Energy Storage and Intercalation Chemistry. *Science* **1976**, 192 (4244), 1126–1127. <https://doi.org/10.1126/science.192.4244.1126>.
- (13) Whittingham, M. S. CHALCOGENIDE BATTERY, US4009052A. **1977**, 5.

- (14) Lin, D.; Liu, Y.; Cui, Y. Reviving the Lithium Metal Anode for High-Energy Batteries. *Nature Nanotech* **2017**, *12* (3), 194–206. <https://doi.org/10.1038/nnano.2017.16>.
- (15) Blomgren, G. E. The Development and Future of Lithium Ion Batteries. *J. Electrochem. Soc.* **2017**, *164* (1), A5019–A5025. <https://doi.org/10.1149/2.0251701jes>.
- (16) Kalyani, P.; Kalaiselvi, N. Various Aspects of LiNiO_2 Chemistry: A Review. *Science and Technology of Advanced Materials* **2005**, *6* (6), 689–703. <https://doi.org/10.1016/j.stam.2005.06.001>.
- (17) Yabuuchi, N.; Ohzuku, T. Novel Lithium Insertion Material of $\text{LiCo}_{1/3}\text{Ni}_{1/3}\text{Mn}_{1/3}\text{O}_2$ for Advanced Lithium-Ion Batteries. *Journal of Power Sources* **2003**, *119–121*, 171–174. [https://doi.org/10.1016/S0378-7753\(03\)00173-3](https://doi.org/10.1016/S0378-7753(03)00173-3).
- (18) Noh, H.-J.; Youn, S.; Yoon, C. S.; Sun, Y.-K. Comparison of the Structural and Electrochemical Properties of Layered $\text{Li}[\text{Ni}_x\text{Co}_y\text{Mn}_z]\text{O}_2$ ($x = 1/3, 0.5, 0.6, 0.7, 0.8$ and 0.85) Cathode Material for Lithium-Ion Batteries. *Journal of Power Sources* **2013**, *233*, 121–130. <https://doi.org/10.1016/j.jpowsour.2013.01.063>.
- (19) Rozier, P.; Tarascon, J. M. Review—Li-Rich Layered Oxide Cathodes for Next-Generation Li-Ion Batteries: Chances and Challenges. *J. Electrochem. Soc.* **2015**, *162* (14), A2490–A2499. <https://doi.org/10.1149/2.0111514jes>.
- (20) Thackeray, M. M.; David, W. I. F.; Bruce, P. G.; Goodenough, J. B. Lithium Insertion into Manganese Spinels. *Materials Research Bulletin* **1983**, *18* (4), 461–472. [https://doi.org/10.1016/0025-5408\(83\)90138-1](https://doi.org/10.1016/0025-5408(83)90138-1).
- (21) Lazzari, M.; Scrosati, B. A Cyclable Lithium Organic Electrolyte Cell Based on Two Intercalation Electrodes. *J. Electrochem. Soc.* **1980**, *127* (3), 773–774. <https://doi.org/10.1149/1.2129753>.
- (22) Yazami, R.; Touzain, Ph. A Reversible Graphite-Lithium Negative Electrode for Electrochemical Generators. *Journal of Power Sources* **1983**, *9* (3), 365–371. [https://doi.org/10.1016/0378-7753\(83\)87040-2](https://doi.org/10.1016/0378-7753(83)87040-2).
- (23) Basu, S.; Somerset, N. J. US4423125A, Bell Laboratories. **1983**, 4.
- (24) Fong, R.; von Sacken, U.; Dahn, J. R. Studies of Lithium Intercalation into Carbons Using Nonaqueous Electrochemical Cells. *J. Electrochem. Soc.* **1990**, *137* (7), 2009–2013. <https://doi.org/10.1149/1.2086855>.
- (25) Fujimoto, M.; Yoshinaga, N.; Furukawa, N.; Nohma, T.; Takahashi, M. LITHIUM SECONDARY BATTERY, US5686138A. **1994**, 55.
- (26) Yoshino, A. The Birth of the Lithium-Ion Battery. *Angew. Chem. Int. Ed.* **2012**, *51* (24), 5798–5800. <https://doi.org/10.1002/anie.201105006>.

- (27) Tarascon, J. M.; Armand, M. Issues and Challenges Facing Rechargeable Lithium Batteries. *Nature* 2001.
- (28) Xu, K. Nonaqueous Liquid Electrolytes for Lithium-Based Rechargeable Batteries. *Chem. Rev.* **2004**, *104* (10), 4303–4418. <https://doi.org/10.1021/cr030203g>.
- (29) Peled, E.; Menkin, S. Review—SEI: Past, Present and Future. *J. Electrochem. Soc.* **2017**, *164* (7), A1703–A1719. <https://doi.org/10.1149/2.1441707jes>.
- (30) Peled, E. The Electrochemical Behavior of Alkali and Alkaline Earth Metals in Nonaqueous Battery Systems—The Solid Electrolyte Interphase Model. *J. Electrochem. Soc.* **1979**, *126* (12), 2047–2051. <https://doi.org/10.1149/1.2128859>.
- (31) Zaban, A.; Aurbach, D. Impedance Spectroscopy of Lithium and Nickel Electrodes in Propylene Carbonate Solutions of Different Lithium Salts A Comparative Study. *Journal of Power Sources* **1995**, *54* (2), 289–295. [https://doi.org/10.1016/0378-7753\(94\)02086-I](https://doi.org/10.1016/0378-7753(94)02086-I).
- (32) Edström, K.; Gustafsson, T.; Thomas, J. O. The Cathode–Electrolyte Interface in the Li-Ion Battery. *Electrochimica Acta* **2004**, *50* (2–3), 397–403. <https://doi.org/10.1016/j.electacta.2004.03.049>.
- (33) Liu, Y.-M.; G. Nicolau, B.; Esbenschade, J. L.; Gewirth, A. A. Characterization of the Cathode Electrolyte Interface in Lithium Ion Batteries by Desorption Electrospray Ionization Mass Spectrometry. *Anal. Chem.* **2016**, *88* (14), 7171–7177. <https://doi.org/10.1021/acs.analchem.6b01292>.
- (34) Bassett, K. L.; Özgür Çapraz, Ö.; Özdogru, B.; Gewirth, A. A.; Sottos, N. R. Cathode/Electrolyte Interface-Dependent Changes in Stress and Strain in Lithium Iron Phosphate Composite Cathodes. *J. Electrochem. Soc.* **2019**, *166* (12), A2707–A2714. <https://doi.org/10.1149/2.1391912jes>.
- (35) Goodenough, J. B.; Kim, Y. Challenges for Rechargeable Li Batteries. *Chem. Mater.* **2010**, *22* (3), 587–603. <https://doi.org/10.1021/cm901452z>.
- (36) Peljo, P.; Girault, H. H. Electrochemical Potential Window of Battery Electrolytes: The HOMO–LUMO Misconception. *Energy Environ. Sci.* **2018**, *11* (9), 2306–2309. <https://doi.org/10.1039/C8EE01286E>.
- (37) Chen, W.; Ambrosio, F.; Miceli, G.; Pasquarello, A. *Ab Initio* Electronic Structure of Liquid Water. *Phys. Rev. Lett.* **2016**, *117* (18), 186401. <https://doi.org/10.1103/PhysRevLett.117.186401>.
- (38) Borodin, O.; Self, J.; Persson, K. A.; Wang, C.; Xu, K. Uncharted Waters: Super-Concentrated Electrolytes. *Joule* **2020**, *4* (1), 69–100. <https://doi.org/10.1016/j.joule.2019.12.007>.

- (39) Yamada, Y.; Yamada, A. Review—Superconcentrated Electrolytes for Lithium Batteries. *Journal of The Electrochemical Society* **2015**, *162* (14), A2406–A2423. <https://doi.org/10.1149/2.0041514jes>.
- (40) Suo, L.; Hu, Y.-S.; Li, H.; Armand, M.; Chen, L. A New Class of Solvent-in-Salt Electrolyte for High-Energy Rechargeable Metallic Lithium Batteries. *Nat Commun* **2013**, *4* (1), 1481. <https://doi.org/10.1038/ncomms2513>.
- (41) Seo, D. M.; Boyle, P. D.; Borodin, O.; Henderson, W. A. Li⁺ Cation Coordination by Acetonitrile—Insights from Crystallography. *RSC Adv.* **2012**, *2* (21), 8014. <https://doi.org/10.1039/c2ra21290k>.
- (42) Kunz, W.; Barthel, J.; Klein, L.; Cartailier, T.; Turq, P.; Reindl, B. Lithium Bromide in Acetonitrile: Thermodynamics, Theory, and Simulation. *J Solution Chem* **1991**, *20* (9), 875–891. <https://doi.org/10.1007/BF01074950>.
- (43) Yamada, Y.; Furukawa, K.; Sodeyama, K.; Kikuchi, K.; Yaegashi, M.; Tateyama, Y.; Yamada, A. Unusual Stability of Acetonitrile-Based Superconcentrated Electrolytes for Fast-Charging Lithium-Ion Batteries. *Journal of the American Chemical Society* **2014**, *136* (13), 5039–5046. <https://doi.org/10.1021/ja412807w>.
- (44) Yamada, Y.; Wang, J.; Ko, S.; Watanabe, E.; Yamada, A. Advances and Issues in Developing Salt-Concentrated Battery Electrolytes. *Nature Energy* **2019**. <https://doi.org/10.1038/s41560-019-0336-z>.
- (45) Sodeyama, K.; Yamada, Y.; Aikawa, K.; Yamada, A.; Tateyama, Y. Sacrificial Anion Reduction Mechanism for Electrochemical Stability Improvement in Highly Concentrated Li-Salt Electrolyte. *J. Phys. Chem. C* **2014**, *118* (26), 14091–14097. <https://doi.org/10.1021/jp501178n>.
- (46) McOwen, D. W.; Seo, D. M.; Borodin, O.; Vatamanu, J.; Boyle, P. D.; Henderson, W. A. Concentrated Electrolytes: Decrypting Electrolyte Properties and Reassessing Al Corrosion Mechanisms. *Energy Environ. Sci.* **2014**, *7* (1), 416–426. <https://doi.org/10.1039/C3EE42351D>.
- (47) Vatamanu, J.; Borodin, O.; Smith, G. D. Molecular Insights into the Potential and Temperature Dependences of the Differential Capacitance of a Room-Temperature Ionic Liquid at Graphite Electrodes. *J. Am. Chem. Soc.* **2010**, *132* (42), 14825–14833. <https://doi.org/10.1021/ja104273r>.
- (48) Jin, J.; Li, H. H.; Wei, J. P.; Bian, X. K.; Zhou, Z.; Yan, J. Li/LiFePO₄ Batteries with Room Temperature Ionic Liquid as Electrolyte. *Electrochemistry Communications* **2009**, *11* (7), 1500–1503. <https://doi.org/10.1016/j.elecom.2009.05.040>.
- (49) Yamada, Y.; Chiang, C. H.; Sodeyama, K.; Wang, J.; Tateyama, Y.; Yamada, A. Corrosion Prevention Mechanism of Aluminum Metal in Superconcentrated Electrolytes. *ChemElectroChem* **2015**, *2* (11), 1687–1694. <https://doi.org/10.1002/celec.201500235>.

- (50) Vatamanu, J.; Borodin, O.; Smith, G. D. Molecular Dynamics Simulation Studies of the Structure of a Mixed Carbonate/LiPF₆ Electrolyte near Graphite Surface as a Function of Electrode Potential. *J. Phys. Chem. C* **2012**, *116* (1), 1114–1121. <https://doi.org/10.1021/jp2101539>.
- (51) Borodin, O.; Ren, X.; Vatamanu, J.; von Wald Cresce, A.; Knap, J.; Xu, K. Modeling Insight into Battery Electrolyte Electrochemical Stability and Interfacial Structure. *Acc. Chem. Res.* **2017**, *50* (12), 2886–2894. <https://doi.org/10.1021/acs.accounts.7b00486>.
- (52) Yamada, Y.; Usui, K.; Chiang, C. H.; Kikuchi, K.; Furukawa, K.; Yamada, A. General Observation of Lithium Intercalation into Graphite in Ethylene-Carbonate-Free Superconcentrated Electrolytes. *ACS Appl. Mater. Interfaces* **2014**, *6* (14), 10892–10899. <https://doi.org/10.1021/am5001163>.
- (53) Wang, J.; Yamada, Y.; Sodeyama, K.; Watanabe, E.; Takada, K.; Tateyama, Y.; Yamada, A. Fire-Extinguishing Organic Electrolytes for Safe Batteries. *Nature Energy* **2018**, *3* (1), 22–29. <https://doi.org/10.1038/s41560-017-0033-8>.
- (54) Yamada, Y.; Yamada, A. Superconcentrated Electrolytes to Create New Interfacial Chemistry in Non-Aqueous and Aqueous Rechargeable Batteries. *Chemistry Letters* **2017**, *46* (8), 1056–1064. <https://doi.org/10.1246/cl.170284>.
- (55) Qian, J.; Henderson, W. A.; Xu, W.; Bhattacharya, P.; Engelhard, M.; Borodin, O.; Zhang, J.-G. High Rate and Stable Cycling of Lithium Metal Anode. *Nat Commun* **2015**, *6* (1), 6362. <https://doi.org/10.1038/ncomms7362>.
- (56) Alvarado, J.; Schroeder, M. A.; Zhang, M.; Borodin, O.; Gobrogge, E.; Olguin, M.; Ding, M. S.; Gobet, M.; Greenbaum, S.; Meng, Y. S.; Xu, K. A Carbonate-Free, Sulfone-Based Electrolyte for High-Voltage Li-Ion Batteries. *Materials Today* **2018**, *21* (4), 341–353. <https://doi.org/10.1016/j.mattod.2018.02.005>.
- (57) Wang, J.; Yamada, Y.; Sodeyama, K.; Chiang, C. H.; Tateyama, Y.; Yamada, A. Superconcentrated Electrolytes for a High-Voltage Lithium-Ion Battery. *Nature Communications* **2016**, *7*, 12032. <https://doi.org/10.1038/ncomms12032>.
- (58) Yamada, Y.; Usui, K.; Sodeyama, K.; Ko, S.; Tateyama, Y.; Yamada, A. Hydrate-Melt Electrolytes for High-Energy-Density Aqueous Batteries. *Nature Energy* **2016**, *1* (10). <https://doi.org/10.1038/nenergy.2016.129>.
- (59) McKinnon, W. R.; Dahn, J. R. How to Reduce the Cointercalation of Propylene Carbonate in Li_xZrS₂ and Other Layered Compounds. *J. Electrochem. Soc.* **1985**, *132* (2), 364–366. <https://doi.org/10.1149/1.2113839>.
- (60) Jeong, S.-K.; Inaba, M.; Iriyama, Y.; Abe, T.; Ogumi, Z. Electrochemical Intercalation of Lithium Ion within Graphite from Propylene Carbonate Solutions. *Electrochem. Solid-State Lett.* **2003**, *6* (1), A13. <https://doi.org/10.1149/1.1526781>.

- (61) Yamada, Y.; Takazawa, Y.; Miyazaki, K.; Abe, T. Electrochemical Lithium Intercalation into Graphite in Dimethyl Sulfoxide-Based Electrolytes: Effect of Solvation Structure of Lithium Ion. *J. Phys. Chem. C* **2010**, *114* (26), 11680–11685. <https://doi.org/10.1021/jp1037427>.
- (62) Yamada, Y.; Yaegashi, M.; Abe, T.; Yamada, A. A Superconcentrated Ether Electrolyte for Fast-Charging Li-Ion Batteries. *Chemical Communications* **2013**, *49* (95), 11194. <https://doi.org/10.1039/c3cc46665e>.
- (63) Petibon, R.; Aiken, C. P.; Ma, L.; Xiong, D.; Dahn, J. R. The Use of Ethyl Acetate as a Sole Solvent in Highly Concentrated Electrolyte for Li-Ion Batteries. *Electrochimica Acta* **2015**, *154*, 287–293. <https://doi.org/10.1016/j.electacta.2014.12.093>.
- (64) Lu, D.; Tao, J.; Yan, P.; Henderson, W. A.; Li, Q.; Shao, Y.; Helm, M. L.; Borodin, O.; Graff, G. L.; Polzin, B.; Wang, C.-M.; Engelhard, M.; Zhang, J.-G.; De Yoreo, J. J.; Liu, J.; Xiao, J. Formation of Reversible Solid Electrolyte Interface on Graphite Surface from Concentrated Electrolytes. *Nano Lett.* **2017**, *17* (3), 1602–1609. <https://doi.org/10.1021/acs.nanolett.6b04766>.
- (65) Chen, S.; Zheng, J.; Yu, L.; Ren, X.; Engelhard, M. H.; Niu, C.; Lee, H.; Xu, W.; Xiao, J.; Liu, J.; Zhang, J.-G. High-Efficiency Lithium Metal Batteries with Fire-Retardant Electrolytes. *Joule* **2018**, *2* (8), 1548–1558. <https://doi.org/10.1016/j.joule.2018.05.002>.
- (66) Angell, C. A.; Liu, C.; Sanchez, E. Rubbery Solid Electrolytes with Dominant Cationic Transport and High Ambient Conductivity. *Nature* **1993**, *362*, 137–139.
- (67) Tamura, T.; Yoshida, K.; Hachida, T.; Tsuchiya, M.; Nakamura, M.; Kazue, Y.; Tachikawa, N.; Dokko, K.; Watanabe, M. Physicochemical Properties of Glyme–Li Salt Complexes as a New Family of Room-Temperature Ionic Liquids. *Chem. Lett.* **2010**, *39* (7), 753–755. <https://doi.org/10.1246/cl.2010.753>.
- (68) Tamura, T.; Hachida, T.; Yoshida, K.; Tachikawa, N.; Dokko, K.; Watanabe, M. New Glyme–Cyclic Imide Lithium Salt Complexes as Thermally Stable Electrolytes for Lithium Batteries. *Journal of Power Sources* **2010**, *195* (18), 6095–6100. <https://doi.org/10.1016/j.jpowsour.2009.11.061>.
- (69) Yoshida, K.; Nakamura, M.; Kazue, Y.; Tachikawa, N.; Tsuzuki, S.; Seki, S.; Dokko, K.; Watanabe, M. Oxidative-Stability Enhancement and Charge Transport Mechanism in Glyme–Lithium Salt Equimolar Complexes. *J. Am. Chem. Soc.* **2011**, *133* (33), 13121–13129. <https://doi.org/10.1021/ja203983r>.
- (70) Doi, T.; Masuhara, R.; Hashinokuchi, M.; Shimizu, Y.; Inaba, M. Concentrated LiPF₆/PC Electrolyte Solutions for 5-V LiNi_{0.5}Mn_{1.5}O₄ Positive Electrode in Lithium-Ion Batteries. *Electrochimica Acta* **2016**, *209*, 219–224. <https://doi.org/10.1016/j.electacta.2016.05.062>.

- (71) Suo, L.; Xue, W.; Gobet, M.; Greenbaum, S. G.; Wang, C.; Chen, Y.; Yang, W.; Li, Y.; Li, J. Fluorine-Donating Electrolytes Enable Highly Reversible 5-V-Class Li Metal Batteries. *Proc Natl Acad Sci USA* **2018**, *115* (6), 1156–1161. <https://doi.org/10.1073/pnas.1712895115>.
- (72) Matsumoto, K.; Inoue, K.; Nakahara, K.; Yuge, R.; Noguchi, T.; Utsugi, K. Suppression of Aluminum Corrosion by Using High Concentration LiTFSI Electrolyte. *Journal of Power Sources* **2013**, *231*, 234–238. <https://doi.org/10.1016/j.jpowsour.2012.12.028>.
- (73) Shiga, T.; Okuda, C.; Kato, Y.; Kondo, H. Highly Concentrated Electrolytes Containing a Phosphoric Acid Ester Amide with Self-Extinguishing Properties for Use in Lithium Batteries. *J. Phys. Chem. C* **2018**, *122* (18), 9738–9745. <https://doi.org/10.1021/acs.jpcc.7b12461>.
- (74) Hess, S.; Wohlfahrt-Mehrens, M.; Wachtler, M. Flammability of Li-Ion Battery Electrolytes: Flash Point and Self-Extinguishing Time Measurements. *J. Electrochem. Soc.* **2015**, *162* (2), A3084–A3097. <https://doi.org/10.1149/2.0121502jes>.
- (75) Nakayama, N.; Nozawa, T.; Iriyama, Y.; Abe, T.; Ogumi, Z.; Kikuchi, K. Interfacial Lithium-Ion Transfer at the LiMn₂O₄ Thin Film Electrode/Aqueous Solution Interface. *Journal of Power Sources* **2007**, *174* (2), 695–700. <https://doi.org/10.1016/j.jpowsour.2007.06.113>.
- (76) Sauvage, F.; Laffont, L.; Tarascon, J.-M.; Baudrin, E. Factors Affecting the Electrochemical Reactivity vs. Lithium of Carbon-Free LiFePO₄ Thin Films. *Journal of Power Sources* **2008**, *175* (1), 495–501. <https://doi.org/10.1016/j.jpowsour.2007.09.085>.
- (77) Tang, W.; Tian, S.; Liu, L. L.; Li, L.; Zhang, H. P.; Yue, Y. B.; Bai, Y.; Wu, Y. P.; Zhu, K. Nanochain LiMn₂O₄ as Ultra-Fast Cathode Material for Aqueous Rechargeable Lithium Batteries. *Electrochemistry Communications* **2011**, *13* (2), 205–208. <https://doi.org/10.1016/j.elecom.2010.12.015>.
- (78) Qu, Q.; Fu, L.; Zhan, X.; Samuelis, D.; Maier, J.; Li, L.; Tian, S.; Li, Z.; Wu, Y. Porous LiMn₂O₄ as Cathode Material with High Power and Excellent Cycling for Aqueous Rechargeable Lithium Batteries. *Energy Environ. Sci.* **2011**, *4* (10), 3985. <https://doi.org/10.1039/c0ee00673d>.
- (79) Alias, N.; Mohamad, A. A. Advances of Aqueous Rechargeable Lithium-Ion Battery: A Review. *Journal of Power Sources* **2015**, *274*, 237–251. <https://doi.org/10.1016/j.jpowsour.2014.10.009>.
- (80) Li, W.; Dahn, J. R.; Wainwright, D. S. Rechargeable Lithium Batteries with Aqueous Electrolytes. *Science* **1994**, *264* (5162), 1115–1118. <https://doi.org/10.1126/science.264.5162.1115>.

- (81) Tian, L.; Yuan, A. Electrochemical Performance of Nanostructured Spinel LiMn_2O_4 in Different Aqueous Electrolytes. *Journal of Power Sources* **2009**, *192* (2), 693–697. <https://doi.org/10.1016/j.jpowsour.2009.03.002>.
- (82) Yadegari, H.; Jabbari, A.; Heli, H. An Aqueous Rechargeable Lithium-Ion Battery Based on LiCoO_2 Nanoparticles Cathode and LiV_3O_8 Nanosheets Anode. *J Solid State Electrochem* **2012**, *16* (1), 227–234. <https://doi.org/10.1007/s10008-011-1315-x>.
- (83) Ruffo, R.; Wessells, C.; Huggins, R. A.; Cui, Y. Electrochemical Behavior of LiCoO_2 as Aqueous Lithium-Ion Battery Electrodes. *Electrochemistry Communications* **2009**, *11* (2), 247–249. <https://doi.org/10.1016/j.elecom.2008.11.015>.
- (84) Ruffo, R.; La Mantia, F.; Wessells, C.; Huggins, R. A.; Cui, Y. Electrochemical Characterization of LiCoO_2 as Rechargeable Electrode in Aqueous LiNO_3 Electrolyte. *Solid State Ionics* **2011**, *192* (1), 289–292. <https://doi.org/10.1016/j.ssi.2010.05.043>.
- (85) Zhao, M. Excellent Rate Capabilities of $(\text{LiFePO}_4/\text{C})/\text{LiV}_3\text{O}_8$ in an Optimized Aqueous Solution Electrolyte. *Journal of Power Sources* **2013**, *6*.
- (86) Vujković, M.; Stojković, I.; Cvjetićanin, N.; Mentus, S. Gel-Combustion Synthesis of LiFePO_4/C Composite with Improved Capacity Retention in Aerated Aqueous Electrolyte Solution. *Electrochimica Acta* **2013**, *92*, 248–256. <https://doi.org/10.1016/j.electacta.2013.01.030>.
- (87) Zhao, M.; Huang, G.; Zhang, B.; Wang, F.; Song, X. Characteristics and Electrochemical Performance of $\text{LiFe}_{0.5}\text{Mn}_{0.5}\text{PO}_4/\text{C}$ Used as Cathode for Aqueous Rechargeable Lithium Battery. *Journal of Power Sources* **2012**, *211*, 202–207. <https://doi.org/10.1016/j.jpowsour.2012.03.049>.
- (88) Wang, H.; Zeng, Y.; Huang, K.; Liu, S.; Chen, L. Improvement of Cycle Performance of Lithium Ion Cell $\text{LiMn}_2\text{O}_4/\text{Li}_x\text{V}_2\text{O}_5$ with Aqueous Solution Electrolyte by Polypyrrole Coating on Anode. *Electrochimica Acta* **2007**, *52* (15), 5102–5107. <https://doi.org/10.1016/j.electacta.2007.02.004>.
- (89) Wessells, C.; Huggins, R. A.; Cui, Y. Recent Results on Aqueous Electrolyte Cells. *Journal of Power Sources* **2011**, *196* (5), 2884–2888. <https://doi.org/10.1016/j.jpowsour.2010.10.098>.
- (90) Tang, W.; Liu, L. L.; Tian, S.; Li, L.; Li, L. L.; Yue, Y. B.; Bai, Y.; Wu, Y. P.; Zhu, K.; Holze, R. LiMn_2O_4 Nanorods as a Super-Fast Cathode Material for Aqueous Rechargeable Lithium Batteries. *Electrochemistry Communications* **2011**, *13* (11), 1159–1162. <https://doi.org/10.1016/j.elecom.2011.09.008>.
- (91) Luo, J.-Y.; Xia, Y.-Y. Aqueous Lithium-Ion Battery $\text{LiTi}_2(\text{PO}_4)_3/\text{LiMn}_2\text{O}_4$ with High Power and Energy Densities as Well as Superior Cycling Stability**. *Adv. Funct. Mater.* **2007**, *17* (18), 3877–3884. <https://doi.org/10.1002/adfm.200700638>.

- (92) Ramanujapuram, A.; Gordon, D.; Magasinski, A.; Ward, B.; Nitta, N.; Huang, C.; Yushin, G. Degradation and Stabilization of Lithium Cobalt Oxide in Aqueous Electrolytes. *Energy Environ. Sci.* **2016**, 9 (5), 1841–1848. <https://doi.org/10.1039/C6EE00093B>.
- (93) Mi, C. H.; Zhang, X. G.; Li, H. L. Electrochemical Behaviors of Solid LiFePO_4 and $\text{Li}_{0.99}\text{Nb}_{0.01}\text{FePO}_4$ in Li_2SO_4 Aqueous Electrolyte. *Journal of Electroanalytical Chemistry* **2007**, 602 (2), 245–254. <https://doi.org/10.1016/j.jelechem.2007.01.007>.
- (94) Mahesh, K. C.; Suresh, G. S.; Venkatesha, T. V. Electrochemical Behavior of $\text{Li}[\text{Li}_{0.2}\text{Co}_{0.3}\text{Mn}_{0.5}]\text{O}_2$ as Cathode Material in Li_2SO_4 Aqueous Electrolyte. *J Solid State Electrochem* **2012**, 16 (11), 3559–3571. <https://doi.org/10.1007/s10008-012-1787-3>.
- (95) Zhou, D.; Liu, S.; Wang, H.; Yan, G. $\text{Na}_2\text{V}_6\text{O}_{16} \cdot 0.14\text{H}_2\text{O}$ Nanowires as a Novel Anode Material for Aqueous Rechargeable Lithium Battery with Good Cycling Performance. *Journal of Power Sources* **2013**, 227, 111–117. <https://doi.org/10.1016/j.jpowsour.2012.11.022>.
- (96) Liu, X.-H.; Saito, T.; Doi, T.; Okada, S.; Yamaki, J. Electrochemical Properties of Rechargeable Aqueous Lithium Ion Batteries with an Olivine-Type Cathode and a Nasicon-Type Anode. *Journal of Power Sources* **2009**, 189 (1), 706–710. <https://doi.org/10.1016/j.jpowsour.2008.08.050>.
- (97) Manjunatha, H.; Suresh, G. S.; Venkatesha, T. V. Electrode Materials for Aqueous Rechargeable Lithium Batteries. *J Solid State Electrochem* **2011**, 15 (3), 431–445. <https://doi.org/10.1007/s10008-010-1117-6>.
- (98) Degoulange, D.; Dubouis, N.; Grimaud, A. Towards the Understanding of Water-in-Salt Electrolytes: Individual Ion Activities and Liquid Junction Potentials in Highly Concentrated Aqueous Solutions. *Physical Chemistry* **2021**, 33.
- (99) Zhao, M. Electrochemical Performance of High Specific Capacity of Lithium-Ion Cell $\text{LiV}_3\text{O}_8/\text{LiMn}_2\text{O}_4$ with LiNO_3 Aqueous Solution Electrolyte. *Electrochimica Acta* **2011**, 4.
- (100) Wang, G. J.; Zhao, N. H.; Yang, L. C.; Wu, Y. P.; Wu, H. Q.; Holze, R. Characteristics of an Aqueous Rechargeable Lithium Battery (ARLB). *Electrochimica Acta* **2007**, 52 (15), 4911–4915. <https://doi.org/10.1016/j.electacta.2007.01.051>.
- (101) Li, W.; McKinnon, W. R.; Dahn, J. R. Lithium Intercalation from Aqueous Solutions. *J. Electrochem. Soc.* **1994**, 141 (9), 7.
- (102) Li, W.; Dahn, J. R. Lithium-Ion Cells with Aqueous Electrolytes. *J. Electrochem. Soc.* **1995**, 142 (6), 1742–1746. <https://doi.org/10.1149/1.2044187>.

- (103) Wang, P.; Yang, H.; Yang, H. Electrochemical Behavior of Li-Mn Spinel Electrode Material in Aqueous Solution. *Journal of Power Sources* **1996**, *63*, 275–278.
- (104) Yu, D. Y. W. Impurities in LiFePO_4 and Their Influence on Material Characteristics. *Meet. Abstr.* **2007**. <https://doi.org/10.1149/MA2007-02/10/646>.
- (105) Manickam, M.; Singh, P.; Thurgate, S.; Prince, K. Redox Behavior and Surface Characterization of LiFePO_4 in Lithium Hydroxide Electrolyte. *Journal of Power Sources* **2006**, *158* (1), 646–649. <https://doi.org/10.1016/j.jpowsour.2005.08.059>.
- (106) He, P.; Wang, Y.; Zhou, H. The Effect of Alkalinity and Temperature on the Performance of Lithium-Air Fuel Cell with Hybrid Electrolytes. *Journal of Power Sources* **2011**, *196* (13), 5611–5616. <https://doi.org/10.1016/j.jpowsour.2011.02.071>.
- (107) Luo, J.-Y.; Cui, W.-J.; He, P.; Xia, Y.-Y. Raising the Cycling Stability of Aqueous Lithium-Ion Batteries by Eliminating Oxygen in the Electrolyte. *Nature Chem* **2010**, *2* (9), 760–765. <https://doi.org/10.1038/nchem.763>.
- (108) Manthiram, A.; Choi, J. Chemical and Structural Instabilities of Lithium Ion Battery Cathodes. *Journal of Power Sources* **2006**, *159* (1), 249–253. <https://doi.org/10.1016/j.jpowsour.2006.04.028>.
- (109) Bin, D.; Wen, Y.; Wang, Y.; Xia, Y. The Development in Aqueous Lithium-Ion Batteries. *Journal of Energy Chemistry* **2018**, *27* (6), 1521–1535. <https://doi.org/10.1016/j.jechem.2018.06.004>.
- (110) Wang, Y.; Luo, J.; Wang, C.; Xia, Y. Hybrid Aqueous Energy Storage Cells Using Activated Carbon and Lithium-Ion Intercalated Compounds. *J. Electrochem. Soc.* **2006**, *153* (8), A1425. <https://doi.org/10.1149/1.2203772>.
- (111) Suo, L.; Borodin, O.; Gao, T.; Olguin, M.; Ho, J.; Fan, X.; Luo, C.; Wang, C.; Xu, K. “Water-in-Salt” Electrolyte Enables High-Voltage Aqueous Lithium-Ion Chemistries. *Science* **2015**, *350* (6263), 938–943. <https://doi.org/10.1126/science.aab1595>.
- (112) Wang, H.; Huang, K.; Zeng, Y.; Yang, S.; Chen, L. Electrochemical Properties of TiP_2O_7 and $\text{LiTi}_2(\text{PO}_4)_3$ as Anode Material for Lithium Ion Battery with Aqueous Solution Electrolyte. *Electrochimica Acta* **2007**, *52* (9), 3280–3285. <https://doi.org/10.1016/j.electacta.2006.10.010>.
- (113) Wojciechowski, J.; Kolanowski, Ł.; Bund, A.; Lota, G. The Influence of Current Collector Corrosion on the Performance of Electrochemical Capacitors. *Journal of Power Sources* **2017**, *368*, 18–29. <https://doi.org/10.1016/j.jpowsour.2017.09.069>.
- (114) Hou, Y.; Wang, X.; Zhu, Y.; Hu, C.; Chang, Z.; Wu, Y.; Holze, R. Macroporous LiFePO_4 as a Cathode for an Aqueous Rechargeable Lithium Battery of High

- Energy Density. *J. Mater. Chem. A* **2013**, *1* (46), 14713. <https://doi.org/10.1039/c3ta13472e>.
- (115) He, K.; Zu, C.; Wang, Y.; Han, B.; Yin, X.; Zhao, H.; Liu, Y.; Chen, J. Stability of Lithium Ion Conductor NASICON Structure Glass Ceramic in Acid and Alkaline Aqueous Solution. *Solid State Ionics* **2014**, *254*, 78–81. <https://doi.org/10.1016/j.ssi.2013.11.011>.
- (116) Imanishi, N.; Matsui, M.; Takeda, Y.; Yamamoto, O. Lithium Ion Conducting Solid Electrolytes for Aqueous Lithium-Air Batteries. *Electrochemistry* **2014**, *82* (11), 938–945. <https://doi.org/10.5796/electrochemistry.82.938>.
- (117) Wang, X.; Qu, Q.; Hou, Y.; Wang, F.; Wu, Y. An Aqueous Rechargeable Lithium Battery of High Energy Density Based on Coated Li Metal and LiCoO₂. *Chem. Commun.* **2013**, *49* (55), 6179. <https://doi.org/10.1039/c3cc42676a>.
- (118) Chang, Z.; Li, C.; Wang, Y.; Chen, B.; Fu, L.; Zhu, Y.; Zhang, L.; Wu, Y.; Huang, W. A Lithium Ion Battery Using an Aqueous Electrolyte Solution. *Sci Rep* **2016**, *6* (1), 28421. <https://doi.org/10.1038/srep28421>.
- (119) Wang, X.; Hou, Y.; Zhu, Y.; Wu, Y.; Holze, R. An Aqueous Rechargeable Lithium Battery Using Coated Li Metal as Anode. *SCIENTIFIC REPORTS* **5**.
- (120) Alloin, F.; Crepel, L.; Cointeaux, L.; Leprêtre, J.-C.; Fusalba, F.; Martinet, S. The Interest of Diazonium Chemistry for Aqueous Lithium-Ion Battery. *J. Electrochem. Soc.* **2013**, *160* (5), A3171–A3178. <https://doi.org/10.1149/2.026305jes>.
- (121) Crepel, L.; Alloin, F.; Lepretre, J.-C.; Martinet, S.; Li, H. (54) ARYL DAZONUMI SALT AND USE IN AN ELECTROLYTIC SOLUTION OF AN ELECTROCHEMICAL GENERATOR. **15**.
- (122) Suo, L.; Borodin, O.; Sun, W.; Fan, X.; Yang, C.; Wang, F.; Gao, T.; Ma, Z.; Schroeder, M.; von Cresce, A.; Russell, S. M.; Armand, M.; Angell, A.; Xu, K.; Wang, C. Advanced High-Voltage Aqueous Lithium-Ion Battery Enabled by “Water-in-Bisalt” Electrolyte. *Angewandte Chemie International Edition* **2016**, *55* (25), 7136–7141. <https://doi.org/10.1002/anie.201602397>.
- (123) Han, S. Anionic Effects on the Structure and Dynamics of Water in Superconcentrated Aqueous Electrolytes. *RSC Adv.* **2019**, *9* (2), 609–619. <https://doi.org/10.1039/C8RA09589B>.
- (124) Lux, S. F.; Terborg, L.; Hachmöller, O.; Placke, T.; Meyer, H.-W.; Passerini, S.; Winter, M.; Nowak, S. LiTFSI Stability in Water and Its Possible Use in Aqueous Lithium-Ion Batteries: pH Dependency, Electrochemical Window and Temperature Stability. *Journal of The Electrochemical Society* **2013**, *160* (10), A1694–A1700. <https://doi.org/10.1149/2.039310jes>.

- (125) Reber, D.; Figi, R.; Kühnel, R.-S.; Battaglia, C. Stability of Aqueous Electrolytes Based on LiFSI and NaFSI. *Electrochimica Acta* **2019**, *321*, 134644. <https://doi.org/10.1016/j.electacta.2019.134644>.
- (126) Ding, M. S.; Xu, K. Phase Diagram, Conductivity, and Glass Transition of LiTFSI–H₂O Binary Electrolytes. *J. Phys. Chem. C* **2018**, *122* (29), 16624–16629. <https://doi.org/10.1021/acs.jpcc.8b05193>.
- (127) Dubouis, N.; France-Lanord, A.; Brige, A.; Salanne, M.; Grimaud, A. Anion Specific Effects Drive the Formation of Li-Salt Based Aqueous Biphasic Systems. *J. Phys. Chem. B* **2021**, *acs.jpcc.1c01750*. <https://doi.org/10.1021/acs.jpcc.1c01750>.
- (128) Zhang, Y.; Lewis, N. H. C.; Mars, J.; Wan, G.; Weadock, N. J.; Takacs, C. J.; Lukatskaya, M. R.; Steinrück, H.-G.; Toney, M. F.; Tokmakoff, A.; Maginn, E. J. Water-in-Salt LiTFSI Aqueous Electrolytes. 1. Liquid Structure from Combined Molecular Dynamics Simulation and Experimental Studies. *J. Phys. Chem. B* **2021**, *125* (17), 4501–4513. <https://doi.org/10.1021/acs.jpcc.1c02189>.
- (129) Lewis, N. H. C.; Zhang, Y.; Dereka, B.; Carino, E. V.; Maginn, E. J.; Tokmakoff, A. Signatures of Ion Pairing and Aggregation in the Vibrational Spectroscopy of Super-Concentrated Aqueous Lithium Bistriflimide Solutions. *J. Phys. Chem. C* **2020**, *124* (6), 3470–3481. <https://doi.org/10.1021/acs.jpcc.9b10477>.
- (130) Tsurumura, T.; Hashimoto, Y.; Morita, M.; Umebayashi, Y.; Fujii, K. Anion Coordination Characteristics of Ion-Pair Complexes in Highly Concentrated Aqueous Lithium Bis(Trifluoromethanesulfonyl)Amide Electrolytes. *Anal. Sci.* **2019**, *35* (3), 289–294. <https://doi.org/10.2116/analsci.18P407>.
- (131) Liu, X.; Yu, Z.; Sarnello, E.; Qian, K.; Seifert, S.; Winans, R. E.; Cheng, L.; Li, T. Microscopic Understanding of the Ionic Networks of “Water-in-Salt” Electrolytes. *Energy Material Advances* **2021**, *2021*, 1–9. <https://doi.org/10.34133/2021/7368420>.
- (132) Watanabe, H.; Arai, N.; Nozaki, E.; Han, J.; Fujii, K.; Ikeda, K.; Otomo, T.; Ueno, K.; Dokko, K.; Watanabe, M.; Kameda, Y.; Umebayashi, Y. Local Structure of Li⁺ in Superconcentrated Aqueous LiTFSI Solutions. *J. Phys. Chem. B* **2021**, *125* (27), 7477–7484. <https://doi.org/10.1021/acs.jpcc.1c04693>.
- (133) González, M. A.; Borodin, O.; Kofu, M.; Shibata, K.; Yamada, T.; Yamamuro, O.; Xu, K.; Price, D. L.; Saboungi, M.-L. Nanoscale Relaxation in “Water-in-Salt” and “Water-in-Bisalt” Electrolytes. *J. Phys. Chem. Lett.* **2020**, *11* (17), 7279–7284. <https://doi.org/10.1021/acs.jpclett.0c01765>.
- (134) Dubouis, N.; Lemaire, P.; Mirvaux, B.; Salager, E.; Deschamps, M.; Grimaud, A. The Role of the Hydrogen Evolution Reaction in the Solid–Electrolyte Interphase Formation Mechanism for “Water-in-Salt” Electrolytes. *Energy & Environmental Science* **2018**, *11* (12), 3491–3499. <https://doi.org/10.1039/C8EE02456A>.

- (135) Borodin, O.; Suo, L.; Gobet, M.; Ren, X.; Wang, F.; Faraone, A.; Peng, J.; Olguin, M.; Schroeder, M.; Ding, M. S.; Gobrogge, E.; von Wald Cresce, A.; Munoz, S.; Dura, J. A.; Greenbaum, S.; Wang, C.; Xu, K. Liquid Structure with Nano-Heterogeneity Promotes Cationic Transport in Concentrated Electrolytes. *ACS Nano* **2017**, *11* (10), 10462–10471. <https://doi.org/10.1021/acsnano.7b05664>.
- (136) Yu, Z.; Curtiss, L. A.; Winans, R. E.; Zhang, Y.; Li, T.; Cheng, L. Asymmetric Composition of Ionic Aggregates and the Origin of High Correlated Transference Number in Water-in-Salt Electrolytes. *J. Phys. Chem. Lett.* **2020**, *11* (4), 1276–1281. <https://doi.org/10.1021/acs.jpcclett.9b03495>.
- (137) Lim, J.; Park, K.; Lee, H.; Kim, J.; Kwak, K.; Cho, M. Nanometric Water Channels in Water-in-Salt Lithium Ion Battery Electrolyte. *J. Am. Chem. Soc.* **2018**, *140* (46), 15661–15667. <https://doi.org/10.1021/jacs.8b07696>.
- (138) Tan, P.; Yue, J.; Yu, Y.; Liu, B.; Liu, T.; Zheng, L.; He, L.; Zhang, X.; Suo, L.; Hong, L. Solid-Like Nano-Anion Cluster Constructs a Free Lithium-Ion-Conducting Superfluid Framework in a Water-in-Salt Electrolyte. *J. Phys. Chem. C* **2021**, *125* (22), 11838–11847. <https://doi.org/10.1021/acs.jpcc.1c01663>.
- (139) Zhang, M.; Hao, H.; Zhou, D.; Duan, Y.; Wang, Y.; Bian, H. Understanding the Microscopic Structure of a “Water-in-Salt” Lithium Ion Battery Electrolyte Probed with Ultrafast IR Spectroscopy. *J. Phys. Chem. C* **2020**, *124* (16), 8594–8604. <https://doi.org/10.1021/acs.jpcc.0c00937>.
- (140) McEldrew, M.; Goodwin, Z. A. H.; Bi, S.; Kornyshev, A. A.; Bazant, M. Z. Ion Clusters and Networks in “Water-in-Salt Electrolytes.” *arXiv:2103.04782 [cond-mat, physics:physics]* **2021**.
- (141) Li, Z.; Bouchal, R.; Mendez-Morales, T.; Rollet, A.-L.; Rizzi, C.; Le Vot, S.; Favier, F.; Rotenberg, B.; Borodin, O.; Fontaine, O.; Salanne, M. Transport Properties of Li-TFSI Water-in-Salt Electrolytes. *J. Phys. Chem. B* **2019**, *123* (49), 10514–10521. <https://doi.org/10.1021/acs.jpcb.9b08961>.
- (142) Amiri, M.; Bélanger, D. Physicochemical and Electrochemical Properties of Water-in-Salt Electrolytes. *ChemSusChem* **2021**, *14* (12), 2487–2500. <https://doi.org/10.1002/cssc.202100550>.
- (143) Zheng, J.; Tan, G.; Shan, P.; Liu, T.; Hu, J.; Feng, Y.; Yang, L.; Zhang, M.; Chen, Z.; Lin, Y.; Lu, J.; Neufeind, J. C.; Ren, Y.; Amine, K.; Wang, L.-W.; Xu, K.; Pan, F. Understanding Thermodynamic and Kinetic Contributions in Expanding the Stability Window of Aqueous Electrolytes. *Chem* **2018**. <https://doi.org/10.1016/j.chempr.2018.09.004>.
- (144) Dubouis, N.; Serva, A.; Salager, E.; Deschamps, M.; Salanne, M.; Grimaud, A. The Fate of Water at the Electrochemical Interfaces: Electrochemical Behavior of Free Water Versus Coordinating Water. *J. Phys. Chem. Lett.* **2018**, *6*.

- (145) Han, M.; Zhang, R.; Gewirth, A. A.; Espinosa-Marzal, R. M. Nanoheterogeneity of LiTFSI Solutions Transitions Close to a Surface and with Concentration. *Nano Lett.* **2021**, *21* (5), 2304–2309. <https://doi.org/10.1021/acs.nanolett.1c00167>.
- (146) Suo, L.; Oh, D.; Lin, Y.; Zhuo, Z.; Borodin, O.; Gao, T.; Wang, F.; Kushima, A.; Wang, Z.; Kim, H.-C.; Qi, Y.; Yang, W.; Pan, F.; Li, J.; Xu, K.; Wang, C. How Solid-Electrolyte Interphase Forms in Aqueous Electrolytes. *Journal of the American Chemical Society* **2017**, *139* (51), 18670–18680. <https://doi.org/10.1021/jacs.7b10688>.
- (147) Steinrück, H.; Cao, C.; Lukatskaya, M. R.; Takacs, C. J.; Wan, G.; Mackanic, D. G.; Tsao, Y.; Zhao, J.; Helms, B. A.; Xu, K.; Borodin, O.; Wishart, J. F.; Toney, M. F. Interfacial Speciation Determines Interfacial Chemistry: X-ray-Induced Lithium Fluoride Formation from Water-in-salt Electrolytes on Solid Surfaces. *Angew. Chem. Int. Ed.* **2020**, anie.202007745. <https://doi.org/10.1002/anie.202007745>.
- (148) Ko, S.; Yamada, Y.; Yamada, A. Formation of a Solid Electrolyte Interphase in Hydrate-Melt Electrolytes. *ACS Appl. Mater. Interfaces* **2019**, acsami.9b13662. <https://doi.org/10.1021/acsami.9b13662>.
- (149) Bouchal, R.; Li, Z.; Bongu, C.; Favier, F.; Freunberger, S. A.; Salanne, M.; Fontaine, O. Competitive Salt Precipitation/Dissolution during Free-Water Reduction in Water-in-Salt Electrolyte. *Angewandte Chemie International Edition* **2020**, *59*, 6.
- (150) Vatamanu, J.; Borodin, O. Ramifications of Water-in-Salt Interfacial Structure at Charged Electrodes for Electrolyte Electrochemical Stability. *The Journal of Physical Chemistry Letters* **2017**, *8* (18), 4362–4367. <https://doi.org/10.1021/acs.jpclett.7b01879>.
- (151) Zhang, R.; Han, M.; Ta, K.; Madsen, K. E.; Chen, X.; Zhang, X.; Espinosa-Marzal, R. M.; Gewirth, A. A. Potential-Dependent Layering in the Electrochemical Double Layer of Water-in-Salt Electrolytes. *ACS Appl. Energy Mater.* **2020**, *3* (8), 8086–8094. <https://doi.org/10.1021/acsaem.0c01534>.
- (152) Coustan, L.; Shul, G.; Bélanger, D. Electrochemical Behavior of Platinum, Gold and Glassy Carbon Electrodes in Water-in-Salt Electrolyte. *Electrochemistry Communications* **2017**, *77*, 89–92. <https://doi.org/10.1016/j.elecom.2017.03.001>.
- (153) Kühnel, R.-S.; Reber, D.; Battaglia, C. Perspective—Electrochemical Stability of Water-in-Salt Electrolytes. *J. Electrochem. Soc.* **2020**, *167* (7), 070544. <https://doi.org/10.1149/1945-7111/ab7c6f>.
- (154) Takenaka, N.; Inagaki, T.; Shimada, T.; Yamada, Y.; Nagaoka, M.; Yamada, A. Theoretical Analysis of Electrode-Dependent Interfacial Structures on Hydrate-Melt Electrolytes. *J Chem. Phys.* **2020**, *152* (12), 124706. <https://doi.org/10.1063/5.0003196>.

- (155) McEldrew, M.; Goodwin, Z. A. H.; Kornyshev, A. A.; Bazant, M. Z. Theory of the Double Layer in Water-in-Salt Electrolytes. *The Journal of Physical Chemistry Letters* **2018**, *9* (19), 5840–5846. <https://doi.org/10.1021/acs.jpclett.8b02543>.
- (156) Liu, S.; Liu, D.; Wang, S.; Cai, X.; Qian, K.; Kang, F.; Li, B. Understanding the Cathode Electrolyte Interface Formation in Aqueous Electrolyte by Scanning Electrochemical Microscopy. *J. Mater. Chem. A* **2019**, *7* (21), 12993–12996. <https://doi.org/10.1039/C9TA03199E>.
- (157) Sun, W.; Suo, L.; Wang, F.; Eidson, N.; Yang, C.; Han, F.; Ma, Z.; Gao, T.; Zhu, M.; Wang, C. “Water-in-Salt” Electrolyte Enabled LiMn₂O₄/TiS₂ Lithium-Ion Batteries. *Electrochemistry Communications* **2017**, *82*, 71–74. <https://doi.org/10.1016/j.elecom.2017.07.016>.
- (158) Yue, J.; Lin, L.; Jiang, L.; Zhang, Q.; Tong, Y.; Suo, L.; Hu, Y.; Li, H.; Huang, X.; Chen, L. Interface Concentrated-Confinement Suppressing Cathode Dissolution in Water-in-Salt Electrolyte. *Adv. Energy Mater.* **2020**, *10* (36), 2000665. <https://doi.org/10.1002/aenm.202000665>.
- (159) Wang, F.; Lin, Y.; Suo, L.; Fan, X.; Gao, T.; Yang, C.; Han, F.; Qi, Y.; Xu, K.; Wang, C. Stabilizing High Voltage LiCoO₂ Cathode in Aqueous Electrolyte with Interphase-Forming Additive. *Energy & Environmental Science* **2016**, *9* (12), 3666–3673. <https://doi.org/10.1039/C6EE02604D>.
- (160) Kühnel, R.-S.; Reber, D.; Remhof, A.; Figi, R.; Bleiner, D.; Battaglia, C. “Water-in-Salt” Electrolytes Enable the Use of Cost-Effective Aluminum Current Collectors for Aqueous High-Voltage Batteries. *Chemical Communications* **2016**, *52* (68), 10435–10438. <https://doi.org/10.1039/C6CC03969C>.
- (161) Han, J.; Zhang, H.; Varzi, A.; Passerini, S. Fluorine-Free Water-in-Salt Electrolyte for Green and Low-Cost Aqueous Sodium-Ion Batteries. *ChemSusChem* **2018**, *11* (21), 3704–3707. <https://doi.org/10.1002/cssc.201801930>.
- (162) Jiang, L.; Liu, L.; Yue, J.; Zhang, Q.; Zhou, A.; Borodin, O.; Suo, L.; Li, H.; Chen, L.; Xu, K.; Hu, Y. High-Voltage Aqueous Na-Ion Battery Enabled by Inert-Cation-Assisted Water-in-Salt Electrolyte. *Adv. Mater.* **2020**, *32* (2), 1904427. <https://doi.org/10.1002/adma.201904427>.
- (163) Reber, D.; Kühnel, R.-S.; Battaglia, C. Suppressing Crystallization of Water-in-Salt Electrolytes by Asymmetric Anions Enables Low-Temperature Operation of High-Voltage Aqueous Batteries. *ACS Materials Lett.* **2019**, *1* (1), 44–51. <https://doi.org/10.1021/acsmaterialslett.9b00043>.
- (164) Suo, L.; Borodin, O.; Wang, Y.; Rong, X.; Sun, W.; Fan, X.; Xu, S.; Schroeder, M. A.; Cresce, A. V.; Wang, F.; Yang, C.; Hu, Y.-S.; Xu, K.; Wang, C. “Water-in-Salt” Electrolyte Makes Aqueous Sodium-Ion Battery Safe, Green, and Long-Lasting. *Advanced Energy Materials* **2017**, *7* (21), 1701189. <https://doi.org/10.1002/aenm.201701189>.

- (165) Zheng, Q.; Miura, S.; Miyazaki, K.; Ko, S.; Watanabe, E.; Okoshi, M.; Chou, C.-P.; Nishimura, Y.; Nakai, H.; Kamiya, T.; Honda, T.; Akikusa, J.; Yamada, Y.; Yamada, A. Sodium- and Potassium-Hydrate Melts Containing Asymmetric Imide Anions for High-Voltage Aqueous Batteries. *Angew. Chem. Int. Ed.* **2019**, *58* (40), 14202–14207. <https://doi.org/10.1002/anie.201908830>.
- (166) Chen, H.; Zhang, Z.; Wei, Z.; Chen, G.; Yang, X.; Wang, C.; Du, F. Use of a Water-in-Salt Electrolyte to Avoid Organic Material Dissolution and Enhance the Kinetics of Aqueous Potassium Ion Batteries. *Sustainable Energy Fuels* **2020**, *4* (1), 128–131. <https://doi.org/10.1039/C9SE00545E>.
- (167) Jiang, L.; Lu, Y.; Zhao, C.; Liu, L.; Zhang, J.; Zhang, Q.; Shen, X.; Zhao, J.; Yu, X.; Li, H.; Huang, X.; Chen, L.; Hu, Y.-S. Building Aqueous K-Ion Batteries for Energy Storage. *Nat Energy* **2019**. <https://doi.org/10.1038/s41560-019-0388-0>.
- (168) Leonard, D. P.; Wei, Z.; Chen, G.; Du, F.; Ji, X. Water-in-Salt Electrolyte for Potassium-Ion Batteries. *ACS Energy Letters* **2018**, *3* (2), 373–374. <https://doi.org/10.1021/acsenergylett.8b00009>.
- (169) Liu, T.; Tang, L.; Luo, H.; Cheng, S.; Liu, M. A Promising Water-in-Salt Electrolyte for Aqueous Based Electrochemical Energy Storage Cells with a Wide Potential Window: Highly Concentrated HCOOK. *Chem. Commun.* **2019**, *55* (85), 12817–12820. <https://doi.org/10.1039/C9CC05927J>.
- (170) Cao, L.; Li, D.; Pollard, T.; Deng, T.; Zhang, B.; Yang, C.; Chen, L.; Vatamanu, J.; Hu, E.; Hourwitz, M. J.; Ma, L.; Ding, M.; Li, Q.; Hou, S.; Gaskell, K.; Fourkas, J. T.; Yang, X.-Q.; Xu, K.; Borodin, O.; Wang, C. Fluorinated Interphase Enables Reversible Aqueous Zinc Battery Chemistries. *Nat. Nanotechnol.* **2021**, *16* (8), 902–910. <https://doi.org/10.1038/s41565-021-00905-4>.
- (171) Ni, Q.; Jiang, H.; Sandstrom, S.; Bai, Y.; Ren, H.; Wu, X.; Guo, Q.; Yu, D.; Wu, C.; Ji, X. A $\text{Na}_3\text{V}_2(\text{PO}_4)_2\text{O}_{1.6}\text{F}_{1.4}$ Cathode of Zn-Ion Battery Enabled by a Water-in-Bisalt Electrolyte. *Adv. Funct. Mater.* **2020**, *30* (36), 2003511. <https://doi.org/10.1002/adfm.202003511>.
- (172) Dong, Q.; Yao, X.; Zhao, Y.; Qi, M.; Zhang, X.; Sun, H.; He, Y.; Wang, D. Cathodically Stable Li-O₂ Battery Operations Using Water-in-Salt Electrolyte. *Chem* **2018**, *4* (6), 1345–1358. <https://doi.org/10.1016/j.chempr.2018.02.015>.
- (173) Yang, C.; Suo, L.; Borodin, O.; Wang, F.; Sun, W.; Gao, T.; Fan, X.; Hou, S.; Ma, Z.; Amine, K.; Xu, K.; Wang, C. Unique Aqueous Li-Ion/Sulfur Chemistry with High Energy Density and Reversibility. *Proc Natl Acad Sci USA* **2017**, *114* (24), 6197–6202. <https://doi.org/10.1073/pnas.1703937114>.
- (174) Park, J. M.; Jana, M.; Nakhani, P.; Kim, B.-K.; Park, H. S. Facile Multivalent Redox Chemistries in Water-in-Bisalt Hydrogel Electrolytes for Hybrid Energy Storage Full Cells. *ACS Energy Lett.* **2020**, 1054–1061. <https://doi.org/10.1021/acsenergylett.0c00059>.

- (175) Zhao, J.; Li, Y.; Peng, X.; Dong, S.; Ma, J.; Cui, G.; Chen, L. High-Voltage Zn/LiMn_{0.8}Fe_{0.2}PO₄ Aqueous Rechargeable Battery by Virtue of “Water-in-Salt” Electrolyte. *Electrochemistry Communications* **2016**, *69*, 6–10. <https://doi.org/10.1016/j.elecom.2016.05.014>.
- (176) Wang, F.; Borodin, O.; Gao, T.; Fan, X.; Sun, W.; Han, F.; Faraone, A.; Dura, J. A.; Xu, K.; Wang, C. Highly Reversible Zinc Metal Anode for Aqueous Batteries. *Nature Materials* **2018**, *17* (6), 543–549. <https://doi.org/10.1038/s41563-018-0063-z>.
- (177) Yang, C.; Chen, J.; Ji, X.; Pollard, T. P.; Lü, X.; Sun, C.-J.; Hou, S.; Liu, Q.; Liu, C.; Qing, T.; Wang, Y.; Borodin, O.; Ren, Y.; Xu, K.; Wang, C. Aqueous Li-Ion Battery Enabled by Halogen Conversion–Intercalation Chemistry in Graphite. *Nature* **2019**, *569* (7755), 245–250. <https://doi.org/10.1038/s41586-019-1175-6>.
- (178) Guo, Q.; Kim, K.-I.; Li, S.; Scida, A. M.; Yu, P.; Sandstrom, S. K.; Zhang, L.; Sun, S.; Jiang, H.; Ni, Q.; Yu, D.; Lerner, M. M.; Xia, H.; Ji, X. Reversible Insertion of I–Cl Interhalogen in a Graphite Cathode for Aqueous Dual-Ion Batteries. *ACS Energy Lett.* **2021**, *6* (2), 459–467. <https://doi.org/10.1021/acsenenergylett.0c02575>.
- (179) Wu, X.; Xu, Y.; Zhang, C.; Leonard, D. P.; Markir, A.; Lu, J.; Ji, X. Reverse Dual-Ion Battery via a ZnCl₂ Water-in-Salt Electrolyte. *J. Am. Chem. Soc.* **2019**, *141* (15), 6338–6344. <https://doi.org/10.1021/jacs.9b00617>.
- (180) Forero-Saboya, J.; Hosseini-Bab-Anari, E.; Abdelhamid, M. E.; Moth-Poulsen, K.; Johansson, P. Water-in-Bisalt Electrolyte with Record Salt Concentration and Widened Electrochemical Stability Window. *J. Phys. Chem. Lett.* **2019**, *10* (17), 4942–4946. <https://doi.org/10.1021/acs.jpcclett.9b01467>.
- (181) Ko, S.; Yamada, Y.; Miyazaki, K.; Shimada, T.; Watanabe, E.; Tateyama, Y.; Kamiya, T.; Honda, T.; Akikusa, J.; Yamada, A. Lithium-Salt Monohydrate Melt: A Stable Electrolyte for Aqueous Lithium-Ion Batteries. *Electrochemistry Communications* **2019**, *104*, 106488. <https://doi.org/10.1016/j.elecom.2019.106488>.
- (182) Reber, D.; Grissa, R.; Becker, M.; Kühnel, R.; Battaglia, C. Anion Selection Criteria for Water-in-Salt Electrolytes. *Adv. Energy Mater.* **2021**, *11* (5), 2002913. <https://doi.org/10.1002/aenm.202002913>.
- (183) Chen, L.; Zhang, J.; Li, Q.; Vatamanu, J.; Ji, X.; Pollard, T. P.; Cui, C.; Hou, S.; Chen, J.; Yang, C.; Ma, L.; Ding, M. S.; Garaga, M.; Greenbaum, S.; Lee, H.-S.; Borodin, O.; Xu, K.; Wang, C. A 63 m Superconcentrated Aqueous Electrolyte for High-Energy Li-Ion Batteries. *ACS Energy Lett.* **2020**, *5* (3), 968–974. <https://doi.org/10.1021/acsenenergylett.0c00348>.
- (184) Lukatskaya, M. R.; Feldblyum, J. I.; Mackanic, D. G.; Lissel, F.; Michels, D. L.; Cui, Y.; Bao, Z. Concentrated Mixed Cation Acetate “Water-in-Salt” Solutions as Green and Low-Cost High Voltage Electrolytes for Aqueous Batteries. *Energy Environ. Sci.* **2018**, *11* (10), 2876–2883. <https://doi.org/10.1039/C8EE00833G>.

- (185) Becker, M.; Reber, D.; Aribia, A.; Battaglia, C.; Kühnel, R.-S. Hybrid Ionic Liquid/Water-in-Salt Electrolytes Enable Stable Cycling of LTO/NMC811 Full Cells. 13.
- (186) Reber, D.; Takenaka, N.; Kühnel, R.-S.; Yamada, A.; Battaglia, C. Impact of Anion Asymmetry on Local Structure and Supercooling Behavior of Water-in-Salt Electrolytes. *J. Phys. Chem. Lett.* **2020**, *11* (12), 4720–4725. <https://doi.org/10.1021/acs.jpclett.0c00806>.
- (187) Becker, M.; Kühnel, R.-S.; Battaglia, C. Water-in-Salt Electrolytes for Aqueous Lithium-Ion Batteries with Liquidus Temperatures Below -10°C . *Chem. Commun.* **2019**, *55* (80), 12032–12035. <https://doi.org/10.1039/C9CC04495G>.
- (188) Nian, Q.; Zhang, X.; Feng, Y.; Liu, S.; Sun, T.; Zheng, S.; Ren, X.; Tao, Z.; Zhang, D.; Chen, J. Designing Electrolyte Structure to Suppress Hydrogen Evolution Reaction in Aqueous Batteries. *ACS Energy Lett.* **2021**, *6* (6), 2174–2180. <https://doi.org/10.1021/acsenergylett.1c00833>.
- (189) Cao, L.; Li, D.; Hu, E. Solvation Structure Design for Aqueous Zn Metal Batteries. *Journal of the American Chemical Society* **6**.
- (190) Hou, Z.; Dong, M.; Xiong, Y.; Zhang, X.; Zhu, Y.; Qian, Y. Formation of Solid–Electrolyte Interfaces in Aqueous Electrolytes by Altering Cation-Solvation Shell Structure. *Adv. Energy Mater.* **2020**, 1903665. <https://doi.org/10.1002/aenm.201903665>.
- (191) Wang, F.; Borodin, O.; Ding, M. S.; Gobet, M.; Vatamanu, J.; Fan, X.; Gao, T.; Eidson, N.; Liang, Y.; Sun, W.; Greenbaum, S.; Xu, K.; Wang, C. Hybrid Aqueous/Non-Aqueous Electrolyte for Safe and High-Energy Li-Ion Batteries. *Joule* **2018**, *2* (5), 927–937. <https://doi.org/10.1016/j.joule.2018.02.011>.
- (192) Chen, J.; Vatamanu, J.; Xing, L.; Borodin, O.; Chen, H.; Guan, X.; Liu, X.; Xu, K.; Li, W. Improving Electrochemical Stability and Low-Temperature Performance with Water/Acetonitrile Hybrid Electrolytes. *Adv. Energy Mater.* **2020**, *10* (3), 1902654. <https://doi.org/10.1002/aenm.201902654>.
- (193) Shang, Y.; Chen, N.; Li, Y.; Chen, S.; Lai, J.; Huang, Y.; Qu, W.; Wu, F.; Chen, R. An “Ether-In-Water” Electrolyte Boosts Stable Interfacial Chemistry for Aqueous Lithium-Ion Batteries. *Adv. Mater.* **2020**, *32* (40), 2004017. <https://doi.org/10.1002/adma.202004017>.
- (194) Hou, X.; Wang, R.; He, X.; Pollard, T. P.; Ju, X.; Du, L.; Paillard, E.; Frielinghaus, H.; Barnsley, L. C.; Borodin, O.; Xu, K.; Winter, M.; Li, J. Stabilizing the Solid-Electrolyte Interphase with Polyacrylamide for High-Voltage Aqueous Lithium-Ion Batteries. *Angew. Chem. Int. Ed.* **2021**, anie.202107252. <https://doi.org/10.1002/anie.202107252>.
- (195) Jaumaux, P.; Yang, X.; Zhang, B.; Safaei, J.; Tang, X.; Zhou, D.; Wang, C.; Wang, G. Localized Water-In-Salt Electrolyte for Aqueous Lithium-Ion Batteries. *Angew.*

- Chem. Int. Ed.* **2021**, *60* (36), 19965–19973.
<https://doi.org/10.1002/anie.202107389>.
- (196) Liu, J.; Yang, C.; Chi, X.; Wen, B.; Wang, W.; Liu, Y. Water/Sulfolane Hybrid Electrolyte Achieves Ultralow-Temperature Operation for High-Voltage Aqueous Lithium-Ion Batteries. *Adv. Funct. Mater.* **2021**, 2106811.
<https://doi.org/10.1002/adfm.202106811>.
- (197) Langevin, S. A.; Tan, B.; Freeman, A. W.; Gagnon, J. C.; Hoffman, C. M.; Logan, M. W.; Maranchi, J. P.; Gerasopoulos, K. UV-Cured Gel Polymer Electrolytes with Improved Stability for Advanced Aqueous Li-Ion Batteries. *Chem. Commun.* **2019**, 55 (87), 13085–13088. <https://doi.org/10.1039/C9CC06207F>.
- (198) Zhang, J.; Cui, C.; Wang, P.-F.; Li, Q.; Chen, L.; Han, F.; Jin, T.; Liu, S.; Choudhary, H.; Raghavan, S. R.; Eidson, N.; von Cresce, A.; Ma, L.; Uddin, J.; Addison, D.; Yang, C.; Wang, C. “Water-in-Salt” Polymer Electrolyte for Li-Ion Batteries. *Energy Environ. Sci.* **2020**, *13* (9), 2878–2887.
<https://doi.org/10.1039/D0EE01510E>.
- (199) Cresce, A. Gel Electrolyte for a 4V Flexible Aqueous Lithium-Ion Battery. *Journal of Power Sources* **2020**, 10.
- (200) He, X.; Yan, B.; Zhang, X.; Liu, Z.; Bresser, D.; Wang, J.; Wang, R.; Cao, X.; Su, Y.; Jia, H.; Grey, C. P.; Frielinghaus, H.; Truhlar, D. G.; Winter, M.; Li, J.; Paillard, E. Fluorine-Free Water-in-Ionomer Electrolytes for Sustainable Lithium-Ion Batteries. *Nature Communications* **2018**, *9* (1). <https://doi.org/10.1038/s41467-018-07331-6>.
- (201) Xie, J.; Liang, Z.; Lu, Y.-C. Molecular Crowding Electrolytes for High-Voltage Aqueous Batteries. *Nat. Mater.* **2020**, *19* (9), 1006–1011.
<https://doi.org/10.1038/s41563-020-0667-y>.
- (202) Huang, M.; Yang, J.; Zhen, S.; Wan, C.; Jiang, X.; Ju, X. Fabrication of High Li:Water Molar Ratio Electrolytes for Lithium-Ion Batteries. *Chinese Chemical Letters* **2021**, *32* (2), 834–837. <https://doi.org/10.1016/j.cclet.2020.05.008>.
- (203) Widstrom, M. D.; Borodin, O.; Ludwig, K. B.; Matthews, J. E.; Bhattacharyya, S.; Garaga, M.; V. Cresce, A.; Jarry, A.; Erdi, M.; Wang, C.; Greenbaum, S.; Kofinas, P. Water Domain Enabled Transport in Polymer Electrolytes for Lithium-Ion Batteries. *Macromolecules* **2021**, *54* (6), 2882–2891.
<https://doi.org/10.1021/acs.macromol.0c01960>.
- (204) Yang, C.; Chen, J.; Qing, T.; Fan, X.; Sun, W.; von Cresce, A.; Ding, M. S.; Borodin, O.; Vatamanu, J.; Schroeder, M. A.; Eidson, N.; Wang, C.; Xu, K. 4.0 V Aqueous Li-Ion Batteries. *Joule* **2017**, *1* (1), 122–132.
<https://doi.org/10.1016/j.joule.2017.08.009>.

- (205) Wang, F.; Lin, C.-F.; Ji, X.; Rubloff, G. W.; Wang, C. Suppression of Hydrogen Evolution at Catalytic Surfaces in Aqueous Lithium Ion Batteries. *J. Mater. Chem. A* **2020**, 8 (30), 14921–14926. <https://doi.org/10.1039/D0TA05568A>.
- (206) Sakai, S.; Yamada, I.; Miyahara, Y.; Kondo, Y.; Yokoyama, Y.; Abe, T.; Miyazaki, K. Surface-Modified $\text{Li}_4\text{Ti}_5\text{O}_{12}$ in Highly Concentrated Aqueous Solutions for Use in Aqueous Rechargeable Lithium Batteries. *J. Electrochem. Soc.* **2020**, 167 (12), 120512. <https://doi.org/10.1149/1945-7111/ababd3>.
- (207) Chen, L.; Cao, L.; Ji, X.; Hou, S.; Li, Q.; Chen, J.; Yang, C.; Eidson, N.; Wang, C. Enabling Safe Aqueous Lithium Ion Open Batteries by Suppressing Oxygen Reduction Reaction. *Nat Commun* **2020**, 11 (1), 2638. <https://doi.org/10.1038/s41467-020-16460-w>.
- (208) Hou, X.; Ju, X.; Zhao, W.; Wang, J.; He, X.; Du, L.; Yan, B.; Li, J.; Paillard, E.; Sun, J.; Lin, H.; Winter, M.; Li, J. $\text{TiO}_2@\text{LiTi}_2(\text{PO}_4)_3$ Enabling Fast and Stable Lithium Storage for High Voltage Aqueous Lithium-Ion Batteries. *Journal of Power Sources* **2021**, 484, 229255. <https://doi.org/10.1016/j.jpowsour.2020.229255>.
- (209) Subramanya, U. Carbon-Based Artificial SEI Layers for Aqueous Lithium-Ion Battery Anodes. *RSC Advances* **2020**, 8.
- (210) Coustan, L.; Zaghib, K.; Bélanger, D. New Insight in the Electrochemical Behaviour of Stainless Steel Electrode in Water-in-Salt Electrolyte. *Journal of Power Sources* **2018**, 399, 299–303. <https://doi.org/10.1016/j.jpowsour.2018.07.114>.
- (211) Hong, W. T.; Risch, M.; Stoerzinger, K. A.; Grimaud, A.; Suntivich, J.; Shao-Horn, Y. Toward the Rational Design of Non-Precious Transition Metal Oxides for Oxygen Electrocatalysis. *Energy Environ. Sci.* **2015**, 8 (5), 1404–1427. <https://doi.org/10.1039/C4EE03869J>.
- (212) Dubouis, N.; Serva, A.; Salager, E.; Deschamps, M.; Salanne, M.; Grimaud, A. The Fate of Water at the Electrochemical Interfaces: Electrochemical Behavior of Free Water vs. Coordinating Water. 7.
- (213) Suo, L.; Han, F.; Fan, X.; Liu, H.; Xu, K.; Wang, C. “Water-in-Salt” Electrolytes Enable Green and Safe Li-Ion Batteries for Large Scale Electric Energy Storage Applications. *J. Mater. Chem. A* **2016**, 4 (17), 6639–6644. <https://doi.org/10.1039/C6TA00451B>.
- (214) Kunduraci, M.; Mutlu, R. N.; Gizir, A. M. Electrochemical Behavior of $\text{LiNi}_{0.6}\text{Mn}_{0.2}\text{Co}_{0.2}\text{O}_2$ Cathode in Different Aqueous Electrolytes. *Ionics* **2020**. <https://doi.org/10.1007/s11581-020-03490-z>.
- (215) Yang, C.; Rousse, G.; Louise Svane, K.; Pearce, P. E.; Abakumov, A. M.; Deschamps, M.; Cibir, G.; Chadwick, A. V.; Dalla Corte, D. A.; Anton Hansen, H.; Vegge, T.; Tarascon, J.-M.; Grimaud, A. Cation Insertion to Break the

- Activity/Stability Relationship for Highly Active Oxygen Evolution Reaction Catalyst. *Nat Commun* **2020**, *11* (1), 1378. <https://doi.org/10.1038/s41467-020-15231-x>.
- (216) Laszczynski, N.; Solchenbach, S.; Gasteiger, H. A.; Lucht, B. L. Understanding Electrolyte Decomposition of Graphite/NCM₈₁₁ Cells at Elevated Operating Voltage. *J. Electrochem. Soc.* **2019**, *166* (10), A1853–A1859. <https://doi.org/10.1149/2.0571910jes>.
- (217) Xiong, D. J.; Ellis, L. D.; Li, J.; Li, H.; Hynes, T.; Allen, J. P.; Xia, J.; Hall, D. S.; Hill, I. G.; Dahn, J. R. Measuring Oxygen Release from Delithiated LiNi_xMn_yCo_{1-x-y}O₂ and Its Effects on the Performance of High Voltage Li-Ion Cells. *J. Electrochem. Soc.* **2017**, *164* (13), A3025–A3037. <https://doi.org/10.1149/2.0291713jes>.
- (218) Jung, R.; Metzger, M.; Maglia, F.; Stinner, C.; Gasteiger, H. A. Oxygen Release and Its Effect on the Cycling Stability of LiNi_xMn_yCo_zO₂ (NMC) Cathode Materials for Li-Ion Batteries. *J. Electrochem. Soc.* **2017**, *164* (7), A1361–A1377. <https://doi.org/10.1149/2.0021707jes>.
- (219) Zheng, J.; Xiao, J.; Xu, W.; Chen, X.; Gu, M.; Li, X.; Zhang, J.-G. Surface and Structural Stabilities of Carbon Additives in High Voltage Lithium Ion Batteries. *Journal of Power Sources* **2013**, *227*, 211–217. <https://doi.org/10.1016/j.jpowsour.2012.11.038>.
- (220) Gambou-Bosca, A.; Bélanger, D. Effect of the Formulation of the Electrode on the Pore Texture and Electrochemical Performance of the Manganese Dioxide-Based Electrode for Application in a Hybrid Electrochemical Capacitor. *J. Mater. Chem. A* **2014**, *2* (18), 6463. <https://doi.org/10.1039/c3ta14910b>.
- (221) Betz, J.; Bieker, G.; Meister, P.; Placke, T.; Winter, M.; Schmich, R. Theoretical versus Practical Energy: A Plea for More Transparency in the Energy Calculation of Different Rechargeable Battery Systems. *Adv. Energy Mater.* **2019**, *9* (6), 1803170. <https://doi.org/10.1002/aenm.201803170>.
- (222) Naik, K. M.; Sampath, S. Cubic Mo₆S₈-Efficient Electrocatalyst Towards Hydrogen Evolution Over Wide PH Range. *Electrochimica Acta* **2017**, *252*, 408–415. <https://doi.org/10.1016/j.electacta.2017.09.015>.
- (223) Prigge, C.; Mueller-Warmuth, W.; Gocke, E.; Schoellhorn, R. Metallike Behavior of Lithium Intercalated in Molybdenum Cluster Chalcogenides. *Chem. Mater.* **1993**, *5* (10), 1493–1498. <https://doi.org/10.1021/cm00034a020>.
- (224) Gocke, E.; Schoellhorn, R.; Aselmann, G.; Mueller-Warmuth, W. Molybdenum Cluster Chalcogenides Mo₆X₈: Intercalation of Lithium via Electron/Ion Transfer. *Inorg. Chem.* **1987**, *26* (11), 1805–1812. <https://doi.org/10.1021/ic00258a034>.

- (225) Xu, K.; von Wald Cresce, A. Li^+ -Solvation/Desolvation Dictates Interphasial Processes on Graphitic Anode in Li Ion Cells. *J. Mater. Res.* **2012**, *27* (18), 2327–2341. <https://doi.org/10.1557/jmr.2012.104>.
- (226) Xu, K.; von Cresce, A.; Lee, U. Differentiating Contributions to “Ion Transfer” Barrier from Interphasial Resistance and Li^+ Desolvation at Electrolyte/Graphite Interface. *Langmuir* **2010**, *26* (13), 11538–11543. <https://doi.org/10.1021/la1009994>.
- (227) Lee, J.-W.; Pyun, S.-I. Investigation of Lithium Transport through LiMn_2O_4 Film Electrode in Aqueous LiNO_3 Solution. *Electrochimica Acta* **2004**, *49* (5), 753–761. <https://doi.org/10.1016/j.electacta.2003.09.029>.
- (228) Abe, T.; Sagane, F.; Ohtsuka, M.; Iriyama, Y.; Ogumi, Z. Lithium-Ion Transfer at the Interface Between Lithium-Ion Conductive Ceramic Electrolyte and Liquid Electrolyte-A Key to Enhancing the Rate Capability of Lithium-Ion Batteries. *J. Electrochem. Soc.* **2005**, *152* (11), A2151. <https://doi.org/10.1149/1.2042907>.
- (229) Hu, J.; Guo, H.; Li, Y.; Wang, H.; Wang, Z.; Huang, W.; Yang, L.; Chen, H.; Lin, Y.; Pan, F. Understanding Li-Ion Thermodynamic and Kinetic Behaviors in Concentrated Electrolyte for the Development of Aqueous Lithium-Ion Batteries. *Nano Energy* **2021**, *89*, 106413. <https://doi.org/10.1016/j.nanoen.2021.106413>.
- (230) Ayeb, A.; Otten, W. M.; Mank, A. J. G.; Notten, P. H. L. The Hydrogen Evolution and Oxidation Kinetics during Overdischarging of Sealed Nickel-Metal Hydride Batteries. *J. Electrochem. Soc.* **2006**, *153* (11), A2055. <https://doi.org/10.1149/1.2336993>.
- (231) Ortiz-Rodríguez, J. C.; Singstock, N. R.; Perryman, J. T.; Hyler, F. P.; Jones, S. J.; Holder, A. M.; Musgrave, C. B.; Velázquez, J. M. Stabilizing Hydrogen Adsorption through Theory-Guided Chalcogen Substitution in Chevrel-Phase Mo_6X_8 (X=S, Se, Te) Electrocatalysts. *ACS Appl. Mater. Interfaces* **2020**, *12* (32), 35995–36003. <https://doi.org/10.1021/acsami.0c07207>.
- (232) Alonso-Vante, N.; Schubert, B.; Tributsch, H. Transition Metal Cluster Materials for Multi-Electron Transfer Catalysis. *Materials Chemistry and Physics* **1989**, *22* (3–4), 281–307. [https://doi.org/10.1016/0254-0584\(89\)90002-3](https://doi.org/10.1016/0254-0584(89)90002-3).
- (233) Dubouis, N.; Yang, C.; Beer, R.; Ries, L.; Voiry, D.; Grimaud, A. Interfacial Interactions as an Electrochemical Tool To Understand Mo-Based Catalysts for the Hydrogen Evolution Reaction. *ACS Catal.* **2018**, *8* (2), 828–836. <https://doi.org/10.1021/acscatal.7b03684>.
- (234) Utsunomiya, T.; Hatozaki, O.; Yoshimoto, N.; Egashira, M.; Morita, M. Influence of Particle Size on the Self-Discharge Behavior of Graphite Electrodes in Lithium-Ion Batteries. *Journal of Power Sources* **2011**, *196* (20), 8675–8682. <https://doi.org/10.1016/j.jpowsour.2011.06.070>.

- (235) Yazami, R.; Ozawa, Y. A Kinetics Study of Self-Discharge of Spinel Electrodes in Li/LixMn₂O₄ Cells. *Journal of Power Sources* **2006**, *153* (2), 251–257. <https://doi.org/10.1016/j.jpowsour.2005.10.012>.
- (236) Ozawa, Y.; Yazami, R.; Fultz, B. Self-Discharge Study of LiCoO₂ Cathode Materials. *Journal of Power Sources* **2003**, *119–121*, 918–923. [https://doi.org/10.1016/S0378-7753\(03\)00227-1](https://doi.org/10.1016/S0378-7753(03)00227-1).
- (237) Notten, P. H. L.; Verbitskiy, E.; Kruijt, W. S.; Bergveld, H. J. Oxygen Evolution and Recombination Kinetics Inside Sealed Rechargeable, Ni-Based Batteries. *J. Electrochem. Soc.* **2005**, *152* (7), A1423. <https://doi.org/10.1149/1.1921849>.
- (238) Bullock, K. R.; McClelland, D. H. The Kinetics of the Self-Discharge Reaction in a Sealed Lead-Acid Cell. *J. Electrochem. Soc.* **1976**, *123* (3), 327–331. <https://doi.org/10.1149/1.2132819>.
- (239) Leblanc, P.; Blanchard, P.; Senyarrich, S. Self-Discharge of Sealed Nickel—Metal Hydride Batteries: Mechanisms and Improvements. *J. Electrochem. Soc.* **1998**, *145* (3), 844–847. <https://doi.org/10.1149/1.1838355>.
- (240) Peled, E.; Golodnitsky, D.; Ardel, G. Advanced Model for Solid Electrolyte Interphase Electrodes in Liquid and Polymer Electrolytes. *J. Electrochem. Soc.* **1997**, *144* (8), L208–L210. <https://doi.org/10.1149/1.1837858>.
- (241) Gauthier, M.; Carney, T. J.; Grimaud, A.; Giordano, L.; Pour, N.; Chang, H.-H.; Fenning, D. P.; Lux, S. F.; Paschos, O.; Bauer, C.; Maglia, F.; Lupart, S.; Lamp, P.; Shao-Horn, Y. Electrode–Electrolyte Interface in Li-Ion Batteries: Current Understanding and New Insights. *J. Phys. Chem. Lett.* **2015**, *6* (22), 4653–4672. <https://doi.org/10.1021/acs.jpcllett.5b01727>.
- (242) Jones, J.; Anouti, M.; Caillon-Caravanier, M.; Willmann, P.; Lemordant, D. Thermodynamic of LiF Dissolution in Alkylcarbonates and Some of Their Mixtures with Water. *Fluid Phase Equilibria* **2009**, *285* (1–2), 62–68. <https://doi.org/10.1016/j.fluid.2009.07.020>.
- (243) Tasaki, K.; Goldberg, A.; Lian, J.-J.; Walker, M.; Timmons, A.; Harris, S. J. Solubility of Lithium Salts Formed on the Lithium-Ion Battery Negative Electrode Surface in Organic Solvents. *J. Electrochem. Soc.* **2009**, *156* (12), A1019. <https://doi.org/10.1149/1.3239850>.
- (244) Strmcnik, D.; Castelli, I. E.; Connell, J. G.; Haering, D.; Zorko, M.; Martins, P.; Lopes, P. P.; Genorio, B.; Østergaard, T.; Gasteiger, H. A.; Maglia, F.; Antonopoulos, B. K.; Stamenkovic, V. R.; Rossmeisl, J.; Markovic, N. M. Electrocatalytic Transformation of HF Impurity to H₂ and LiF in Lithium-Ion Batteries. *Nat Catal* **2018**, *1* (4), 255–262. <https://doi.org/10.1038/s41929-018-0047-z>.
- (245) Vincze, J.; Valiskó, M.; Boda, D. The Nonmonotonic Concentration Dependence of the Mean Activity Coefficient of Electrolytes Is a Result of a Balance between

- Solvation and Ion-Ion Correlations. *The Journal of Chemical Physics* **2010**, *133* (15), 154507. <https://doi.org/10.1063/1.3489418>.
- (246) McEldrew, M.; Goodwin, Z. A. H.; Bi, S.; Bazant, M. Z.; Kornyshev, A. A. Theory of Ion Aggregation and Gelation in Super-Concentrated Electrolytes. *J. Chem. Phys.* **2020**, *152* (23), 234506. <https://doi.org/10.1063/5.0006197>.
- (247) Liu, D.; Yu, Q.; Liu, S.; Qian, K.; Wang, S.; Sun, W.; Yang, X.-Q.; Kang, F.; Li, B. Evolution of Solid Electrolyte Interface on TiO₂ Electrodes in an Aqueous Li-Ion Battery Studied Using Scanning Electrochemical Microscopy. *J. Phys. Chem. C* **2019**, *acs.jpcc.9b01412*. <https://doi.org/10.1021/acs.jpcc.9b01412>.
- (248) Zhang, H.; Wang, D.; Shen, C. In-Situ EC-AFM and Ex-Situ XPS Characterization to Investigate the Mechanism of SEI Formation in Highly Concentrated Aqueous Electrolyte for Li-Ion Batteries. *Applied Surface Science* **2020**, *507*, 145059. <https://doi.org/10.1016/j.apsusc.2019.145059>.
- (249) He, M.; Guo, R.; Hobold, G. M.; Gao, H.; Gallant, B. M. The Intrinsic Behavior of Lithium Fluoride in Solid Electrolyte Interphases on Lithium. *Proc Natl Acad Sci USA* **2020**, *117* (1), 73–79. <https://doi.org/10.1073/pnas.1911017116>.
- (250) Aurbach, D.; Ein-Ely, Y.; Zaban, A. The Surface Chemistry of Lithium Electrodes in Alkyl Carbonate Solutions. *J. Electrochem. Soc.* **1994**, *141* (1), L1–L3. <https://doi.org/10.1149/1.2054718>.
- (251) Guo, R.; Wang, D.; Zuin, L.; Gallant, B. M. Reactivity and Evolution of Ionic Phases in the Lithium Solid–Electrolyte Interphase. *ACS Energy Lett.* **2021**, *6* (3), 877–885. <https://doi.org/10.1021/acsenergylett.1c00117>.
- (252) Zhang, X.-Q.; Cheng, X.-B.; Chen, X.; Yan, C.; Zhang, Q. Fluoroethylene Carbonate Additives to Render Uniform Li Deposits in Lithium Metal Batteries. *Adv. Funct. Mater.* **2017**, *27* (10), 1605989. <https://doi.org/10.1002/adfm.201605989>.
- (253) Aurbach, D. A Short Review of Failure Mechanisms of Lithium Metal and Lithiated Graphite Anodes in Liquid Electrolyte Solutions. *Solid State Ionics* **2002**, *148* (3–4), 405–416. [https://doi.org/10.1016/S0167-2738\(02\)00080-2](https://doi.org/10.1016/S0167-2738(02)00080-2).
- (254) Li, C.; Lan, Q.; Yang, Y.; Shao, H.; Zhan, H. Flexible Artificial Solid Electrolyte Interphase Formed by 1,3-Dioxolane Oxidation and Polymerization for Metallic Lithium Anodes. *ACS Appl. Mater. Interfaces* **2019**, *11* (2), 2479–2489. <https://doi.org/10.1021/acsami.8b16080>.
- (255) Wrogemann, J. M.; Künne, S.; Heckmann, A.; Rodríguez-Pérez, I. A.; Siozios, V.; Yan, B.; Li, J.; Winter, M.; Beltrop, K.; Placke, T. Development of Safe and Sustainable Dual-Ion Batteries Through Hybrid Aqueous/Nonaqueous Electrolytes. *Adv. Energy Mater.* **2020**, *10* (8), 1902709. <https://doi.org/10.1002/aenm.201902709>.

- (256) Zhang, X.; Dong, M.; Xiong, Y.; Hou, Z.; Ao, H.; Liu, M.; Zhu, Y.; Qian, Y. Aqueous Rechargeable Li^+/Na^+ Hybrid Ion Battery with High Energy Density and Long Cycle Life. *Small* **2020**, *16* (41), 2003585. <https://doi.org/10.1002/sml.202003585>.
- (257) Miyazaki, K.; Takenaka, N.; Watanabe, E.; Iizuka, S.; Yamada, Y.; Tateyama, Y.; Yamada, A. First-Principles Study on the Peculiar Water Environment in a Hydrate-Melt Electrolyte. *J. Phys. Chem. Lett.* **2019**, *10* (20), 6301–6305. <https://doi.org/10.1021/acs.jpcclett.9b02207>.
- (258) Nikitina, V. A.; Zakharkin, M. V.; Vassiliev, S. Yu.; Yashina, L. V.; Antipov, E. V.; Stevenson, K. J. Lithium Ion Coupled Electron-Transfer Rates in Superconcentrated Electrolytes: Exploring the Bottlenecks for Fast Charge-Transfer Rates with LiMn_2O_4 Cathode Materials. *Langmuir* **2017**, *33* (37), 9378–9389. <https://doi.org/10.1021/acs.langmuir.7b01016>.
- (259) Brouillette, D.; Perron, G.; Desnoyers, J. E. Apparent Molar Volume, Heat Capacity, and Conductance of Lithium Bis(Trifluoromethylsulfone)Imide in Glymes and Other Aprotic Solvents. *Canadian Journal of Physics* **1997**, No. 75, 1608–1614.
- (260) Marković, N. M.; Grgur, B. N.; Ross, P. N. Temperature-Dependent Hydrogen Electrochemistry on Platinum Low-Index Single-Crystal Surfaces in Acid Solutions. *J. Phys. Chem. B* **1997**, *101* (27), 5405–5413. <https://doi.org/10.1021/jp970930d>.
- (261) Tang, Y.; Zhang, Y.; Li, W.; Ma, B.; Chen, X. Rational Material Design for Ultrafast Rechargeable Lithium-Ion Batteries. *Chem. Soc. Rev.* **2015**, *44* (17), 5926–5940. <https://doi.org/10.1039/C4CS00442F>.
- (262) Yoo, H. D.; Markevich, E.; Salitra, G.; Sharon, D.; Aurbach, D. On the Challenge of Developing Advanced Technologies for Electrochemical Energy Storage and Conversion. *Materials Today* **2014**, *17* (3), 110–121. <https://doi.org/10.1016/j.mattod.2014.02.014>.
- (263) Köhler, U.; Antonius, C.; Bäuerlein, P. Advances in Alkaline Batteries. *Journal of Power Sources* **2004**, *127* (1–2), 45–52. <https://doi.org/10.1016/j.jpowsour.2003.09.006>.
- (264) Tarascon, J.-M.; Gozdz, A. S.; Schmutz, C.; Shokoohi, F.; Warren, P. C. Performance of Bellcore's Plastic Rechargeable Li-Ion Batteries. *Solid State Ionics* **1996**, *86–88*, 49–54. [https://doi.org/10.1016/0167-2738\(96\)00330-X](https://doi.org/10.1016/0167-2738(96)00330-X).
- (265) Lepoivre, F.; Grimaud, A.; Larcher, D.; Tarascon, J.-M. Long-Time and Reliable Gas Monitoring in Li-O_2 Batteries via a Swagelok Derived Electrochemical Cell. *J. Electrochem. Soc.* **2016**, *163* (6), A923–A929. <https://doi.org/10.1149/2.0421606jes>.

- (266) Lepoivre, F. Study and Improvement of Non-Aqueous Lithium-Air Batteries via the Development of a Silicon-Based Anode. *Thesis manuscript* **2016**.
- (267) Wei Yin. Fundamental Understanding of High-Energy-Density Li-Ion Batteries and beyond : Structure-Property Relationships and Reaction Chemistries. *Thesis manuscript* **2019**.
- (268) Yin, W.; Mariyappan, S.; Grimaud, A.; Tarascon, J. M. Rotating Ring Disk Electrode for Monitoring the Oxygen Release at High Potentials in Li-Rich Layered Oxides. *J. Electrochem. Soc.* **2018**, *165* (14), A3326–A3333. <https://doi.org/10.1149/2.0481814jes>.
- (269) Jones, J.; Anouti, M.; Caillon-Caravanier, M.; Willmann, P.; Sizaret, P.-Y.; Lemordant, D. Solubilization of SEI Lithium Salts in Alkylcarbonate Solvents. *Fluid Phase Equilibria* **2011**, *305* (2), 121–126. <https://doi.org/10.1016/j.fluid.2011.03.007>.
- (270) Jones, J.; Anouti, M.; Caillon-Caravanier, M.; Willmann, P.; Lemordant, D. Lithium Fluoride Dissolution Equilibria in Cyclic Alkylcarbonates and Water. *Journal of Molecular Liquids* **2010**, *153* (2–3), 146–152. <https://doi.org/10.1016/j.molliq.2010.02.006>.
- (271) Han, K. S.; Yu, Z.; Wang, H.; Redfern, P. C.; Ma, L.; Cheng, L.; Chen, Y.; Hu, J. Z.; Curtiss, L. A.; Xu, K.; Murugesan, V.; Mueller, K. T. Origin of Unusual Acidity and Li^+ Diffusivity in a Series of Water-in-Salt Electrolytes. *J. Phys. Chem. B* **2020**, *124* (25), 5284–5291. <https://doi.org/10.1021/acs.jpcc.0c02483>.

APPENDIX

- APPENDIX - CHAPTER 1

Table A.1. 1 Summary of the main salts listed in Chapter 1.

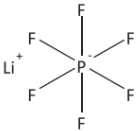
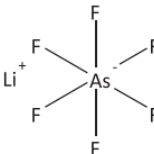
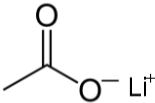
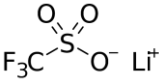
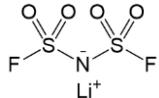
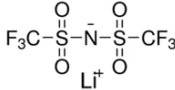
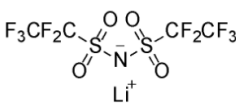
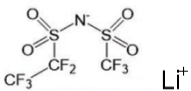
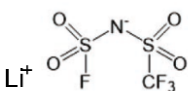
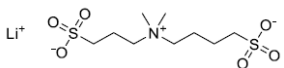
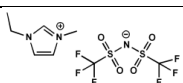
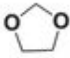

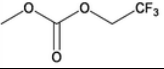
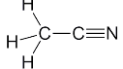
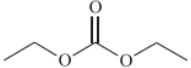
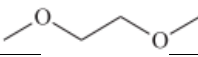
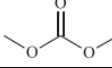
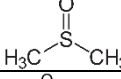
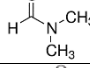
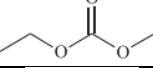
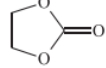
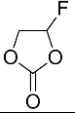
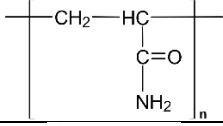
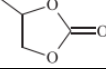
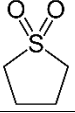
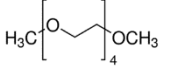
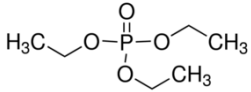
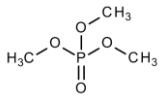
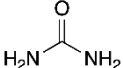
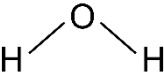
Name	Abbreviation	Chemical formula
Lithium hexafluorophosphate	LiPF ₆	
Lithium hexafluoroarsenate	LiAsF ₆	
Lithium acetate	LiAc	
Lithium trifluoromethanesulfonate or Lithium triflate	LiOTf	
Lithium bis(fluorosulfonyl)imide	LiFSI	
Lithium bis(trifluoromethanesulfonyl)imide	LiTFSI	
Lithium bis(pentafluoroethanesulfonyl)imide	LiBETI	
Lithium pentafluoroethanesulfonyl (trifluoromethanesulfonyl)imide	LiPTFSI	
Lithium (fluorosulfonyl)(trifluoromethylsulfonyl)imide	LiFTFSI	
Lithium propylsulfonate-butylsulfonate-dimethyl-amine	LiMM3411	
1-Ethyl-3-methylimidazolium bis(trifluoromethylsulfonyl)imide	EMim TFSI	

Table A.1. 2 Summary of the main solvents listed in Chapter 1.

Name	Abbreviation	Chemical formula
1,3-dioxolane	DOL	
1,5-pentanediol	PD	
2-fluoroethyl methyl carbonate	FEMC	
Acetonitrile	ACN	
Diethylcarbonate	DEC	
Dimethoxyethane	DME	
Dimethyl carbonate	DMC	
Dimethyl sulfoxide	DMSO	
Dimethylformamide	DMF	
Ethyl methyl carbonate	EMC	
Ethylene carbonate	EC	
Fluoroethylene carbonate	FEC	
Polyacrylamide	PAM	
Propylene carbonate	PC	
Sulfolane	SL	
Tetraethylene glycol dimethyl ether	TEGDME	
Triethyl phosphate	TEP	
Trimethyl phosphate	TMP	
Urea	Urea	
Water	H ₂ O	

SEI formation mechanisms in *Water-in-salt* electrolyte

The first SEI formation mechanism reported relies on the direct electrochemical reduction of anion or anion clusters, such as $\text{Li}_2(\text{TFSI})^{+146}$. Alike in organic superconcentrated electrolyte, anions would partially donate electrons to Li^+ to form $\text{Li}_2(\text{TFSI})^+$ complex, therefore lowering the anion LUMO and increasing its reduction potential^{43,45,54}, as revealed by quantum chemistry calculation¹⁴⁶ (see Figure A.1. 1a). Similarly, the electronic structure of water isolated monomers or clusters changes, leading to an inversion of the LUMO levels between water and anion, thus promoting anion reduction at low potential²⁵⁷. In addition, Li_2CO_3 and Li_2O were determined as contributors due to the complementary reduction of CO_2 and O_2 dissolved gases in the electrolyte¹⁴⁶ (Equation A.1. 1 and Equation A.1. 2). However, as discussed in section 1.2, the determination of HOMO/LUMO energy level is not sufficient to explain changes in interfacial reactivity. Therefore, other SEI mechanisms were discussed in literature. Dubouis *et al.*¹³⁴ observed that the HER occurs at potential above 2 V vs Li^+/Li in WiSE, and that TFSI⁻ anions chemically degrade in the strong alkaline environment produced by HER (see Figure A.1. 1b). Based on this mechanism, LiOH and CF_x elements were found to contribute to the SEI composition. Eventually, complementary to the chemical degradation path, Bouchal *et al.*¹⁴⁹ suggested that a dynamic precipitation/dissolution of LiTFSI salt also contributes to the SEI, as also reported by Nikitina *et al.*²⁵⁸.

Moreover, the SEI formation may be influence by the preferential adsorption of Li^+ on the electrode surface. For instance, the strong Li^+ adsorption on Pt surface brings more water to the interface¹⁵⁴ promoting water reduction as shown by observing almost no changes in HER onset potential on Pt compared to Al, enabling a downshift of HER. A part from the HER catalysis related to the electrode material and the Li^+ cation, hypothesis based on MD simulations proposed that the electrode material also influences the anion orientation, thus modifying the SEI formation¹⁵⁴. However, these hypothesis remain under debate.

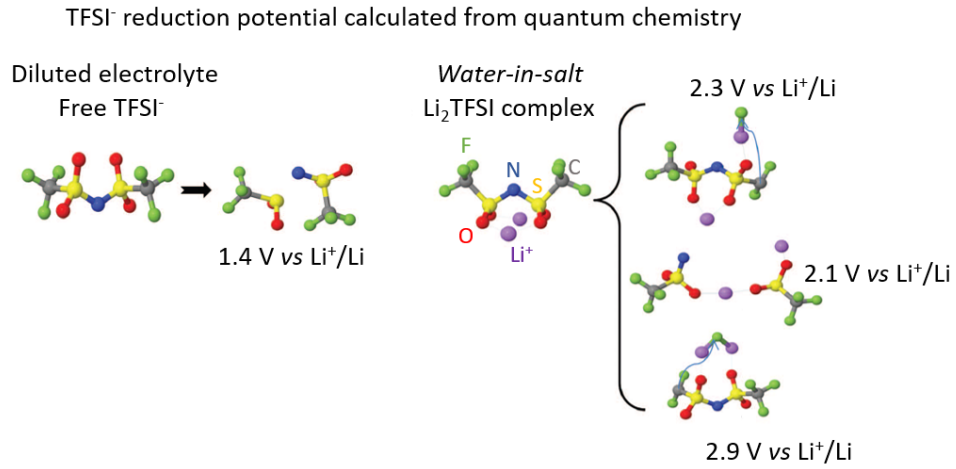
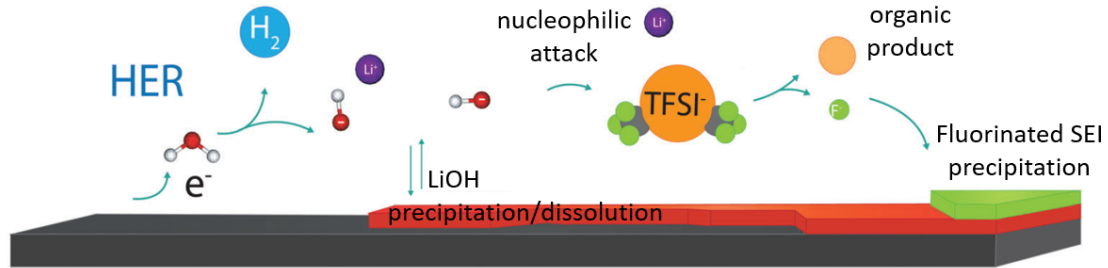
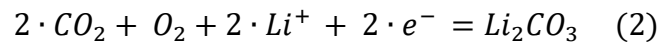
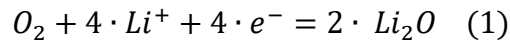
a Electrochemical reduction of TFSI⁻b Chemical degradation of TFSI⁻

Figure A.1. 1 (a) Predicted reduction potentials from quantum chemistry calculations. Adapted from Ref¹¹¹. (b) Schematic illustration of the formation of the SEI following a “water reduction mediated mechanism” occurring in 20 m LiTFSI WiSE. Adapted from Ref¹³⁴.

Equation A.1. 1: Electrochemical reduction of dissolved O₂ (1) and CO₂ (2) contributing to SEI formation.



Equation A.1. 2: Chemical reaction contributing to SEI formation.

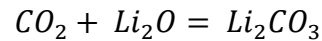
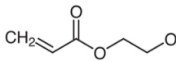
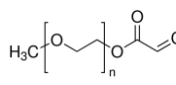
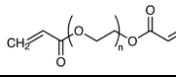
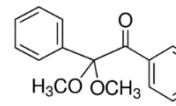


Table A.1. 3 Summary of the polymer coating used to prevent HER.

PGE	Abbreviat ion	Name	Chemical formula	Role and (mass ratio)	Polyme r matrix to electrol yte (mass ratio)
UV- curable	HEA	2-hydroxyethyl acrylate		Monomer (89)	25
	MPEGA	poly(ethylene glycol) methyll ether acrylate		Co- monomer (9)	
	PEGDA	poly(ethylene glycol) diacrylate		Cross- linker(2)	
	DMPA	2,2-dimethoxy-2- phenylacetophenoe		Photo- initiator (0.2 wt%)	
	Electrolyte				75
	LiTFSI:H2O:TMP ¹⁹⁹ 37:40:23 (molar ratio)				
	21 m LiTFSI : 7 m LiOtf ¹⁹⁷				
Molecu lar crowdi ng	PEG/PEO	poly(ethylene glycol)/poly(ethylene oxide)			
	Electrolyte				
	2 m LiTFSI in PEG _{0.94} (H2O) _{0.06}				

- APPENDIX - CHAPTER 3

Energy density and specific energy as function of electrolyte volume

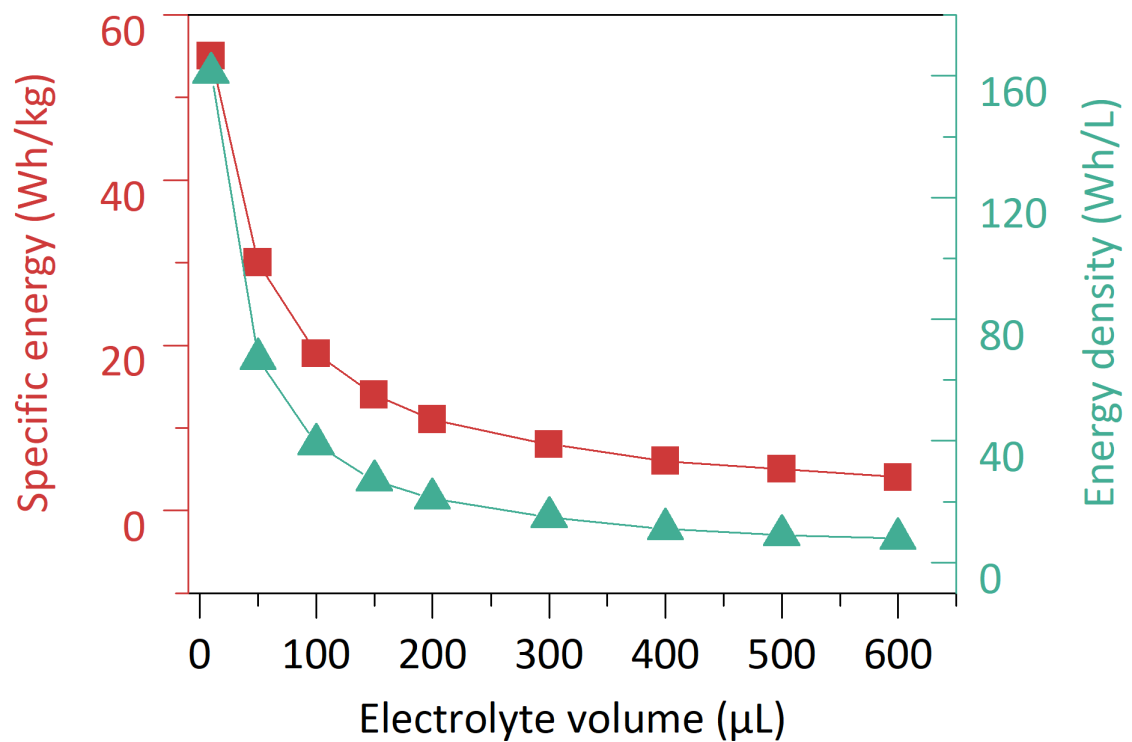


Figure A.3. 1 Specific energy and energy density as function of the electrolyte volume calculated thanks to the model developed by Betz et al.²²¹.

Cycling behavior in 3-electrodes set up

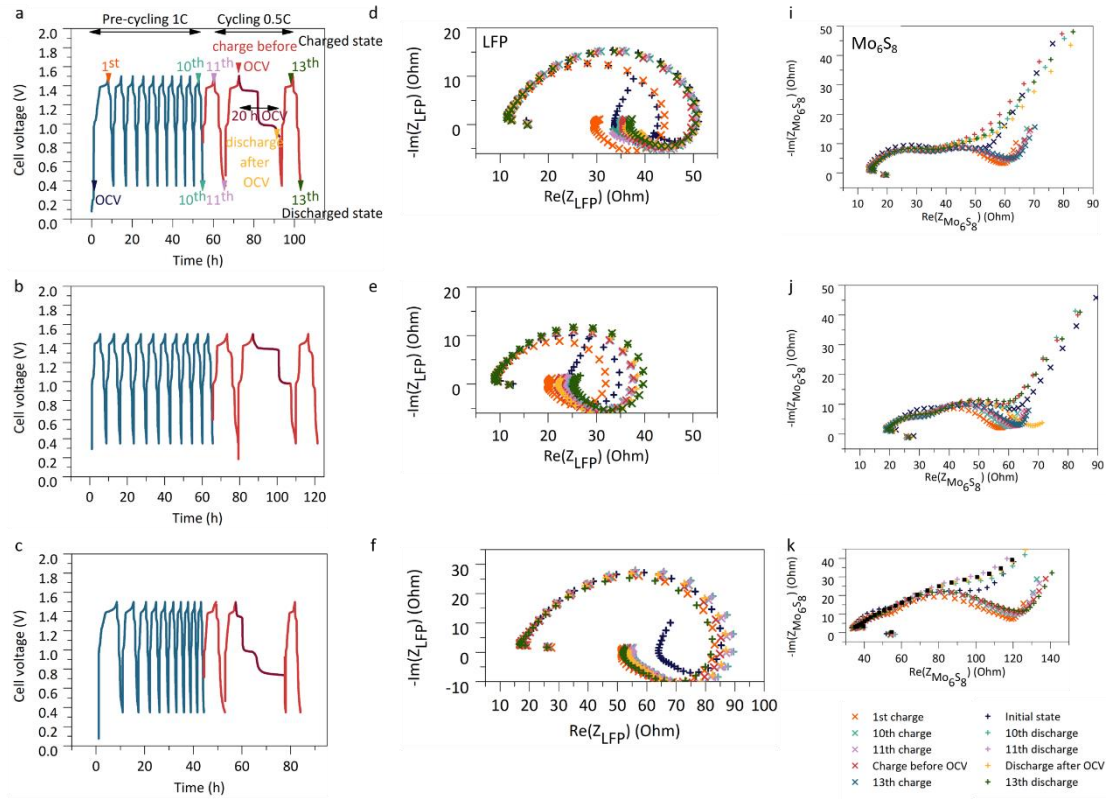


Figure A.3. 2 (a-c) Illustration of the protocol used to assess SEI stability over self-discharge cycling. Potential as function of time for 3 cells using a 3-electrodes cell based on Mo_6S_8 as counter electrode, LFP as working electrode and a ring of $\text{Li}_{0.5}\text{FePO}_4$ as reference in 20 m LiTFSI. (d-f) Nyquist plot obtained by electrochemical impedance spectroscopy of LFP determined over cycling. (g-i) Nyquist plot obtained by electrochemical impedance spectroscopy of Mo_6S_8 determined over cycling. Frequency range was comprised between 1 MHz and 50 mHz with a signal amplitude of 20 mV.

Three cells were assembled to assess SEI stability over cycling. Despite the poor performances obtained when using a 3-electrodes cell, their cycling curves show a rather good reproducibility. In addition, electrochemical impedance spectroscopy assessed on LFP gives similar response (see Figure A.3. 2d-f). Such observations are further confirmed by the Mo_6S_8 impedance spectra (see Figure A.3. 2g-i) that are only affected by the cell SOC and not the SEI evolution. Therefore, as shown in Figure A.3. 3 showing detailed EIS spectra as function of the cell SOC, the contribution of the LFP counter electrode to the cell impedance does not vary throughout the experiment, thus confirming that the high capacity loading of LFP: Mo_6S_8 (4:1) is enough to consider our set-up as a *pseudo*-half-cell and to prevent LFP impedance to be impacted by the cell

SOC. However, a clear inductive loop is shown on the LFP spectra. Issues in positioning the electrode toward the reference electrode may explain such behavior.

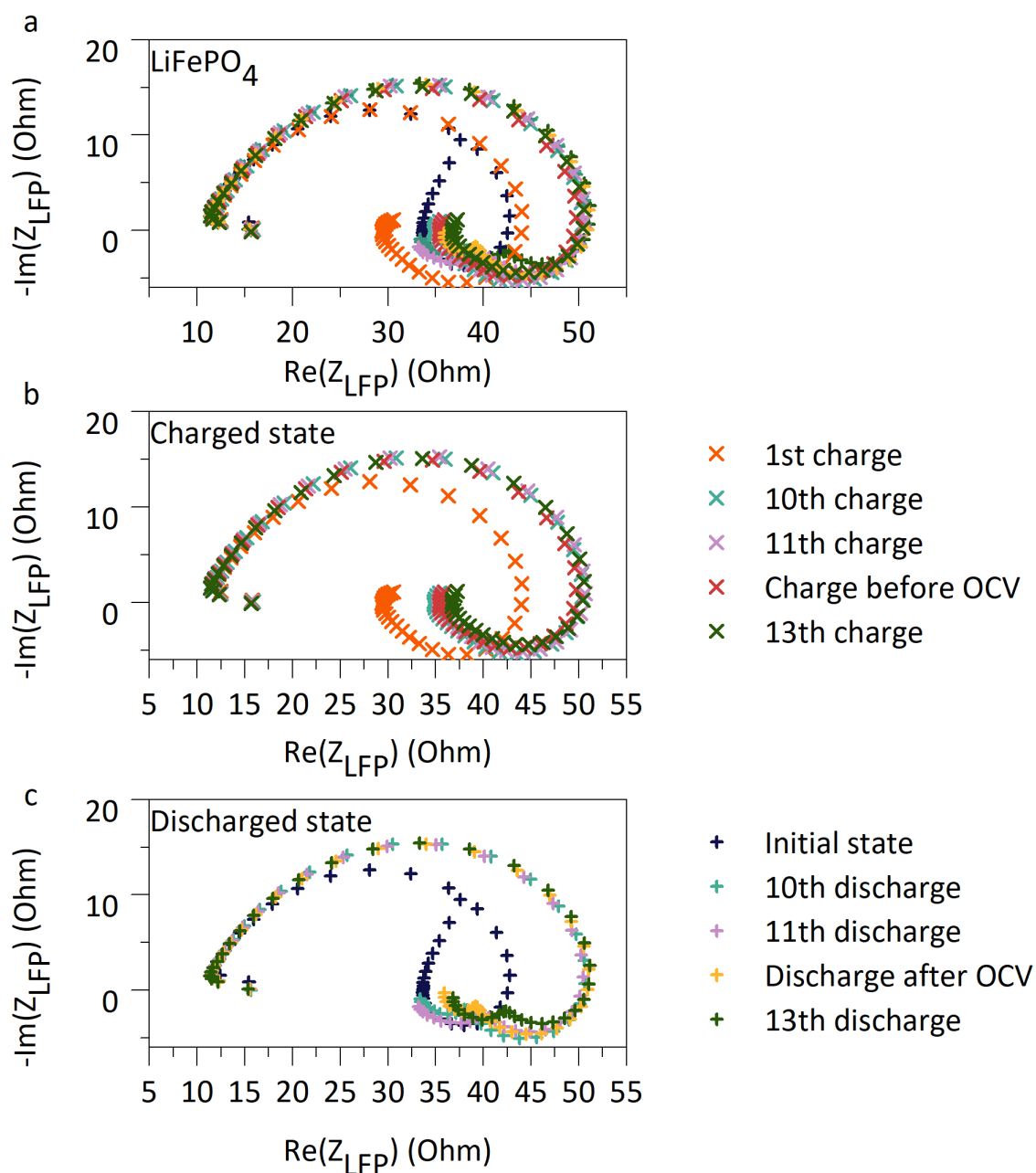


Figure A.3. 3 Nyquist plot obtained by electrochemical impedance spectroscopy of LFP working electrode over cycling. Frequency range was comprised between 1 MHz and 50 mHz with a signal amplitude of 20 mV. (a) Summary of Nyquist plot obtained during cycling, (b) Nyquist plot obtained at charged state, (c) Nyquist plot of LFP at discharged state.

Differential scanning calorimetry (DSC)

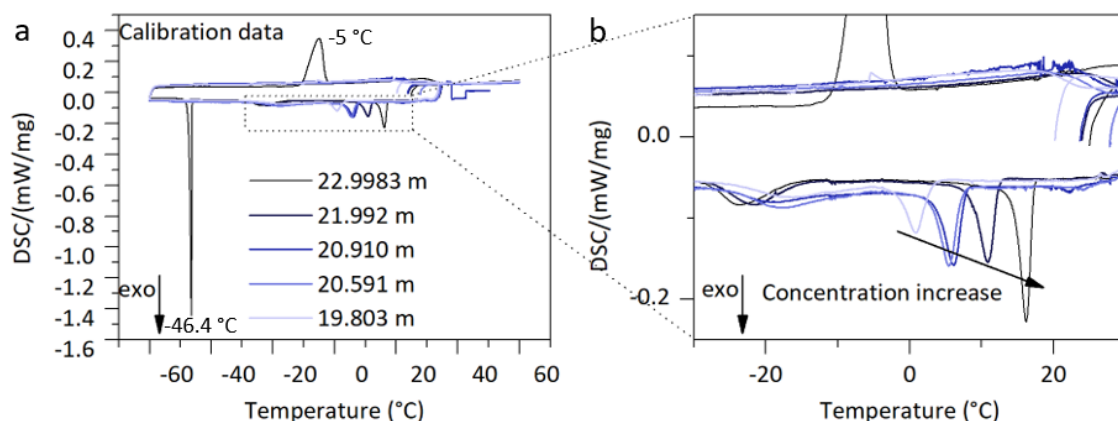


Figure A.3. 4 Differential scanning calorimetry (DSC) experiments performed at 2 °C/min between 35 °C and -60 °C upon cooling and back to 60 °C on heating. (a) Electrolytes with different concentrations used for calibration (19.803 m, 20.591 m, 20.910 m, 21.992, 22.9983 m), (b) zoom on the crystallization peak of calibration data.

To assess the impact of water consumption by recording the evolution of water content in the electrolyte as function of cycle number and self-discharge period, a calibration curve is determined. To do so, separators are soaked with electrolytes with known concentrations and DSC experiments are performed (see Figure A.3. 4a and b). A first exothermic peak is observed between 0 °C and 20 °C, shifting to greater temperature with increasing concentration, which is attributed to the beginning of the $\text{H}_2\text{O}\cdot\text{LiTFSI}$ crystallization¹²⁶. To be consistent between melting of pure components and the liquidus of transition of adjacent phases, phase transitions in WiSE are assessed at peak temperature, rather than onset temperature, as reported by Ding *et al.*¹²⁶. A second peak at ≈ -20 °C following the crystallization of $(\text{H}_2\text{O})_4\text{Li}\cdot\text{TFSI}$ ¹²⁶ is then observed. These two peaks could be related to the liquidus (between 0 °C to 20 °C) and solidus (≈ -20 °C) temperature of 20 m LiTFSI electrolyte, as reported in the phase diagram proposed by Ding *et al.*¹²⁶ (see Figure 1. 17). Nonetheless, the associated temperatures measured in our experiments differ from the one reported by Ding *et al.*, with the solidus temperature reported at -8.7 °C for LiTFSI concentration comprised between 13.9 m and 55.5 m, while we observed a solidus temperature at ≈ -20 °C. Finally, upon heating, an endothermic “wave” that corresponds to the melting point of $\text{H}_2\text{O}\cdot\text{LiTFSI}$ is observed, in agreement with previous DSC experiments carried out on 21 m LiTFSI^{111,163}. This wave shifts to higher temperature with increase in concentration in line with the trend observed for crystallization.

Besides, for the 22.993 m electrolyte an exothermic peak is observed at -46.4 °C upon cooling, followed by an endothermic peak upon heating at ≈ -5 °C (see Figure A.3. 4a). Based on the shape of the -46.4 °C peak, one can hypothesize that it is related to the crystallization of a pure component, presumably water. However, the corresponding endothermic peak (≈ -5 °C) does not correspond to the melting of a pure component. This behavior could be related to the incongruent melting of unstable solvates, as reported by Perron *et al.*²⁵⁹. Similar peaks were also observed by Reber *et al.*¹⁶³ for a 21 m LiTFSI solution but at temperature lower than -60 °C for the exothermic peak. However, considering the 20.910 and 21.992 m electrolyte, we did not observe this peak. The difference may be related to the use of mesocarbon microbeads to promote crystallization previously employed by Reber *et al.*¹⁶³.

Based on the results shown in Figure A.3. 4, the following fit is obtained:

$$T_{\text{crystallization peak}} = 4.68 \cdot C_{\text{LiTFSI}}^{\text{mol/kg}} - 91.5 \text{ with } R^2 = 0.997.$$

Activation energy of direct HER in 20 m LiTFSI

Pressure cell experiments

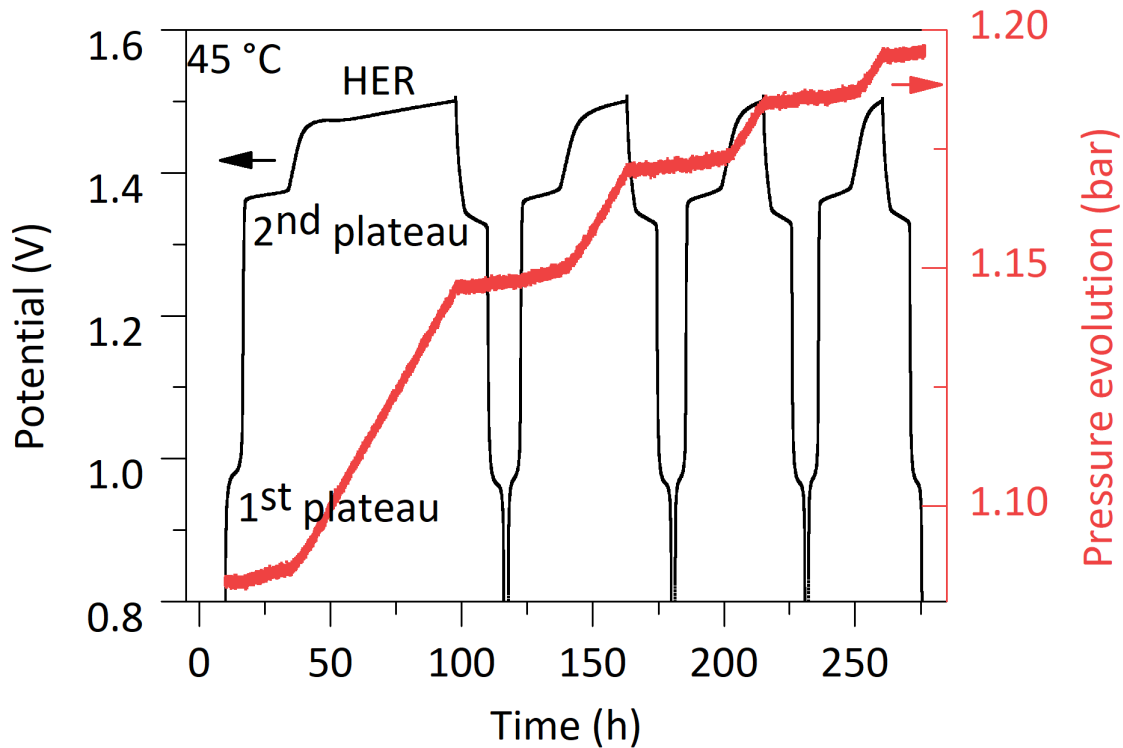


Figure A.3. 5 Potential (black line) and pressure evolution (red line) as function of time for a cell cycled at 0.15 C at 45 °C. Prior to the cycling step, the cell was pre-cycled at 1C and 25 °C for 10 cycles.

Figure A.3. 5 shows the pressure evolution as function of time for a cell which is cycled at 45 °C with a C-rate of 0.15C. Prior to this cycling test, the cell underwent a pre-cycling step of 10 cycles performed at 1C, 25 °C. Contrary to what is observed at 25 °C or 35 °C, a pure HER plateau appears above 1.4 V. Indeed, due to the low C-rate and the manually-applied pressure in Swagelok cell, parasitic reactions are favored when increasing temperature thus explaining the appearance of such plateau at 45 °C and 55 °C.

Gas calculations made to determine the activation energy of HER on Mo₆S₈ take into consideration the pure HER plateau to calculate H₂ evolution. In addition, the hydrogen rate ($\ln\left(\frac{\Delta P/P_0}{\Delta t}\right)$) calculated at 55 °C using two cells give close values ranging from -7 to -7.3 suggesting that the experiments are reproducible.

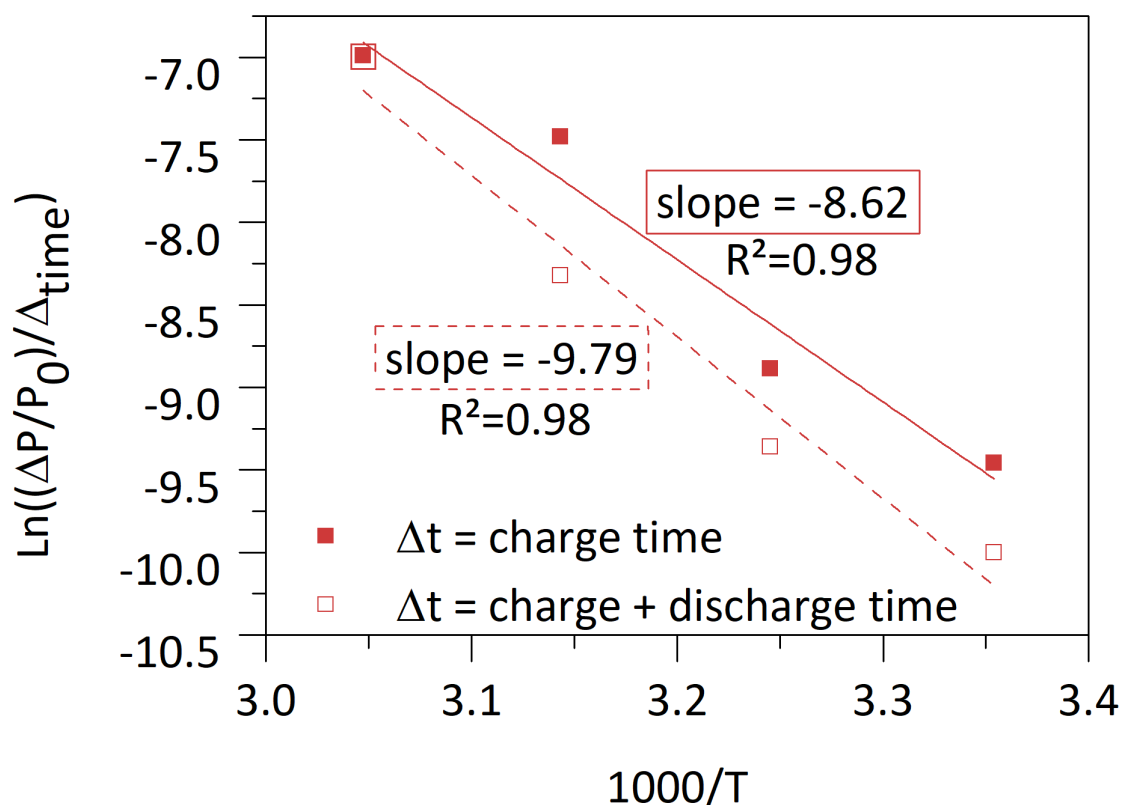


Figure A.3. 6 Arrhenius plot obtained from cycling of $\text{Mo}_6\text{S}_8/\text{LFP}$ pressure cell in 20 m LiTFSI as function of temperature. The logarithm of the hydrogen rate $((\Delta P/P_0)/\Delta_{\text{time}})$ as function of the inverse of temperature. Hydrogen rate is calculated considering charge time (full line) or charge and discharge time (dash line).

Eventually, Figure A.3. 6 shows the Arrhenius plot considering either the charge time or the charge and discharge time as the time during which hydrogen is produced. The rather close value of the slope (-8.62 and -9.79) found tend to confirm that hydrogen is majorly produced during charge thus further confirming the hypothesis used in this study.

Electrochemical cell: HER on Pt

Temperature-controlled CV were performed in an electrochemical cell to determine HER activation energy on Pt in 20 m LiTFSI; the corresponding polarization curves and Tafel plots are shown in Figure A.3. 7a and b. Looking into the polarization curves, limitations regarding the experiment can be observed since an overpotential of 600 mV must be applied to reach the potential range in which HER occurs.

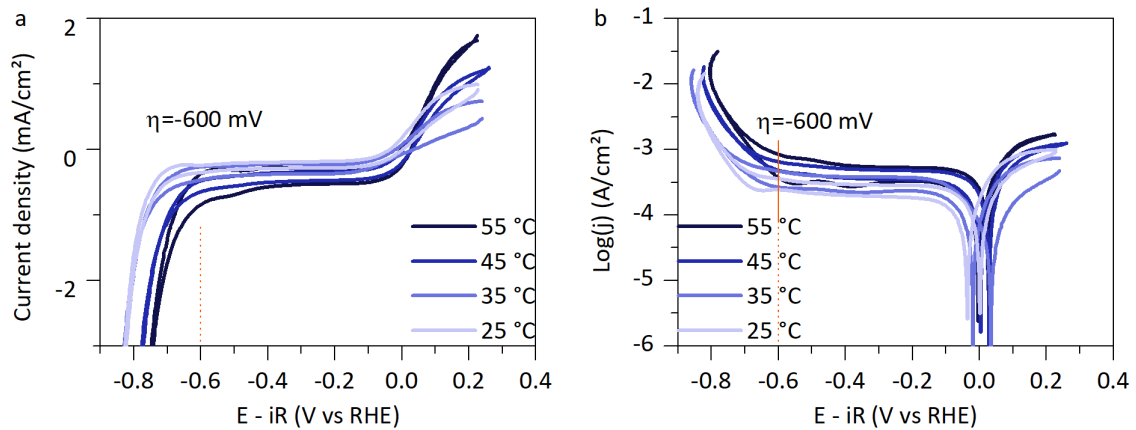


Figure A.3. 7 (a) Cyclic voltammetry performed at 50 mV/s in 20 m LiTFSI in a 3-electrodes cell using Pt disk connected to a rotating disk electrode ($\omega=1600$ rpm) as working electrode, Pt wire as counter electrode and a leakless electrode as reference electrode. (b) Tafel representation of the cyclic voltammetry.

The most accurate approach to extract the activation energy for the HER relies on analysis made in the so-called micropolarization region²⁶⁰, at potentials very close to the equilibrium potential in order to reduce effects related to mass transport. To assess the kinetic parameters, one need to verify that all the mass-transport limitation is not influencing the electrochemistry. The effect of mass transport can be quantified thanks to Koutecky-Levich equation (see Equation A.3. 1).

Equation A.3. 1

$$\frac{1}{j_{measured}} = \frac{1}{j_k} + \left(\frac{1}{0.62nFAD^{\frac{-2}{3}}\nu^{\frac{1}{6}}C_{bulk}} \right) \omega^{-1/2}$$

with j_k the kinetic current (A), n the number of electron transferred, F the Faraday constant (C/mol), A the electrode area (m²), D the diffusion coefficient for the reactant (m²/s), ν the kinematic viscosity (m²/s), C_{bulk} the concentration in the bulk (mol/m³) and ω the rotation speed (rad/s).

Thus, in the absence of mass transport control, the second term of the equation is constant regardless of the rotation speed of the RDE. Figure A.3. 8 shows the inverse of the forward current density determined at an overpotential of -600 mV as function of the inverse of the square root of the rotation speed. One can note that from 25 °C to 45 °C, the reaction is mix-controlled by mass transport and kinetics both limiting the current in the 600 mV overpotential range studied in this work. At 55 °C, Koutecky-Levich analysis shows less influence of mass transport on the current density. Besides, changes

in the active surface area of the Pt electrode occur upon polarization, due to the SEI formation and the surface passivation. This effect is observed by the crossover of the curves between the forward and the backward scan (see Figure A.3. 7).

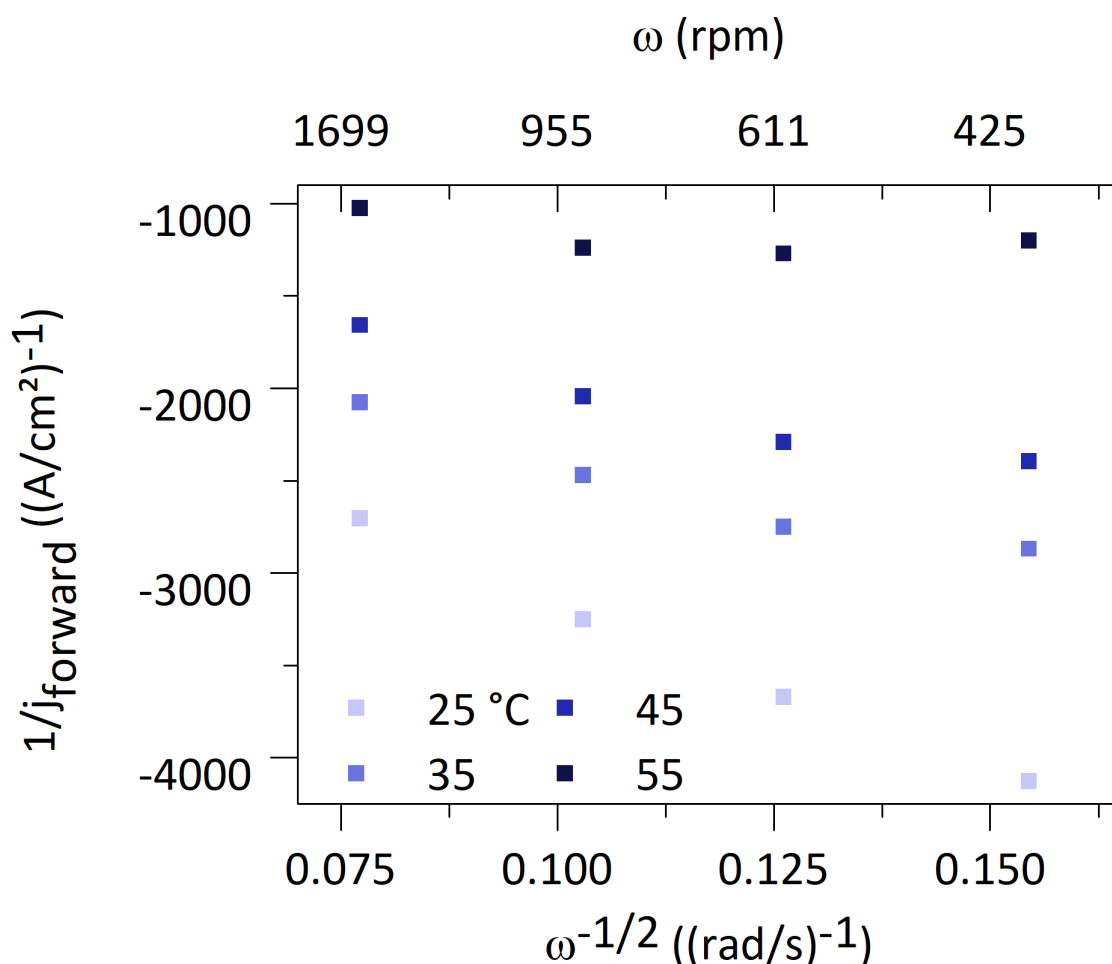


Figure A.3. 8 Koutecky-Levich analysis. Inverse of the forward current assess at an overpotential $\eta = -600$ mV as function of the inverse of the square root of the rotating speed of the rotating disk electrode (RDE). Four rotating speed were considered: 400 rpm, 600 rpm, 900 rpm and 1600 rpm. All measurements were conducted in a 3-electrodes electrochemical cell using Pt disk as working electrode, Pt wire as counter electrode and a leakless reference. Temperature was controlled to 25 °C, 35 °C, 45 °C and 55 °C.

Altogether, these parameters suggest that caution must be taken when discussing the activation energy measured to be ≈ 10 kJ/mol at an overpotential (η) of -600 mV and a rotation speed (ω) of 1600 rpm (see Figure A.3. 9). Indeed, 58 kJ/mol must be added to obtain the activation energy at the equilibrium potential.

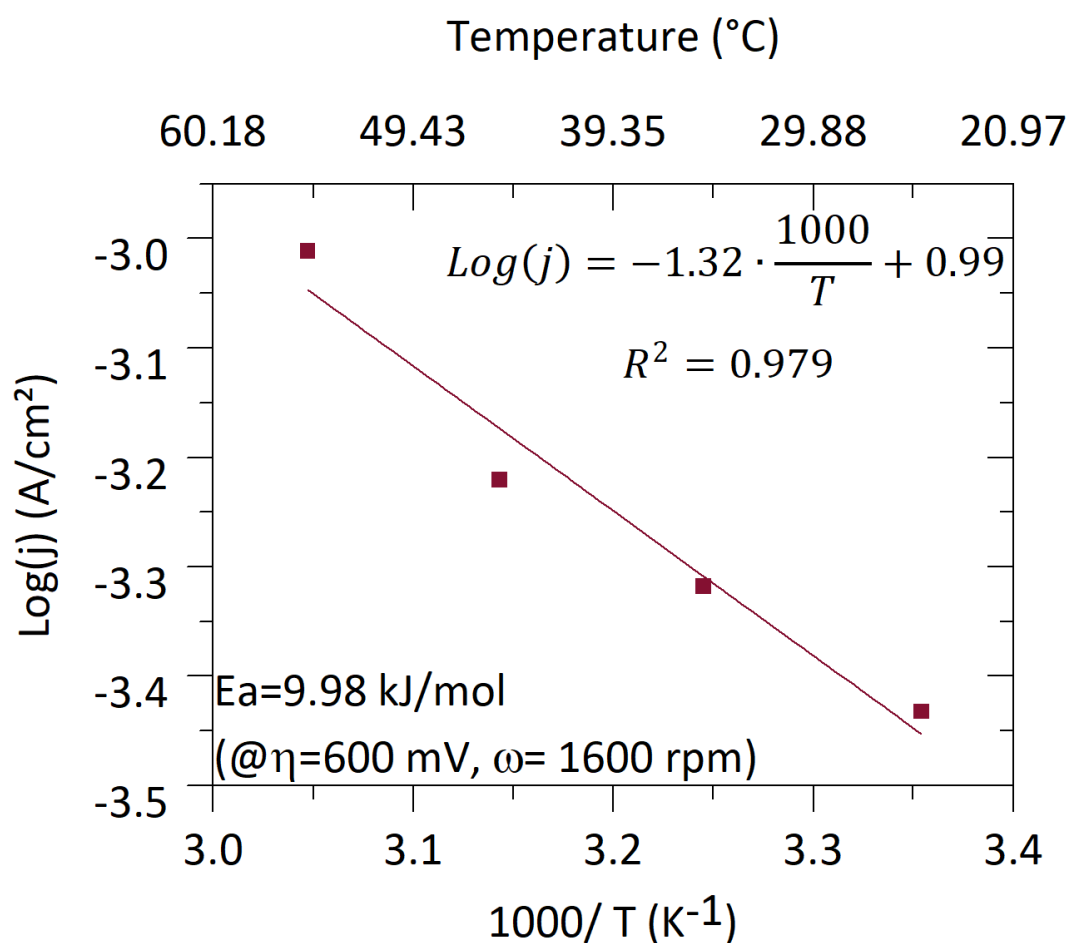


Figure A.3. 9 Arrhenius analysis made at an overpotential of -600 mV, a rotating speed of 1600 rpm. All measurements were conducted in a 3-electrodes electrochemical cell using Pt disk connected to a rotating disk electrode as working electrode, Pt wire as counter electrode and a leakless reference in 20 m LiTFSI electrolyte. Temperature was controlled to 25 $^{\circ}\text{C}$, 35 $^{\circ}\text{C}$, 45 $^{\circ}\text{C}$ and 55 $^{\circ}\text{C}$.

Spider chart data

Data used to make the spider chart shown in Figure 3. 14 are either directly taken from literature or experimentally assess (in the case of WiSE-based LIB) and then calculated thanks to the model develop by Betz *et al.* ²²¹. Table A.3. 1, Table A.3. 2 and Table A.3. 3 summarize the data used to draw the comparative spider chart. Rate capability of Lead-acid, Ni-Cd, Ni-MH and LIB devices were extracted and calculated from Ref^{8,221,261,262}.

Table A.3. 1 Summary of specific energy and energy density as function of the technology.

Technology	Devices	Specific energy (Wh/kg _{cell})		Energy density (Wh/L _{cell})	
		Min	Max	Min	Min
Lead-acid	Grid/ Vehicles	30 ⁹	60 ^{5,6}	80 ⁶	130 ⁶
Ni-Cd	Portable/ Vehicles	30 ⁷	60 ⁸	55 ⁷	150 ²⁶³
Ni-MH	Portable/ Vehicles	42 ⁵	110 ⁵	135 ⁷	275 ²⁶³
NMC111/graphite adapted from Ref ²²¹	18650	196		422	
Superconcentrate d aqueous adapted from Ref ²²¹	18650	54 Mo ₆ S ₈ /LFP (WiSE)	99 LTO/NMC (WiBS)	161 Mo ₆ S ₈ /LFP (WiSE)	247 LTO/NMC (WiBS)

Table A.3. 2 Summary of Self-discharge rate as function of the technology.

Technology	Self-discharge rate (%/month)	
Ref ⁷	Min	Max
Lead-acid	1	15
Ni-Cd	5	20
Ni-MH	15	30
NMC111/graphite	2	10
20m LiTFSI (experimental)	30	75

Table A.3. 3 Summary of the operating temperature range as function of the technology.

Technology	Operating temperature (°C)	
	Min	Max
Lead-acid	-40 ⁵	60 ⁵
Ni-Cd	-20 ⁷	70 ⁷
Ni-MH	-30 ⁵	65 ⁵
NMC111/graphite	-20 ⁵	60 ⁵
20m LiTFSI (experimental)	20	40

Table A.3. 4 Summary of the energy efficiency as function of the technology.

Technology	Energy efficiency	
	Min	Min
Lead-acid	70 ⁵	85 ⁶
Ni-Cd	72,5 ⁸	85 ⁶
Ni-MH	70 ⁸	90 ⁷
NMC111/graphite	90 ⁶	95 ⁵
20m LiTFSI (experimental)	92	92

In their study, Betz *et al.*²²¹ split the energy density and specific energy calculations in six steps from a theoretical point (Step 1) of view to a practical one (from Step 2 to Step 6) as described in Figure A.3. 10.

Table A.3. 5, Table A.3. 6, Table A.3. 7, Table A.3. 8, Table A.3. 9 and Table A.3. 10 detail the parameter and calculations made thanks to the model developed by

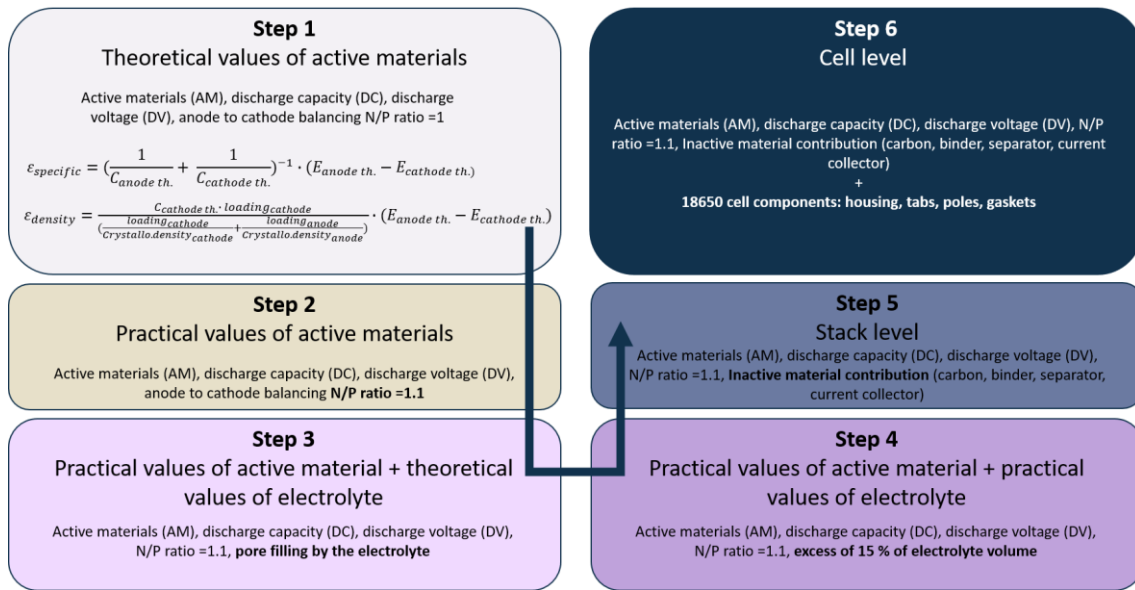


Figure A.3. 10 Illustration of the steps used in Ref. ²²¹ to determine the energy density and specific energy of a LIB cell as function of the influence of the different cell component.

Table A.3. 5 Energy density of 5 LIB as function of the step considered in calculation.

Energy Density (Wh/L)	Step 1 (AM, Theo. DC and DV)	Step 2 (AM, prac. DC and DV)	Step 3 (With Elyte)	Step 4 (With Elyte Excess)	Step 5 (Stack level)	Step 6 (Cell level 18650)
NMC vs. Graphite (organic)	1846	1275	762	718	514	422
Mo ₆ S ₈ vs. LFP (WiSE)	488	397	252	239	196	161
Mo ₆ S ₈ vs. NMC (WiSE)	852	542	333	314	235	193
LTO vs. NMC (WiBS)	951	667	415	393	301	247
LTO vs. LCO (WiBS) (Yamada data)	1008	644	391	369	272	224

Table A.3. 6 Specific energy of 5 LIB as function of the step considered in calculation.

Specific Energy (Wh/kg)	Step 1 (AM, Theo. DC and DV)	Step 2 (AM, prac. DC and DV)	Step 3 (With Elyte)	Step 4 (With Elyte Excess)	Step 5 (Stack level)	Step 6 (Cell level 18650)
NMC vs. Graphite (organic)	596	380	302	293	239	196
Mo ₆ S ₈ vs. LFP (WiSE)	110	89	73	71	64	55
Mo ₆ S ₈ vs. NMC (WiSE)	170	110	91	88	79	68
LTO vs. NMC (WiBS)	254	174	136	131	117	99
LTO vs. LCO (WiBS) (Yamada)	262	161	125	121	107	90

Table A.3. 7 Active materials parameter taken into account the model.

Active Materials parameters (Step 1)		Mo ₆ S ₈	LTO	NMC ₁₁₁	LFP	Graphite	LCO
Formula		Mo ₆ S ₈	Li ₄ Ti ₂ O ₁₂	LiNi _{0.1} Mn _{0.3} Co _{0.3} O ₂	LiFePO ₄	C ₆	LiCoO ₂
Theoretical Discharge Capacity (DC)	[mAh g ⁻¹]	128	175	298.5	172	372	274
Practical Discharge Capacity (modified with c-rate)	[mAh g ⁻¹]	120	150	170	165	360	137
Crystallographic density active material (AM)	[g cm ⁻³]	5,20	3,38	4,60	3,70	2,20	4,93
Max volume change during (dis)charge		0,1%	0,2%	2,4%	-6,6%	12,8%	1,9%
Electrode Porosity		30%	30%	30%	30%	32%	30%
Discharge voltage (DV) (in organic electrolyte)		1,9	1,5	3,8	3,4	0,2	3,95

Table A.3. 8 Cell parameters, inactive cell component and housing properties used in the LIB model by the 6 steps of calculations.

Battery Systems parameters		NMC vs. Graphite (organic)	Mo ₆ S ₈ vs. LFP (WiSE)	Mo ₆ S ₈ vs. NMC (WiSE)	LTO vs. NMC (WiBS)	LTO vs. LCO (Yamada data)
AM Mass Fraction Cathode		0,96	0,96	0,96	0,96	0,96
Binder Mass Fraction Cathode		0,02	0,02	0,02	0,02	0,02
Conductive Additive Mass Fraction Cathode		0,02	0,02	0,02	0,02	0,02
Active Mass Fraction Anode		0,96	0,96	0,96	0,96	0,96
Binder Mass Fraction Anode		0,03	0,02	0,02	0,02	0,02
Conductive Additive Mass Fraction Anode		0,01	0,02	0,02	0,02	0,02
Theoretical Elyte Excess Additionally to Pore Volume		0	0	0	0	0
Practical Elyte Excess Additionally to Pore Volume		0,15	0,15	0,15	0,15	0,15
Theoretical Mean Discharge Voltage	[V]	3,6	1,5	1,9	2,3	2,45
Practical Mean Discharge Voltage	[V]	3,4	1,35	1,65	2,3	2,35
Theoretical Ratio Capacity Anode/ Cathode		1	1	1	1	1
Practical Ratio Capacity Anode/ Cathode		1,1	1,1	1,1	1,1	1,1
Thickness Cathode	[μm]	100	100	100	100	100
Thickness Separator	[μm]	20	20	20	20	20
Density Elyte	[μm]	1,3	1,64	1,64	1,783	1,783
Volume in 18650 for Jelly Roll	[mL]	14,55	14,55	14,55	14,55	14,55
Mass Cell components	[g]	6,9	6,9	6,9	6,9	6,9
Outer Volume 18650	[mL]	17,71	17,71	17,71	17,71	17,71
Inactive Cell Component (Step 5)	Thickness [μm]	Spec. Mass [mg cm ⁻²]	Density [g cm ⁻³]	Porosity	Passive components/ housing Panasonic NCR18650B (Step 6)	Approximate weight [g]
Binder PVdF (Solef 5130)			1,80		Packaging foil	0,31
Conductive Additive (Imerys C65)			2,25		Steel can	3,65
Pos. Current Collector (Al; per coated side)	7,5	2,025	2,70		Insulator disk (2×),	0,13
Neg. Current Collector (Cu; per coated side)	5	4,48	8,96		Positive pole/negative pole Positive pole incl. CID, PTC, and gasket	1,56
Liquid Electrolyte (LP30)			1,30		Negative pole Jelly roll	0,69
20 m LITFSI (WiSE)			1,64		Ni mandrels (2×, wrapped Ni foil)	0,56
20 m LiTFSI + 7 m LiBETI (WiBS)			1,78		Sum inactive	6,9
Separator (Celgard2320)			0,95	0,39		

Table A.3. 9 Electrolyte properties used to describe a LIB cell in the model.

Battery Systems (Electrolyte Calculations)		NMC vs. Graphite (organic)	Mo _{0.5} S _{0.5} vs. LFP (WiSE)	Mo _{0.5} S _{0.5} vs. NMC (WiSE)	LTO vs. NMC (WiBS)	LTO vs. LCO (Yamada)
Loading Pos. Electrode AM Area Mass	[mg cm ⁻²]	20,00	20,00	20,00	20,00	9,72
Density Separator + Elyte	[g cm ⁻³]	1,09	1,22	1,22	1,27	20,00
Specific Mass Separator	[mg cm ⁻²]	1,16	1,16	1,16	1,16	1,27
Specific Mass Separator + Elyte	[mg cm ⁻²]	2,17	2,44	2,44	2,55	1,16
Loading of Elyte in Separator	[mg cm ⁻²]	1,01	1,28	1,28	1,39	2,55
Loading Elytes in Cathode	[mg cm ⁻²]	3,90	4,92	4,92	5,35	1,39
Loading Practical Elyte in Anode	[mg cm ⁻²]	3,03	4,37	4,50	5,97	5,35
Total Volume Elyte in Pores (A+C+S)	[μL cm ⁻²]	6,11	6,44	6,52	7,13	4,81
Resulting Elyte to AM mass ratio	[μL mg ⁻¹]	0,31	0,32	0,33	0,36	6,48
Theoretical Elyte Excess Additionally to Pore Volume		0,00	0,00	0,00	0,00	0,32
Practical Elyte Excess Additionally to Pore Volume		0,15	0,15	0,15	0,15	0,00
Theoretical Ratio needed Elyte/ Cathode AM	[μL mg ⁻¹]	0,31	0,32	0,33	0,36	0,15
Practical Ratio Needed Elyte/ Cathode AM	[μL mg ⁻¹]	0,35	0,37	0,38	0,41	0,32
Theoretical Total Volume Elyte per Area	[μL cm ⁻²]	6,11	6,44	6,52	7,13	0,37
Practical Total Volume Elyte per Area	[μL cm ⁻²]	7,02	7,41	7,50	8,20	6,48
Theoretical Total Mass Elyte per Area	[mg cm ⁻²]	7,94	10,56	10,70	12,71	7,45
Practical Total Mass Elyte per Area	[mg cm ⁻²]	9,13	12,15	12,30	14,61	11,55
Theoretical Total Volume Elyte Excess per Area	[μL cm ⁻²]	0,00	0,00	0,00	0,00	13,28
Practical Total Volume Elyte Excess per Area	[μL cm ⁻²]	0,92	0,97	0,98	1,07	0,00
Theoretical Thickness Elyte excess	[μm]	0,00	0,00	0,00	0,00	0,97
Practical Thickness Elyte excess	[μm]	9,16	9,68	9,78	10,69	0,00

Table A.3. 10 Summary of the battery system calculation made with the model.

Battery Systems (General Calculations)		NMC vs. Graphite (organic)	Mo _{0.5} S _{0.5} vs. LFP (WiSE)	Mo _{0.5} S _{0.5} vs. NMC (WiSE)	LTO vs. NMC (WiBS)	LTO vs. LCO (Yamada data)
Density Composite Cathode	[g cm ⁻³]	4,50	3,63	4,50	4,50	4,83
Density Composite Anode	[g cm ⁻³]	2,19	5,07	5,07	3,33	3,33
Density of AM in Cathode Coating	[g cm ⁻³]	3,02	2,44	3,02	3,02	3,25
Theoretical Volumetric Capacity Cathode Coating	[mAh cm ⁻³]	902,06	419,92	902,06	902,06	889,02
Practical Volumetric Capacity Cathode Coating	[mAh cm ⁻³]	513,74	402,83	513,74	513,74	444,83
Loading Cathode AM Areal Mass	[mg cm ⁻²]	20,00	20,00	20,00	20,00	20,00
Capacity area Theoretical Cathode	[mAh cm ⁻²]	5,97	3,44	5,97	5,97	5,48
Capacity area Practical Cathode	[mAh cm ⁻²]	3,40	3,30	3,40	3,40	2,74
Capacity area Theoretical Anode	[mAh cm ⁻²]	5,97	3,44	5,97	5,97	5,48
Capacity area Practical Anode	[mAh cm ⁻²]	3,74	3,63	3,74	3,74	3,01
Loading Theoretical Anode AM Area Mass	[mg cm ⁻²]	16,05	26,88	46,64	34,11	31,29
Loading Practical Anode AM Area Mass	[mg cm ⁻²]	10,39	30,25	31,17	24,93	20,09
Theoretical Anode Thickness	[μm]	112,35	78,83	136,81	152,64	140,01
Practical Anode Thickness	[μm]	72,72	88,73	91,42	111,56	89,91
Practical Additional Thickness (Dis-)charge Anode due to shrinking/expansion	[μm]	8,12	0,08	0,08	0,19	0,16
Practical Additional Thickness (Dis-)charge Cathode due to shrinking expansion	[μm]	2,34	-6,34	2,34	2,34	1,82
Total Stack Thickness with Elyte Excess	[μm]	224,84	227,16	238,63	259,79	236,60
Mass with Elyte Excess	[mg cm ⁻²]	48,45	69,71	70,81	66,63	60,25
Total Stack Volumetric Energy with Elyte Excess	[Wh L ⁻¹]	514,13	196,12	235,09	301,01	272,14
Total Stack Gravimetric Energy with Elyte Excess	[Wh kg ⁻¹]	238,60	63,91	79,23	117,37	106,86
Mass of Jelly Roll in 18650	[g]	31,35	44,65	43,17	37,31	37,05

MATERIALS & METHODS

1 Material preparation

1.1 Materials synthesis and characterization

LiFePO₄ (LFP) and LiNi_{0.6}Mn_{0.2}Co_{0.2}O₂ (NMC₆₂₂) were purchased from Umicore. LiTi₂(PO₄)₃ (LTP) was prepared by solid-state reaction of stoichiometric amounts of Li₂CO₃ (>99 %, Sigma Aldrich), TiO₂ (>99 %, Sigma Aldrich) and NH₄H₂PO₄ (98 %, Alfa Aesar). The precursors were grinded and heated at 200 °C for 2 h and finally 930 °C for 24 h in air. Mo₆S₈ was either obtained from ISCR (Institut des Sciences Chimiques de Rennes) or synthesized using the following protocol. Solid-state reaction was carried out by grinding and heating to 1050 °C (2 °C/min) for 72 h in a sealed tube stoichiometric amounts of Cu, Mo (99.95 %, Alfa Aesar) and S (99.98 %, Sigma Aldrich). An excess of 3.7 % (molar ratio) in Cu was then added and tube vacuum sealed and heated at 1050 °C for 24 h (2 °C/min). When MoS₂ impurities were detected, the as-synthesized powder was treated under H₂ reductive atmosphere in a boat crucible for 12 h (5 °C/min). The resulting sample was then acid-leached overnight in HCl 6 M under oxygen bubbling. The powder and the supernatant were separated by centrifugation and the samples were washed with distilled water until pH=7, prior to being dried at 80 °C under vacuum overnight.

X-ray diffraction (XRD) was performed to confirm the LTP and Mo₆S₈ phases purity using a BRUKER D8 Advance diffractometer with Cu K α radiation ($\lambda_{K\alpha 1}$ = 1.54056 Å, $\lambda_{K\alpha 2}$ = 1.54439 Å).

1.2 Electrode formulation

1.2.1 Bellcore technique

For battery assembly, Mo₆S₈, NMC₆₂₂, LFP and LTP composite self-standing electrodes are fabricated using Bellcore technique²⁶⁴. Active materials (AM), Carbon super P (Csp, Timcal) and PVdF-HFP (Poly(vinylidene fluoride-hexafluoropropylene, Solvay) are grinded with the following weight ratio: 73 wt% of AM, 8 wt% of Csp and 19 wt% of PVdF-HFP for Mo₆S₈ and LFP and 60 wt% of AM, 20 wt% of Csp and 20 wt% of PVdF-HFP for NMC₆₂₂ and LTP. NMC₆₂₂ and LTP are mixed with Csp for 20 min using the Spex miller with a ball to powder weight ratio of 11 for LTP and 8 for NMC₆₂₂ prior to be mixed with PVdF-HFP. Targeted loadings are summarized in Table M.M. 1.

Table M.M. 1 Summary of the practical capacity and targeted loadings considered in the study and experimental ones used.

Active material	Practical capacity (mA.h/g)	Targeted loading (mg/cm ²)	Experimental loading (mg/cm ²)
Mo ₆ S ₈	128	7	5.10 ± 1.12
LFP	172	21	16.07 ± 1.60
LTP	138	9.6	10.76 ± 1.19
NMC ₆₂₂	170	7	7.60 ± 0.67

The mixture is then dissolved in acetone with in the proportion of 120 mg_{total mass of powder}/mL_{acetone} and sonicated during 30 min. DBP (Dibutylphthalate, 99 % Sigma Aldrich) is added as plasticizer and the slurry heated at 50 °C for one hour under stirring. Then, the slurry is casted in a petri-dish and left to dry at least one hour (see Figure M.M. 1a).

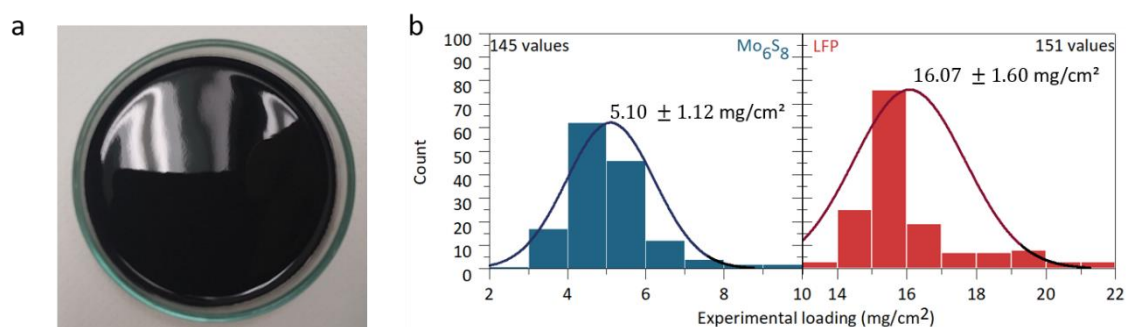


Figure M.M. 1 (a) Photography of a Mo₆S₈ composite Bellcore electrode casted in a petri-dish. (b) Distribution of Mo₆S₈ (blue) and LFP (red) electrode loading. Lines corresponds to normal distribution.

Electrodes are washed 3 times for 30 min in diethyl ether (99 %min, Alfa Aesar) to create porosity by removing DBP and dried at 80 °C under vacuum overnight. Finally, electrodes are punched with a 0.5 inch diameter. Loading distribution is shown in Figure M.M. 1b. for the ≈ 150 first electrodes, demonstrating good reproducibility. Despite the differences between experimental loadings and targeted ones: ≈ 25 % lower for Mo₆S₈ and LFP and ≈ 10 % higher for NMC₆₂₂ and LTP, the balancing between the electrodes is maintained to 4.2 for LFP: Mo₆S₈ and 1.15 for LTP:NMC₆₂₂.

1.2.2 Alternative process of electrode fabrication

For the overcapacitive carbon YP50 counter electrodes, self-standing PTFE electrodes are prepared by mixing YP50 and PTFE (Polytetrafluoroethylene, 60 wt% dispersion in water) at a mass ratio of 9:1 in isopropanol. Isopropanol volume is added gradually until an appropriate slurry is obtained. Then, the slurry is laminated several times following a

puff pastry technique to obtain films of loadings around 20 mg/cm². Finally, electrodes are dried at 80°C under vacuum.

NMC₆₂₂ electrochemical signature in LP30 is obtained using the powder mixture of NMC₆₂₂ and Csp at a weight ratio of 8:2.

1.3 Electrolyte preparation

1.3.1 Aqueous electrolyte

Aqueous superconcentrated electrolytes mainly rely on the use of Lithium bis(trifluoromethanesulfonyl)imide (LiTFSI, LiN(SO₂CF₃)₂) which was obtained from Solvay or Solvionic and used as received. Lithium bis(pentafluoroethanesulfonyl)imide (LiBETI, LiN(SO₂CF₂CF₃)₂) was purchased from TCI Chemicals and used as received to make *Water-in-bisalt* (WiBS) electrolyte.

20 m, 15 m, 10 m, 7 m, 5 m, 3m and 1 m (mol/kg) of LiTFSI or 20 m LiTFSI : 8 m LiBETI electrolyte solutions were prepared by mixing LiTFSI and LiBETI salts with Milli-Q ultrapure water following Equation M.M. 1.

Equation M.M. 1:

$$m_{water} = \frac{m_{salt}}{C_{mol/kg} \cdot M}$$

with m_{water} , the mass of water to be added (kg); m_{salt} , the mass of salt (g); $C_{mol/kg}$, the expected concentration (mol/kg) and M , the molar mass of the salt (g/mol).

Table M.M. 2 summarizes some physico-chemical properties for the two main electrolyte used in this study: 20 m LiTFSI and 20 m LiTFSI : 8 m LiBETI.

Table M.M. 2 Electrolyte properties and amount of water available in 20 m LiTFSI or 20 m LiTFSI : 8 m LiBETI as function of the electrolyte volume considered.

Electrolyte	Velectrolyte [μL]	ρ [g/mL]	m [g]	ω_{H_2O}	ω_{LiTFSI}	M_{H_2O} [g/mol]	n_{water} [mmol]
20 m LiTFSI	200	1.696	0.339	0.148	0.852	18	2.79
20 m LiTFSI	250	1.696	0.424				3.49

20 m LiTFSI : 8 m LiBETI		1.783 ⁵⁸	0.446	0.10	0.9		2.48
--------------------------------	--	---------------------	-------	------	-----	--	------

with $V_{electrolyte}$, volume of 20 m LiTFSI electrolyte/cell (μL); ρ , density in (g/mL) measured by densimeter; m , the mass of electrolyte (g); ω_{H_2O} , water mass fraction; ω_{LiTFSI} , LiTFSI mass fraction; M_{H_2O} , molar mass of water (g/mol); n_{water} , the total amount of water available (mol).

The amount of water in these electrolytes can be calculated according to Equation M.M. 2.

Equation M.M. 2:

$$n_{water} (mol) = \frac{\omega_{H_2O} \cdot V_{electrolyte} \cdot \rho}{M_{H_2O}}$$

1.3.2 Organic electrolyte

Pure organic solvents EC (Ethylene carbonate), DMC (Dimethyl carbonate), 1,3-dioxolane (DOL), 1,2-dimethoxyethane (DME) were purchased from Sigma Aldrich. Fluoroethylene carbonate (FEC) was purchased from TCI Chemicals. EC:DMC (1:1 vol%) and DOL:DME (1:1 vol%) were prepared by mixing the appropriate amount of solvents. To prepare the electrolytes (7M LiFSI in FEC, 1M LiTFSI : 2M LiFSI in DOL:DME + 3% LiNO_3), salts were dried in a vacuum oven at 110 °C prior to mixing. As-prepared electrolytes were dried over molecular sieves before use.

To perform the calibration for the fluoride ion selective electrode in organic electrolyte, EC:DMC (1:1 %vol) from Dodochem was used. LP30 (1 mol/L LiPF_6 in EC:DMC (1:1 %vol)) used for cycling experiments was purchased from Dodochem. All pure solvents were dried over molecular sieve prior to be used for solubility measurements.

1.4 Li/LiF and Li/Al₂O₃ coating preparation

1.4.1 LiF coating

LiF coating of approximately 30 nm thickness were deposited onto metallic Li following by reacting NF_3 with metallic Li ($\text{NF}_3 + 3 \text{ Li} \rightarrow 3 \text{ LiF} + \frac{1}{2} \text{ N}_2$) at 175 °C for one hour, as described in He *et al.*²⁴⁹. Current collectors were made of stainless steel (SS). SS/Li/LiF samples were 1.27 cm in diameter for E-SEM, SEM and XRD experiments. SS/Li/LiF samples were 0.9 cm in diameter for GC-TCD tests.

1.4.2 Al₂O₃ coating

The Al₂O₃ layers were deposited on the top of metallic Li samples using an atomic layer deposition (ALD) Picosun R-200 Advanced reactor which is a hot wall, flow through type reaction chamber operating in thermal ALD mode using O₃ (ozone) deposition process. The AC series (AC-bench 2025) ozone generator offers state-of-the-art silent corona discharge ozone generating technology based on O₂ (99.5 %) / N₂ (0.5 %) mixing gas. The deposition temperature range was set to 140 °C, *i.e.* at a threshold level well below the metallic Li melting temperature (\approx 180 °C). Trimethylaluminium (TMA) served as precursor ($\delta t_{\text{TMA}} = 0.1$ s) and O₃ ($\delta t_{\text{O}_3} = 0.6$ s) as reactant (second precursor) to achieve the deposition of homogenous and conformal Al₂O₃ layers (2 to 10 nm-thick).

2 Electrochemical characterizations

2.1 Two-electrode cells: Coin-cell and Swagelok

To perform electrochemical characterization, two set ups were used, either Swagelok® type cells or coin cells, as described in Figure M.M. 2 and Figure M.M. 3, respectively. Swagelok devices enable to easily recover the battery assembly (electrode/active material, separator etc.). However, the mechanical pressure applied to the cell is hardly reproducible due to the manual pressing of the plungers, which may influence the electrochemical behavior of the Swagelok cells and hamper the comparison from one cell to another. On the contrary, due to the sealing step using a crimping machine, the pressure applied is constant for coin cells (0.8 T) and reproducible between cells. Thus, coin cell 2032 were preferred for concentration, long-term cycling and self-discharge experiments in 2-electrode set-up.

In both set-ups, the battery relies on the same assembly. Self-standing negative and positive electrodes of 1.27 cm² surfaces were used. Two Whatman glass fibers are used as separators and soaked with electrolyte. On one side, the electrode is directly placed on the plunger or the coin cell casing. On the other side, a disk of stainless steel is placed between the electrode and plunger/casing separated by a spring.

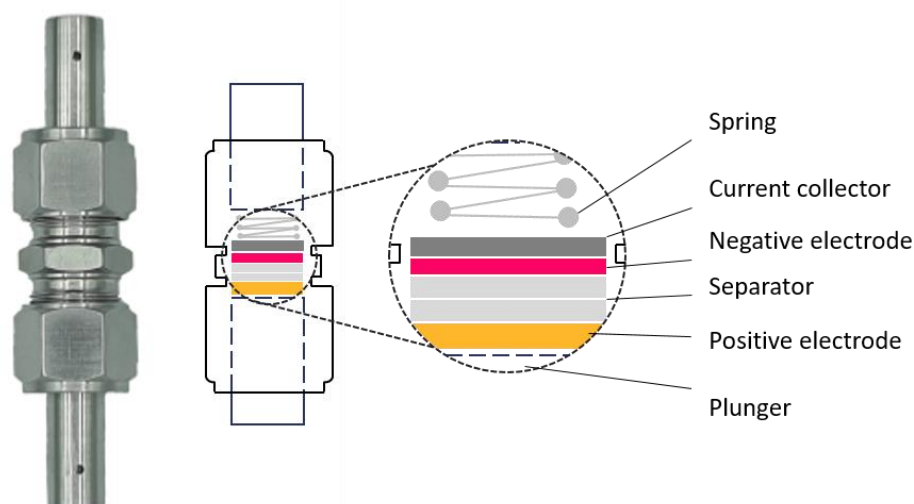


Figure M.M. 2 Swagelok photography and corresponding scheme of the battery assembly.

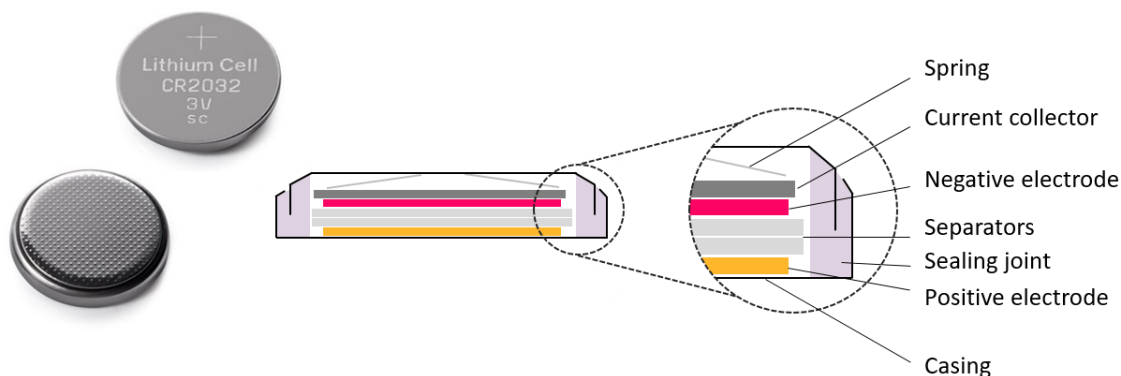


Figure M.M. 3 Coin cell photography and corresponding scheme of the battery assembly.

2.2 Three-electrode cell

The three-electrode cells used in this study are based on Swagelok 3-way T-connector. The third electrode is inserted by the side opening connection, as illustrated in Figure M.M. 4 and in Figure M.M. 5. Two types of three-electrode design were used, either PFA-based or stainless steel-based ones.

Li^+ insertion/de-insertion reversibility in active material (see Chapter 2) was tested using a three-electrode PFA-based Swagelok cell (see Figure M.M. 4) with two glassy carbon rods as current collectors. Self-standing composite active material electrode were used as working electrode and self-standing YP50 electrode as counter electrode. An Ag/AgCl reference electrode was used as reference electrode. Two Whatman glass fiber separators were used. Cyclic voltammetry was performed at 1 mV/s.

SEI stability during self-discharge protocol determined by electrochemical impedance spectroscopy (EIS) was assessed using a stainless steel 3-electrode Swagelok (see Chapter 3). Mo_6S_8 composite electrode was used as counter electrode and LFP composite electrode as working electrode. The reference electrode was based on a ring of $\text{Li}_{0.5}\text{FePO}_4$ deposited onto a stainless steel gauze (see picture in Figure M.M. 5b). Two glass fibers separators were used between the negative and the reference electrode and two glass fibers separators were placed between the reference electrode and the positive electrode. 200 μL of electrolyte were injected in the cell. After a 10 cycles pre-cycling step at 1C, 0.5C cycling steps with a 20 h OCV resting period after the 2nd charge were carried out. Potentio-electrochemical impedance spectroscopy (PEIS) was performed between 1 MHz and 50 mHz with an amplitude of 20 mV.

$\text{Li}_{0.5}\text{FePO}_4$ was obtained by electrochemical partial delithiation. Around 500 mg of LFP was used in a big Swagelok cell with a foil of scratched metallic Li as negative. Two Whatman glass fibers were soaked with LP30 electrolyte. LFP powder and glass fibers separators were separated with a celgard separator, enabling the recovery of the powder. The cell was cycled at C/40 until reaching half lithiated $\text{Li}_{0.5}\text{FePO}_4$ state (assessed by time limitation). Once the partially delithiated LFP was recovered, the powder was washed 3 times in DMC to remove electrolyte traces, and dried under vacuum at 80 °C overnight. Bellcore composite electrode were then made.

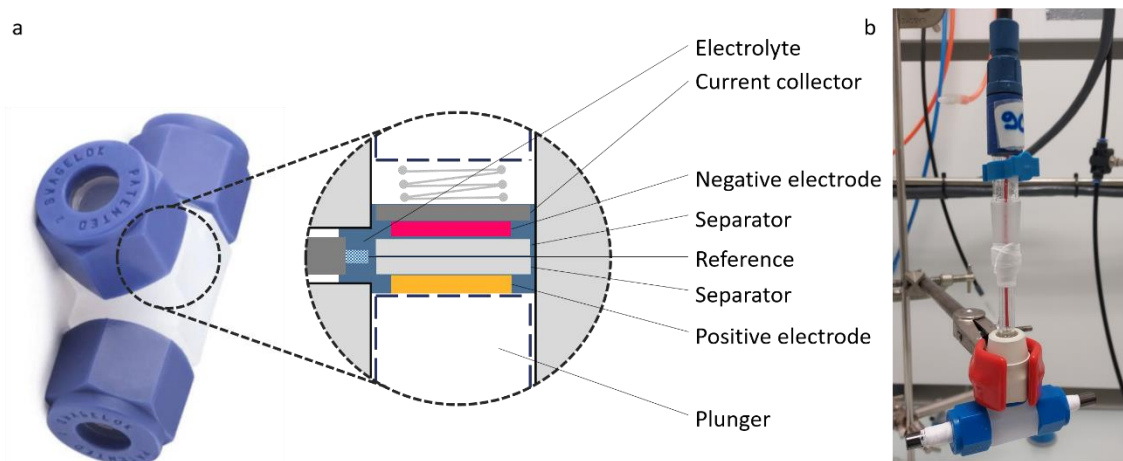


Figure M.M. 4 (a) Three-electrode PFA Swagelok photography and the corresponding scheme of the battery assembly. (b) Photography of the third electrode.

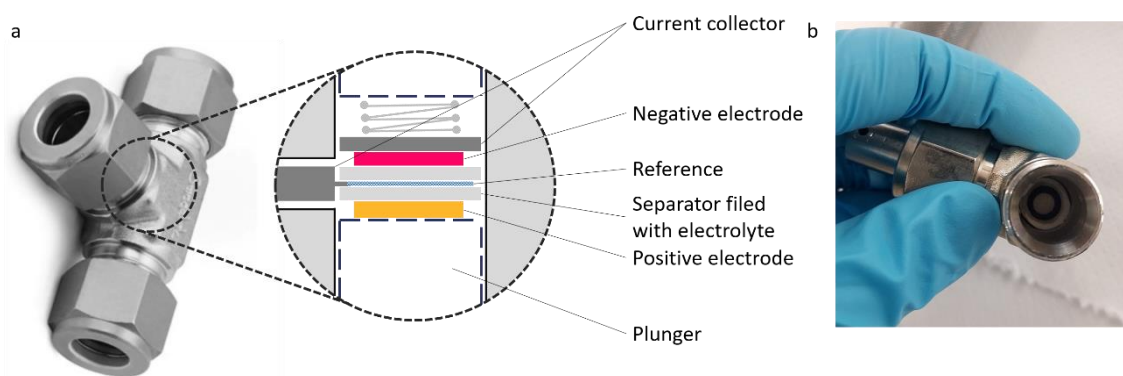


Figure M.M. 5 (a) Three-electrode stainless steel Swagelok photography and the corresponding scheme of the battery assembly. (b) Photography of the third electrode.

2.3 Operando pressure measurement: pressure cells and OEMS cell

Operando gas monitoring during cycling (see Chapter 2) was performed using homemade pressure cell previously developed in the lab,^{265,266} as reported in Figure M.M. 6. This cell consists of Swagelok cell in which the battery assembly is placed, a gas reservoir of ≈ 10 mL separates the battery assembly from the pressure sensor (on the top of the cell) directly connected and controlled by the potentiostat. The 10 mL gas reservoir was chosen to obtain a good signal to noise ratio, as pressure increase from gas production does not exceed 100 mbar. Moreover, to maximize the pressure sensed by the gauge, the electrode at which gas is produced is placed on the top of the battery assembly, facing the pressure sensor. All gas-monitoring experiments were performed in a temperature-controlled oven. Besides, a 10-hours resting period was used before starting the electrochemical protocol to enable the pressure to be stable.

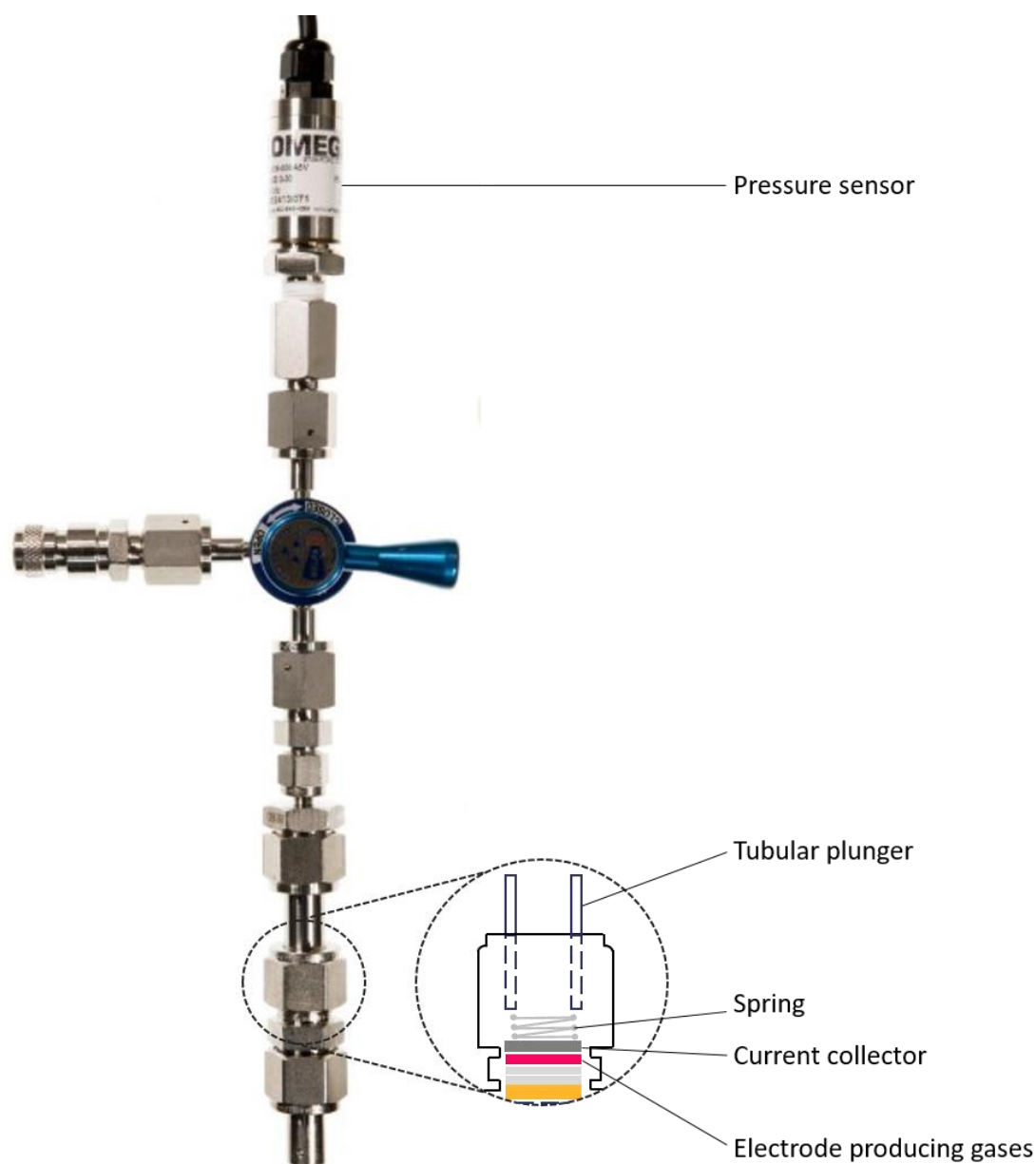


Figure M.M. 6 Pressure cell photography and corresponding scheme of the cell assembly.

Furthermore, gas identification (see Chapter 2) is performed by connecting a homemade battery cell to a mass spectrometer (MS), as detailed in Ref^{267,268}. The MS is an ExQ gas analysis system (Hidden Analytical, USA) composed of a HAL (Hidden Analytical) series quadrupole mass spectrometer, an ultra-high vacuum (UHV) mass spectrometer vacuum chamber, a vacuum pumping system and a QIC series capillary inlet. The whole system is controlled by a MASsoft 7 professional software. A photograph of the cell is shown in Figure M.M. 7a. After assembly, the online electrochemical mass spectrometry (OEMS) cell is transferred in a temperature-controlled oven (IPP260, Memmert, see Figure M.M. 7b). Then, the gas line and the cell are flushed and

pressurized to ≈ 1.3 bar with pure argon to avoid any contamination from ambient air or glove box atmosphere. Prior to perform the galvanostatic cycling, the OEMS cell valve connected to the mass spectrometer capillary is opened and the cell is held at open circuit voltage for ≈ 5 hours to reach a gas-liquid equilibrium inside the cell, and therefore to obtain a stable baseline value for all the partial pressure signals. During the OEMS measurements, the internal cell pressure was measured by the pressure sensor fixed on the gas line and the produced gaseous species were continuously sampled from the cell head space to the mass spectrometer via a thin capillary (1/16" diameter) at a leak rate of $12.5 \mu\text{L}/\text{min}$. The partial pressures are eventually determined for each gas based on their mass to charge ratio (m/z). Indeed, after ionization in the ionization source of the MS, separation in the mass analyzer and further detection in the ion detector, the partial pressures at $m/z = 2$, $m/z = 32$ and $m/z = 44$ were used to determine the evolution of H_2 , O_2 and CO_2 .

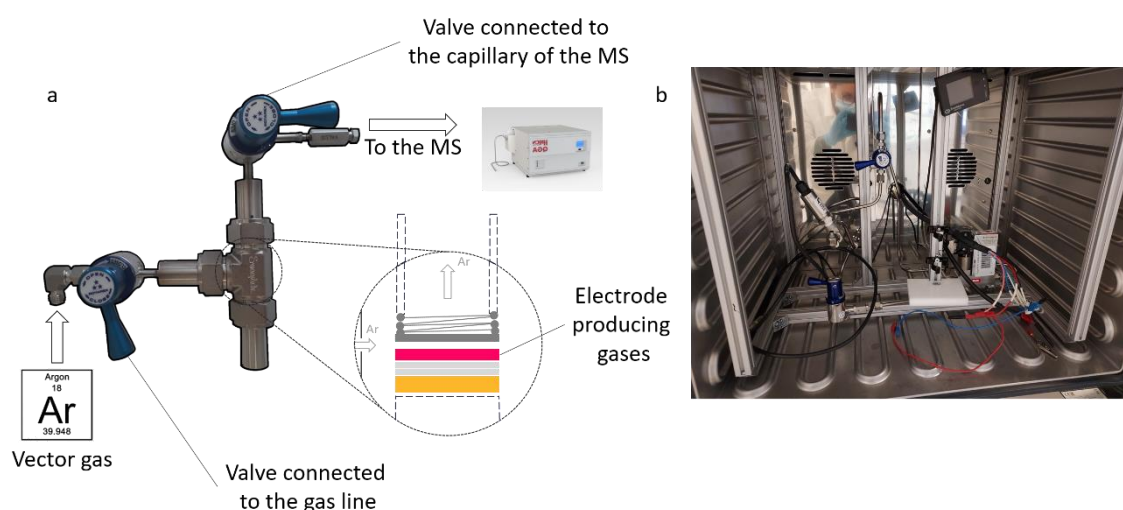


Figure M.M. 7 (a) Photography and scheme of the battery assembly used to perform online electrochemical mass spectrometry (OEMS). (b) Photography of the set-up used in the temperature-controlled oven.

All battery cells were assembled in an Ar-filled glovebox (MBRAUN). Electrolytes were saturated with argon prior to any experiment and to get entered into the glove-box to avoid oxygen contamination. $\text{Mo}_6\text{S}_8/\text{LFP}$ (1:4) full cells were assembled using stainless steel as current collectors. $\text{LTP}/\text{NMC}_{622}$ (1.1:1) full cells were assembled using stainless steel current collector for the negative electrode (LTP) and titanium for the positive one (NMC_{622}). Room temperature electrochemical tests were performed using a BCS-805 potentiostat (Bio-Logic). 55°C galvanostatic cycling, pressure cells (25°C) and OEMS (25°C , 55°C) experiments were performed in a temperature-controlled oven using a MPG2

multichannel potentiostat (Bio-Logic). C-rate was set as 1C being equal to one Li^+ cation inserted in one hour.

2.4 Electrochemical cell: glassware for temperature dependence study

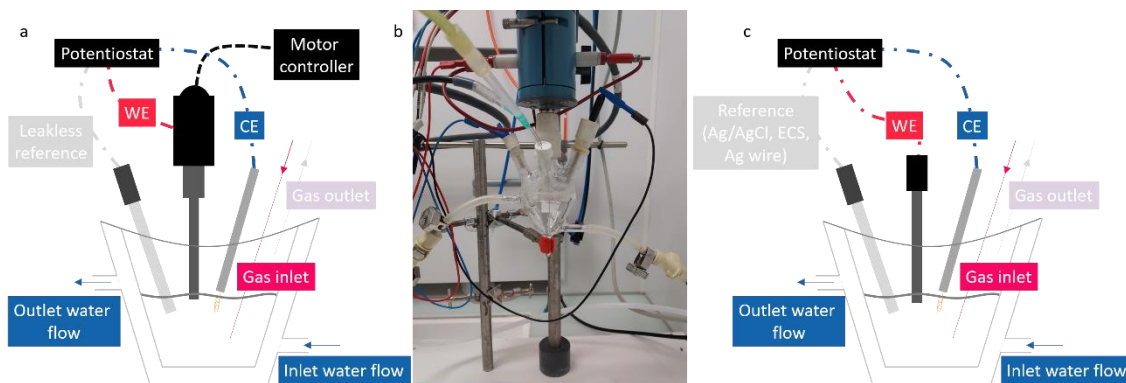


Figure M.M. 8 (a) Scheme of the electrochemical cell used for RDE measurements. (b) Photography of the set-up and (c) Scheme of the electrochemical cell used for electrochemical stability window (ESW) determination and SEI stability.

Figure M.M. 8 illustrates the three-electrode set-up using an electrochemical glass cell for electrochemical characterizations. A jacketed cell connected with a chiller was used for temperature-dependent measurements. Working electrode was mirror polished prior to any electrochemical measurements with a Presi® polishing machine using alumina solution of 6 μm , 0.3 μm and 0.04 μm solutions were used. Clean working electrodes were used for each measurement.

The activation energy for the hydrogen evolution reaction (HER) measurements, shown in Chapter 3, were performed on a biologic VSP potentiostat with a glassy carbon electrode mounted on a rotating disk electrode setup (RDE, PINE Inc, US.). Leakless electrode (Edaq ET069) and Pt wire were used as reference and counter electrodes, respectively. The leakless reference electrode is based on a Ag/AgCl reference electrode separated from the solution by a conductive junction. Temperature was set to 25 °C, 35 °C, 45 °C and 55 °C. 4 mL of 20 m LiTFSI were added in the glass cell and fresh electrolyte was used for each temperature to avoid electrolyte crystallization due to repeated water reduction and degassing. The leakless reference electrode was calibrated vs a reversible hydrogen electrode (RHE) as function of temperature before each experiment. For that, after bubbling the solution under Argon flow for 5 min to remove oxygen dissolved in the electrolyte, the cell was left at OCV for 50 min to ensure homogeneous temperature. The solution was then bubbled under H_2 flow for 5 min and

the potential of the leakless electrode measured against that of Pt. For each temperature, rotating speed was set to 400, 600, 900 and 1600 tr/min. Cyclic voltammetry experiments were performed at 50 mV/s from 0 V vs Ref to -1.2 V vs Ref. Prior to perform cyclic voltammetry, ohmic drop determination was assessed at 200 kHz. Table M.M. 3 summarizes the potential of the leakless reference electrode vs the RHE and the ohmic drop determination found experimentally.

Table M.M. 3 Calibration parameters for the determination of HER activation energy on Pt in 20 m LiTFSI by electrochemical cell.

Temperature (°C)	E_{ref} vs RHE (mV)	Ohmic drop (Ω)
25	237	77
35	243	50
45	268	48
55	235	46

Data analysis was performed by rescaling the potential toward RHE and removing Ohmic drop contribution. Current density at an overpotential (η) of -600 mV was determined. Only the forward current was used in the study.

Electrochemical stability window (ESW) (see Chapter 2) and SEI stability were determined by cyclic voltammetry (see Chapter 3) experiments performed in a 3-electrode electrochemical glass cell described in Figure M.M. 8b. The ESW was determined by performing CV using current collector materials (stainless steel or titanium) as working electrode. Pt wire was use as counter electrode and Ag/AgCl reference was used as reference electrode. The SEI stability was studied using a PTFE embedded glassy carbon disc (4 mm diameter, Pine Research Instrumentation) as working electrode and Pt wire as counter electrode. Silver wire was used as *pseudo*-reference. Cyclic voltammetry experiments were performed on a VMP3 potentiostat (Bio-Logic). 100 mV/s scan rate was applied for ESW determination and 50 mV/s for SEI stability. All potentials were converted vs Li^+/Li scale.

3 Physico-chemical characterizations

3.1 Density measurements

The densities of solutions containing a precisely known amount of salt (m_{salt}) and water (m_{water}) were measured with an electronic densitometer (Anton Paar, DMA 35 Basic).

3.2 Differential scanning calorimetry (DSC)

The differential scanning calorimetry (DSC) measurements were done using a NETZSCH DSC 204F1 instrument. Calibration was done measuring samples prepared by adding two droplets of LiTFSI-based electrolyte on a 5 mm-diameter glass fiber separators (Whatman). Prior to any experiment, electrolytes are bubbled 15 min under Ar and separators are kept in the glovebox. The addition of electrolyte and the transfer in the aluminum pan were done in ambient atmosphere as fast as possible to reduce exposure to air and contamination by water traces. Unlike in previous reports, no mesocarbon microbeads (MCMB) were added in the calibration for promoting crystallization and avoiding supercooling¹²⁶. This choice was made to remain close to the experimental conditions for which coin cells are assembled with no MCMB.

The concentrations of the electrolyte used for calibration were calculated thanks to Equation M.M. 1 to be 19.803 m, 20.591 m, 20.910 m, 21.992 m and 22.9983 m. This small range of concentration for calibration was chosen remain in a concentration region in which the liquidus line can be consider as linear (as shown in Chapter 1, Figure 1.17).

For electrolyte samples analyzed after cycling, Mo₆S₈/LFP coin cells were cycled during 15, 50 and 100 cycles at 0.5 C using 60 μ L of 20 m LiTFSI electrolyte. Two glass fiber separators were used. Coin cells samples were opened in glovebox atmosphere and 5 mm diameter samples were punched in the middle of the two separators, assuming that the electrolyte concentration is homogeneously distributed. Once punched, the samples were transfer in the Al pan that is sealed outside the glovebox.

For the DSC measurements, the following protocol was applied. The temperature was first set to increase from 25 °C to 35 °C to ensure liquid state of the electrolyte, followed by a cool down step to - 60° °C and a heating step up to 60 °C, all at 2 °C/min under nitrogen cooling.

3.3 Fluoride ion selective electrode (ISE)

3.3.1 Calibration of the ISE

To determine the solubility limit of fluoride in both aqueous and organic-based solution, a fluoride ISE from Hach Lang (Intellical, ISEF121) was used. Prior to any solubility measurements, the electrode was calibrated using the protocols described below.

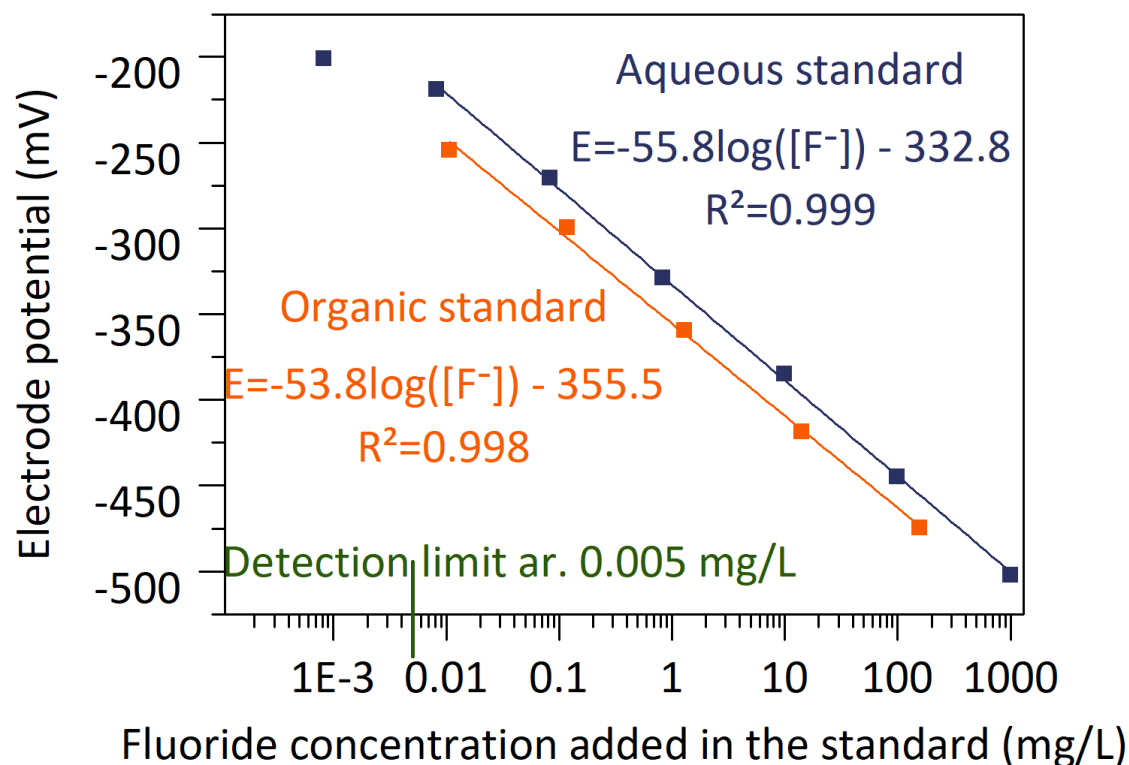


Figure M.M. 9 Calibration curve of the fluoride ion selective electrode (ISE) obtained for organic (orange line) and aqueous (blue line) standard.

3.3.1.1 Aqueous standard preparation

Standard aqueous solutions (25 mL minimum) were prepared by dissolving sodium fluoride (NaF, Alfa Aesar) in pure mQ-water at a concentration of 1000 mg/L. From this solution, solutions of concentration of 100 mg/L; 10 mg/L; 1 mg/L; 0.1 mg/L; 0.01 mg/L were prepared by dilution. Measurements for high concentration levels (≥ 10 mg/L) were conducted by adding one pillow of TISAB (ionic strength buffer -succinic acid- TISAB, Hach) to 25 mL of NaF solution. Low-concentration measurements (from 1 mg/L and below) were conducted according to the following protocol: a TISAB pillow was added to 25 mL of milli-Q ultrapure water and 5 mL of the as-prepared solution was added to the NaF solution. Solutions were stirred and $[F^-]$ was measured.

3.3.1.2 Organic standard preparation

Organic standard solutions were prepared by dilution of 1 mol/L of TBAF in THF solution (tetrabutylammonium fluoride solution, 1.0 M in tetrahydrofuran, Sigma Aldrich) in EC:DMC (Dodochem, 1:1 vol%) at an initial concentration of fluoride of 1900 mg/L. By continuous dilution of a factor 11, standards with lower concentration were prepared adding 300 μ L of the organic standard to 3 mL of EC:DMC solution. The

following standard concentrations were prepared: 157 mg/L; 14 mg/L; 1.30 mg/L; 0.12 mg/L and 0.011 mg/L. These organic standards were then diluted by adding 2 mL in a 20 mL TISAB:H₂O aqueous solution (1 TISAB pillow for 20 mL mQ-water) to perform the experiments. Solutions were stirred and [F⁻] was measured.

The potential and the temperature of the standard solutions were recorded by the F⁻ ISE under stirring in a plastic beaker. The calibration curve obtained in both aqueous and organic media are presented in Figure M.M. 9. A slope of -55.8 mV/decade is obtained at 23 °C in aqueous standards while slope of -53.8 mV/decade is found in organic standard at 23 °C. The theoretical slope is -58.7 mV/decade, and both calibrations were considered to be sufficiently accurate to perform LiF solubility measurements.

3.3.2 Solubility limit protocol and measurement

Commercial lithium fluoride (LiF powder, 300 mesh, Sigma Aldrich) was used in solubility tests. Saturated solutions were prepared as follows: excess amount of LiF were added to the solution. The solution was (i) let to stir overnight (or more) at constant temperature and (ii) let to rest before the formation of a precipitate could be visually observed. The solution was then centrifuged for 10 min at 6000 tr/min and the supernatant filtered using a PTFE or a polypropylene 0.2 µm pores filter. Solubility limit measurements were performed at the thermodynamic equilibrium. Therefore, we do not expect the solubility measurements to be dependent on the particulate size neither on their morphologies.

One may note that in the study by Jones *et al.*^{242,269,270} solutions were not filtered but the LiF solubility was measured from the supernatant after 24 h of decantation. This preparation led to a colloidal solution in which ion aggregation may be present. On the contrary, Tasaki *et al.*²⁴³ used a 2 µm pores filter to avoid the presence of any undissolved salt, and thus to obtain non-colloidal solution. As explained by Jones *et al.*^{242,269,270}, measuring colloidal solutions allows for the determination of the “real” solubility, as it takes into consideration all species in solution, *i.e.* from solvated ions to aggregates. Hence, their solubility value is said to be closer to the salt species behavior in the electrolyte. However, in our case, measurements in colloidal solution gave poorly reproducible results as the amounts of aggregates and remaining undissolved salt could vary depending on the supernatant collected. Therefore, we decided to measure non-colloidal solubility by filtering the supernatant with a 0.2 µm filter. Using our protocol, the LiF solubility limit measured in pure water (0.93 g / L at 23 °C) is close from the 1.11 g / L at 25 °C reported in the literature without filtration²⁴², thus validating our

measurement protocol. Moreover, bearing in mind that superconcentrated aqueous electrolytes were reported to be acidic,²⁷¹ our solubility measurements take into account this effect and its potential impact on the LiF solubility. Indeed, the addition of the ionic strength buffer and dilution protocol lead to pH value within the range of 5.5 to 6, as estimated with a glass pH electrode.

Regarding the samples measured at 55°C, all the laboratory equipment (pipettes, centrifuge tube, filter etc.) were heated at 55°C to avoid temperature artefacts. 2 mL of the saturated solutions were then diluted in 20 mL of milli-Q ultrapure water to prepare a diluted LiF-saturated electrolyte. Once the dilution was performed, the LiF concentration in solution was found far from the solubility limit. We therefore concluded that temperature control was unnecessary.

Three measurements were performed for each sample tested, except for 20 m LiTFSI : 8 m LiBETI. The mean value and standard deviation (3σ) are shown.

3.3.3 Fluoride concentration in LiF layer

Theoretical concentration of fluoride in LiF layer was calculated as following. Considering a LiF layer of 30 nm in thickness (as determined by SEM observation), 1.27 cm in diameter and considering the density of LiF to be 2.64 g/cm³, the mass of LiF is expected to be 1.68 .10⁻⁵ g. For a 10 nm thick layer, the mass of LiF is expected to be 3.34 .10⁻⁶ g. The mass of LiF divided by the electrolyte volume in which it is dissolved gives the theoretical concentration ($[F^-]_{theoretical}$).

Experimental fluoride concentration determination of Li/LiF sample was performed as follow: a Li/LiF sample is dissolved in a certain amount (125 or 150 mL) of TISAB:H₂O buffer solution until pH is measured to be in the range 5.5 to 6. Then, $[F^-]$ is measured and compared to the $[F^-]$ expected when considering complete dissolution of the entire 30 nm thickness.

Relative deviation is calculated following Equation M.M. 3.

Equation M.M. 3:

$$relative\ deviation = \frac{[F_{theoretical}^-] - [F_{experimental}^-]}{[F_{theoretical}^-]} \times 100$$

1.1 SEM and E-SEM

3.3.4 SEM

Scanning electron microscopy (SEM) images of the Li/LiF samples were taken with a Zeiss Merlin scanning electron microscope at an accelerating voltage of 1 kV. Samples were transferred to the SEM without exposure to air via a transfer vessel (Semilab Inc.) built for the Zeiss SEM airlock. The average and standard deviation of the LiF layer thickness were determined by measurements at five random positions on the edge of LiF layer in the cross-section view with tilt angle correction.

3.3.5 E-SEM

Li, Li/LiF and Li/Al₂O₃ samples of 1.27 cm, 1.27 cm and 0.7 cm in diameter, respectively, are affixed to sample holders using Cu tape in an Ar-filled glovebox (< 0.1 ppm O₂, < 0.1 ppm H₂O). The samples are transferred from the Ar-filled glovebox to an environmental SEM (ESEM Quattro S by Thermo Fisher Scientific) with minimal exposure to air and loaded into the chamber under high vacuum. The SEM is used in high-vacuum (0 % relative humidity, RH) and environmental (5, 30, 45, 60, 75 and 90 % RH, see Figure M.M. 10) mode for SEM imaging at 20 °C with a GSED detector in secondary electron (topography) mode. After recording a reference image at 0 % RH in high-vacuum mode, the SEM is operated in E-SEM mode at 5 % RH. The samples are then exposed to 15 % RH for 2 minutes and imaged at 5 % RH; alternating between reaction (high RH for 2 minutes) and imaging (always 5 % RH) conditions and repeated for 30, 45, 60, 75 and 90 % RH (see depiction of samples exposed to 30, 60 and 90 % RH and imaged at 5 % RH in Chapter 2). The SEM images are taken at 1.5/1.8 nA and 10/15 kV at a working distance of 8 mm, and a resolution of 1536 x 1024 pixel with a horizontal field width of 207 µm.

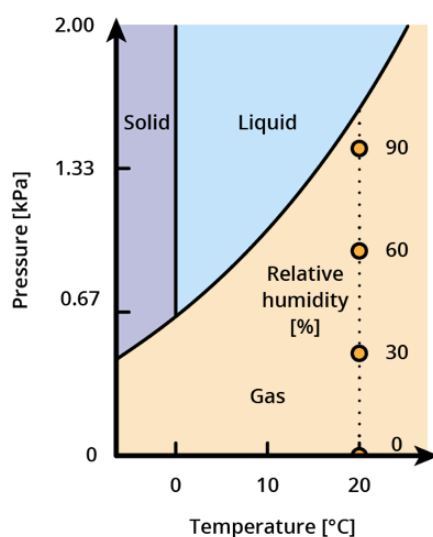


Figure M.M. 10 Working principle of increasing humidity in E-SEM.

3.4 Gas chromatography

Inside an Ar-filled glovebox (< 0.1 ppm O_2 , < 0.1 ppm H_2O), a gas-tight cell made from chemically-inert polyetheretherketone (PEEK) was assembled with Li/LiF or Li/ Al_2O_3 samples inside. The cell has a 5.5 mL gas headspace, inlet and outlet valves, and septa through which liquids can be injected and gas from the headspace can be extracted with gas-tight syringe. The gas-tight cell was then taken outside of the glovebox, connected to an Ar tank (R300, Airgas) and purged for 5 min at 100 mg_{Ar}/min . The cell was then filled with Ar to a pressure of 30 psi. 250 μL of electrolyte (20 m LiTFSI or 20 m LiTFSI : 8 m LiBETI) was then injected into the cell through a septum with a gas-tight syringe. Every 15 min, a 2.5 mL gas sample was collected with a gas-tight syringe and the remaining Ar headspace was purged with fresh Ar at 100 mg_{Ar}/min for 1 minute and the pressure set back to 30 psi. The gas samples were then injected into an Agilent 7890B gas chromatography instrument equipped with thermal conductivity (TCD) and flame ionization (FID) detectors for gas analysis, calibrated using 15 ppm and 1 vol% gas standards in N_2 (Supelco). The TCD detector was used for H_2 and CO_2 quantification, and the FID detector was used for CH_4 , C_2H_2 , C_2H_4 , C_2H_6 and CO quantification.

The pre-soaking of the LiF-coated samples was done by pipetting 50 μL (or 2 mL for pure FEC) of the organic electrolytes on LiF-coated Li samples inside a glovebox, which was left to react for 1 h, and subsequently dried under antechamber vacuum for 1 h before exposure to aqueous superconcentrated electrolytes. As the exposure to organic FSI-based electrolytes lasts one hour followed by a one-hour drying step, FSI^- is not directly exposed to water. If so, the time during which (two hours) the remaining traces

of FSI⁻ anions may be exposed to either WiSE or WiBS is far shorter than the time necessary to detect a significant FSI⁻ hydrolysis ²⁷.

3.5 XPS

X-ray photoelectron spectroscopy (XPS) was conducted on a PHI VersaProbe II X-ray Photoelectron Spectrometer. Samples were transferred to XPS in an air-sensitive transfer vessel to minimize exposure to air. Binding energies were calibrated by the adventitious carbon peak at 284.8 eV.

4 Data treatment

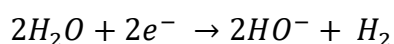
4.1 Pressure cell data treatment

4.1.1 Contribution to direct HER in Mo₆S₈/LFP cell irreversible capacity

Calculations of the amount of gas evolved during cycling can be done using two different experimental set-ups. The first one is using pressure cell data while the second one is using OEMS data. Assumptions made are the following:

- The HER mechanism considered during these calculations is the direct two electrons HER (see Equation M.M. 4).

Equation M.M. 4: Direct HER



- We estimated that the pressure evolution occurs only during second insertion plateau during charge, as observed in Figure M.M. 11.

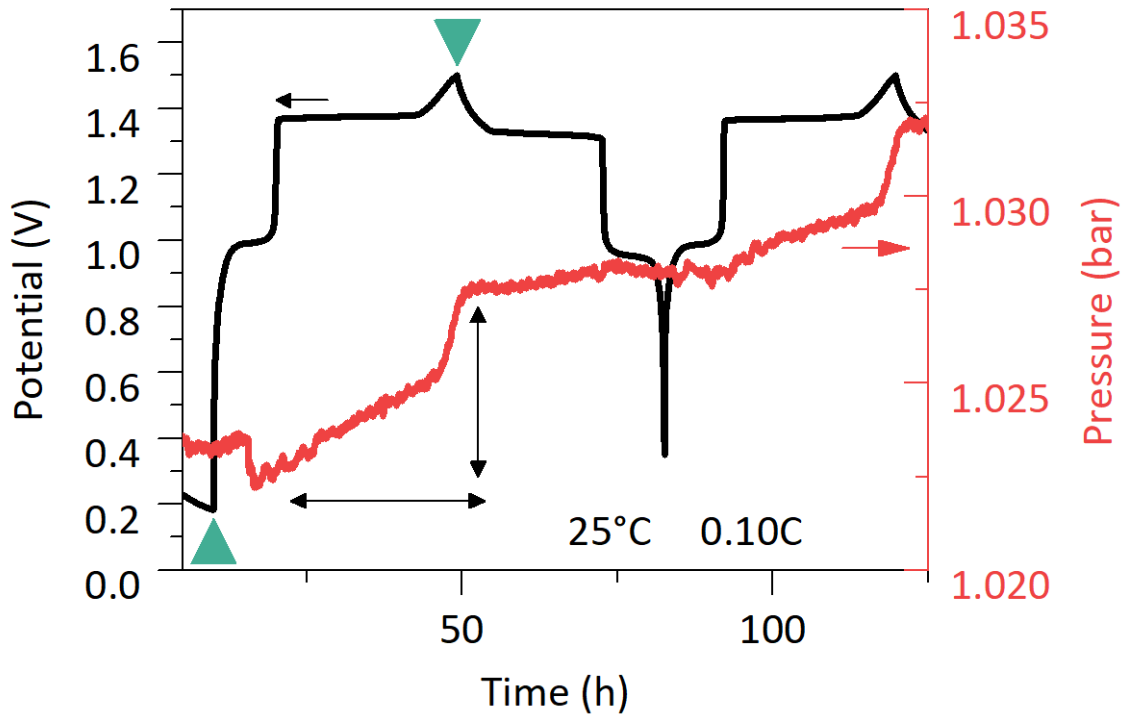


Figure M.M. 11 Illustration of *operando* gas monitoring during pressure cell experiment (based on $\text{Mo}_6\text{S}_8/\text{LFP}$ in 20 m LiTFSI). Black line represents potential as function of time. Red line is the pressure as function of time. Experiment performed at 0.10C, 25 °C.

Pressure cell data are smoothed according to adjacent-averaging method on 30 points in Originlab software version 8. Figure M.M. 11 shows both the pressure evolution and the potential as a function of time. From the ideal gas law (see Equation M.M. 5), variation of pressure can be linked to the amount of mole of gas produced. All pressure analysis were performed by taking as minimal and maximal pressure values the pressure values corresponding to the green arrows as shown in Figure M.M. 11. The relation between the amount of gas evolved and the capacity is given by the Faraday's law (see Equation M.M. 6). In addition, the irreversible capacity (see Equation M.M. 7) is determined by cycling performances analysis. Then, the irreversible capacity due to HER is rationalized by the total irreversible capacity, as described in Equation M.M. 8.

Equation M.M. 5: Ideal gas law

$$n_{\text{gas}}(\text{mol}) = \frac{\Delta P \cdot V}{R \cdot T} (\text{mol})$$

with ΔP the pressure increase during cycling (Pa); V the volume of the pressure cell (m^3) (here, 9.17 mL), R the molar gas constant (J/mol/K) and T the temperature (K).

Equation M.M. 6: Faraday's law

$$Q_{HER}(C) = 2n_{gas}F$$

with n_{gas} (mol) defined by Equation M.M. 5, F the Faraday constant (96500 C/mol), 2 the number of electron exchanged.

Equation M.M. 7: Irreversible capacity calculation

$$Q_{irr}(C) = Q_{charge} - Q_{discharge}$$

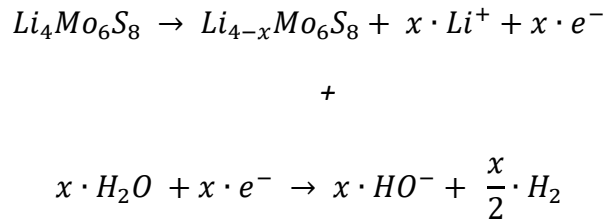
with Q_{charge} , the charge capacity of a cell, $Q_{discharge}$ the discharge capacity.

Equation M.M. 8:

$$\frac{Q_{HER}}{Q_{irr}}$$

4.1.2 Indirect HER in Mo₆S₈/LFP

The indirect HER mechanism can be expressed by the Equation M.M. 9, as being the sum of the following two half reactions:



Equation M.M. 9: Indirect HER

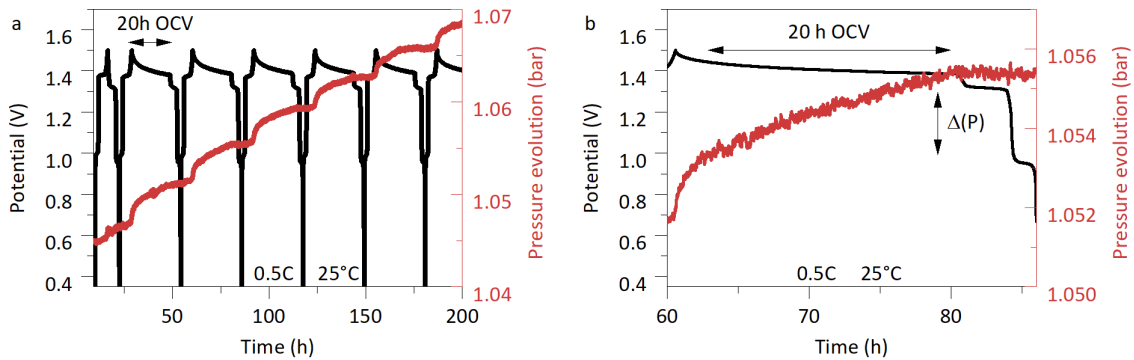
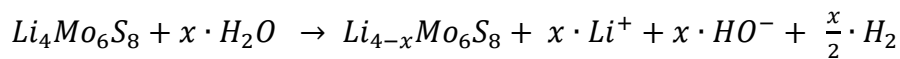


Figure M.M. 12 Illustration of pressure cell experiment using self-discharge protocol. Black line represents the potential as function of time. Pressure evolution as function of

time is shown by the red line. (a) Repeated self-discharge period. (b) Zoom on open circuit voltage (OCV) period. Experiments performed at 0.5C, 25 °C.

The amount of mole of hydrogen produced during self-discharge can be calculated from the Equation M.M. 5 and related to a capacity loss by HER ($Q_{HER \text{ due to resting}}$) thanks to Equation M.M. 6. The capacity loss by parasitic reaction ($Q_{lost \text{ by HER}}$) during resting period was calculated according to Equation M.M. 10 from cycling data. Then, the proportion of HER in the total capacity loss during self-discharge is calculated thanks to Equation M.M. 11.

Equation M.M. 10:

$$Q_{lost \text{ by HER}} = Q_{discharge}^n - Q_{discharge}^{n+1} \text{ (C)}$$

Equation M.M. 11:

$$ratio = \frac{Q_{HER \text{ due to resting}}}{Q_{lost \text{ by HER}}}$$

4.2 Online electrochemical mass spectrometry (OEMS) analysis. Determination of the amount of moles of hydrogen produced during direct HER.

Two hydrogen evolution slopes are observed during charge (see red arrows, part 1 and 2 in Figure M.M. 13). At the end of charge (part 2), one can assume that the only reaction occurring is the HER. Therefore, the capacity corresponds to the capacity due to HER ($\Delta Q_{HER \text{ part 2}}$). Two C-rate were used: 0.15C and 0.10C. Table M.M. 4 summarizes the parameters that enable to find the conversion constant between uma and mole of hydrogen produced during cycling, following Equation M.M. 12 and Equation M.M. 13. Once the conversion parameter found, the total amount of hydrogen produced during charge can be calculated and compared to the irreversible capacity, alike what is done to analyze results from pressure cells (see Equation M.M. 6, Equation M.M. 7 and Equation M.M. 8).

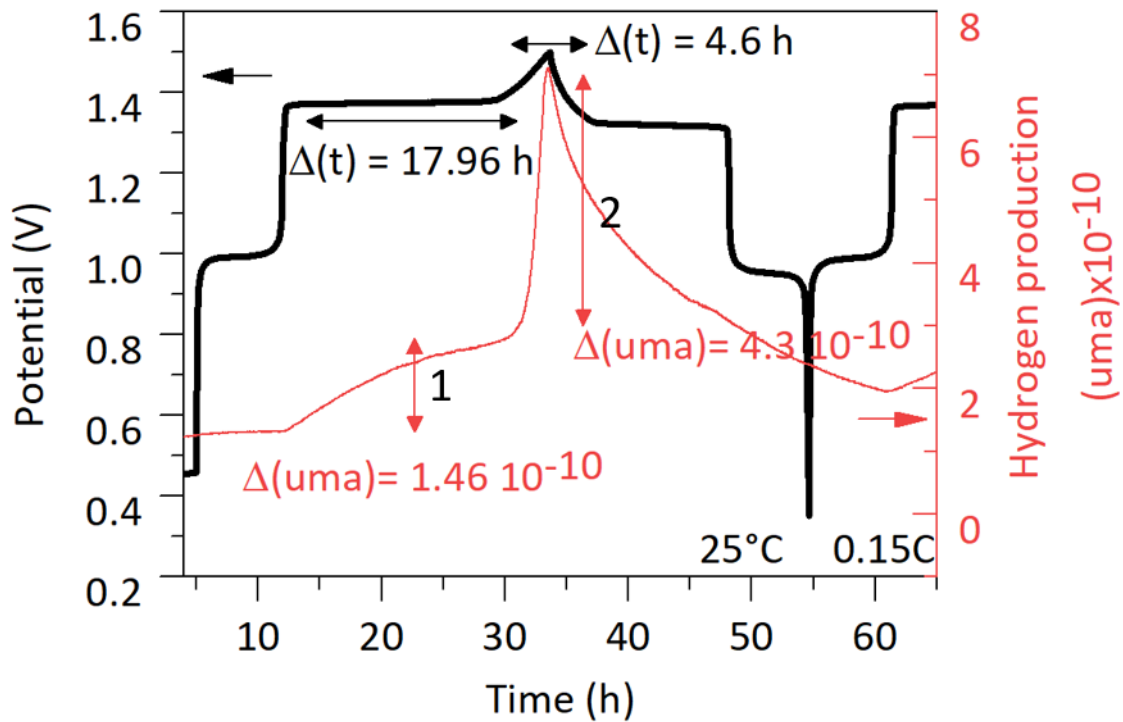


Figure M.M. 13 Illustration of *operando* gas monitoring during OEMS experiment (based on $\text{Mo}_6\text{S}_8/\text{LFP}$ in 20 m LiTFSI). Black line represents potential as function of time. Red line is the hydrogen evolution as function of time. Experiments performed at 0.15C, 25 °C.

Table M.M. 4 Summary of parameters used to obtain the conversion constant between uma and moles of hydrogen produced during cycling.

C-rate	Current (mA)	$\Delta Q_{\text{HER part 2}}$ (C)	$n_{\text{H}_2 \text{ part 2}} (\mu\text{mol})$ $n_{\text{H}_2 \text{ part 2}} (\text{uma})$	$1 \cdot 10^{-10}$ Uma to μmol	$n_{\text{H}_2 \text{ total}} (\mu\text{mol})$
0.15C	0.0303	0.501	2.60 $4.3 \cdot 10^{-10}$	0.605	3.48
0.10C	0.0117	0.216	1.117 $8.712 \cdot 10^{-11}$	0.1822	0.216

Equation M.M. 12:

$$\Delta Q_{\text{HER part 2}} = i \Delta(t)_{\text{part 2}} (C)$$

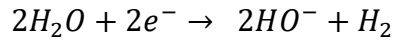
Equation M.M. 13:

$$n_{\text{H}_2} = \frac{\Delta Q_{\text{HER part 2}}}{2F} (\text{mol})$$

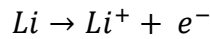
4.3 Gas calculation: GC-TCD/FID results

Metallic Li consumption during GC-TCD experiments were calculated by comparing the initial amount of Li available in the sample with the amount of hydrogen produced, which corresponds to a molar balance of one mole of H_2 produced for two moles of

metallic Li consumed, according to Equation M.M. 14. Table M.M. 5 lists the experimental parameters needed to calculate the amount of hydrogen produced. All the calculations consider hydrogen as being solely produced by direct HER. Equation M.M. 15, Equation M.M. 16 and Equation M.M. 17 detail the calculations needed to determine the ratio of metallic Li consumed by water reduction.



+



Equation M.M. 14:

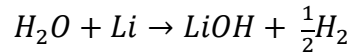


Table M.M. 5 Experimental parameters for GC-TCD/FID calculations.

Volume of the cell V_{cell} (mL)	Total pressure P_{tot} (bar)	Temperature T (°C)	Ideal gas constant R (J/mol/K)	Thick-ness of Li foil* e (μm)		Diameter of Li foil \varnothing (mm)		Li density ρ (g/cm ³)	Molar mass of Li M (g/mol)
5.5	3.06	20	8.314	LiF	Al ₂ O ₃	LiF	Al ₂ O ₃	0.534	6.941
				100	30.5	9	7		

*based on SEM observation

Equation M.M. 15: Amount of mole of gas available in the cell's headspace.

$$n_{cell}^{gas} = \frac{P_{tot} (Pa) \cdot V_{cell} (m^3)}{R \cdot T} = 689.8 \mu mol$$

Equation M.M. 16: Amount of mole of metallic Li initially available.

$$n_{Li\ foil} = \frac{\rho \cdot \pi \cdot \varnothing^2 \cdot e}{4 \cdot M} = 489 \mu mol (LiF) \text{ or } 90 \mu mol (Al_2O_3)$$

$$n_{Hydrogen} = n_{cell}^{gas} \cdot x_{Hydrogen}^* (mol)$$

Equation M.M. 17:

$$Ratio\ of\ Li\ consumed = \frac{2 \cdot n_{Hydrogen}}{n_{Li\ foil}}$$

The molar ratio of hydrogen ($x_{Hydrogen}^$) is obtained from the sum of the amount of H₂ measured after each 15 min interval.

4.4 Activation energy determination

Table M.M. 6 summarizes the cycling performances obtained during the pre-cycling step at 25 °C prior to perform the temperature-dependence study. One can notice that similar behaviors are obtained regardless the cell considered.

Table M.M. 6 Cycling performances obtained during pre-cycling step of Arrhenius study. Mean charge and discharge capacity obtained during 10 pre-cycling cycles at 25 °C for each temperature tested. Cells are based on Mo₆S₈/LFP full cells cycled using 20 m LiTFSI.

Protocol	Number of cells	Temperature (°C)	15	25	35	45	55
HER direct by pressure cell	1	$Q_{\text{charge}}^{\text{pre-cycling at 25 °C}}$ (mA.h/g)	/	103 ± 7	103 ± 7	108 ± 6	106 ± 6
		$Q_{\text{discharge}}^{\text{pre-cycling at 25 °C}}$ (mA.h/g)	/	100 ± 4	95 ± 1.5	103 ± 3	102 ± 4
HER direct by CC-CV coin cells	2	$Q_{\text{charge}}^{\text{pre-cycling at 25 °C}}$ (mA.h/g)	/	117 ± 2	117 ± 2	112 ± 2	117 ± 2
		$Q_{\text{discharge}}^{\text{pre-cycling at 25 °C}}$ (mA.h/g)	/	109 ± 1	112 ± 2	109 ± 1	115 ± 2
HER indirect by self-discharge on 2nd plateau	3 (except 2 at 15 °C)	$Q_{\text{charge}}^{\text{pre-cycling at 25 °C}}$ (mA.h/g)	106 ± 4	109 ± 3	108 ± 3.5	107 ± 3	109 ± 3
		$Q_{\text{discharge}}^{\text{pre-cycling at 25 °C}}$ (mA.h/g)	103 ± 3	107 ± 2	105 ± 2	105 ± 2	106 ± 2
HER indirect by self-discharge on 1st plateau	3	$Q_{\text{charge}}^{\text{pre-cycling at 25 °C}}$ (mA.h/g)	113 ± 2	107 ± 4	118 ± 5	109 ± 4	/
		$Q_{\text{discharge}}^{\text{pre-cycling at 25 °C}}$ (mA.h/g)	111 ± 1	103 ± 2	115 ± 4	106 ± 3	/

1.2 Impact of the electrolyte volume on cell performances: number of cycles before crystallization at 21 m LiTFSI

For the 20 m LiTFSI electrolyte with the properties described in Table M.M. 1, the amount of mole of water in 20 m LiTFSI is defined according to Equation M.M. 18.

Equation M.M. 18:

$$n_{20\text{ m LiTFSI}}^{\text{water}} = \frac{\rho_{20\text{ m LiTFSI}} \cdot V_{\text{electrolyte}} \cdot \omega_{\text{water}}}{M_{\text{water}}} \text{ (mol)}$$

with $\rho_{20\text{ m LiTFSI}}$, the density (g/cm³); $V_{\text{electrolyte}}$, the electrolyte volume (cm³); ω_{water} , the mass fraction of water and M_{water} , the molar mass of water (g/mol).

Fixing the amount of salt between 21 m LiTFSI and in 20 m LiTFSI (thus only considering water consumption), the amount of mole of water in 21 m LiTFSI is defined according to Equation M.M. 19.

Equation M.M. 19:

$$n_{21\text{ m LiTFSI}}^{\text{water}} = \frac{m_{\text{LiTFSI}}}{C \cdot M_{\text{LiTFSI}} \cdot M_{\text{water}}} \text{ (mol)}$$

with m_{LiTFSI} , the mass of LiTFSI salt initially present in 20 m LiTFSI (g); C , the expected concentration (here 21 m LiTFSI) (mol/kg); M_{LiTFSI} , the molar mass of LiTFSI (g/mol).

One cycling protocol consists of 10 cycles performed at 1C as pre-cycling step followed by a cycling step performed at 0.5C consisting of charge/discharge/charge followed by 20 h of OCV and a discharge/charge/discharge. The amount of mole of water consumed during such protocol is calculated by Equation M.M. 20, and values are summarized in Table M.M. 7

Equation M.M. 20:

$$n_{\text{during protocol}}^{\text{water consumed}} = 2 \cdot \frac{Q_{\text{irr}}^{\text{HER}}}{z \cdot F} \text{ (mol)}$$

with 2, a factor corresponding to the stoichiometric coefficient between H₂ and H₂O production; $Q_{\text{irr}}^{\text{HER}}$, the irreversible capacity due to HER during both cycling and resting period (C); z , the number of electron involved in the HER reaction; F , the faraday constant (C/mol). $Q_{\text{irr}}^{\text{HER}}$, the irreversible capacity due to HER is calculated assuming that HER account for 70 % of the irreversible capacity during cycling and 100 % of the irreversible capacity during self-discharge.

Equation M.M. 21 details the calculation made to determine the number of times the protocol described above can be repeated before 21 m LiTFSI concentration is reached due to water consumption.

Equation M.M. 21:

$$N_{before\ 21\ m\ LiTFSI}^{protocol} = \frac{n_{20\ m\ LiTFSI}^{water} - n_{21\ m\ LiTFSI}^{water}}{n_{during\ protocol}^{water\ consumed}}$$

Table M.M. 7 Amount of water available in 20 m LiTFSI and 21 m LiTFSI assuming the initial same amount of LiTFSI salt in both electrolyte. Amount of water consumed per protocol (μmol). Number of protocol that can be done before electrolyte crystallization.

$V_{\text{electrolyte}}$ (μL)	$n_{20\ m\ LiTFSI}^{\text{water available}}$ (mol)	$n_{21\ m\ LiTFSI}^{\text{water available}}$ (mol)	$n_{\text{during protocol}}^{\text{water consumed}}$ (μmol)	$N_{before\ 21\ m\ LiTFSI}^{protocol}$
9.4	0.000131221	0.000125338	≈ 5	1.2
50	0.000697244	0.000665981	4.151	7.5
100	0.001394489	0.001331962	4.396	14.2
150	0.002091733	0.001997943	5.429	17.3
200	0.002788978	0.002663923	4.391	28.5
300	0.004183467	0.003995885	4.270	43.9
400	0.005577956	0.005327847	5.570	44.9
500	0.006972444	0.006659809	3.767	83
600	0.008366933	0.00799177	3.917	95.8

5 Python

Fitting data for solubility is thus obtained by using “curve_fit” function from SciPy in Python.

LIST OF ABBREVIATIONS

a_{F^-}	Activity of F^-
a_{Li^+}	Activity of Li^+
Å	Angstrom
AC	Acetate
ACN	Acetonitrile
$Al(OH)_3$	Aluminum hydroxyde
Al_2O_3	Aluminum oxide
ALD	Atomic layer deposition
AM	Active material
CCCV	Constant current constant voltage
Cd	Cadmium
CE	Coulombic efficiency
C-rate	Cycling-rate
Csp	Carbon super P
CV	Cyclic voltametry
DBP	Dibutylphthalate
DEC	Diethylcarbonate
DMC	Dimethyl carbonate
DME	Dimethoxyethane
DMF	Dimethylformamide
DMPA	2,2-dimethoxy-2-phenylacetophenoe
DMSO	Dimethyl sulfoxide
DOL	1,3-dioxolane
DSC	Differential scanning calorimetry
E	Potential
e	Thickness
EC	Ethylene carbonate
EIS	Electrochemical impedance spectroscopy
EMC	Ethyl methyl carbonate
EMim TFSI	1-Ethyl-3-methylimidazolium bis(trifluoromethylsulfonyl)imide
E-SEM	Environmental-scanning electron microscopy
ESW	Electrochemical stability window
F	Faraday constant
$[F^-]_{lim}$	Maximum of F^- concentration
FEC	Fluoroethylene carbonate
FEMC	2-fluoroethyl methyl carbonate
GC	Glassy carbon
GC-TCD/FID	Gas chromatography-thermal conductivity/flame ionization detectors
GPE	Gel polymer electrolyte
H_2O	Water
H_2SO_4	Sulfuric acid
HEA	2-hydroxyethyl acrylate
HER	Hydrogen evolution reaction

HFE	Hughly fluorinated ether
i	Current
IEA	International energy agency
IL	Ionic liquids
ISE	Ion selective microscope
KCl	Potassium chloride
KOH	Potassium hydroxide
K_s	Constant of dissolution of LiF
KTFSI	Potassium(I) Bis(trifluoromethanesulfonyl)imide
LCO	LiCoO_2 Lithium cobalt oxide
LFP	Lithium iron phosphate
$[\text{Li}^+]_{\text{lim}}$	Maximum of Li^+ concentration
$[\text{Li}^+]_{\text{electrolyte}}$	Concentration of Li^+ in the electrolyte
$[\text{Li}^+]$	Concentration of Li^+
$\text{Li}(\text{H}_2\text{O})_4^+$	Hydrated lithium cluster
Li_2CO_3	Lithium carbonate
LiAc	Lithium acetate
LiAsF_6	Lithium hexafluoroarsenate
LiB	Li-ion battery
LiBETI	Lithium bis(pentafluoroethanesulfonyl)imide
LiFSI	Lithium bis(fluorosulfonyl)imide
LiTFSI	Lithium (fluorosulfonyl)(trifluoromethylsulfonyl)imide
LiMM_{3411}	Lithium propylsulfonate-butylsulfonate-dimethyl-amine
LiNO_3	Lithium nitrate
LiOtf	Lithium trifluoromethanesulfonate or Lithium triflate
LiPF_6	Lithium hexafluorophosphate
LiPTFSI	Lithium pentafluoroethanesulfonyl (trifluoromethanesulfonyl)imide
LiTFSI	Lithium bis(trifluoromethanesulfonyl)imide
LP30	1 mol/L LiPF_6 in EC:DMC (1:1 vol%)
LSV	Linear scanning voltametry
LTO	Lithium titanate
M	Molar mass
m/z	Mass to charge ratio
ME_3EtN^+	Trimethylethylammonium
MPEGA	poly(ethylene glycol) methyl ether acrylate
MS	Mass spectrometer
m_{salt}	Mass of salt
m_{water}	Mass of water
N/P	Negative to positive capacity ratio
NCA	Lithium nickel cobalt aluminum oxide
n_{gas}	Amount of mole of gas produced
$n_{20\text{ m LiTFSI}}^{\text{water}}$	Amount of mole of water in 20 m LiTFSI

n_{Hydrogen}	Amount of mole of hydrogen
$n_{\text{Li foil}}$	Amount of mole of metallic Li
$n_{\text{cell}}^{\text{gas}}$	Amount of mole of gas in the cell
Ni-Cd	Nickel-Cadmium
Ni-MH	Nickel Metal Hydride
NiOOH	Nickel oxide hydroxide
NMC/NCM	Lithium nickel manganese cobalt oxide
\varnothing	Diameter
OCV	Open circuit voltage
OEMS	Online electrochemical mass spectrometry
OER	Oxygen evolution reaction
PAM	Polyacrylamide
Pb	Lead
PC	Propylene carbonate
PEG/PEO	poly(ethylene glycol)/poly(ethylene oxide)
PEGDA	poly(ethylene glycol) diacrylate
PEIS	Potential-electrochemical impedance spectroscopy
PFA	Perfluoroalkoxy alkane
PVdF-HFP	Poly(vinylidene fluoride-hexafluoropropylene)
Q_{charge}	Charge capacity
$Q_{\text{discharge}}$	Discharge capacity
Q_{HER}	Capacity due to HER
Q_{irr}	Irreversible capacity
$Q_{\text{HER due to resting}}$	Capacity due to HER during resting
$Q_{\text{discharge}}^n$	Discharge capacity at cycle number n
$Q_{\text{discharge}}^{n+1}$	Discharge capacity at cycle number n+1
$Q_{\text{lost by HER}}$	Capacity lost by HER
R	Constant of ideal gas law
RDE	Rotating disk electrode
RH	Relative humidity
RHE	Reversible hydrogen electrode
RT	Room temperature
SEI	Solid electrolyte interphase
SL	Sulfolane
SLI	Starting lighting ignition
SOC	State-of-charge
SPE	Solid polymer electrolyte
SS	Stainless steel
T	Temperature
TBAF in THF	Tetrabutylammonium fluoride solution in Tetrahydrofuran
TEA ⁺	Tetraethylammonium
TEGDME	Tetraethylene glycol dimethyl ether
TEP	Triethyl phosphate

TISAB	Total ionic strength adjustment buffer
TMA	Trimethylaluminium
TMP	Trimethyl phosphate
TMSB	Tris(trimethylsilyl)borate
UHV	Ultra-High Vacuum
UPS	Unit power supply
USD	United States Dollar
V	Volume
VRLA	Valve Regulated Lead Acid
WiSE	Water-in-salt electrolyte
XRD	X-ray diffraction
Zn(TFSI) ₂	Zinc(II) Bis(trifluoromethanesulfonyl)imide
ΔP	Pressure increase
$\bar{\gamma}_{Li^+F^-}$	Mean ionic activity coefficient of the LiF salt
γ_{F^-}	Ionic coefficient of F ⁻
γ_{Li^+}	Ionic activity coefficient of Li ⁺
η	Viscosity
$\lambda_{K\alpha 1}$	Wave length of Cu K α radiation
ρ	Volumetric mass
σ	Conductivity
ω	Mass fraction
$x_{Hydrogen}^*$	Mole fraction of hydrogen

RÉSUMÉ EN FRANÇAIS

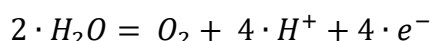
Le remplacement des énergies fossiles par leurs pendants renouvelables est au cœur de la transition énergétique mise en place pour limiter le changement climatique. Cependant, les limitations d'émissions de gaz à effet de serre (tels que le dioxyde de carbone CO_2 ou le méthane CH_4) peuvent entrer en conflit avec la demande croissante en énergie. Bien que la pandémie de la Covid 19 aie contracté la demande mondiale en énergie de 4 % en 2020, l'augmentation attendue en 2021 est de 4.1 %, selon les prévisions de l'IEA (Agence internationale de l'Energie). Ceci est notamment due à la croissance de la consommation dans les pays émergents et dans les économies en développement. La mise en place de politiques publiques efficaces et d'investissements massifs (jusqu'à quatre mille milliards de dollars par an jusqu'en 2030 comme mentionné dans le rapport sur les perspectives énergétiques mondiales publié par l'IEA en 2021) est nécessaire pour atteindre les objectifs discutés lors de l'Accord de Paris pour le climat, qui vise à limiter l'augmentation de température à 2 °C, voir 1.5 °C, d'ici la fin du siècle. Des modifications dans les modes de production d'énergie, la réduction de la consommation d'énergie des infrastructures déjà présentes et l'amélioration de l'efficacité énergétique peuvent être vus comme les principaux axes de développement permettant de réussir la transition énergétique. Pour atteindre ces objectifs, le développement de l'électrification est l'un des moyens envisagés. Cette tendance est confirmée par les prévisions de demande en électricité qui devrait augmenter de 4.5 % en 2021, soit cinq fois plus que la baisse de consommation de 2020. Toutefois, la production d'électricité par les énergies renouvelables telles que le solaire ou l'éolien est intermittente rendant primordiale le développement de dispositifs de stockage.

Parmi les dispositifs de stockage, l'utilisation de batteries permet de stocker par voie électrochimique l'énergie produite de manière intermittente. Ces dernières reposent sur deux électrodes, une positive et une négative dont les potentiels redox sont différents. Afin d'assurer le transport ionique, les deux électrodes sont séparées par un électrolyte, composé d'un solvant et d'un sel support. Le passage des électrons et donc du courant est assuré par le circuit électrique externe. Depuis la réalisation de la première batterie acide-plomb en 1859 par Gaston Planté, de nombreuses avancées ont été réalisées au niveau de la chimie de la batterie, de l'ingénierie et de l'optimisation de la cellule ainsi que du développement des usines de production, permettant d'améliorer les performances et la fiabilité tout en réduisant les coûts. Depuis sa première commercialisation en 1991 pour des appareils électroniques, les dernières années ont vu l'avènement de la technologie batterie Li-ion pour de nouveaux marchés comme les véhicules électriques. Cette technologie repose sur le mécanisme dit « rocking chair » d'intercalation des cations Li^+ dans les électrodes, et les prévisions de croissance du

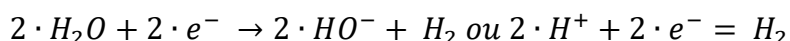
marché des batteries Li-ion (LIB) montrent que la demande va continuer d'augmenter dans les années à venir, avec des prévisions de marché atteignant 16 mille milliards de dollars en 2050. L'anticipation des questions de recyclage des batteries ainsi que le développement de matériaux plus durables sont donc des enjeux cruciaux. Or, l'un des désavantages des LIB actuellement commercialisées concerne l'électrolyte. En effet, celui-ci repose sur l'utilisation de solvants organiques, inflammables et toxiques qui questionnent la sécurité et la durabilité de ces systèmes. Le remplacement ces solvants par l'eau pourrait alors apporter une solution face à ces enjeux.

Les batteries rechargeables reposant sur un électrolyte aqueux sont connues et commercialisées depuis de nombreuses années. On peut notamment citer les batteries de type Acide-plomb utilisées comme batterie de démarrage dans les voitures, Nickel-Cadmium (Ni-Cd), présentes dans les premiers téléphones portables ou Nickel-Métal Hydrure (Ni-MH) commercialisées sous format AA ou AAA et dans les premiers véhicules hybrides électriques (tel que la Toyota Prius). Cependant, leur densité d'énergie et leur énergie spécifique sont limitées par l'étroitesse de la fenêtre électrochimique de l'eau (1.23 V thermodynamiquement). Au-delà des limites de cette fenêtre, les réactions parasites d'oxydation de l'eau (*oxygen evolution reaction* (OER), en anglais) et de réduction de l'eau (*hydrogen evolution reaction* (HER), en anglais) ont lieu au détriment de la stabilité de l'électrolyte, comme décrit par les Equation Résumé. 1 et Equation Résumé. 2, respectivement.

Equation Résumé. 1: Réaction d'oxydation de l'eau



Equation Résumé. 2: Réaction de réduction de l'eau



Concernant les batteries LIB aqueuses, la dégradation de l'électrolyte a lieu avant l'intercalation des cations Li^+ . Contrairement aux batteries LIB commerciales, la formation d'une interphase solide/électrolyte (*Solid electrolyte interphase*, en anglais (SEI)) n'est pas observée. Or, la formation de cette dernière est à l'origine de la plus grande densité d'énergie des batteries LIB commerciales car elle permet d'opérer au-delà des limites de la fenêtre électrochimique de stabilité. En effet, les électrolytes organiques classiquement utilisés, et plus précisément les solvants, sont instables à bas potentiels ($E < 1 \text{ V vs } Li^+/Li$), *i.e.*, aux potentiels où opèrent les électrodes négatives telles que le graphite. La dégradation de l'électrolyte au niveau de l'électrode négative au cours des premiers cycles d'utilisation forme une couche passivante, isolante

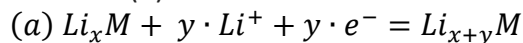
électroniquement et conductrice ionique qui prévient la dégradation supplémentaire de l'électrolyte et assure le maintien des performances. Cette couche est généralement issue des produits de décomposition du solvant, structurée par une couche interne riche en composés inorganiques et une couche externe riche en composés organiques. Pour résumer, l'absence de formation de SEI est l'un des freins au déploiement à grande échelle des batteries LIB reposant sur un électrolyte aqueux.

En 2015, le développement d'un électrolyte aqueux superconcentrés formé de 21 mol/kg de sel de LiTFSI, c'est-à-dire, un électrolyte dont la masse et le volume de sels sont supérieurs à ceux du solvant, a permis d'étendre la fenêtre électrochimique jusqu'à 3 V. Ces travaux sont inspirés par des études préalablement conduites sur des électrolytes organiques superconcentrés qui ont montré l'influence positive de l'augmentation de la concentration sur les propriétés de l'électrolyte. Dans le cas d'un électrolyte aqueux, l'augmentation de la concentration modifie la structure de l'électrolyte en créant deux réseaux interpénétrés : un réseau riche en anion, ici TFSI⁻, et un réseau riche en eau qui maintient le transport rapide des cations Li⁺ malgré la diminution du nombre de porteurs de charges dissociés. La réactivité interfaciale est aussi impactée. Au niveau de l'électrode positive, les anions TFSI⁻ peuplent l'interface par un effet de double couche permettant de repousser les molécules d'eau et donc de prévenir l'oxydation de l'eau. Au niveau de l'électrode négative, le dépôt d'une couche inorganique passivante par la dégradation du sel atteste de la formation d'une SEI. Ces changements de propriétés physico-chimiques et de réactivité interfaciale laissent penser que des batteries basées sur des électrolytes aqueux pourraient concurrencer les performances des batteries commerciales tout en améliorant leur durabilité. Ainsi, l'objectif de cette thèse est d'étudier la viabilité de l'utilisation d'électrolyte aqueux superconcentrés pour une application dans les LIB.

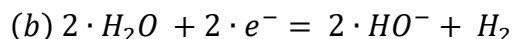
Pour cela, la mise en place d'une étude systématique a été réalisée au niveau des limites cathodiques (à l'électrode négative) et anodique (à l'électrode positive) afin de déterminer la stabilité de l'électrolyte basé sur 20 m LiTFSI en fonction des conditions d'opération. Bien que l'augmentation de la concentration ait montré un impact positif sur les performances, ces résultats peuvent être nuancés lors de changements de vitesse de cyclage qui mettent en évidence la présence de réactions parasites. Afin d'étudier la nature des réactions parasites, l'association de mesures en cellule de pression et de spectrométrie de masse couplée au cyclage électrochimique ont montré que la réaction de réduction de l'eau a lieu, à la fois pendant le cyclage et pendant les périodes de repos,

i.e. pendant l'autodécharge, comme décrit par les Equation Résumé. 3, Equation Résumé. 4 et Equation Résumé. 5.

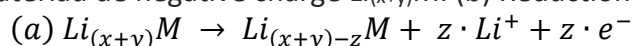
Equation Résumé. 3 : Réactions (a) d'insertion des cations Li^+ dans l'électrode négative Li_xM déchargée en parallèle de la (b) réduction directe de l'eau lors d'un cyclage continu.



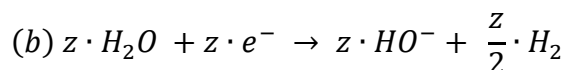
with $0 \leq x, 0 < y$, Li_xM , insertion material



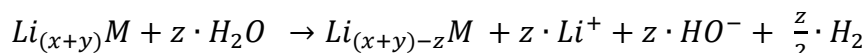
Equation Résumé. 4 : Demi-réaction redox du mécanisme d'autodécharge. (a) Désinsertion du matériau de négative chargé $\text{Li}_{(x+y)}\text{M}$. (b) Réduction de l'eau.



$$0 \leq x, 0 < y, 0 < z \leq y$$



Equation Résumé. 5 : Réaction global du mécanisme d'autodécharge.



De plus, bien que le mécanisme d'autodécharge soit en partie réversible vis-à-vis du lithium, la consommation d'eau est préjudiciable car irréversible. Enfin, l'utilisation de 20 m LiTFSI : 8 m LiBETI permet de compléter l'étude afin d'appréhender le comportement général des électrolytes aqueux superconcentrés. De la même manière que pour l'électrolyte basé sur 20 m LiTFSI, la réduction de l'eau a lieu pendant le cyclage et les périodes de repos, mais avec une moindre intensité. A l'électrode positive, des mesures de gaz ont montré que l'impact de l'oxydation de l'eau était limité. Le principal obstacle des électrolytes aqueux superconcentrés provient donc de l'électrode négative et de la stabilité de la SEI.

L'étude de la stabilité de la SEI native a été menée par des caractérisations électrochimiques (voltamétrie cyclique et spectroscopie d'impédance électrochimique). Les résultats montrent la passivation de la surface, mais la faible efficacité de celle-ci vis-à-vis de la réduction de l'eau. Cette dernière est mise en valeur par des expériences de calorimétrie à balayage différentiel qui atteste d'un décalage du pic de cristallisation de l'électrolyte après des phases de cyclage continu et d'autodécharge témoignant de l'augmentation de concentration. Par ailleurs, pour comprendre la différence de vitesses de consommation d'eau lors des phases de cyclage et d'autodécharge, les énergies

d'activation de la réduction directe de l'eau lors du cyclage et des phénomènes d'autodécharge ayant lieu pendant les phases de repos ont été étudiées. Les énergies d'activation trouvées sont semblables pour les phénomènes d'autodécharge et de réduction de l'eau (≈ 20 kJ/mol), suggérant que l'autodécharge est gouvernée par la réduction de l'eau plutôt que par la désinsertion du lithium. Pour résumer, l'impact néfaste de la réduction de l'eau pendant l'autodécharge et le cyclage soulignent l'instabilité de la SEI.

Aussi, le composé inorganique de fluorure de lithium (LiF) a été reporté comme l'un des contributeurs majeurs de la SEI. L'évaluation de la solubilité de LiF dans différents milieux tels que l'eau pure, 1 mol/kg LiTFSI, 20 mol/kg LiTFSI et 20 mol/kg LiTFSI : 8 mol/kg LiTFSI montre que, en considérant une épaisseur de LiF de ≈ 10 nm, semblable à l'épaisseur d'une SEI native, LiF ne devrait pas être dissout dans les électrolytes aqueux superconcentrés. Par conséquent, une couche artificielle de LiF déposée sur une électrode de lithium métal, dénotée par la suite Li/LiF, a été utilisée pour imiter le comportement d'une SEI native et évaluer l'efficacité d'une couche inorganique pour prévenir de la réduction de l'eau.

La technique de microscopie électronique à balayage environnementale permet d'observer la réactivité des échantillons de Li/LiF à une augmentation graduelle de l'humidité dans la chambre du microscope (de 0 % RH à 90 % RH). Ces observations, couplées à des mesures de chromatographie en phase gazeuse, démontrent que la couche de LiF n'empêche pas l'eau d'accéder à l'interface de Li. Contrairement à ce qui est observé lors de l'exposition d'un échantillon de Li/LiF à un électrolyte organique tel que LP30 (1 mol/L LiPF_6 in EC:DMC (1:1)), l'exposition à un électrolyte aqueux superconcentré ne permet pas d'auto-passiver l'échantillon. Cette absence d'auto-passivation est confirmée par la réalisation de mesures similaires sur des échantillons protégés par une couche de Al_2O_3 . En conclusion, ces résultats montrent que, bien que LiF ne se dissout pas dans les électrolytes aqueux superconcentrés, l'absence d'auto-passivation ne prévient pas la réaction de réduction de l'eau qui a lieu à travers les défauts de structures de la couche de LiF comme des fissures ou de la microporosité.

Pour surmonter ces obstacles, une étape de pré-imprégnation dans deux électrolytes organiques, 1 mol/L LiTFSI : 2 mol/L LiFSI dans DOL:DME + 3 % LiNO_3 ou 7 mol/L LiFSI dans FEC, connus pour former des SEI riches en LiF dans leur couche interne et des composés organiques dans leur couche externe, a été réalisée. Les mesures de chromatographie en phase gazeuse montrent une diminution de la production

d'hydrogène lors de l'exposition aux électrolytes aqueux superconcentrés des échantillons pré-imprégnés. La réalisation de mesures par spectrométrie photo électronique par rayons X (XPS) met en lumière le dépôt de composés issu de la dégradation du sel provenant de la solution de pré-imprégnation. Par conséquent, l'utilisation d'une couche artificielle de LiF couplée à la pré-imprégnation dans un électrolyte organique démontrent le caractère essentiel des propriétés auto-réparatrices de la SEI pour l'utilisation d'électrode négative dont le potentiel se situe en deçà de la limite de stabilité de la fenêtre électrochimique.

Enfin, la réalisation d'une figure de mérite permet de comparer les performances des batteries LIB basées sur les électrolytes aqueux superconcentrés avec celles des batteries LIB commerciales ainsi que les performances des batteries aqueuses rechargeables telles que les batteries Acide-plomb, Ni-Cd ou Ni-MH. L'utilisation d'un électrolyte tel que 20 m LiTFSI limite la fenêtre de fonctionnement d'une batterie à environ 2 V, afin d'éviter la contribution néfaste des réactions parasites. Ceci se fait au détriment de la densité d'énergie et de l'énergie spécifique (limitées au niveau des batteries type Ni-MH). De plus, alors que des solutions d'ingénierie ont été mis en place dans les batteries aqueuses rechargeable afin de gérer les gaz générés pendant le cyclage (O_2 ou H_2), la superconcentration peut causer la cristallisation rapide de l'électrolyte dans le cas de cellule type « vented » ou « flooded » qui évacue l'augmentation de pression sans compensation de l'eau consommée. Par ailleurs, paradoxalement, peu d'oxygène est produit au niveau de l'électrode positive tandis que la production d'hydrogène a lieu en parallèle de l'insertion des Li^+ à la négative, ce qui empêche l'implémentation du cycle de recombinaison de l'eau. En effet, dans les cellules types « sealed » ou certaines cellules types « vented », la batterie est dimensionnée afin que l'électrode positive soit limitante. En cas de surcharge, seule la réaction parasite d'oxydation de l'eau doit avoir lieu, l'oxygène produit à la positive diffuse alors dans l'électrolyte jusqu'à la négative où il est recombéné en eau, évitant à la fois la consommation irréversible d'eau et la production d'hydrogène.

En dehors des considérations énergétiques, un inconvénient majeur des électrolytes aqueux superconcentrés est leur haut point de fusion qui provoque la cristallisation rapide de l'électrolyte et empêche généralement leur utilisation à des températures inférieures à la température ambiante. L'introduction d'ions asymétriques permet d'abaisser cette température et de diminuer la quantité d'eau dite libre, c'est-à-dire non liée à un cation lithium en augmentant la solubilité. L'utilisation de co-solvant organique modifie la sphère de solvation des cations Li^+ , en réduisant la quantité d'eau dans la

sphère de solvation tout en promouvant la décomposition du co-solvant organique lors de la formation de la SEI. Cependant, l'eau reste l'une des composantes de la première sphère de solvation des cations Li^+ laissant penser que ces stratégies ne permettent pas pour l'instant de résoudre le challenge cathodique, qui atteste de la présence de molécule d'eau à l'interface de l'électrode négative à bas potentiel favorisant leur réduction. Pour résumer, les électrolytes aqueux superconcentrés font encore face à de nombreux freins qui empêchent, à l'heure actuelle, leur commercialisation. Parmi les stratégies envisagées pour améliorer ces systèmes, l'une d'elle repose sur l'intégration d'une couche polymère sur l'électrode négative pour à la fois empêcher physiquement l'accès de l'eau à l'interface négative et participer à la formation de la SEI par décomposition partielle ou totale de cette couche polymère. Malgré la publication de cellules basées sur une électrode de graphite recouverte d'un gel composé de 0.5 mol/L de LiTFSI dans un électrolyte basé sur le mélange HFE:DMC (1,1,2,2-tetrafluoroethyl-2',2',2'-trifluoroethyl ether :dimethylcarbonate), nous n'avons pour l'heure pas encore réussi à reproduire ces résultats afin de tester la viabilité de cette solution.

Towards aqueous superconcentrated electrolytes and their use in Li-ion battery

The development of superconcentrated aqueous electrolytes, namely *Water-in-salt electrolytes* (WiSE), from 2015 onwards has renewed the interest for aqueous-based Li-ion battery (LIB). Indeed, they were proposed to overcome issues related to safety and sustainability of common carbonate-based organic solvent while solving the poor performances of diluted aqueous electrolyte due to the narrow electrochemical stability window (ESW) of water (1.23 V). Such achievements are largely attributed to modification of the electrolyte structure upon increase in concentration that changes the physico-chemical properties and the interfacial reactivity. An inorganic LiF-based solid electrolyte interphase (SEI) was reported to be formed, opening the path for the use of low potential negative electrodes, further increasing the energy density of these batteries.

This work aims to provide answers regarding the viability of WiSE in LIB. By conducting a systematic study of the impact of superconcentration on battery performances as function of the operating conditions, we demonstrate that the SEI is not able to prevent water reduction following the hydrogen evolution reaction (HER), neither during cycling nor during resting period, *i.e.* self-discharge. Indeed, the rates for water consumption calculated during cycling and resting period are found within the same order of magnitude, highlighting the SEI limitation to prevent water reduction although the surface is passivated. Determining the activation energies for HER during cycling and self-discharge, we suggest that self-discharge is more likely driven by water reduction than Li⁺ deintercalation. Eventually, LiF solubility measurements, gas chromatography tests and environmental scanning electron microscopy suggest that SEI instability is related to structural defects that cannot be self-passivated in WiSE. A presoaking step in organic electrolyte of an artificial Li/LiF layer reduces water consumption and thus confirms the need for the SEI to self-repair.

Keywords: aqueous Li-ion batteries, *Water-in-salt*, SEI stability, superconcentrated electrolyte

Vers des électrolytes aqueux superconcentrés et leur application pour une utilisation batterie Li-ion

Depuis 2015, le développement des électrolytes aqueux superconcentrés, dénommés « *Water-in-salt electrolytes* » (WiSE), a suscité un regain d'intérêt pour les batteries Li-ion (LIB) aqueuses. Les WiSE proposent une alternative aux électrolytes organiques commerciaux qui posent des problèmes de sécurité et de durabilité, tout en résolvant les faibles performances des électrolytes aqueux dilués limitées par l'étroitesse de la fenêtre électrochimique (1.23 V). En effet, la superconcentration influe sur les propriétés physico-chimiques et la réactivité interfaciale. La formation d'une interphase solide/électrolyte inorganique (SEI) riche en fluorure de lithium (LiF) ouvre la voie à l'utilisation d'électrode négative à bas potentiel et donc à l'augmentation de la densité d'énergie de ces batteries.

Cette thèse étudie la viabilité des électrolytes WiSE dans les LIB. Grâce à la mise en place d'une étude systématique, l'impact de la superconcentration sur les performances des batteries en fonction des conditions d'opération montre que la SEI formée ne prévient pas de la réduction de l'eau, appelée réaction d'évolution de l'hydrogène (HER) ni pendant le cyclage ni pendant les périodes de repos, *i.e.* l'autodécharge. L'évaluation des vitesses de consommation de l'eau souligne les limites des propriétés protectrices de la SEI malgré la passivation de l'interface. Par ailleurs, la détermination des énergies d'activation de la HER directe, ayant lieu pendant le cyclage, et du phénomène d'autodécharge suggère que l'autodécharge est gouvernée par la HER. Enfin, l'évaluation de la solubilité de LiF dans les WiSE, des observations au microscope environnemental à balayage électronique et des mesures de chromatographie en phase gaz suggèrent que l'instabilité de la SEI est d'avantage reliée à des défauts microstructuraux qui ne peuvent pas être comblés dû à l'absence d'auto-passivation de l'interface. Une étape de pré-imprégnation dans un électrolyte organique réduit la consommation d'eau, confirmant la nécessité de propriétés d'autoréparation de la SEI.

Mots-Clés : Batteries Li-ion aqueuses, *Water-in-salt*, stabilité de la SEI, électrolytes superconcentrés